Design of Semiconductor/ Oxide Heterostructures for Enhanced Photoelectrochemical Water Splitting

A Dissertation Submitted to the

Indian Institute of Technology Guwahati

in Partial Fulfilment for the Degree of

DOCTOR of PHILOSOPHY

By

Tushar Kanta Sahu

DEPARTMENT OF CHEMISTRY

INDIAN INSTITUTE OF TECHNOLOGY GUWAHATI

GUWAHATI, ASSAM, INDIA

DECEMBER 2020

Design of Semiconductor/ Oxide Heterostructures for Enhanced Photoelectrochemical Water Splitting

A Dissertation Submitted to the

Indian Institute of Technology Guwahati

in Partial Fulfilment for the Degree of

DOCTOR of PHILOSOPHY

By

Tushar Kanta Sahu

Roll No. 156122009

DEPARTMENT OF CHEMISTRY

DEPARTMENT OF CHEMISTRY

INDIAN INSTITUTE OF TECHNOLOGY GUWAHATI

GUWAHATI, ASSAM, INDIA

DECEMBER 2020

STATEMENT

I hereby declare that the scientific findings included in this thesis entitled, "**Design of Semiconductor/ Oxide Heterostructures for Enhanced Photoelectrochemical Water Splitting**" is the outcome of research work carried out by me under the supervision of Prof. Mohammad Qureshi, at Department of Chemistry, Indian Institute of Technology Guwahati, Guwahati, Assam, India, for the award of the degree of Doctor of Philosophy.

The work embodied in this thesis is the result of original research done by me except where otherwise stated in this thesis with proper citations. I confirm that the investigations were conducted in accord with the ethics policies and integrity standards of Indian Institute of Technology Guwahati and that the research data are presented honestly and without prejudice. The thesis work has not been submitted for a degree or professional qualification to any other university or institution.

IIT Guwahati Tushar Kanta Sahu

December 2020

Dr. Mohammad Qureshi
Professor
Department of Chemistry
Indian Institute of Technology Guwahati
Guwahati – 781036, India
Tel: +91 – 361 – 2582320;
Fax: +91 – 361 – 2582349
Email: mq@iitg.ac.in

Certificate

Certified that the work described in this thesis entitled "**Design of Semiconductor/ Oxide Heterostructures for Enhanced Photoelectrochemical Water Splitting**" by Mr. Tushar Kanta Sahu, Department of Chemistry, Indian Institute of Technology Guwahati has been carried out under my supervision and has not been submitted elsewhere for a degree.

Guwahati
December 2020

Mohammad Qureshi
Thesis supervisor
Department of Chemistry
Indian Institute of Technology Guwahati
Guwahati – 781039, Assam, India

ACKNOWLEDGEMENT

Undertaking this PhD has been a truly life-changing experience for me and it would not have been possible to do without the support and guidance that I received from many people.

It is a genuine pleasure to express my deep sense of thanks and gratitude to my mentor and thesis adviser, Professor Mohammad Qureshi, for his continuous support throughout my PhD tenure. I sincerely thank him for his constant guidance, encouragement and freedom to work which assisted me in completing the work assembled in the thesis. I could not have imagined having a better advisor and mentor for my research study.

I an extremely grateful to my doctoral committee members, Dr. Kalyan Raidongia, Prof. Aditya Narayan Panda, Dr. Uttam Manna and Dr. Shyam Prasad Biswas for their assistance and suggestions throughout my PhD work. I sincerely thanks to my collaborators, Dr. Sonia Arora, Prof. Parameswar Krishnan Iyer, Dr. Nageswara Rao Peela and Devipriya Gogoi for their continuous helps and support. I would like to thank all faculty members and staff members of Chemistry department. My sincere thanks to the staffs of Central Instruments Facility, for their help and in hand guidance to several analytical instruments, required during my research work. Special thanks to Milan and Sujit for teaching me the operation of FETEM instrument. I wish to express my sincere gratitude to IIT Guwahati for all the facilities that were made available to me and the Ministry of Human Resource Development (MHRD), India for the financial support.

I would like to thanks my past and present lab members - Dr. Tridip, Dr. Anindya, Dr. Shaad, Dr. Avishek, Dr. Gaurangi, Suhaib, Adit, Moite, Manoj, Sourav, Nitul and Alpana for their timely help, support and for creating a pleasant atmosphere in the lab. I would specially like to thanks Dr. Gaurangi, Dr. Avishek and Dr. Shaad for teaching me basics, experiments and handling instruments in the initial periods of my research work.

I extend my sincere thanks to my beloved friends Biswajit, Vinod, Munendra, Rupinder, Umesh, Bipin, Ashish, Jagnyesh and Chiranjib for all the love and support throughout this time. I take this opportunity to thanks Sudam, Shraban, Debu, Sourav, Prakash, Sanatan, Bharat, Sushanta, Kamal and Bidyasagar for their encouragement and love.

Apart from the research activities, the joyous and memorable time spent with my friends and seniors, Balaram Da, Dileep Da, Swarup Da, Aneeta Nani, Trushna Nani, Biswajit, Niranjan

and Prakash is unforgettable. Thank you guys for always being there for me in my good and bad times.

Finally, my Ph. D. endeavor could not have been completed without the endless love, unending support, tolerance and blessings from my family. I would like to express my deepest gratitude to my parents for all the unconditional love and sacrifices they have made for the sake of my upbringing. I am also grateful to my sister, brother and cousins for their affection and deep concern for my career.

Still many names are missing whose contribution and help is worth mentioning.

Tushar

TABLE OF CONTENTS

Dedicated

To

My Beloved Parents

Thesis Title: **Design of Semiconductor/ Oxide Heterostructures for Enhanced Photoelectrochemical Water Splitting**

Name of the Candidate: Tushar Kanta Sahu

Registration Number: 156122009

Thesis Supervisor: Prof. Mohammad Qureshi

Department: Chemistry

Institute: Indian Institute of Technology Guwahati, Assam – 781039, India.

Thesis Overview

Chapter 1: Introduction and Literature Survey

Recent progress in rational design and synthesis of several semiconductors and metal oxide based heterostructures based on their performances, accountable for the light harvesting ability, better photogenerated electron-hole separation and charge transfer have been discussed in the present chapter. An overview on photoelectrochemical technology, basic concepts and working principle of photoelectrochemical water splitting are briefly discussed. This chapter also includes a brief literature survey of current state-of-the art scenario and challenges related to the design and development of semiconductors, utilized for photoelectrochemical applications. Advantages of different narrow band gap photoanodic materials have been discussed to improve the charge separation as well as light harvesting ability of the photoanodic material. With respect to present state of art, different surface modification strategies which have been used for tuning the surface activity are costly, low abundance and environmental unfriendly. Therefore, with low cost and environmentally benign photoanodes different strategies have been applied to overcome the drawbacks encountered by these materials. A brief discussion related to the development of different metal oxide based photoelectrode, their advantages and disadvantages, and related

mechanisms for PEC performances are also included. This chapter is concluded with a brief literature survey and motivation behind designing different metal oxides based photoelectrodes.

Chapter 2: Experimental Section

Comprehensive routes for the synthesis and fabrication of materials and basic instrumentation techniques used for material characterization have been discussed in chapter **2**. This chapter also includes photoanode preparation, sensitization and characterization of the photoelectrochemical devices using various instrumental techniques/methods. Photoelectrochemical parameters of photoanodes are characterized using instrumental techniques such as CHI 1120B (current–voltage characteristics), IQE–200 (incident photon-to-current efficiency, IPCE analyzer) and CHI 660D (electrochemical impedance spectroscopy, EIS measurements). This chapter is concluded with the fabrication of photoanode materials directly over conductive substrate for the utilization of photoelectrochemical water oxidation. The amount of hydrogen and oxygen generated by the photoanodes during PEC water oxidation was measured by gas chromatography.

Chapter 3: Surface Passivation of Zinc Ferrite as an Effective Strategy for Enhanced Photoelectrochemical Water Oxidation: Fabrication and Photoelectrochemical Characterizations [Chem. Commun., 2018, 54, 10483]

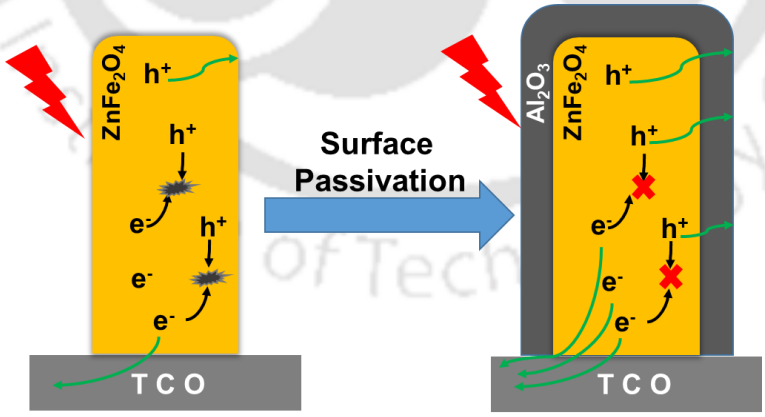

Figure 1. Schematic representation of electron-hole recombination with and without the presence of surface overlayer in $ZnFe_2O_4$ photoanode.

In this Chapter, effect of surface overlayer on the photoelectrochemical properties of zinc ferrite is investigated using Al_2O_3 as an overlayer. Enhanced performance of zinc ferrite is attributed to the cumulative effects of this composite i.e., (i) the compactness and the crystallinity of the $ZnFe_2O_4$ nanorods increased with increasing the annealing temperature to 800 °C (ii) 1-D structure of zinc ferrite gives rise to efficient charge separation and provides a very short diffusion path for holes to reach the electrode/electrolyte interface, (iii) the Zn 2p, Fe 2p and O 1s peaks in $ZnFe_2O_4$–Al_2O_3 slightly shifted towards the higher binding energies compared to $ZnFe_2O_4$, due to the chemical interaction between $ZnFe_2O_4$ and the Al_2O_3 layer. With a thin Al_2O_3 overlayer with zinc ferrite, the photocurrent increased up to 0.484 mA cm^{-2}, which was around 7-fold and 3-fold higher than those of $ZnFe_2O_4$-550 and $ZnFe_2O_4$-800, respectively. Increased PEC performance is mainly due to (i) increase in compactness and improved crystallinity with higher annealing temperature, (ii) thin alumina overlayer reportedly contributed to the change of the lattice strain of $ZnFe_2O_4$ layers which decreased the density of surface trap states and (iii) surface passivation of $ZnFe_2O_4$ rather than the contribution of the oxygen evolution reaction (OER) from the passivation layer. Further, electrochemical impedance spectroscopic (EIS) analyses showed an efficient interfacial charge transfer by reducing the recombination processes i.e., the back transferring of photo-excited electron at electrode/electrolyte interface. Figure **1** depicts the schematic representation of mechanism involves in enhanced photoelectrochemical performance of zinc ferrite with and without a surface overlayer. Morphological features of as-synthesized $ZnFe_2O_4$ and their utilization in PEC study are depicted in the figure **2** and **3**, respectively.

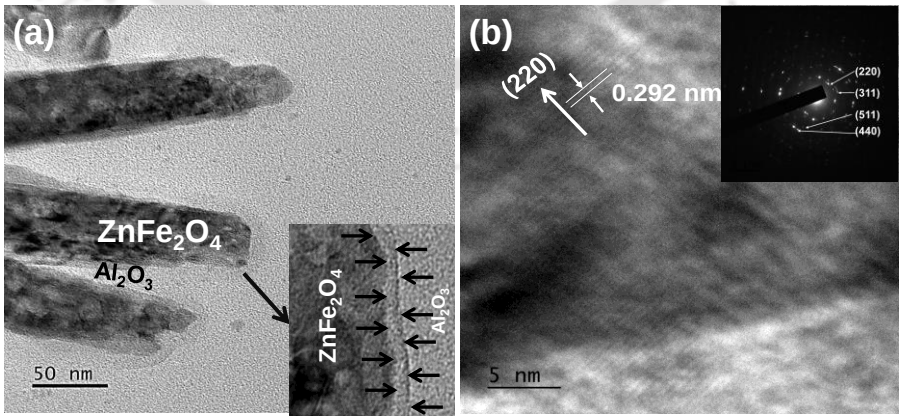

Figure 2. (a) FETEM of $ZnFe_2O_4$–Al_2O_3 (the inset showing the uniform coating of alumina with a thickness of around 5 nm). (b) HR-TEM of $ZnFe_2O_4$–Al_2O_3 (the inset showing the selected area electron diffraction (SAED) pattern of $ZnFe_2O_4$–Al_2O_3).

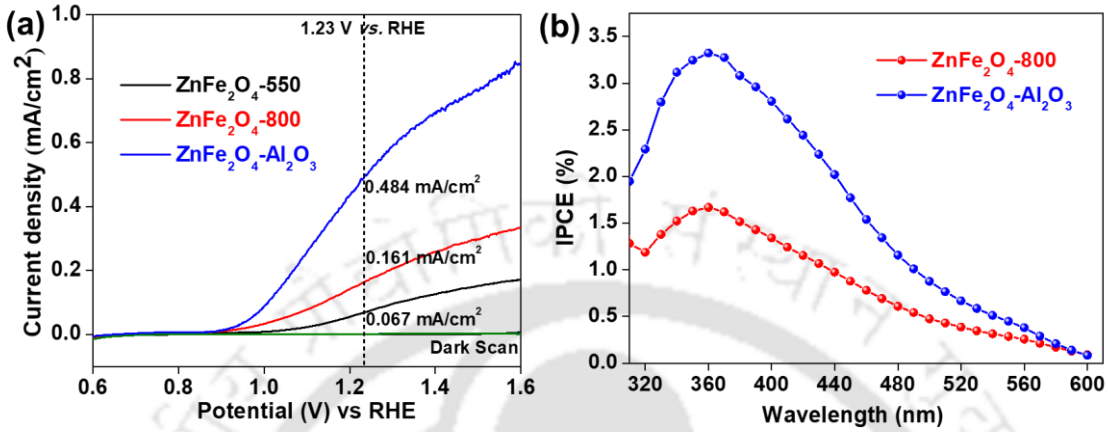

Figure 3. (a) J–V curves of all the photoanodes under light illumination at a scan rate of 10 mV s^{-1} in 1 M NaOH and (b) the IPCE spectra of the as-prepared photoanodes at 1.23 V vs. RHE.

Chapter 4: Sequential Metal and Non-metal Incorporation in Hematite Photoanode: Fabrication, Bulk and Interfacial Charge Transfer Dynamics and Photoelectrochemical Water Oxidation Performance [ACS Appl. Energy Mater. 2019, 26, 4325]

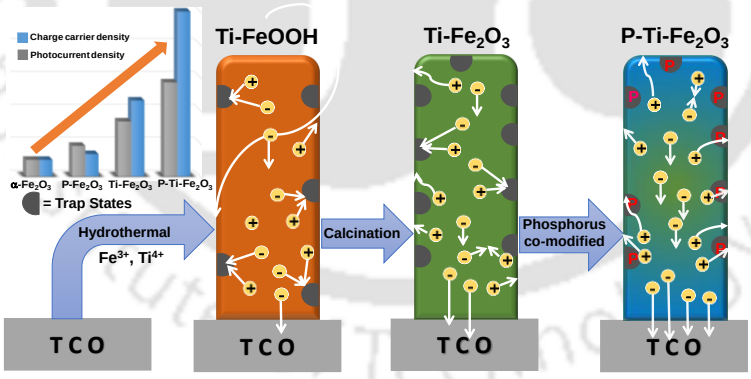

Figure 4. Schematic illustration of synthetic route for Titanium and Phosphorus incorporated hematite photoanode depicting trap states and charge separation with and without modification. The charge carrier density and photocurrent density vs. different photoanodes with and without modification are also depicted.

This Chapter demonstrates the design and synthesis of a stable hematite photoanode with sequential metal and non-metal incorporation to resolve the limiting factors such as low carrier density and high charge recombination which hinder its practical applications. Comprehensive

morphological, optical, and photoelectrochemical properties of the doped hematite photoanodes are presented to understand the mechanisms by which the dopant incorporation impacts the photoelectrode performance. A photocurrent density of 2.56 mA/cm^2 at 1.23 V vs. RHE was observed for Ti and P co-modified hematite with an unprecedented cathodic shift of the onset potential of ~90mV. The enhanced PEC performance can be attributed to the combined effect of faster carrier mobility due to Ti-doping and reduced surface trap states due to P-modification results in better current density in the case of co-modified hematite. Therefore, the P-modification on Ti-doped hematite may reduce the surface electron−hole recombination and decreases the surface hole accumulation on hematite surface.

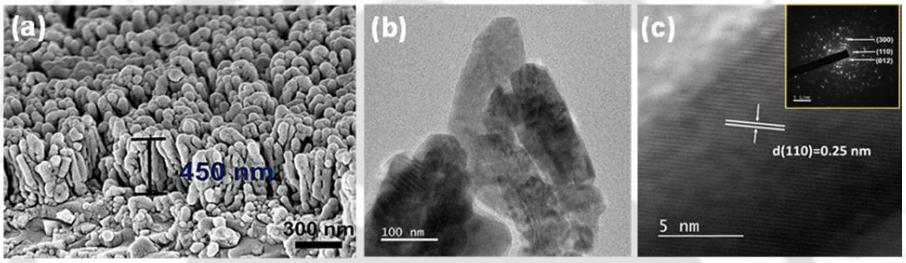

Figure 5. (a) Cross-sectional FESEM image of P−Ti−Fe_2O_3, (b) FETEM image of P−Ti−Fe_2O_3, (c) HRTEM of P−Ti−Fe_2O_3. Inset to (c) shows the SAED pattern of P−Ti−Fe_2O_3.

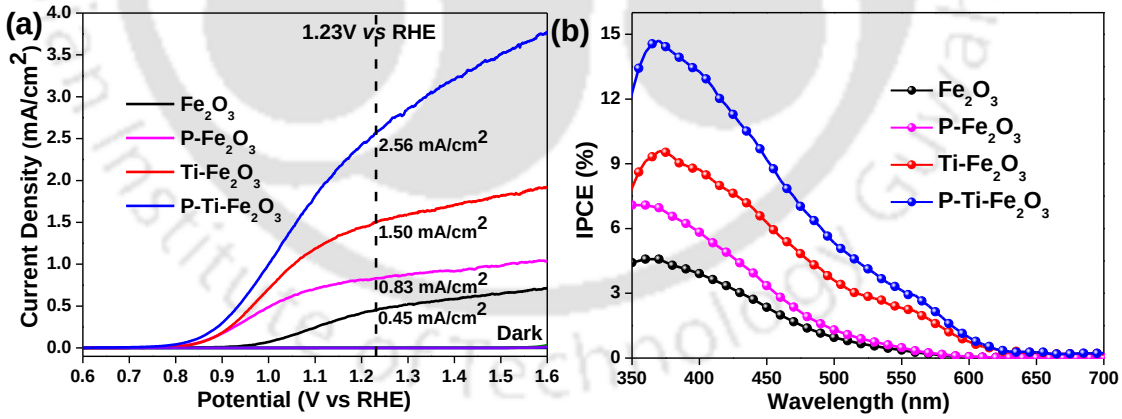

Figure 6. (a) Current density (J) vs. applied voltage (V) curves of bare as well as modified hematite photoanodes under light illumination at a scan rate of 10 mV/s in 1 M NaOH and (b) IPCE values collected for a-Fe_2O_3, P-Fe_2O_3, Ti-Fe_2O_3 and P-Ti-Fe_2O_3 photoanodes.

Figure **4** depicts the schematic illustration of synthetic routes for the fabrication of phosphorus and titanium incorporated hematite photoanode with *in situ* doping of titanium and *ex situ* doping

of phosphorus. Morphological features of bare as well as modified hematite and photoelectrochemical performance of modified hematite are depicted in the figure **5** and **6**, respectively.

Chapter 5: Boron Nitride Quantum Dots as a Hole Extractor for Fluorine Doped Hematite Photoanode: Fabrication, Effect on Interfacial Charge Transfer Properties and Photoelectrochemical Water Oxidation Performance [J. Power Sources, 2020, 445, 227341]

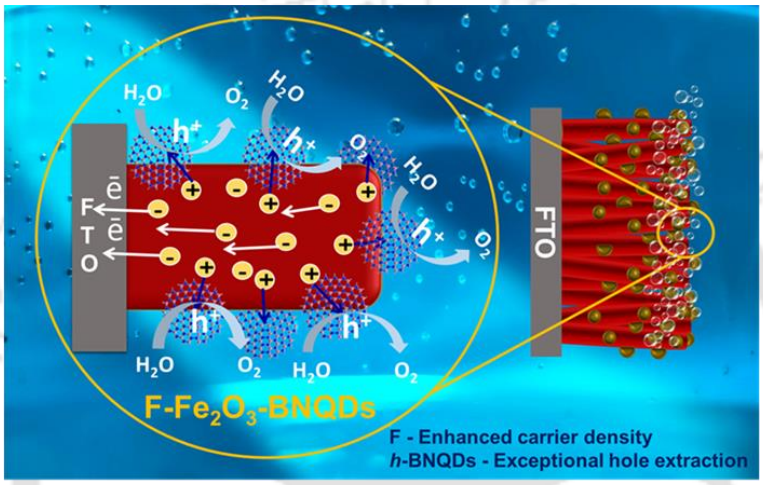

Figure 7. Schematic representation of BNQDs modified fluorine doped hematite photoanode showing the enhanced hole extraction ability of BNQDs which leads to efficient water oxidation.

This Chapter demonstrates a facile one step low temperature hydrothermal route for the controlled synthesis of boron nitride quantum dots (BNQDs), assembled with fluorine doped hematite photoanode. The sluggish water oxidation kinetics in hematite photoanode is dominated by unfavorable recombination of photogenerated holes which restrict the efficiency of photoelectrochemical (PEC) water splitting. BNQDs has high negative charge density, particularly on the edge geometry, therefore it can act as an efficient hole extractor, which enhances the carrier separation on hematite surface and decreases the hole trapping probability. This work emphasizes on two important parameters, i.e. (i) enhancement in carrier density via fluorine doping directly onto the substrate using soluble precursor, organic Selectflour {1-Chloromethyl-4-fluoro-1, 4-diazoniabicyclo[2.2.2]octane bis(tetrafluoroborate)} (ii) modification with BNQDs to provide a simple, novel and effective strategy for the design and development of more efficient PEC water splitting systems. A ~6 fold increase in PEC with a

photocurrent density of 2.25 mA/cm^2 (at 1.23V vs. RHE) is achieved for the co-modified hematite photoanode. Schematic representation of BNQDs modified fluorine doped hematite photoanode showing the enhanced hole extraction ability of BNQDs which leads to efficient water oxidation is shown in figure **7**. Morphological characterizations of as-fabricated BNQDs modified F-doped hematite and its photoelectrochemical performances based on its hole extracting ability are depicted in the figure **8** and **9**, respectively.

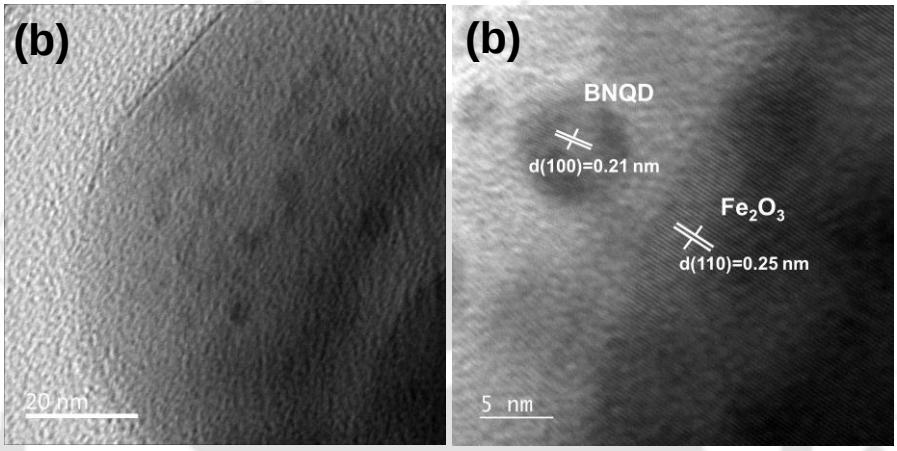

Figure 8. (a) FETEM image and the corresponding (b) HRTEM of boron nitride quantum dots (BNQDs), (c) FETEM image and the corresponding (d) HRTEM of F-Fe_2O_3-BNQDs.

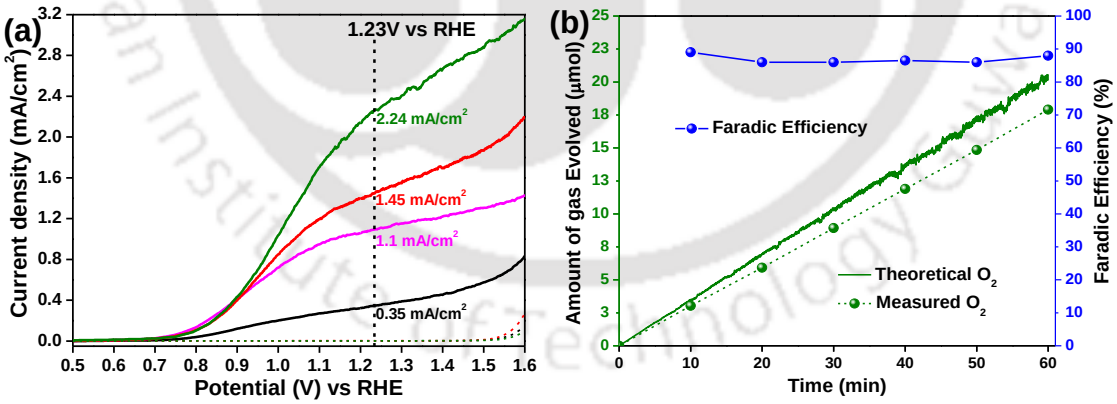

Figure 9. (a) Linear sweep voltammograms of all photoanodes under light illumination and (b) faradic efficiency test of F-Fe_2O_3-BNQDs for oxygen evolution.

Chapter 6: Cobalt - Cerium Mixed Double Hydroxide as Co-catalyst over $BiVO_4$ Photoanode: Role of Cerium, its Effect on Water Oxidation Kinetics, Stability and Photoelectrochemical Performance [ACS Appl. Energy Mater. 2020, 3, 5610]

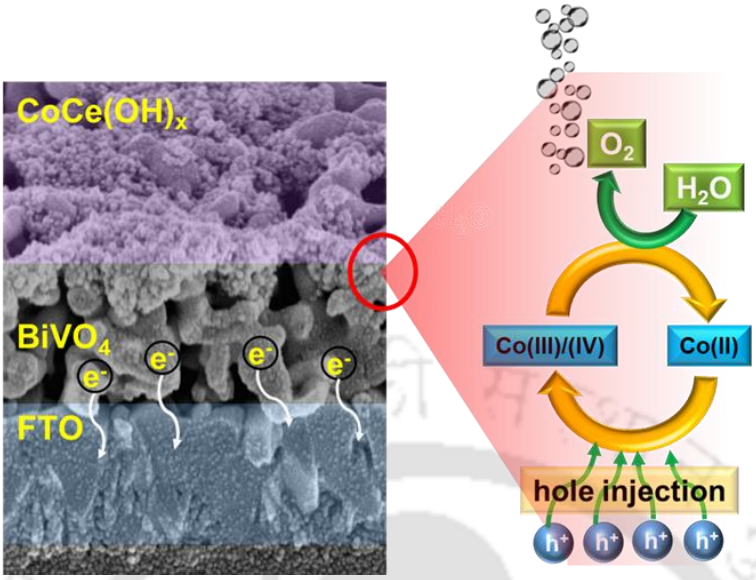

Figure 10. Schematic representation showing probable mechanism resulting enhanced water oxidation kinetics of $BiVO_4$ photoanode with $CoCe(OH)_x$ co-catalyst modification.

This chapter presents the surface co-catalytic modification of $BiVO_4$ for promoting water oxidation kinetics to enhance the interfacial charge transfer, lowering of onset potential, resulting in an efficient photoelectrochemical (PEC) water oxidation. We have designed the $BiVO_4$ photoanode, coupled with a mixed metal hydroxide containing cobalt and rare-earth element cerium, where the addition of catalytically silent cerium to $Co(OH)_x$ not only enhanced the stability, but also improved the water oxidation kinetics. With $CoCe(OH)_x$ catalytic overlayer, a ~370 mV onset cathodic shift is observed, indicative of an efficient charge injection and enhanced surface oxidation kinetics with a photocurrent density reaching up to 3.74 mA/cm^2 and a solar-to-hydrogen efficacy of 4.3%. The water oxidation performance of $BiVO_4$ - $CoCe(OH)_x$ could be attributed to the synergistic effect of both cobalt and cerium, where cerium incorporation enhanced the surface passivation aiding the stability of the photoanode and formation of Co(II)/(III) active sites fasten the surface kinetics of $BiVO_4$. An average Faradaic yield of ~94% suggests that majority of the holes have been utilized for water oxidation. We believe that the present design of $BiVO_4$ photoanode with mixed metal hydroxide provides a promising and efficient strategy for modification of photoanode with stable and highly active oxygen evolution co-catalysts. Morphological features of modified $BiVO_4$ photoanode and photoelectrochemical performances are shown in the figure **11** and **12**, respectively. Cyclic

voltammetry of the photoanodes gives the probable mechanism for efficient PEC performances as shown in figure **13**.

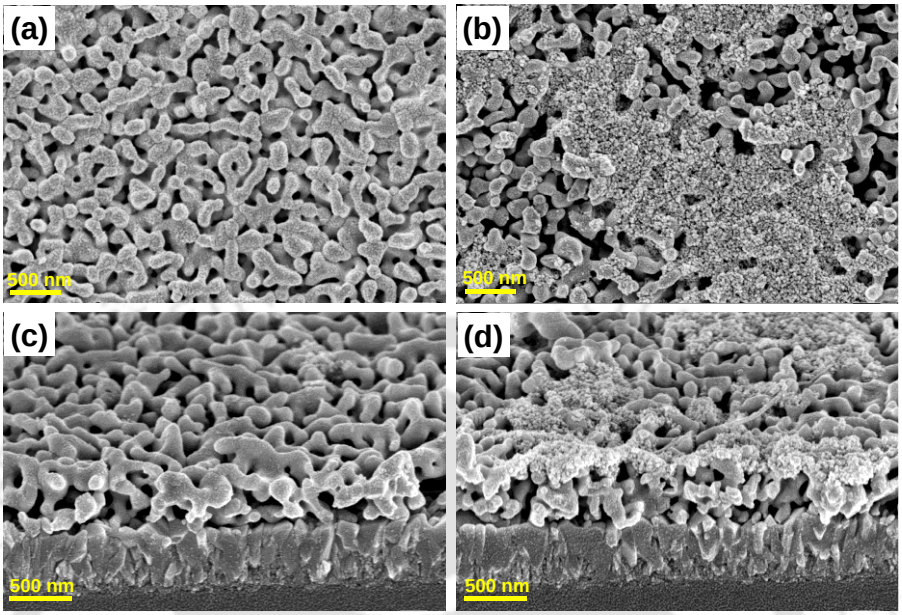

Figure 11. FESEM images with top and cross-sectional view of (a,c) $BiVO_4$ and (b, d) $BiVO_4$- $CoCe(OH)_x$ with worm-like shaped three-dimensional structure.

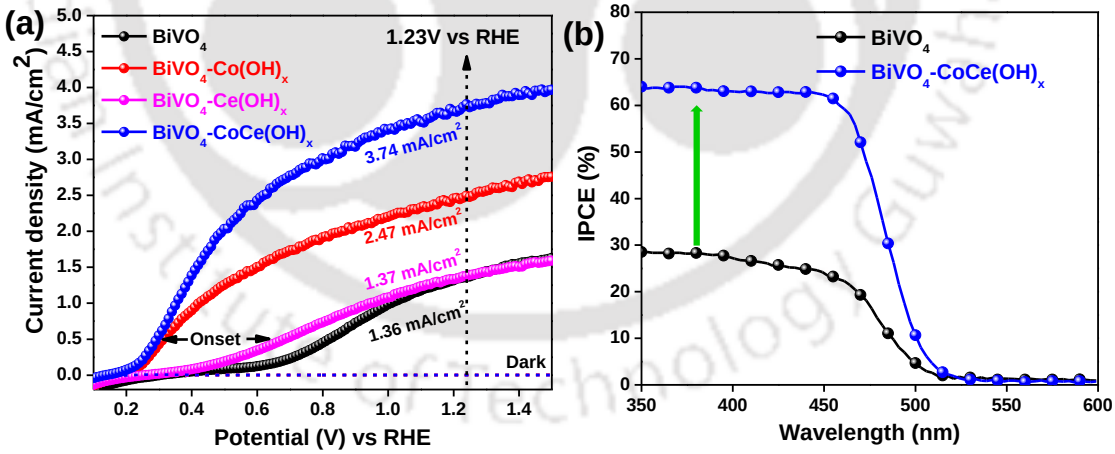

Figure 12. (a) Current density-voltage (J–V) curve for all the photoanodes. (b) IPCE plots for $BiVO_4$ and $BiVO_4$-$CoCe(OH)_x$.

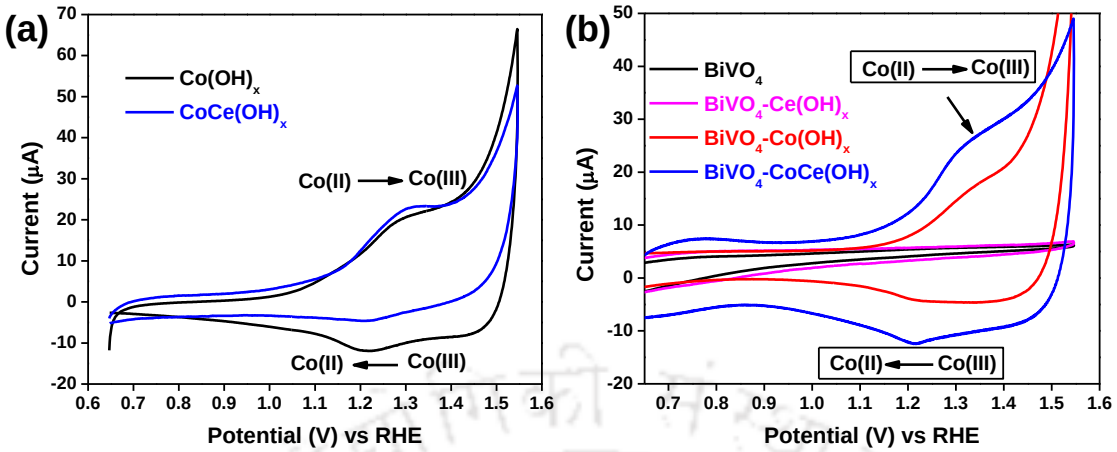

Figure 13. (a) Cyclic voltammetry measurement of $Co(OH)_x$ and $CoCe(OH)_x$ and (b) Cyclic voltammetry measurement of all the photoanodes before illumination.

Conclusions and Overview

In conclusion, we have tuned the surface activities of semiconductor metal oxides using different surface modification strategies. Various surface modification strategies such as passivation layer, active layer, hole extractor and co-catalyst are explored to modify the metal oxide photoanodes. We have used narrow band gap (2~2.5 eV) metal oxide semiconductor materials to fabricate the hybrid photoanodes for photoelectrochemical water oxidation. High performances photoelectrochemical devices have been fabricated utilizing the surface modification strategies by enhancing charge carrier density, efficient electron-hole separation and water oxidation kinetics of the photoanode materials. The present method for the modification of different photoanodes with surface modifiers are simple and effective, and might provide several ways of getting stable and high-performance photoelectrodes.

CHAPTER 1

Introduction and Literature Survey

In this chapter, motivation behind the research on photoelectrochemical water splitting is described. The increasing demand for energy and the impacts of global warming across the globe are urging us to discover alternative renewables and eco-friendly solutions. Solar energy, which has the potential to meet the world's energy demand, will be highlighted in the thesis. It also presents various characteristics of metal oxide based photoanodes for solar water splitting to produce hydrogen and oxygen discussing the advantages and disadvantages for solar water splitting followed by different approach to address the well-described limitations of these photoanodes.

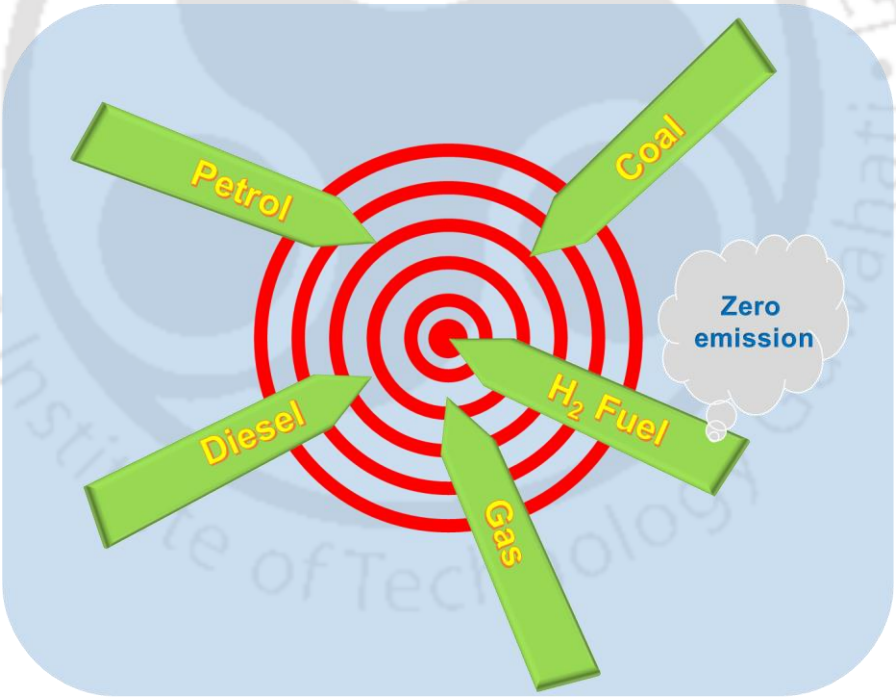

1.1 GLOBAL ENERGY CRISIS AND CLIMATE CHANGE: AN OVERVIEW

Energy supply and climate change are the two main challenges that the world is going to face in the coming decades and both are strongly linked to each other. After the industrial revolution, the world has experienced an exponential increase in the energy demand. The world population is currently estimated to be ~7.8 billion with a power consumption of ~25 terawatts (TW, 25×10^{12} Joules s^{-1}). [1,2,3] It will likely increase to ~9 billion in 2050 with an estimated power consumption of ~40 TW.[3] Our current energy system primarily depends on non-renewable depleting resource fossil fuels such as oil, coal and natural gases. Moreover, the unavoidable emission of greenhouse gases into the atmosphere, particularly carbon dioxide (CO_2) is always accompanied by the use of fossil fuels, which causes global warming apart from other undesirable effects.[4] The CO_2 released to the atmosphere causes an increase in the average temperature of the earth by absorbing infrared radiation. Within the last decades this emissions of CO_2 have been dramatically increased and are estimated to continue rising each year by almost 3%.[5] If the amount of CO_2 emissions by fossil fuels remain same, the associated greenhouse gases stocking of the atmosphere will stance a severe environmental threat to human civilization.

Every year, the cost and difficulty of mitigating greenhouse emissions increase as reported by the International energy agency (IEA).[3] To reduce the greenhouse emissions, the energy sector must play a critical role. Development of new technologies are necessary to meet the current and future energy demands without producing any greenhouse gases. Currently, more than two-thirds of the world's greenhouse gas is produced from use of energy, which are generated from oil and coal consumption. According to the Intergovernmental Panel on Climate Change (IPCC) report, the increase in temperature caused by global warming must not exceed 2 °C and the CO_2 concentration in the atmosphere has to be kept below 450 ppm in order to avoid disastrous consequences.[6] To achieve this, the CO_2 emissions have to be reduced worldwide. In this regard, the awareness of climate change and its consequences are getting more attention globally. With an increase in energy consumption, low carbon emission technologies have to be improved as the alternatives to conventional energy sources. The 2015 United Nations Climate

Change Conference, which has been signed by 197 countries, sets out to reduce the emission of gases that contribute to global warming and a framework to avoid dangerous climate change by averting the global temperatures from increasing more than 2 °C.[7] In this severe scenario, we need to look into renewable energy sources for a sustainable energy solution to address the future energy supply and climate change.

1.2 RENEWABLE ENERGY SOURCES

The advancement in new technologies are necessary to counter the energy demands and to use environment-friendly carbon-free and renewable or carbon-neutral energy sources as a replacement of current carbon-rich fossil fuels. With the use of renewable and carbon-free energy sources such as wind power, solar power, nuclear power, geothermal and hydroelectric energy, etc., CO_2 emissions can be significantly reduced. Also, these renewable energy sources have the potential to meet the world's energy demand. The even distribution of these renewable energy sources globally has an advantage over conventional energy sources as the latter is only geographically concentrated. The current estimated energy reserves available on the earth is provided in **Figure 1.1** which signify that solar energy has the leading position among all others renewable and non-renewable energy sources.[8] The Sun's annual flow of energy to the earth's surface is in several orders of magnitude compared to all other recoverable energy reserves on earth. The Sun provides around 1,73,000 TW of energy to the earth's surface, which is thousands of times above the needs of humankind.[9] Clearly, to meet all energy needs for the lifetime of the solar system, solar energy is much more than enough. Still, developing economically feasible technologies for harnessing, storage and utilization of solar energy is quite challenging. However, no other sustainable energy source comes close to solar power. It is the only renewable energy source that has enough potential to gratify the current and future energy demands with zero carbon emission.

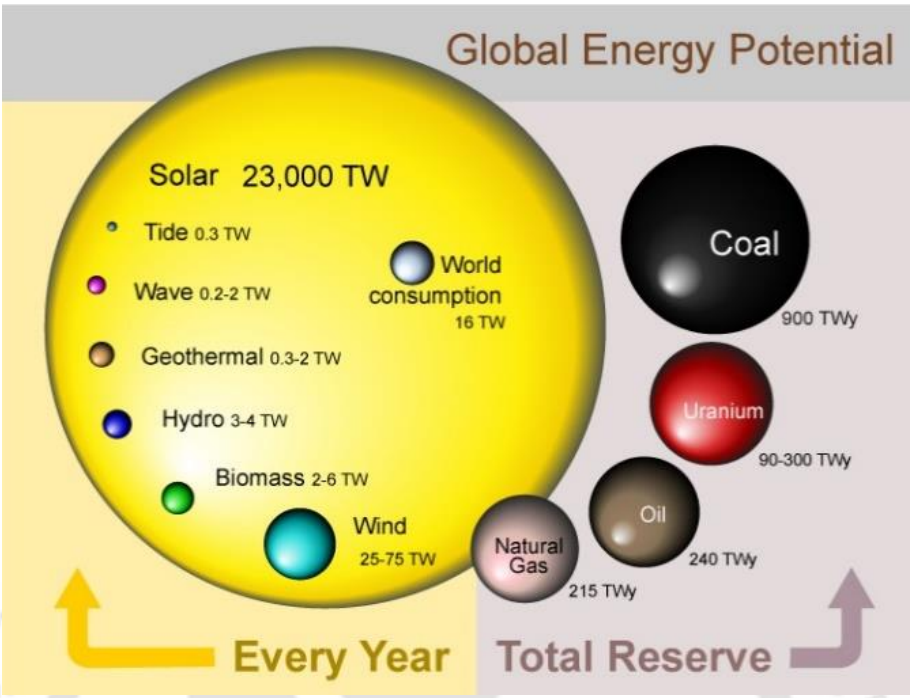

Figure 1.1 Estimated energy reserves available on the earth which can be utilized for energy generation. (Source: https://commons.wikimedia.org/wiki/File:Global_Energy_Potential_2014_08_09.svg)

For the proper harnessing of solar power, among many technologies available solar thermal, photovoltaic and solar fuels are the prominent one. Today, photovoltaic is one of the fastest-growing industries with the most widely distributed technology.[10] But the electricity produced has an intrinsic difficulty in terms of storage in photovoltaic.[11] So, conversion of solar energy to chemical energy with ease in storage or a fuel is an ideal alternative to properly utilize solar energy. Among many technologies used for harnessing solar energy based fuels, generation of hydrogen (H_2) from water through solar-driven water splitting has established itself as a promising fuel, especially in internal combustion engines or fuel cells without any CO_2 emission.[12]

Hydrogen, also known as zero-emission fuel has a higher calorific value of ~141.7 MJ kg^{-1} as compared to many conventional source of energy such as diesel (45.6 MJ kg^{-1}), gasoline (46.4 MJ kg^{-1}), methane (55.5 MJ kg^{-1}) and kerosene (46.2 MJ kg^{-1}).[13,14] However, the current major source of H_2 which is produced in industrial scale is by steam reforming methane gas or from coal gasification, which in turn, emit large amount of greenhouse gases.[15] Hence, there is an urgent need of an alternative technology for the efficient production of H_2 fuel with

sustainability, carbon-free, cost-efficient and high efficacy on an industrial scale. For the evaluation of the viability of H_2 production by using renewable energy sources including water electrolysis have been recently published by an extensive techno-economic analysis (TEA) reports.[16] Among different technologies used for the production of H_2 fuel, PEC water splitting has the potential to become an extensive pathway for future energy production.

1.3 PHOTOELECTROCHEMICAL WATER SPLITTING

Harvesting clean and sustainable solar-derived hydrogen fuel from water is an attractive and desirable path to resolve the energy challenge through photoelectrochemical (PEC) water splitting**.** In general, PEC water splitting systems function in the same way to that of the conventional electrolysis system, where water oxidation to produce oxygen and water reduction to produce hydrogen occurs at the anode and cathode, respectively.[17,18] The main benefit of the PEC cell is that both H_2 and O_2 can separately generated during the process.[19] In the operation of a PEC cell, at least one of the both electrodes essentially be a semiconductor with light-absorbing ability.[20] Generally, when an n-type semiconductor as a photoanode is irradiated by sunlight, it generates electron-hole pairs due to photoexcitation of electrons from the valence band (VB) of the photoanode to the conduction band (CB) leaving behind the hole at the VB. In this process, when the holes (h^+) at the VB comes to the surface of the photoanode, it promotes water oxidation to release O_2 molecules. On the other hand, the electrons (e^-) moves to the cathode surface through the external circuit to promote water reduction to release H_2 molecule.[21-23] The chemical reaction that occurs in the respective electrodes during PEC process is as following equations with a schematic representation shown in **Figure 1.2**:[24,25]

$$\text{Cathode: } 2H^+ + 2e^- \rightarrow H_2\ ;\ E^0_{\text{reduction}} = 0V \quad (1.1)$$

$$\text{Photoanode: } 2H_2O + 4h^+ \rightarrow O_2 + 4H^+\ ;\ E^0_{\text{oxidation}} = 1.23V \quad (1.2)$$

$$\text{Overall water} - \text{splitting: } 2H_2O \rightarrow 2H_2(g) + O_2(g) \quad (1.3)$$

According to the Nernst equation and above chemical reactions, a least voltage of 1.23 V is required for the overall water splitting reaction, which is the minimum photon energy thermodynamically, required dissociating water into H_2 and O_2. Therefore, a semiconductor material with a lowest band gap of 1.23 eV is essential to facilitate water splitting. In particular, for driving the two half reactions using the photogenerated charge carriers upon light irradiation, the valence band at the equilibrated interface has to be more positive than 1.23 V vs. NHE (normal hydrogen electrode) and the conduction band at the equilibrated interface has to be more negative than 0 V vs. NHE.[26]

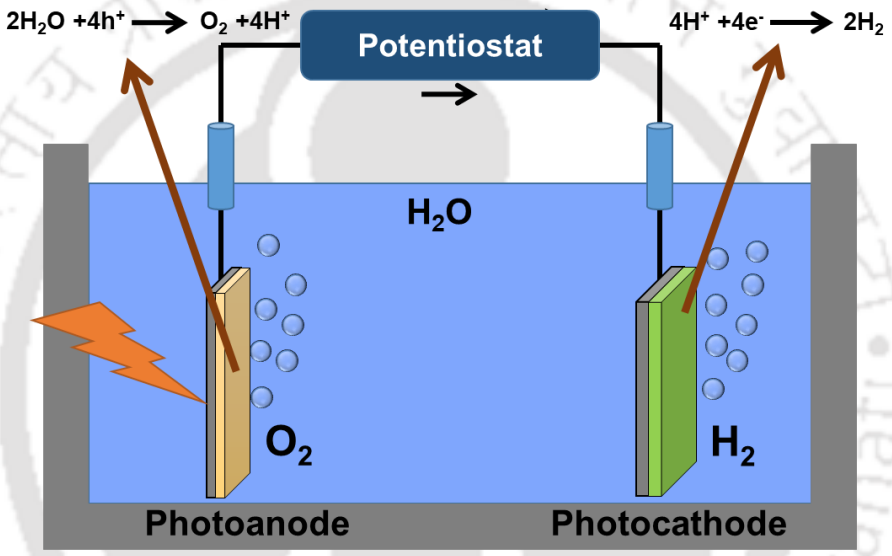

Figure 1.2 Schematic of a photoelectrochemical cell. The water reduced at the photocathode to produce H_2, and the water is oxidized at the photoanode to produce O_2.

While semiconductors are the primary driving force for water splitting reaction under illumination, some other aspects also limit the efficiency of a PEC device. Since most of the solar irradiation fall on earth surface is in visible range, choosing a semiconductor material with a proper band gap that can absorb maximum light is necessary.[27] In general, recombination of photogenerated charge carriers at the semiconductor-liquid interface arises due to lattice and surface defects during the water splitting reaction. The compulsion of an over- potential to drive two half reactions and slow kinetics at the solid-liquid interfaces during charge separation processes makes it quite challenging to find a suitable photoelectrode material.[28] Considering the above kinetic losses, semiconductors with a band gap of 1.6-2.4 eV are suitable to promote the

solar-driven water splitting process.[29] That's why, for the development of efficient photoelectrochemical devices based on semiconductor technology, it is essential to understand the thermodynamics, kinetics, and physical parameters of the solid-liquid interface and the catalyst surface.

1.4 STRATEGIES TO IMPROVE PHOTOELECTROCHEMICAL PERFORMANCE

Production of H_2 on a catalyst material is the focus of most investigations in the PEC water splitting process. However, O_2 evolution at the photoanode should not be ignored, as it provides electrons for the reduction of water to produce H_2 gas at the cathode. So, for efficient production of H_2, water oxidation at the photoanode is an important preliminary reaction. From **equation (1.2)**, we can see that generation of one O_2 molecule requires extraction of four electrons and four protons from two water molecules. In order to oxidize water in one step, the accumulation and storage of four oxidizing electron–holes close together by the photoanode is very difficult. This results in both kinetic and thermodynamic complexity that hinders the overall water splitting.[30] Therefore, for developing successful PEC devices with high solar-to-chemical conversion efficiencies, design and development of robust and effective PEC water oxidation photoanodes is a significant and necessary fundamental aspect.

In general, photoelectrochemical water oxidation involves a sequence of multiple competing or synergistic steps, including harvesting of solar-light, generation of charges upon light illumination, charge separation, recombination of photogenerated charges, charge transport and surface reaction.[31,32] Preferably, a photoanode should meet the following critical criteria for water oxidation, such as (1) thermodynamically VB of the photoanode should be more positive than standard redox potential of H_2O/O_2 which is 1.23 V vs. NHE (normal hydrogen electrode); (2) efficient absorption of light to use more of the broad range of solar spectrum; (3) efficient photogenerated charge separation by avoiding recombination of charges; (4) effective charge transfer to the photoanode surface; (5) photoanode with more than enough surface active sites; (6) faster water oxidation kinetics at the photoanode surface for O_2 evolution; and (7) cost-effective and stable in wide-range of pH and electrolytes.[33] Schematic representation of PEC processes and the factors that influences its performance is shown in **Figure 1.3**. Although, many

photoanode materials are thermodynamically suitable with proper VB edge for water oxidation, due to their inability to fulfill the above mentioned criteria; most of them show very low water oxidation activity.[34-36] The rational design and fabrication of highly efficient photocatalytic materials for water oxidation thus remains a great challenge.

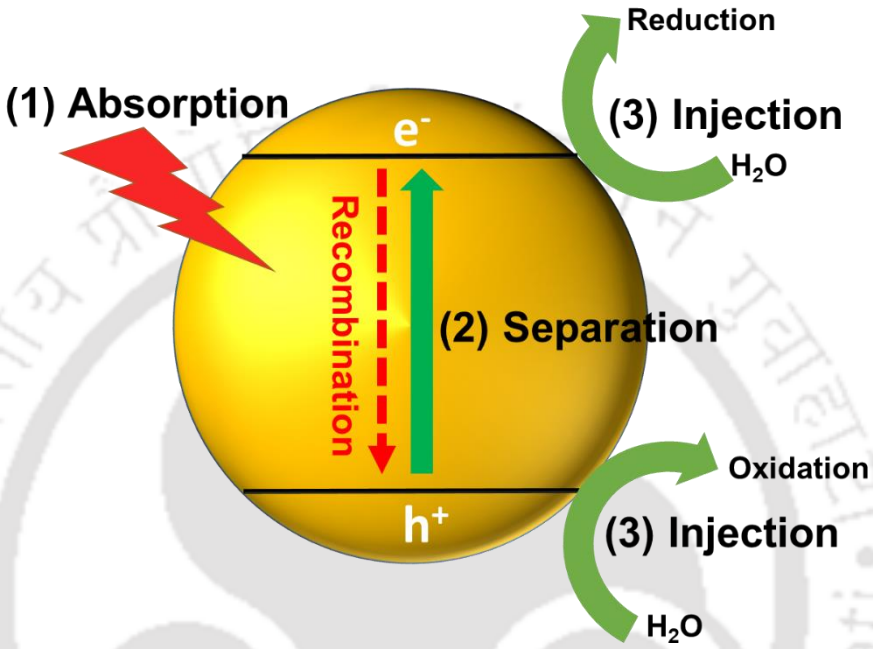

Figure 1.3 PEC processes and the factors that influences its performance.

The efficiency of each step should be improved to achieve a high solar-to-hydrogen (STH) efficacy of a PEC system. Selecting a suitable material such as metal oxides based semiconductor with earth abundance and proper band gap to design a photoanode is crucial for improving the PEC efficiency. Many strategies have been applied to metal oxide based photoanodes to improve the efficiency of each step as mentioned above, which includes (i) nanostructuring (ii) elemental doping, (iii) semiconductor heterojunctions, (iv) surface passivation, (v) hole extractors, and (vi) co-catalyst modification which is summarized in **Figure 1.4**.

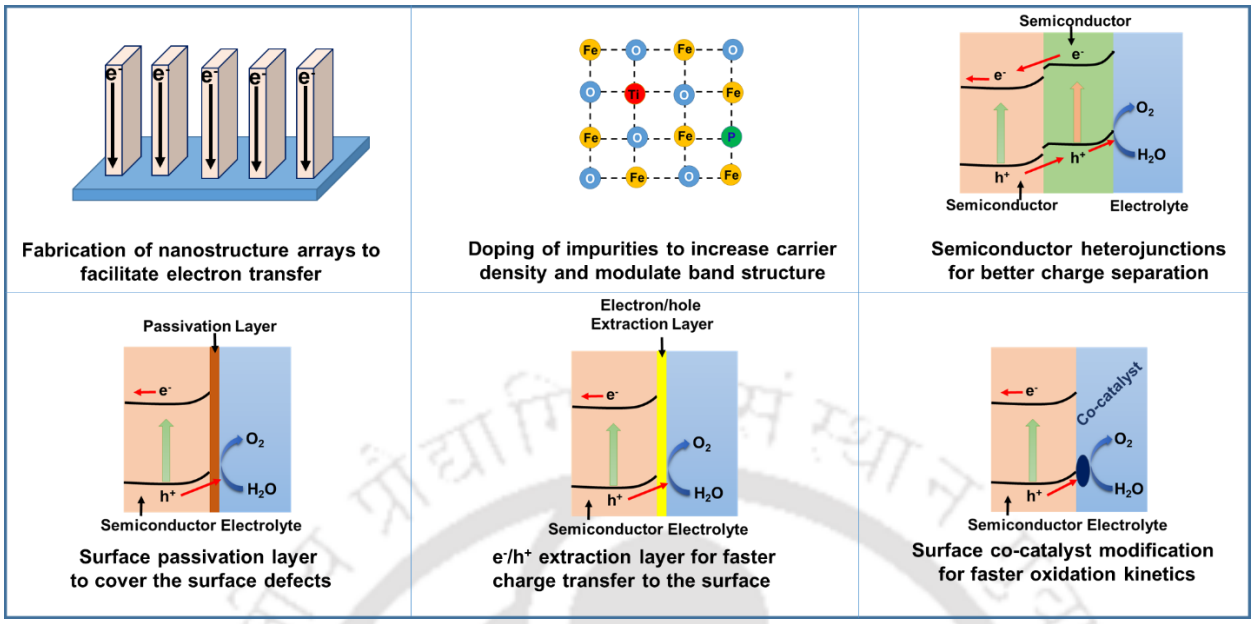

Figure 1.4 Schematics of different strategies for the improvement of metal oxide based photoanodes for PEC water splitting. [Reproduced from *Adv. Funct. Mater.* 2019, **29**, 1808032]

1.4.1 Nanostructuring of photoanodes

Efficient suppression of the photogenerated electrons and holes recombination have direct impact on the efficiency of PEC water splitting. However, in planar films the recombination of photogenerated electrons and holes are more prominent which results in low photocurrent. Also, conventional mesoporous films composed of nanoparticles do not meet this requirement due to the presence of grain boundaries in large numbers. These large grain boundaries increase the possibility of recombination of photogenerated charge carriers by acting as carrier trapping sites.[37] To solve this issue, use of highly ordered nanostructure arrays such as nanotube, nanorod, nanowire, and nanosheet can be a viable alternative to suppress the charge carrier recombination. Herein, the minority carriers diffusion distance to the surface of the material can be shorten with extremely ordered configurations of nanostructured photoanodes, which may result in the suppression of the photogenerated carriers recombination.[38] In this regard, one dimensional (1D) nanostructures can increase in the optical path length for efficient harvesting of solar light and a smooth pathway for electronic carrier transport. For example, 1D-nanostructures such as α-Fe_2O_3 nanorods,[39] nanowires,[40] nanotubes,[41] nanobelts,[42] TiO_2 nanotubes,[43] and ZnO nanorods[44] exhibited enhanced photoelectrochemical performance for

water oxidation. Hematite nanostructure with cauliflower morphology and doping minimizes the hole diffusion length to reach hematite/electrolyte interface with efficient light absorption for boosting the PEC performance.[45] Two-dimensional (2-D) nano-architectures generally possess large surface area which is beneficial for the a better contact between the photoanode and electrolyte.[46] Also, 2-D nanostructures with lower thickness are helpful for photoanodes with short hole diffusion length for migration of holes to the surface.[47] For example, WO_3 nanosheets,[48] nanoplates,[49] $BiVO_4$ nanoworms,[50] Fe_2O_3 nanosheets,[51,52] and Bi_2MoO_6[53] have achieved improvement in PEC performance due to better separation and transport of photogenerated charge carriers. Three dimensional (3-D) nanostructures, which has synergistic properties of both 1D and 2D nanostructures is another effective way for reducing overpotential for catalytic activity, efficient absorption of light and larger photoanode/electrolyte interfacial area.[54] Different 3D nanostructures such as $ZnFe_2O_4$ inverse opal structure,[55] TiO_2 nanotunnels,[56] Fe_2O_3 urchin-like structure,[57] showed promising performance for PEC water oxidation. Therefore, nanostructuring of metal oxide based photoanode is expected to be more efficient in transportation and separation of charge carriers by offering reduced diffusion length for minority carriers and large photoanode/electrolyte interfacial area for water oxidation.[58] Examples of some nanostructured morphologies are presented in **Figure 1.5**.

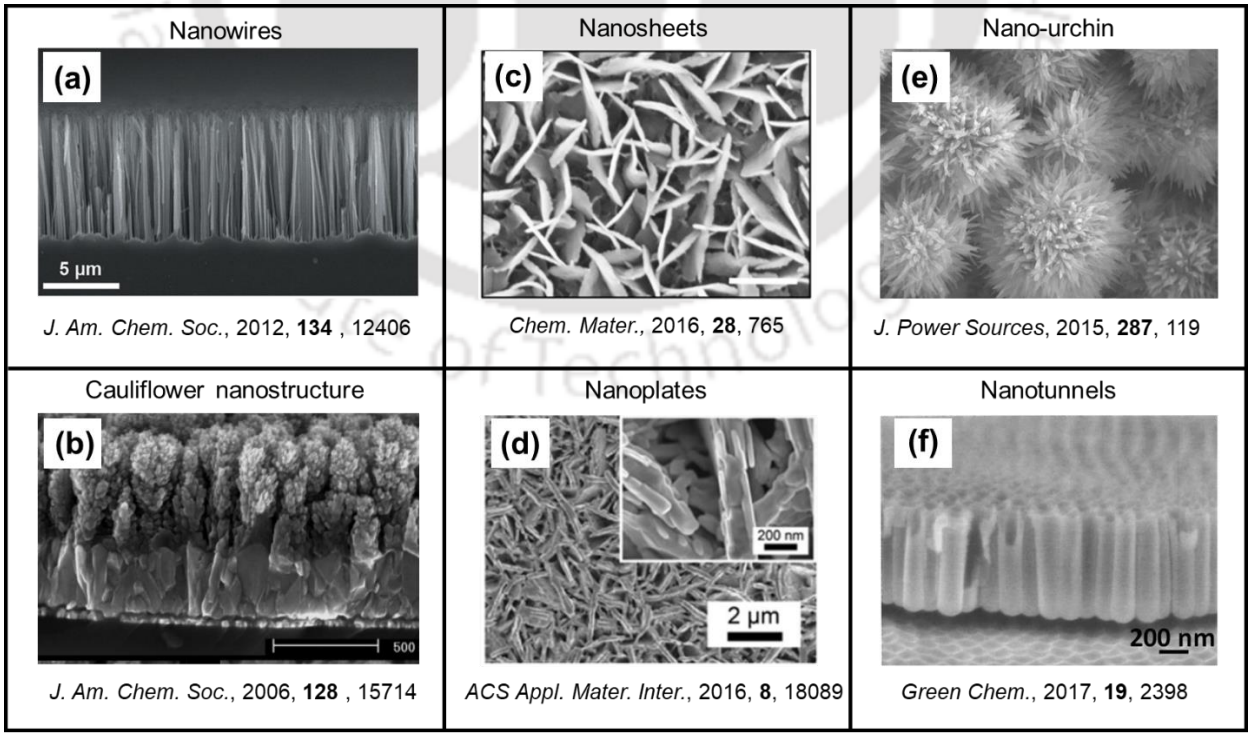

Figure 1.5 Some examples related to utilization of different nanostructure morphologies as photoanodes in PEC water oxidation. [Reprinted from above mentioned references, copyright@ American Chemical Society, Elsevier and Royal Society of Chemistry]

1.4.2 Elemental doping

The electrical and optical properties of metal oxide based photoanodes can be improved intrinsically by means of doping foreign elements or creation of intrinsic defects. Integration of cations or anions into metal oxide lattice enhances light absorption and electrical conductivity through bandgap tuning and regulation of charge carrier density.[59] Introduction of impurity energy states narrow the band gap of metal oxides through elemental doping which also red shifts the absorption. Also, most of the metal-oxide semiconductors are n-type conductive due to their natural feature of oxygen vacancies (O_V).[60] Overall, doping of foreign atoms into the metal oxide lattice plays a critical role on tailoring the electron conductivity, band gap, crystallinity, growth orientation, size and shape, etc. as confirmed by numerous theoretical as well as experimental studies.[61-66] The effect of doping also influences by the synthesis methods used, such as *in situ* or *ex situ* doping. Doping through *in situ* methods generally results in uniform distribution of dopants, whereas in *ex situ* methods dopants concentration gradually decreases from the surface to the bulk of the photoanodes.[67,68] As hematite suffers from extremely low electron mobility, many metal and non-metal dopants have been introduced to its lattice for improved electron mobility for boosting the PEC performance. For metal doping, Sn,[69-71] Ti,[72-74] Zr,[75,76] Mn,[77] Nb,[78] and Ta,[79] etc., have been extensively used, whereas for non-metal doping, P,[80,81] S,[82] and F[83] have been used to improve the PEC water oxidation. Doping of In to $BiVO_4$ not only tuned the band gap, it also changed the morphology and enhanced the surface charge separation of $BiVO_4$ photoanode.[84] Mo doping to $BiVO_4$ enhanced the electron mobility and inhibited electron-hole recombination, thereby improving the PEC performance.[85,86] The concentration of doping also plays a crucial role in separation and transportation of charge carriers. As the concentration of charge carriers is directly proportional to bend bending and inversely proportional to the width of the depletion layer, with higher concentrations the depletion layer will be too narrow to efficiently separate the charge carriers.[87] With high concentrations, the formation of defects will lead to more numbers of recombination centers.[88] Therefore, optimizing the concentration of dopants is necessary to enhance the efficiency of

photoanodes. Self-doping is another strategy to improve the PEC performance of metal oxide based photoanodes. Improved performance have been achieved with self-doping in Ti^{3+} doped TiO_2, Fe^{3+}/Fe^{2+} doped $FeVO_4$ and V^{4+} doped $BiVO_4$ due to enhancement in electrical conductivity.[89-91] Although doping with foreign elements can extend the optical and electronic properties of metal oxides, limited success have been achieved due to low photoactivity. Co-doping is another strategy to improve the performance of metal oxide photoanodes by means of synergistic effects of advantages of both dopants. Sn/Be doped Fe_2O_3, Sn/Zr doped Fe_2O_3 and Sn/Co doped Fe_2O_3 have found to improve the PEC water oxidation due to enhanced electrical conductivity.[92-94] Therefore, it is necessary to control the concentration of dopants and its distribution within the photoanode to develop efficient strategies.

1.4.3 Semiconductor heterojunctions

The internal driving force of a single component is relatively weak for efficient separation and transport of photogenerated charge carriers. So, an external driving force is necessary to improve the charge separation and transportation. Construction of heterojunctions between two semiconductors with proper band alignment is an efficient strategy for harnessing more light compared to single semiconductor and also facilitate improved charge separation. Formation of a build-in electric field in between these semiconductor materials is the main driving force for efficient separation of photo induced charge carriers.[95] Combining two n-type photoelectrodes can form n-n heterojunction, where the conduction band position of the photoelectrode on the electrolyte side should be higher than the photoelectrode attached to the conductive substrate side. In this type of heterojunction the holes accumulate on the photoelectrode present on the electrolyte side to generate O_2 by oxidising water. For example, n-n heterojunctions such as $WO_3/BiVO_4$,[96-98] $ZnO/BiVO_4$,[99] WO_3/Fe_2O_3,[100] $TiO_2/ZnFe_2O_4$,[101] and Fe_2O_3/Fe_2TiO_5[102] were demonstrated for improved charge separation and transportation for enhanced PEC performance. Moreover, p-n type heterojunctions also can be used for the PEC water oxidation similar to n-n heterojunctions, where the p-type photoelctrode present on the electrolyte side. Many p-n heterojunctions based combinations such as p-Co_3O_4/n-Fe_2O_3,[103] p-$CuBi_2O_4$/n-$BiVO_4$,[104] p-Cu_2O/n-$BiVO_4$[105] and p-NiO/n-Fe_2O_3[106] have been studied for their improved PEC water oxidation performance. Z-scheme heterojunction is another strategy where holes from VB of one semiconductor combine with electrons from CB of another semiconductor,

where water oxidation occurs at the semiconductor present on the electrolyte side. For example, $Se/BiVO_4$[107] and $ZnO/Au/SnO_2$[108] represents Z-scheme heterojunctions for improved interfacial charge transfer. Besides heterojunction strategies, homojunction based photoanodes can enhance the charge separation by avoiding formation of crystal lattice mismatch which also act as deep traps for charge recombination.[109] For example, WO_{3-x}/WO_3 homojunction, $Mg\text{-}Fe_2O_3/P\text{-}Fe_2O_3$ homojunction and $Zn:BiVO_4/Mo:BiVO_4$ homojunction showed improvement in PEC performance due to built-in electric field and lattice mismatch elimination.[110-112]

1.4.4 Surface passivation

The surface state or surface defect is a crucial drawback of metal-oxide based photoanodes for PEC water oxidation which leads to recombination of photogenerated charge carriers at the photoanode/electrolyte interfaces.[113] This surface trapping sites can be effectively eliminated by passivation of surface states using various thin oxide overlayers to promote extraction of charge carriers at the photoanode/electrolyte interfaces.[114] On the other hand, it also enhances the stability of the photoanode for PEC water oxidation.[115] However, the thickness of the overlayer should be such that it should not affect the light harvesting efficiency of the photoanodes. Usually, a thin passivation layer promotes the charge transfer across the interfaces through tunnelling effect.[116] As crystal boundary is the origin of surface states, amorphous oxide layer is found to be much effective for passivation of surface states, enabling efficient extraction of holes from the photoanode/electrolyte interface. The thickness of the amorphous layer should be minimal due to its poor conductivity. Thin oxide layers of Ga_2O_3, Al_2O_3, TiO_2 and ZnO, etc., were explored to minimize the negative effects of surface states.[117-119] With an effective contact between the photoanode and non-catalytic oxide layers the surface recombination is greatly decreased by releasing the lattice strain from the photoanode.[118] We can say that, surface passivation is a good strategy to suppress the recombination at the surface states of the semiconductor, with a possibility to change the onset potential. In addition it can protect the photoelectrode from chemical dissolution and corrosion.

1.4.5 Co-catalyst modification

Water oxidation reaction requires a large overpotential due to its complicated four-electron and four-proton process, which leads to sluggish kinetics at the photoanode/electrolyte

interface. The modification of photoanodes with oxygen evolution catalyst, commonly known as co-catalyst, play vital role for the reduction of overpotential, fasten the kinetics at the photoanode/electrolyte interface by suppressing surface recombination and enhance the durability of the photoanode. Typically, a thin layer co-catalyst are deposited over the photoanode surface to minimize their light absorption or scattering. Though noble metal based OECs such as RuO_2 and IrO_2 are efficient and stable under working conditions, they are expensive due to their low earth-abundance, which makes them less suitable for practical applications.[120] First-row transition metal and metal oxides are usually used as co-catalyst to overcome the limitation of poor OER kinetics to achieve a higher activity and decent reaction rates due to their low-cost. Among different metal oxide based OECs, cobalt oxide has emerged as efficient water oxidation co-catalysts and can operate under neutral conditions.[121,122] Nocera and co-workers reported cobalt-phosphate (Co-Pi) as an efficient oxygen evolving catalyst deposited through electrodeposition over photoanode.[122] Co-Pi has gained a lot of interest since its development because of requirement of low overpotential to oxidize water at neutral pH. The mechanism of catalytic activity of cobalt based oxides and hydroxides for water oxidation is well understood, while the mechanism involving Co-Pi is still not very clear. The former involves the formation of high-valent Co(IV)–O intermediates through Co^{II}/Co^{III} and Co^{III}/Co^{IV} redox couples which can store up to four holes from the valence band of photoanode. After the injection of holes into the electrolyte for the water oxidation to generate O_2, it again regenerates Co^{II} centers.[123,124] Besides cobalt based co-catalyst, nickel and iron based co-catalysts have been extensively investigated for their excellent electrocatalytic activity.[59] Also, more complexed co-catalysts involving mixed metal such as NiFe oxide/hydroxide has been introduce because of their transparency towards visible light irradiation. Recently, layered double hydroxides (LDHs) have been attracted as effective co-catalyst due to their compatibility with semiconductors combination with low cost. LDHs based on metals including Fe, Ni, Co and Mn were effective as co-catalysts for efficient separation of photogenerated charge carriers and acceleration of PEC water oxidation.[59] However, rare-earth based co-catalyst materials have not been explored much despite have many advantages over transition-metal based co-catalysts. There are ample opportunities to explore new combinations of various metal oxide and hydroxide base co-catalysts to further improve the PEC performance of photoanodes.

1.4.6 Electron/hole extraction layer

Recently, van de Krol et al. re-stated the roles of some oxygen evolution co-catalysts from the perspectives of the surface recombination and surface reaction kinetics.[125] They pointed out that the water oxidation ability of co-catalyst is strongly limited due to insufficient hole extraction from the photoanodes resulting in a small thermodynamic driving force. This limitation hinders the performance of photoanode/OEC, and to overcome this, band bending of photoanode at the electrode/electrolyte interface must be improved.[126] For instance, FeOOH have been used as to extract and transport holes from $BiVO_4$ to NiOOH co-catalyst, as FeOOH has lower hole transport resistance than NiOOH.[127] In another report, it is suggested that deposition of a layer of p-type material over $BiVO_4$/co-catalyst surface can be beneficial for faster extraction of holes due to formation of p-n junction.[128] Gong et. al found that use of a p-type co-catalyst material over $BiVO_4$ photoanode can enhance both hole extraction and water oxidation kinetics simultaneously.[129] In a more recent article, Zhang et. al used black phosphorene as an hole extraction layer to further enhance the capability of co-catalyst for water oxidation in $BiVO_4$ photoanode.[130] A thin interlayer of polyaniline in between $BiVO_4$ core and NiOOH shell act as an excellent hole-transporting layer for enhanced PEC performance.[131] Tuning the hole accumulation behavior of catalyst during OER is another distinct way to enhance the OER performance for water splitting.[132] Therefore, promoting hole extraction from photoanode to oxygen evolution co-catalysts by improving their interface resistance still holds broad interest and significance for enhancing the PEC performance. Utilization of zero dimensional (0-D) quantum dots and two-dimensional (2-D) materials with thin nanosheet structures can be utilized as a hole extraction layer without affecting the light absorption of the photoanodes.

1.5 MOTIVATION AND OBJECTIVES OF THE PRESENT WORK

Metal oxide based photoanodes such as Fe_2O_3, $BiVO_4$ and WO_3 are promising materials for PEC water splitting because of their favorable narrow band gap with an appropriate VB position with respect to water oxidation level, earth-abundance and stability. However, four decades after the demonstration of TiO_2 based PEC water splitting by Honda and Fujishima in 1972, still the reported efficiencies remains too low to be utilized for practical applications.[133] Lack of suitable materials with intrinsic properties is a key challenge responsible for the sluggish

progress which hinders the PEC process. Also, the recombination at the photoanode/electrolyte interface is the key drawback which needs further improvement for reaching nearer to the theoretical efficiency. Although many attempts have been applied to enhance the surface properties of the photoanode, the bulk properties of the photoanodes are also the limiting factors for recombination losses of charge carriers before coming to the surface for chemical reactions. These key shortcomings of metal oxide based photoanodes should be addressed to further improve their PEC performance. The objectives of the present thesis work are as follows:

(1) Design and fabrication of new photoanode materials that possess unique combinations of properties suitable for the purpose of PEC water splitting
(2) Construction of various novel morphologies of existing photoanodes to overcome key shortcomings of these materials
(3) Combination of different strategies such as nanostructuring, material doping, heterojunctions, surface passivation and co-catalyst modification for highly efficient and stable photoanodes
(4) Utilization of less explored materials with unique properties as a supporting material for improving the intrinsic properties of various photoanodes
(5) A better understanding of charge transfer mechanism at different interfaces with the abovementioned strategies
(6) Use of simple, innovative and cost effective fabrication and synthetic methods to obtain efficient photoanode materials

1.6 REFERENCES

(1) J. Barber *Chem. Soc. Rev.*, 2009, **38**, 185.
(2) *IPCC Panel Reports on Climate Change and Biodiversity*, April 2002.
(3) International Energy Agency (IEA), *Key World Energy Statistics*, 2020.
(4) *World Energy Assessment: Energy and the Challenge of Sustainability*, November 2015.
(5) R. Lindsey, *Climate Change: Atmospheric Carbon Dioxide*, August 2020.
(6) European Environment Agency (EEA), *https://www.eea.europa.eu*
(7) *https://en.wikipedia.org/wiki/2015_United_Nations_Climate_Change_Conference*

(8) S. Yun , Y. Qin , A. R. Uhl , N. Vlachopoulos , M. Yin , D. Li , X. Han and A. Hagfeldt, *Energy Environ. Sci.*, 2018, **11**, 476.

(9) D. J. C. MacKay, *Phil. Trans. R. Soc. A.* 2013, **371**, 20110431.

(10) International Renewable Energy Agency (IRENA), *Future of Solar Photovoltaic Deployment, investment, technology, grid integration and socio-economic aspects*, November 2019

(11) V. Vega-Garita, L. Ramirez-Elizondo, N. Narayan and P. Bauer, *Prog. Photovoltaics*, 2018, **27**, 346.

(12) J. H. Kim, D. Hansora, P. Sharma, J.-W. Jang and J. S. Lee, *Chem. Soc. Rev.*, 2019, **48**, 1908.

(13) S. S. Lam, V. Nguyen, M. T. N. Dinh, D. Q. Khieu, D. D. La, H. T. Nguyen, D. V. N. Vo, R. S. Varma, M. Shokouhimehr, C. C. Nguyen, Q. V. Le and W. Peng. *J. Mater. Chem. A*, 2020, **8**, 10571.

(14) P. Nikolaidis and A. Poullikkas, *Renew. Sust. Energ. Rev.*, 2017, **67**, 597.

(15) F. Dalena, A. Senatore, M. Basile, S. Knani, A. Basile and A. Iulianelli, *Membranes*, 2018, **8**, 98.

(16) International Renewable Energy Agency (IRENA), *Hydrogen from Renewable Power TECHNOLOGY OUTLOOK FOR THE ENERGY TRANSITION*, September 2018

(17) Baxter , Z. Bian , G. Chen , D. Danielson , M. S. Dresselhaus , A. G. Fedorov , T. S. Fisher , C. W. Jones , E. Maginn , U. Kortshagen , A. Manthiram , A. Nozik , D. Rolison , T. Sands , L. Shi , D. Sholl and Y. Wu , *Energy Environ. Sci.*, 2009, **2**, 559.

(18) C. Ros, T. Andreu and J. R. Morante, *J. Mater. Chem. A*, 2020, **8**, 10625.

(19) L. G. Bloor, R. Solarska, K. Bienkowski, P. J. Kulesza, J. Augustynski, M. D. Symes and L. Cronin, *J. Am. Chem. Soc.*, 2016, **138**, 6707.

(20) F. Decker and S. Cattarin, *PHOTOELECTROCHEMICAL CELLS-Overview in Encyclopedia of Electrochemical Power Sources*, 2009, 1-9.

(21) M. Grätzel, *Nature*, 2001, **414**, 338.

(22) A. J. Bard , A. B. Bocarsly , F. F. Fan , E. G. Walton and M. S. Wrighton , *J. Am. Chem. Soc.*, 1980, **102**, 3671.

(23) J. R. Bolton , S. J. Strickler and J. S. Connolly , *Nature*, 1985, **316**, 495.

(24) S. Chen, D. Huang, P. Xu, W. Xue, L. Lei, M. Cheng, R. Wang, X. Liu and R. Deng, *J. Mater. Chem. A*, 2020, **8**, 2286.

(25) W. Yang, R. R. Prabhakar, J. Tan, S. D. Tilley and J. Moon, *Chem. Soc. Rev.*, 2019, **48**, 4979.

(26) M. Ahmed and G. Xinxin, *Inorg. Chem. Front.*, 2016, **3**, 578.

(27) P. M. Ushasree and B. Bora, *Silicon Solar Cells, in Solar Energy Capture Materials*, 2019,1-55.

(28) J. Li and N. Yu, *Catal. Sci. Technol.*, 2015, **5**, 1360.

(29) R. Asmatulund and W. S. Khan, *Electrospun nanofibers for catalyst applications, Synthesis and Applications of Electrospun Nanofibers*, 2019, 153-173.

(30) L. Yang, H. Zhou, T. Fan and D. Zhang, *Phys. Chem. Chem. Phys.*, 2014, **16**, 6810.

(31) H. Zhou, Y. Qu, T. Zeid and X. Duan, *Energy Environ. Sci.*, 2012, **5**, 6732.

(32) H. Tong, S. Ouyang, Y. Bi, N. Umezawa, M. Oshikiri and J. Ye, *Adv. Mater.*, 2012, **24**, 229.

(33) X. Chen, S. Shen, L. Guo and S. S. Mao, *Chem. Rev.*, 2010, **110**, 6503.

(34) Z. F. Huang, L. Pan, J. J. Zou, X. Zhang and L. Wang, *Nanoscale*, 2014, **6**, 14044.

(35) S. Cho, J. W. Jang, K. H. Lee and J. S. Lee, *APL Materials*, 2014, **2**, 010703.

(36) F. E. Osterloh and B. A. Parkinson, *MRS Bull.* 2011, **36**, 17.

(37) P. Peerakiatkhajohn, J.-H. Yun, S. Wang and L. Wang, *J. of Photonics for Energy*, 2016, **7**, 012006.

(38) F. L. Souza, K. P. Lopes, E. Longo and E. R. Leite, *Phys. Chem. Chem. Phys.*, 2009, **11**, 1215.

(39) Y. Fu, C. L. Dong, Z. Zhou, W. Y. Lee, J. Chen, P. Guo, L. Zhao and S. Shen, *Phys. Chem. Chem. Phys.*, 2016, **18**, 3846.

(40) M. T. Mayer, C. Du and D. Wang, *J. Am. Chem. Soc.*, 2012, **134**, 12406.

(41) T. J. LaTempa, X. Feng, M. Paulose and C. A. Grimes, *J. Phys. Chem. C*, 2009, **113**, 16293.

(42) M. Marelli, A. Naldoni, A. Minguzzi, M. Allieta, T. Virgili, G. Scavia, S. Recchia, R. Psaro and V. D. Santo, *ACS Appl. Mater. Interfaces*, 2014, **6**, 11997.

(43) A. M. Mohamed, A. S. Aljaber, S. Y. AlQaradawi and N. K. Allam, *Chem. Commun.*, 2015, **51**, 12617.

(44) D. Commandeur, G. Brown, E. Hills, J. Spencer and Q. Chen, *ACS Appl. Nano Mater.*, 2019, **2**, 1570.

(45) A. Kay, I. Cesar and M. Grätzel, *J. Am. Chem. Soc.*, 2006, **128**, 15714.

(46) Y. Hou, Z. Wen, S. Cui, X. Guo and J. Chen, *Adv. Mater.*, 2013, **25**, 6291.

(47) S. Shen, S. A. Lindley, X. Chen and J. Z. Zhang, *Energy Environ. Sci.*, 2016, **9**, 2744.

(48) Y. Liu, L. Liang, C. Xiao, X. Hua, Z. Li, B. Pan andY. Xie, *Adv. Energy Mater.*, 2016, **6**, 1600437.

(49) X. Feng, Y. Chen, Z. Qin, M. Wang and L. Guo, *ACS Appl. Mater. Interfaces*, 2016, **8**, 18089.

(50) Y. Kuang, Q. Jia, H. Nishiyama, T. Yamada, A. Kudo and K. Domen, *Adv. Energy Mater.*, 2016, **6**, 1501645.

(51) P. Peerakiatkhajohn, J.-H. Yun, H. Chen, M. Lyu, T. Butburee and L. Wang, *Adv. Mater.*, 2016, **28**, 6405.

(52) O. Zandi, A. R. Schon, H. Hajibabaei and T. W. Hamann, *Chem. Mater.*, 2016, **28**, 765.

(53) M. Wu, Y. Wang, Y. Xu, J. Ming, M. Zhou, R. Xu, Q. Fu and Y. Lei, *ACS Appl. Mater. Interfaces*, 2017, **9**, 23647.

(54) J. R. McKone, E. L. Warren, M. J. Bierman, S. W. Boettcher, B. S. Brunschwig, N. S. Lewis and H. B. Gray, *Energy Environ. Sci.*, 2011, **4**, 3573.

(55) A. G. Hufnagel, K. Peters, A. Müller, C. Scheu, D. Fattakhova-Rohlfing, and T. Bein, *Adv. Funct. Mater.*, 2016, **26**, 4435.

(56) R. Takakura, T. Oshikiri, K. Ueno, X. Shi, T. Kondo, H. Masuda and H. Misawa, *Green Chem.*, 2017, **19**, 2398.

(57) A. G. Tamirat, W.-N. Su, A. A. Dubale, C.-J. Pan, H.-M. Chen, D. W. Ayele, J.-F. Lee and B.-J. Hwang, *J. Power Sources*, 2015, **287**, 119.

(58) Y. Ling and Y. Li, *Part. Part. Syst. Charact.*, 2014, **31**, 1113.

(59) M. Xiao, B. Luo, Z. Wang, S. Wang and L.Wang, *Sol. RRL*, 2020, **4**, 1900509.

(60) Y. Yang, S. Niu, D. Han, T. Liu, G. Wang and Y. Li, *Adv. Energy Mater.*, 2017, **7**, 1700555.

(61) X. Shi, S. Siahrostami, G.-L. Li, Y. Zhang, P. Chakthranont, F. Studt, T. F. Jaramillo, X. Zheng and J. K. Norskov, *Nat. Commun.*, 2017, **8**, 701.

(62) J. Liu, C. Liang, H. Zhang, Z. Tian and S. Zhang, *J. Phys. Chem. C*, 2012, **116**, 4986.

(63) M. N. Huda, Y. Yan and M. M. Al-Jassim, *J. Appl. Phys.*, 2011, **109**, 113710.

(64) J. Su, J. Wang, C. Liu, B. Feng, Y. Chen and L. Guo, *RSC Adv.*, 2016, **6**, 101745.

(65) Z. Zhou, P. Huo, L. Guo and O. V. Prezhdo, *J. Phys. Chem. C*, 2015, **119**, 26303.

(66) J. Xie, W. Liu, J. Xin, F. Lei, L. Gao, H. Qu, X. Zhang and Y. Xie, *ChemSusChem*, 2017, **10**, 4465.

(67) R. Asahi, T. Morikawa, T. Ohwaki, K. Aoki and Y. Taga, *Science*, 2001, **293**, 269.

(68) X. Chen and S. S. Mao, *Chem. Rev.*, 2007, **107**, 2891.

(69) Y. Ling, G. Wang, D. A. Wheeler, J. Z. Zhang and Y. Li, *Nano Lett.*, 2011, **11**, 2119.

(70) K. Sivula, R. Zboril, F. Le Formal, R. Robert, A. Weidenkaff, J. Tucek, J. Frydrych and M. Grätzel, *J. Am. Chem. Soc.*, 2010, **132**, 7436.

(71) X. Meng, G. Qin, W. A. Goddard III, S. Li, H. Pan, X. Wen, Y. Qin and L. Zuo, *J. Phys. Chem. C*, 2013, **117**, 3779.

(72) J. A. Glasscock, P. R. F. Barnes, I. C. Plumb and N. Savvides, *J. Phys. Chem. C*, 2007, **111**, 44.

(73) M. Zhang, W. Luo, Z. Li, T. Yu and Z. Zou, *Appl. Phys. Lett.*, 2010, **97**, 042105.

(74) M. N. Huda, A. Walsh, Y. Yan, S. H. Wei and M. M. Al-Jassim, *J. Appl. Phys.*, 2010, **107**, 123712.

(75) R. Franking, L. Li, M. A. Lukowski, F. Meng, Y. Tan, R. J. Hamers and S. Jin, *Energy Environ. Sci.*, 2013, **6**, 500.

(76) S. H. Shen, P. H. Guo, D. A. Wheeler, J. G. Jiang, S. A. Lindley, C. X. Kronawitter, J. Z. Zhang, L. J. Guo and S. S. Mao, *Nanoscale*, 2013, **5**, 9867.

(77) Gurudayal, S. Y. Chiam, M. H. Kumar, P. S. Bassi, H. L. Seng, J. Barber and L. H. Wong, *ACS Appl. Mater. Interfaces*, 2014, **6**, 5852.

(78) Y. Fu, C.-L. Dong, W.-Y. Lee, J. Chen, P. Guo, L. Zhao and S. Shen, *ChemNanoMat*, 2016, **2**, 704.

(79) A. Hiltunen, T. Iivonen, R. Ulkuniemi, K. Lahtonen, H. Ali-Löytty, K. Mizohata, M. Valden, M. Leskelä and N. V. Tkachenko, *J. Mater. Chem. A*, 2019, **7**, 3206.

(80) Y. Zhang, S. Jiang, W. Song, P. Zhou, H. Ji, W. Ma, W. Hao, C. Chen and J. Zhao, *Energy Environ. Sci.*, 2015, **8**, 1231.

(81) Q. Rui, L. Wang, Y. Zhang, C. Feng, B. Zhang, S. Fu, H. Guo, H. Hu and Y. Bi, *J. Mater. Chem. A*, 2018, **6**, 7021.

(82) H. Bemana and S. Rashid-Nadimi, *Electrochim. Acta*, 2017, **229**, 396.

(83) Y. Zhu, J. Xu, H. Jiang, D. Niu, X. Zhang and S. Hu, *CrystEngComm*, 2018, **20**, 6430.

(84) X. Zhong, H. He, M. Yang, G. Ke, Z. Y. Zhao, F. Dong, B. Wang, Y. Chen, X. Shi and Y. Zhou, *J. Mater. Chem. A*, 2018, **6**, 10456.

(85) B. Pattengale and J. Huang, *Phys. Chem. Chem. Phys.*, 2016, **18**, 32820.

(86) S. K. Pilli, T. E. Furtak, L. D. Brown, T. G. Deutsch, J. A. Turner and A. M. Herring, *Energy Environ. Sci.*, 2011, **4**, 5028.

(87) G. Wang, Y. Ling, H. Wang, L. Xihong and Y. Li, *J. Photochem. Photobiol C Photochem. Rev.*, 2014, **19**, 35.

(88) X. Zhang, H. Li, S. Wang, F.-R. F. Fan and A. J. Bard, *J. Phys. Chem.*, C 2014, **118**, 16842.

(89) J. Lee, Z. Li, L. Zhu, S. Xie and X. Cui, *Appl. Catal. B-Environ.*, 2018, **224**,715.

(90) W. Wang, Y. Zhang, L. Wang and Y. Bi, *J. Mater. Chem. A*, 2017, **5**, 2478.

(91) G. Wang, Y. Ling, X. Lu, F. Qian, Y. Tong, J. Z. Zhang, V. Lordi, C. Rocha Leao and Y. Li, *J. Phys. Chem. C*, 2013, **117,** 10957.

(92) A. Annamalai, H. H. Lee, S. H. Choi, S. Y. Lee, E. Gracia-Espino, A. Subramanian, J. Park, K. Kong and J. S. Jang, *Sci. Rep.*, 2016, **6**, 23183.

(93) A. G. Tamirat, W.-N. Su, A. A. Dubale, H.-M. Chen and B.-J. Hwang, *J. Mater. Chem. A*, 2015, **3**, 5949.

(94) J. Wang, C. Du, Q. Peng, J. Yang, Y. Wen, B. Shan and R. Chen, *Int. J. Hydrogen Energy*, 2017, **42**, 29140.

(95) G. Yun, M. Balamurugan, H.-S. Kim, K.-S. Ahn and S. H. Kang, *J. Phys. Chem. C*, 2016, **120**, 5906.

(96) P. M. Rao, L. Cai, C. Liu, I. S. Cho, C. H. Lee, J. M. Weisse, P. Yang and X. Zheng, *Nano Lett.*, 2014, **14**, 1099.

(97) J. H. Seo, G. Park, K. H. Oh, S. H. Kang, H. C. Lee, S. K. Cho and K. M. Nam, *J. Electroanal. Chem.*, 2017, **789**, 17.

(98) S. Y. Chae, C. S. Lee, H. Jung, O.-S. Joo, B. K. Min, J. H. Kim and Y. J. Hwang, *ACS Appl. Mater. Interfaces*, 2017, **9**, 19780.

(99) J.-S. Yang and J.-J. Wu, *Nano Energy*, 2017, **32**, 232.

(100) Y. Li, L. Zhang, R. Liu, Z. Cao, X. Sun, X. Liu and J. Luo, *ChemCatChem*, 2016, **8**, 2765.

(101) X.-L. Zheng, C.-T. Dinh, F. P. G. de Arquer, B. Zhang, M. Liu, O. Voznyy, Y.-Y. Li, G. Knight, S. Hoogland, Z.-H. Lu, X.-W. Du and E. H. Sargent, *Small*, 2016, **12**, 3181.

(102) C. Li, T. Wang, Z. Luo, S. Liu and J. Gong, *Small*, 2016, **12**, 3415.

(103) S. -S. Yi, B. -R. Wulan, J. -M. Yan and Q, Jiang, *Adv. Funct. Mater*, 2019, **29**, 1801902.

(104) S. Liu, J. Zhou, Y. Lu and J. Su, *Sol. Energy Mater. Sol. Cells*, 2018, **180**, 123.

(105) S. Bai, J. Liu, M. Cui, R. Luo,J. He and A. Chen, *Dalton Trans.*, 2018, **47**, 6763.

(106) A. K. Singh and D. Sarkar, *Nanoscale*, 2018, **10**, 13130.

(107) S. N. F. M. Nasir, H. Ullah, M. Ebadi, A. A. Tahir, J. S. Sagu and M. A. M. Teridi, *J. Phys. Chem. C*, 2017, **121**, 6218.

(108) J. M. Li, H. Y. Cheng, Y. H. Chiu and Y. J. Hsu, *Nanoscale*, 2016, **8**, 15720.

(109) N. Wang, M. Liu, H. Tan, J. Liang, Q. Zhang, C. Wei, Y. Zhao, E. H. Sargent and X. Zhang, *Small*, 2017, **13**, 1603527.

(110) F. Zhan, Y. Liu, K. Wang, X. Yang, M. Liu, X. Qiu, J. Li and W. Li, *ACS Appl. Mater. Interfaces*, 2019, **11**, 39951.

(111) J. M. Lee, J. H. Baek, T. M. Gill, X. Shi, S. Lee, I. S. Cho, H. S. Jung and X. Zheng, *J. Mater. Chem. A*, 2019, **7**, 9019.

(112) F. Li, J. Li, F. Li, L. Gao, X. Long, Y. Hu, C. Wang, S. Wei, J. Jin and J. Ma, *J. Mater. Chem. A*, 2018, **6**, 13412.

(113) M. J. Kenney, M. Gong, Y. Li, J. Z. Wu, J. Feng, M. Lanza and H. Dai, *Science* 2013, **342**, 836.

(114) Y. Hou, F. Zuo, A. Dagg and P. Feng, *Nano Lett.*, 2012, **12**, 6464.

(115) Š. Hajduk, S. P. Berglund, M. Podlogar, G. Dražic´, F. F. Abdi, Z. C. Orel and M. Shalom, *Adv. Mater. Interfaces*, 2017, **4**, 1700924.

(116) E. W. Cowell, N. Alimardani, C. C. Knutson, J. F. Conley, D. A. Keszler, B. J. Gibbons and J. F. Wager, *Adv. Mater.* 2011, **23**, 74.

(117) F. L. Formal, M. Gr¨atzel and K. Sivula, *Adv. Funct. Mater.*, 2010, **20**, 1099.

(118) T. Hisatomi, J. Brillet and M. Cornuz, *Faraday Discuss.*, 2012, **155**, 223.

(119) T. Hisatomi, H. Dotan and M. Stefik, *Adv. Mater.*, 2012, **24**, 2699.

(120) C. Jiang, S. J. A. Moniz, A. Wang, T. Zhang and J. Tang, *Chem. Soc. Rev.*, 2017, **46**, 4645

(121) A. Kay, I. Cesar and M. Grätzel, *J. Am. Chem. Soc.*, 2006, **128**, 15714.

(122) M. W. Kanan and D. G. Nocera, *Science*, 2008, **321**, 1072.

(123) D. K. Zhong and D. R. Gamelin , *J. Am. Chem. Soc.*, 2010, **132** , 4202.

(124) D. K. Zhong, M. Cornuz, K. Sivula, M. Grätzel and D. R. Gamelin, *Energy Environ. Sci.*, 2011, **4**, 1759.

(125) C. Zachäus, F. F. Abdi, L. M. Peter and R. van de Krol, *Chem. Sci.*, 2017, **8**, 3712.

(126) B. J. Trześniewski, I. A. Digdaya, T. Nagaki, S. Ravishankar, I. Herraiz-Cardona, D. A. Vermaas, A. Longo, S. Gimenez and W. A. Smith, *Energy Environ. Sci.*, 2017, **10**, 1517.

(127) T. W. Kim and K.-S. Choi, *Science*, 2014, **343**, 990.

(128) M. Zhong, T. Hisatomi, Y. Kuang, J. Zhao, M. Liu, A. Iwase, Q. Jia, H. Nishiyama, T. Minegishi, M. Nakabayashi, N. Shibata, R. Niishiro, C. Katayama, H. Shibano, M. Katayama, A. Kudo, T. Yamada and K. Domen, *J. Am. Chem. Soc.*, 2015, **137**, 5053.

(129) X. Chang, T. Wang, P. Zhang, J. Zhang, A. Li and J. Gong, *J. Am. Chem. Soc.*, 2015, **137**, 8356.

(130) K. Zhang, B. Jin, C. Park, Y. Cho, X. Song, X. Shi, S. Zhang, W. Kim, H. Zeng and J. H. Park, *Nat. Commun.*, 2019, **10**, 2001.

(131) X. Wang, K.-H. Ye, X. Yu, J. Zhu, Y. Zhu and Y. Zhang, *J. Power Sources*, 2018, **391**, 34.

(132) P. Zhang, W. Wang, H. Wang, Y. Li and C. Cui, *ACS Catal.*, 2020, **10**, 10427.

(133) A. Fujishima and K. Honda, *Nature*, 1972, **238**, 37.

CHAPTER 2

Experimental Section

This chapter discusses the basic instrumentation techniques and methodologies used for material characterization, fabrication of metal oxide based photoanodes. Characterization technique of the devices using basic and specific instrumental techniques/methods are included. A short introduction to photoelectrochemical performance parameters and electrochemical impedance spectroscopy (EIS) measurement is also given.

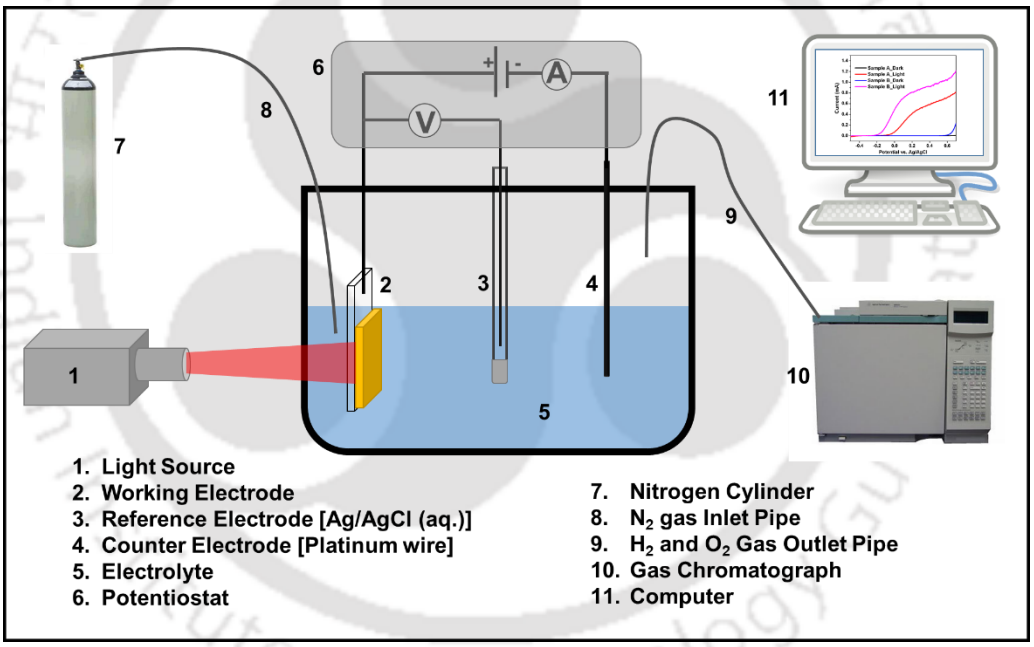

2.1 INTRODUCTION

This chapter discusses the procedures for synthesis and fabrication of metal oxide based photoanodes for photoelectrochemical (PEC) water splitting. Materials and chemicals used for the synthesis and fabrication of PEC devices are listed. Basic characterization techniques and methods used to characterize as synthesized materials and photoelectrochemical devices have been listed. Experimental set up for the measurement of photoelectrochemical devices are also discussed. Different performance parameters which are crucial for analysing the efficiency of PEC devices are included with a brief outline.

2.2 CHEMICALS AND REAGENTS USED

Fluorine doped tin oxide (FTO) substrate (Sigma Aldrich), anhydrous ferric chloride (Merck, Sigma Aldrich), zinc nitrate hexahydrate (Sigma Aldrich), cobalt nitrate hexahydrate (Sigma Aldrich), sodium nitrate (Merck), aluminium nitrate nonahydrate (Merck), hydrochloric acid (Merck), sodium hydroxide (Sigma-Aldrich), sodium hydrogen phosphate (Merck), titanium tetraisopropoxide (Spectrochem), boric acid (Merck), Selectfluor {1-Chloromethyl-4-fluoro-1, 4-diazoniabicyclo[2.2.2]octane bis(tetrafluoroborate)} (Sigma Aldrich), melamine (Sigma Aldrich), bismuth nitrate pentahydrate (Sigma Aldrich), potassium iodide (Merck), nitric acid (Merck), p-benzoquinone (Sigma Aldrich), dimethyl sulfoxide (DMSO) (Merck), vanadyl acetylacetonate ($VO(acac)_2$) (Sigma Aldrich) , cerium nitrate hexahydrate (Sigma Aldrich), urea (Sigma Aldrich), and ammonium fluoride (Sigma Aldrich). All the reagents and chemicals used in the synthesis and fabrication of different materials are of analytical grade and used as received without further purification. Milli-Q water (18.2 MΩ-cm) is used for all the synthesis protocol.

2.3 CHARACTERIZATION OF AS-SYNTHESIZED MATERIALS AND PHOTOELECTROCHEMICAL DEVICES

All synthesized materials and as-fabricated photoelectrochemical devices were characterized using various analytical techniques. Instrumental tools used in the present studies involve:

(1) The crystalline structure and phase purity of all the materials were identified by powder X-ray diffraction (PXRD) analysis using Bruker D2 PHASER X-ray diffractometer with Cu–Kα X-ray generator (λ = 1.54 Å), Rigaku RINT 2500 TTRAX-III, with Cu–Kα (λ = 1.54 Å) X-ray source and Rigaku SmartLab9kW using Cu Kα (λ = 1.54 Å) as the source with 9kW power.

(2) UV-Visible absorption spectra were performed on JASCO Model V−650 and Shimadzu (UV-2600) diffuse reflectance spectrophotometer by using $BaSO_4$ as the reference.

(3) Horiba Jobin Vyon Laser Micro Raman System (Model- LabRam HR) with 488/514/633 nm laser excitation was used to analyze phase composition of all materials.

(4) The Fourier transform infrared (FT-IR) spectra were recorded using PerkinElmer Spectrum Two instrument in KBr pellets by scratching the as prepared films.

(5) Steady state photoluminescence (PL) measurements were recorded using a Horiba−Jobin Yvon Fluoromax-4 spectrophotometer.

(6) Surface morphological structures of as-synthesized materials were analyzed by field emission scanning electron microscopic (FESEM) analysis using Zeiss (Gemini) and Zeiss (Sigma) instruments, operating at the voltages of 3 kV−10 kV.

(7) Field emission transmission electron microscopy (FETEM) was carried out using JEOL (JEM-2100F) instrument with an operating voltage of 200 kV for the morphology, elemental mapping and selected area electron diffraction (SAED) patterns of the samples.

(8) Elemental and compositional analysis of the thin-films were verified by performing energy-dispersive X-ray spectroscopy (EDS) analysis using INCA, Oxford instruments.

(9) X-ray photoelectron spectroscopy (XPS) measurements were carried out using an ESCALAB Xi+ (Made: Thermo Fisher Scientific Pvt. Ltd., UK) photoelectron spectrometer (**Chapter 3 & 4**) and PHI 5000 Versa Probe III photoelectron spectrometer (**Chapter 6**) with a monochromatized Al-Kα (hν = 1486.6 eV) X-ray source. In this

analysis, all the peaks were referenced with respect to C 1s spectrum (284.77 eV) to compensate the surface charging effect and by the help of XPSPEAK 4.1 software, all XPS core level spectral data were analyzed. All the XPS data were fitted thorough background correction (Tougaard) available in the software.

(10) Surface area and roughness of the photoanodic films were analyzed by an atomic force microscope (AFM, Asylum Cypher, Oxford Instruments) in **Chapter 4 & 5** for the calculation of carrier density from Mott-Schottky plot.

(11) Electrochemical analysis such as cyclic voltammetry (CV) and open circuit potential (OCP) were recorded on a CHI1120B electrochemical workstation.

(12) A Newport ORIEL IQE–200 instrument fitted with a 250 W quartz tungsten halogen lamp was utilized to measure the incident photon to current conversion efficiency (IPCE) of solar device. Tungsten halogen lamp is calibrated by standard Si and Ge diodes.

(13) Electrochemical impedance spectroscopic (EIS) analyses of the devices were performed using an electrochemical work station provided by CH instruments model CHI760D, Inc., Austin, TX.

2.4 PHOTOELECTROCHEMICAL MEASUREMENTS

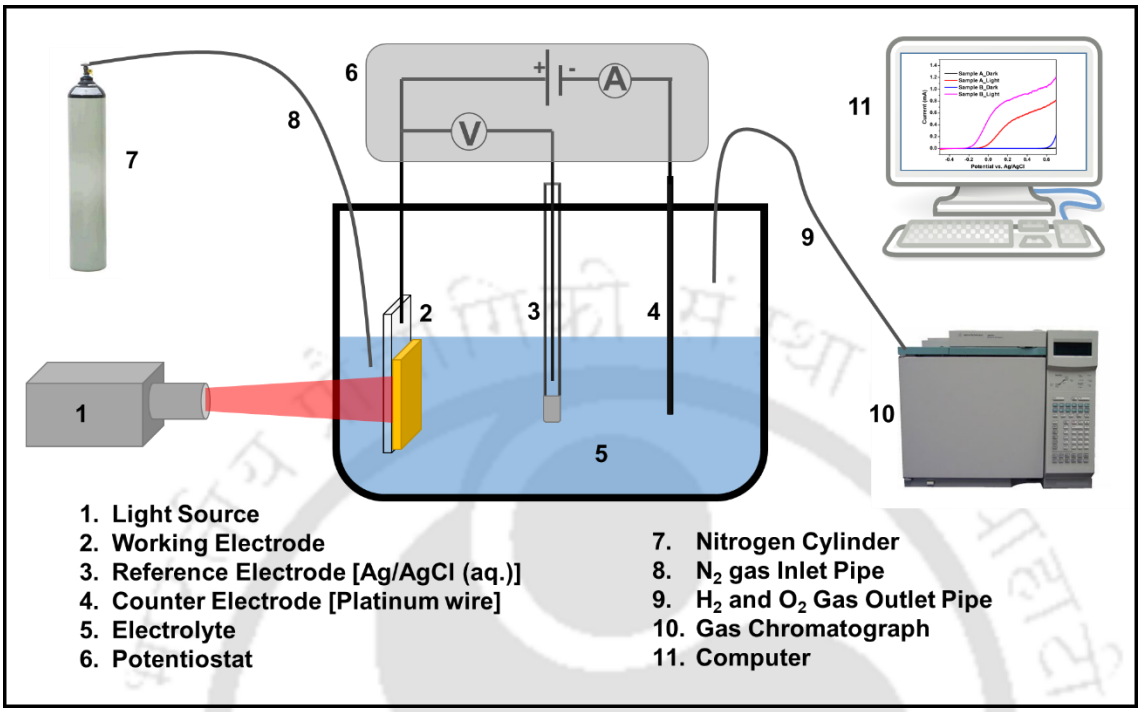

Figure 2.1 Schematic representation of the experimental setup for photoelectrochemical water splitting.

The photoelectrochemical measurements of the samples were performed with an electrochemical analyzer (model-CHI1120B) in a three-electrode system. 1M NaOH solution (**Chapter 2, 3 & 4**) and 0.5M KBi (**Chapter 6**), were used as electrolytes during measurements. As fabricated samples were used as working electrodes, Ag/AgCl (aqueous) electrode was used as reference and a Pt wire was used as counter electrode. The electrolyte solution was purged with nitrogen gas for 30 min before PEC measurements to remove any dissolved oxygen present in the electrolyte solution. All the potential applied were converted into RHE potential by following formula[1]:

$$E_{RHE} = E_{Ag/AgCl} + (0.059V \times pH) + E^{o}_{Ag/AgCl} \quad (2.1)$$

where E_{RHE} is the converted potential *vs.* RHE, $E_{Ag/AgCl}$ is the experimentally measured potential *vs.* Ag/AgCl (sat. KCl), $E^{o}_{Ag/AgCl}$ is the standard potential of Ag/AgCl reference electrode against the RHE (0.1976 V) and pH is the pH of the electrolyte. Epoxy adhesive (Araldite®) was used to

cover the photoanodes leaving an exposed thin film area of 0.25 cm^2.The light source was provided by a 300 W halogen lamp (Osram Sylvania, USA, in **Chapter 3, 4 & 5**) and solar simulator with an AM 1.5G filter (Photo Emission Tech., Inc., model 300WSS-PC, **Chapter 6**), and the light intensity was adjusted to 100 mW/cm^2. The electrochemical impedance spectra (EIS) were measured using an electrochemical work station (Model CHI760D, Inc., Austin, TX) in 1 M NaOH or 0.5M KBi aqueous solution in a frequency range of 10,000 Hz to 0.1 Hz with an amplitude of 10 mV in the dark. Mott–Schottky curves were obtained in a DC potential range from -01 to +01 V vs. Ag/AgCl with a frequency of 1000 Hz under dark conditions. Gas evolution test was analysed by online Gas Chromatograph (model- Agilent 7820A). The schematic representation of the experimental setup for photoelectrochemical water splitting is shown in **Figure 2.1**.

2.5 PHOTOELECTROCHEMICAL PERFORMANCE PARAMETERS

2.5.1 Incident photon-to-current conversion efficiency (IPCE)

Quantum efficiencies such as incident photon-to-current conversion efficiency (IPCE) is considered as an essential measurement to evaluate the performance of a photoelectrochemical device. The IPCE is defined as the numbers of incident photons that are converted to photocurrent by a photoelectrode as a function of wavelength. It can be expressed as (**equation 2.2**)[2]:

$$\mathrm{IPCE} = 1240 \times \frac{J_{sc}}{\lambda \times \mathrm{P_{mono}}(\lambda)} \qquad (2.2)$$

Where, P_{mono} is the light intensity at each wavelength(λ).

2.5.2 Faradaic efficiency/yield

Faradaic efficiency reports the percentage of the charges passed during an electrochemical reaction that are used for a desired reaction (i.e., O_2 production, H_2 production). Therefore, in order to calculate Faradaic efficiency for O_2 or H_2 evolution of a photoelectrode, the amount of H_2 and O_2 produced are needed in addition to the photocurrent density. It is the most useful method to verify that the generated photocurrent is in fact due to water splitting and not photocorrosion of the electrodes or other side reactions. The Faradaic efficiency can be obtained by dividing the

actual amount of H_2 and O_2 produced by the expected amount of H_2 and O_2 based on the total charge passed during the water splitting reaction using the following equations:[3,4]

$$\text{FE of } O_2(\%) = \frac{4\times n_{O_2}\,(\text{mol})\times F\,(\text{C mol}^{-1})}{\text{Charge passed through WE (C)}} \quad (2.3)$$

$$\text{FE of } H_2(\%) = \frac{2\times n_{H_2}\,(\text{mol})\times F\,(\text{C mol}^{-1})}{\text{Charge passed through WE (C)}} \quad (2.4)$$

The charge passed through the WE for oxygen evolution can be calculated as follows:

$$\text{Charge passed through WE (C)} = (\text{photocurrent (A)} \times \text{time(t)}) \quad (2.5)$$

The unit of gas evolution is moles; J_{SC} is the photocurrent density (A cm^{-2}) generated during the measurement time t (seconds); A is the illumination area of the photoelectrode (cm^2); e is the charge of an electron (1.602×10^{19} C) and N_A is the Avogadro constant (6.02×1023 mol^{-1}). The amounts of evolved gases can be analyzed by gas chromatography (GC) in the case of oxygen, by using a suitable oxygen electrode or fluorescence detector.[2]

2.5.3 Solar-to-hydrogen (STH) conversion efficiency

For evaluating PEC water splitting performance of a material, solar-to hydrogen (STH) conversion efficiency is the most overreaching of all efficiency value to report. From STH, one can directly get the material's ability to produce hydrogen gas from solar water splitting. It is defined as chemical energy of the hydrogen produced divided by the solar energy input from sunlight incident on the process. The STH efficiency can be calculated for the following equations[5]:

$$\eta_{STH}(\%) = \left[\frac{(\text{mmol } H_2\ s^{-1})\times(237\ \text{kJ mol}^{-1})}{P_{Total}(\text{mW cm}^{-2})\times \text{Area}(\text{cm}^2)}\right]_{AM1.5G} \times 100 \quad (2.6)$$

$$\eta_{STH}(\%) = \left[\frac{J_{sc}(\text{mA cm}^{-2})\times(1.23\ \text{V})\times\eta_F}{P_{Total}(\text{mW cm}^{-2})}\right]_{AM1.5G} \times 100 \quad (2.7)$$

Where, P_{Total} is the power input from illumination, *Area* is the geometric area, J_{SC} is the short-circuit photocurrent density and η_F is the faradic efficiency for hydrogen evolution. **Equation**

(2.6) calculates the STH efficiency based on direct measurement of true H_2 production rate by an analytical method such as gas chromatography. Alternatively, by using **equation (2.7)** the STH efficiency can be calculated from the photocurrent density (J_{SC}). However, the STH efficiency is valid when there is no external biased applied to the PEC system and it is of no use if a bias is necessary for overall water splitting. When an external bias is applied between the working and counter electrodes in the PEC system, it is required to subtract the electrical energy and thus it requires a new efficiency value separate from STH. The applied bias photon-to-current efficiency (ABPE) is frequently used instead of STH as the application of a bias generally increases the current drawn from the device according to **equation 2.8**.[3] ABPE is not a true solar-to-hydrogen measurement, it serves as a diagnostic measurement in materials development.

$$\text{ABPE}\ (\%) = \left[\frac{J_{sc}(\text{mA cm}^{-2})\times(1.23-V_b)(V)\times\eta_F}{P_{Total}(\text{mW cm}^{-2})}\right] \quad (2.8)$$

Where, J_{sc} is the photocurrent density obtained under an applied bias V_b.

2.6 ELECTROCHEMICAL IMPEDANCE SPECTROSCOPY (EIS) ANALYSIS

The conductivity of the PEC system determines the charge transfer efficiency in the electric circuit. Usually, it can be measured by electrochemical impedance spectroscopy (EIS), which is one of the universal and powerful modulation techniques and is helpful for further understanding the complex reaction at the photoelectrode surface. It allows sample characterization in electrolyte under bias potential, which is one of the major advantages of EIS compared with other spectroscopic techniques.

2.6.1 Nyquist plots

EIS experiments are composed of applying a small-amplitude sinusoidal signal to the photoanodes at a certain bias and measuring the response of the system to the perturbation. During an EIS experiment, the current density of the electrode is recorded while applying an alternating

current signal with different frequencies (usually 0.1 Hz < f < 10^6 Hz) to the system. By EIS characterization, Nyquist plot (real vs. imaginary impedance) can be obtained. In the spectrum, the *X*-axis is the real impedance (*Z′*, in the unit of Ohms), while the *Y*-axis represents the imaginary impedance (*Z″*, in the unit of Ohms).[6] Theoretically, a typical Nyquist plot can be divided into two parts: high frequency region and low frequency region, as shown in **Figure 2.2(a)**. High frequency region can be observed close to the original point of the plot. In this region, the photo-electrochemical process is controlled by the rate of charge transfer and the curve exhibits the shape of a semicircle which hints the existence of an interface. In low frequency region (large impedance, far from the origin), the process is determined by the rate of mass transfer.[7] Sometimes, there are more than one semicircles on the Nyquist plot. It can be ascribe to a multiple-step electron-or charge-transfer process mediated via surface states or reaction intermediates. The shape of the curves could be affected by the intrinsic or electrochemical properties of electrodes, electrolytes, and the conditions of the experiments.[8] The parameters from the Nyquist plot can be determined by fitting the frequency responses with an equivalent circuit model as shown in inset of **Figure 2.2(a)**.

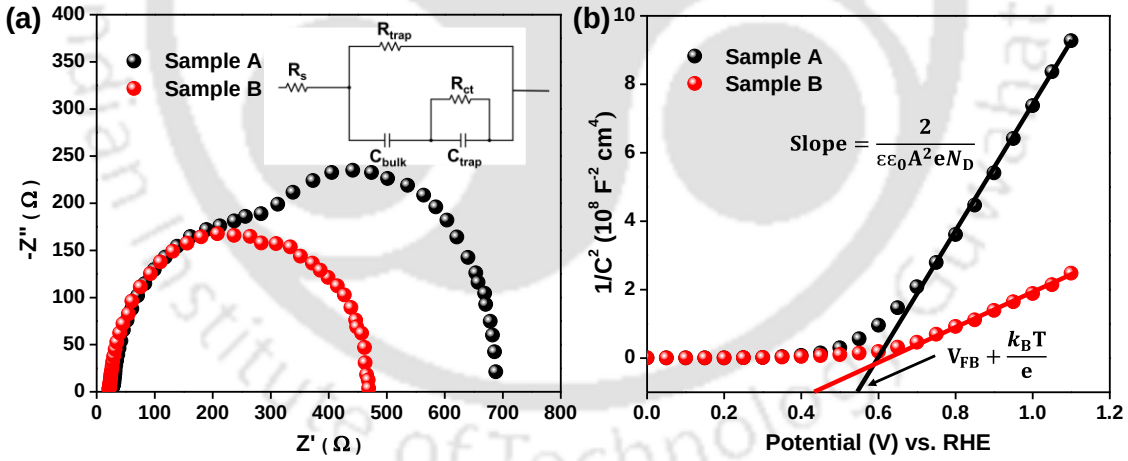

Figure 2.2 (a) Nyquist plot with equivalent circuit used to interpret the EIS data and (b) a typical Mott-Schottky plot.

The resistance accounting for surface-state trapping electrons from the conduction band and holes from the valence band, acting as a recombination center, is given by R_{trap}. Surface states affect the charge transfer of holes to the donor species in solution, which could be described as a

resistance R_{ct}. A smaller R_{ct} specifies a lower charge-transfer resistance in the photoande. The trap-state capacitance was denoted as C_{trap}, and the space-charge depletion region capacitance a C_{bulk}. Finally, R_S is the series resistance of the cell.[9]

2.6.2 Mott-Schottky plots

Mott–Schottky plots are a characterization method based on the Mott–Schottky theory now widely used in many areas. The charge-carrier concentration (or density, as it is called in some references) in semiconductors is one of the main factors that affects the charge-transport properties, which, in turn, affects their photocurrent densities. In this way, the investigation of Mott–Schottky plots is a good approach to obtain qualitative information about the charge-transport properties. The flat band potential, E_{FB}, is the potential at which the electric potential drop between the electrode surface and the bulk is zero. It establishes the position of the semiconductor energy bands with respect to the redox potentials of the electroactive species in the electrolyte. To obtain the value of E_{FB} by Mott– Schottky measurements, a potentiostat with a three-electrode system, similar to that used for photocurrent measurements, can be used. Then, the Mott–Schottky equation can be used to obtain the value of E_{FB} after obtaining the Mott–Schottky plots. The flat band (E_{FB}) and carrier density (N_D) of the photoanodes can be calculated from the following formula (**equation 2.9**):[10,11]

$$\frac{1}{C^2} = \frac{1}{A^2 N_D e \varepsilon \varepsilon_0}\left[E - E_{FB} - \frac{kT}{e}\right] \quad (2.9)$$

where C is the capacitance of the semiconductor, A is the surface area of the photoelectrode, N_D is the electron carrier density of semiconductor, e is the fundamental charge constant, ε_0 is the permittivity of the vacuum, ε is the relative permittivity of the semiconductor, E is the applied potential, k is the Boltzmann constant, and T is the temperature.

2.7 REFERENCES

(1) C. Miao, T. Shi, G. Xu, S. Ji and C. Ye, *ACS Appl. Mater. Interfaces*, 2013, **5**, 1310.

(2) C. Jiang, S. J. A. Moniz, A. Wang, T. Zhang and J. Tang, *Chem. Soc. Rev.*, 2017, **46**, 4645.

(3) J. H. Kim, D. Hansora, P. Sharma, J.-W. Jang and J. S. Lee, *Chem. Soc. Rev.*, 2019, **48**, 1908.

(4) Z. Chen, H. Dinh and E. Miller, *Photoelectrochemical Water Splitting*, Springer, 2013.

(5) G. V. Govindaraju, G. P. Wheeler, D. Lee and K. S. Choi, *Chem. Mater.*, 2017, **29**, 355.

(6) X.-T. Xu, L. Pan, X. Zhang, L. Wang and J.-J. Zou, *Adv. Sci.*, 2019, **6**, 1801505.

(7) A. J. Bard, L. R. Faulkner, J. Leddy and C. G. Zoski, *Electrochemical Methods: Fundamentals and Applications*, Wiley, 1980.

(8) C. Cao and J. Zhang, *An Introduction to Electrochemical Impedance Spectroscopy*, Science Press, 2002.

(9) B. Klahr, S. Gimenez, F. Fabregat-Santiago, T. Hamann and J. Bisquert, *J. Am. Chem. Soc.*, 2012, **134**, 4294.

(10) C. Adel, B. M. Fethi and B. Brahim, *Appl. Phys. A: Mater. Sci. Process.*, 2016, **122**, 62.

(11) H. Dotan, K. Sivula, M. Grätzel, A. Rothschild and S. C. Warren, *Energy Environ. Sci.*, 2011, **4**, 958.

CHAPTER 3

Surface Passivation of Zinc Ferrite as an Effective Strategy for Enhanced Photoelectrochemical Water Oxidation: Fabrication and Photoelectrochemical Characterizations

This chapter presents solution processed fabrication of one-dimensional (1-D) $ZnFe_2O_4$ nanorods directly onto the fluorine doped tin oxide (FTO) substrate. The effect of different annealing temperatures on their photoelectrochemical efficacies have been explored. Also the effect of surface passivation overlayer on the surface defects and back transfer of electrons have been studied, which directly affect the photoelectrochemical water oxidation performance of $ZnFe_2O_4$.

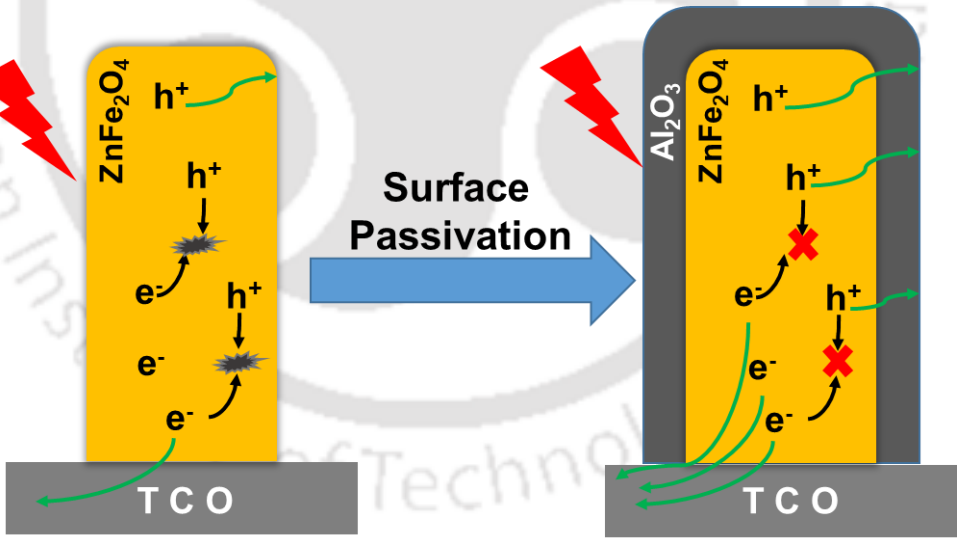

ChemComm

T. K. Sahu *et al.*, 2018, **54**, 10483

3.1 INTRODUCTION

Spinel zinc ferrite ($ZnFe_2O_4$) is an n-type semiconductor, having a narrow band gap of around 2.0 eV.[1] Owing to its excellent optical properties, better photo-stability and a suitable band gap, it acts as an efficient photoactive material. However, the photoelectrochemical (PEC) water oxidation of $ZnFe_2O_4$ has not been widely studied. There are very few reports on $ZnFe_2O_4$ based modification, where it was mostly utilised as a supporting material and did not show any significant photoactivity, owing to the need for high temperature (more than 1000 °C) for the crystallization of ferrite materials.[2-7] Thus, the fabrication of such types of materials directly onto a conductive glass substrate is a challenging task. In the recent past, there have been some reports on the fabrication of $ZnFe_2O_4$ onto a conductive glass substrate by means of more complicated methods.[8-14] Photocurrent yields are still found to be very much lower as compared to other metal oxide semiconductors although it has higher theoretical photoconversion efficiency, due to the formation of surface states owing to its high temperature synthesis. Passivation of surface states could be one of the efficient methods to reduce surface recombination of photogenerated charge carriers in semiconductor photoanodes.[15] Recently, there have been reports on the surface passivation of metal oxides to reduce the surface recombination and back transfer of charge carriers, thus reducing the recombination.[15-21] The main purpose of these non-catalytic oxide overlayers is to passivate the surface states of photoanodes. Indeed, it has been found that surface recombination decreases after the introduction of oxide overlayers, which is also known to release the lattice strain in photoanodes with fewer surface traps.[15,16] Among the methods used for the fabrication of $ZnFe_2O_4$ photoelectrodes, the solvothermal route is more convenient for one-dimensional (1-D) nanorod growth.[12] In this work, we have fabricated solution processed 1-D $ZnFe_2O_4$ nanorods directly onto a fluorine doped tin oxide (FTO) substrate and studied the effect of different annealing temperatures on their photoelectrochemical efficacies. An alumina overlayer was deposited over $ZnFe_2O_4$ photoanode by chemical bath deposition (CBD) method and its effect on the surface states have been explored. Systematic structural and opto-electrical characterizations of pristine and surface passivated photoanodes have been carried out to understand their PEC performance.

Part of this chapter has been published in **Chem. Commun., 2018, 54, 10483.**

3.2 EXPERIMENTAL METHODS

3.2.1 *In situ* growth of $ZnFe_2O_4$ by β-FeOOH route

The $ZnFe_2O_4$ photoanode was fabricated on the FTO substrate by modification of a previously reported two-step solution method.[12,13] First, to a 100 mL teflon-lined stainless steel autoclave containing 30 mL of an aqueous solution of 0.15 M $FeCl_3$ and 1 M $NaNO_3$ and 158 µL HCl (36%), four pieces of cleaned FTO substrate were put with the conducting layer facing upward. The autoclave was heated at 95 °C for 4 h in a hot air oven. This results in the formation of a uniform layer of yellow β-FeOOH nanorods over the FTO substrate. The β- FeOOH-coated substrate was then washed with deionized water and ethanol to remove any residual salt. The as-prepared β-FeOOH film were dipped in to a solution containing 1M $Zn(NO_3)_2.6H_2O$ for 30 min. The wet film was transferred to a furnace which was already heated to 550 °C and annealed for 2 h. During the annealing process, the β-FeOOH nanorods turned into $ZnFe_2O_4$ nanorods wrapped with an excess ZnO layer. This unwanted ZnO skin was removed by soaking the film in 1 M NaOH solution for 12 h with stirring. To reduce the surface defect sites, the $ZnFe_2O_4$ nanorods were treated again at 550°C for 1 h or 800°C for 10 min.

3.2.2 Synthesis of Al_2O_3 coated $ZnFe_2O_4$ nanorods

The as-prepared $ZnFe_2O_4$-800 films were coated with Al_2O_3 overlayers by chemical bath deposition (CBD) method.[18] In this method, the $ZnFe_2O_4$ films were dipped in to a 200 mL solution containing 1 g. of $Al(NO_3)_3.9H_2O$ and 0.8 g of urea for 60 min at 90°C. After that, the films were washed with distilled water, dried and annealed at 550°C for 2 h in a muffle furnace. The as prepared film was named as $ZnFe_2O_4$-Al_2O_3. Schematic representation of fabrication of photoanodes starting from fabrication of β-FeOOH, $ZnFe_2O_4$ and $ZnFe_2O_4$-Al_2O_3 are shown in **Scheme 3.2.1**. The picture shows the prepared $ZnFe_2O_3$-550°C, $ZnFe_2O_4$-800°C and $ZnFe_2O_4$-Al_2O_3 films from left to right, respectively, with a characteristic yellow color.

Part of this chapter has been published in **Chem. Commun., 2018, 54, 10483.**

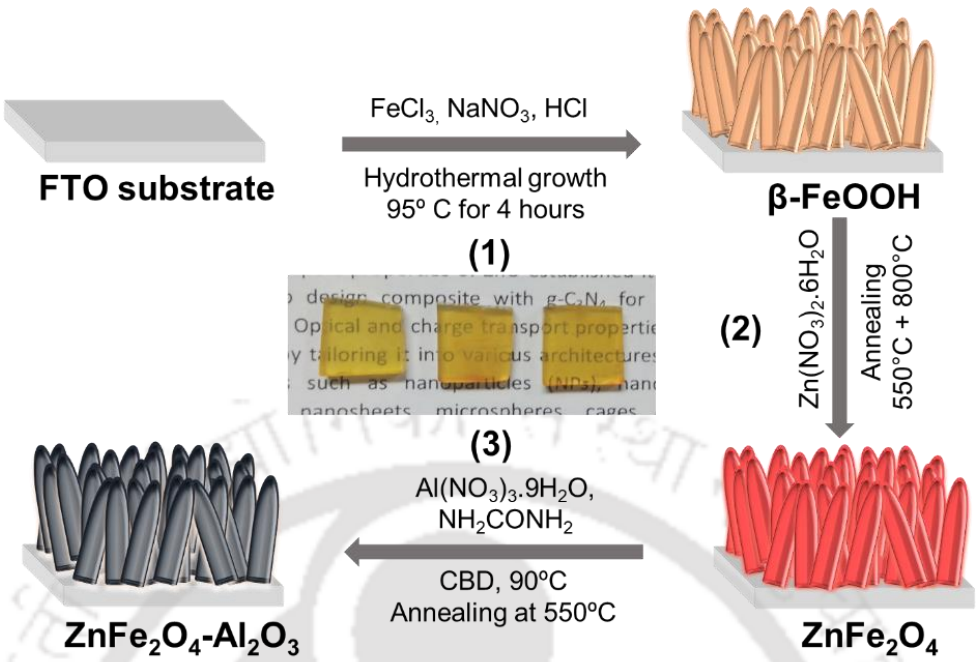

Scheme 3.2.1 Step-by-step fabrication of $ZnFe_2O_4$-Al_2O_3 photoanode (1) Fabrication of β-FeOOH nanorods over FTO substrate, (2) conversion of β-FeOOH to $ZnFe_2O_4$ by wet dipping of Zn precursor followed by annealing and (3) deposition of Al_2O_3 over $ZnFe_2O_4$ by chemical bath deposition (CBD) method. The picture shows the prepared $ZnFe_2O_3$-550°C, $ZnFe_2O_4$-800°C and $ZnFe_2O_4$-Al_2O_3 films from left to right, respectively.

3.3 RESULTS AND DISCUSSIONS

3.3.1 Powder x-ray diffraction (XRD) and Raman analysis

The formation and phase purity of the fabricated films were confirmed by powder X-ray diffraction analysis as shown in **Figure 3.3.1(a)**. The powder XRD of β-FeOOH was well matched with JCPDS card 75-1549. For $ZnFe_2O_4$, the peaks at 2θ = 30° represent the (220) crystal planes and 2θ=35.2° represent the (311) crystal planes of the cubic spinel $ZnFe_2O_4$ (The olive vertical lines represent peaks of cubic spinel $ZnFe_2O_4$, JCPDS card 01-089-4926). There were no impurities of ZnO or Fe_2O_3 present in the XRD pattern of $ZnFe_2O_4$, which confirms its purity. The weak XRD peaks of $ZnFe_2O_4$ became sharp with further temperature treatment at 800°C. The crystallinity of $ZnFe_2O_4$ was improved after annealing at 800 °C. As the films were directly grown over FTO substrate, the peaks of SnO_2 were clearly visible. After the deposition of the amorphous Al_2O_3 layer, there was a slight decrease in sharpness of the $ZnFe_2O_4$ peaks, may be due to the amorphous nature of Al_2O_3.[22]

Part of this chapter has been published in **Chem. Commun., 2018, 54, 10483.**

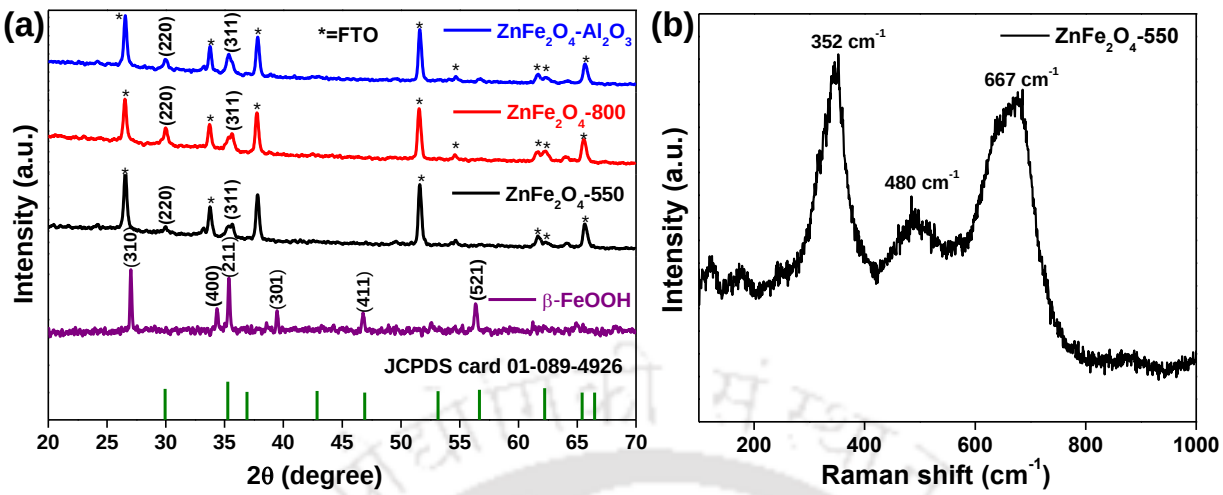

Figure 3.3.1 (a) Powder XRD of β-FeOOH, $ZnFe_2O_4$-550, $ZnFe_2O_4$-800 and $ZnFe_2O_4$-Al_2O_3 and Raman spectrum of $ZnFe_2O_4$-550.

The Raman spectrum shown in **Figure 3.3.1(b)** shows that $ZnFe_2O_4$ has a spinel structure with space group *Fd3m*. Out of five Raman modes three were observed at 352 cm^{-1}, 480 cm^{-1} and 667 cm^{-1}. The motion of oxygen in tetrahedral AO_4 groups happens at modes above 600 cm^{-1}. These modes can be assigned to A_{1g} symmetry and the other low frequency modes to both E_g and F_{2g} which were the characteristics of the octahedral sites (BO_6).[8,23]

3.3.2 UV-visible absorption spectra and FTIR analysis

UV-visible spectral analysis was conducted to check the optical absorption characteristics of the photoelectrodes (**Figure 3.3.2(a)**). No significant differences in the absorption spectra of the $ZnFe_2O_4$ and $ZnFe_2O_4$–Al_2O_3 photoelectrodes were observed. This result implies that no intermediate bands were formed between the band-gap edges of $ZnFe_2O_4$ after the incorporation of the Al_2O_3 layer. FTIR spectroscopy shown in **Figure 3.3.2(b)** confirmed that aluminium hydroxide was first formed onto the surface of $ZnFe_2O_4$ during the CBD reaction and then it was dehydroxylated to form Al_2O_3 after annealing at 550 °C. The wavenumber of 1040 cm^{-1} could be assigned to Al-OH bending. The peaks at 3450, 3367 cm^{-1} might be attributed to Al-OH stretching. The peak at 1375 cm^{-1} corresponding to C=O was identified to the urea used in the CBD bath, which will be removed during the annealing treatment. The H-O-H bending exhibits the peak of 1623 cm^{-1}, indicating the absorption of water. [18]

Part of this chapter has been published in **Chem. Commun., 2018, 54, 10483.**

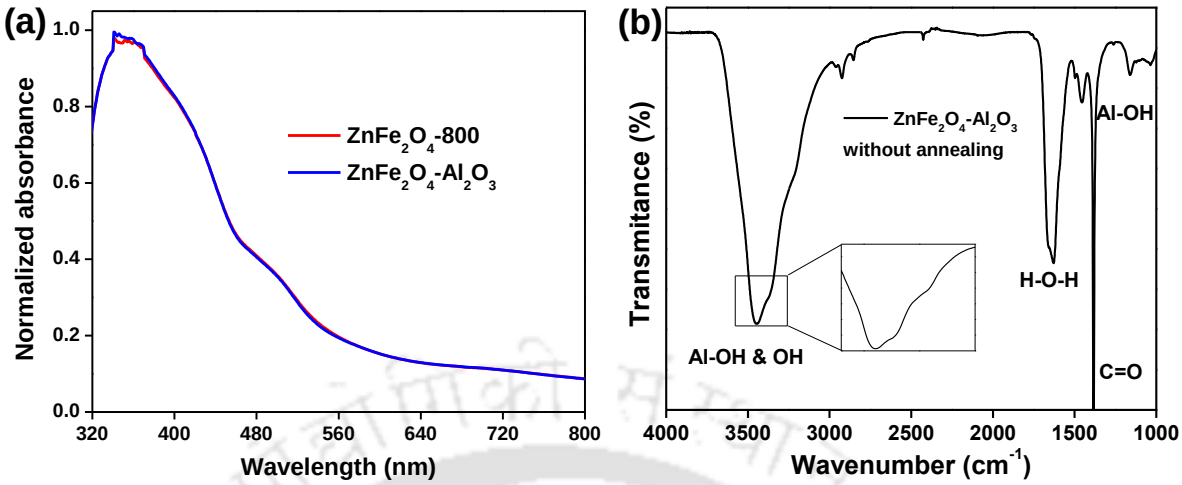

Figure 3.3.2 (a) UV-visible spectra of $ZnFe_2O_4$-800 and $ZnFe_2O_4$-Al_2O_3 and (b) FT-IR spectrum of $ZnFe_2O_4$-$Al(OH)_3$ treated with CBD process without annealing.

3.3.3 X-ray photoelectron spectroscopy (XPS) analysis

The surface properties of the as-synthesized compounds and the electronic structure of the constituent elements were probed using X-ray photoelectron spectroscopy (XPS). **Figure 3.3.3(a)** shows the typical XPS survey spectra of as-synthesized $ZnFe_2O_4$-800 and $ZnFe_2O_4$–Al_2O_3 with the presence of all constituent elements. **Figure 3.3.3(b)** shows the Zn 2p core-level spectra of $ZnFe_2O_4$ and $ZnFe_2O_4$–Al_2O_3. In $ZnFe_2O_4$, two peaks appeared at binding energies (BEs) of 1020.6 eV and 1043.7 eV corresponding to Zn $2p_{3/2}$ and Zn $2p_{1/2}$, respectively. In $ZnFe_2O_4$–Al_2O_3, two peaks appeared at the BEs of 1020.7 eV and 1043.8 eV corresponding to Zn $2p_{3/2}$ and Zn $2p_{1/2}$, respectively. In both $ZnFe_2O_4$ and $ZnFe_2O_4$–Al_2O_3, the peak separation energy (Δ BE) is 23.1 eV, suggesting the presence of Zn(II) in these compounds.[10] **Figure 3.3.3(c)** shows the Fe 2p core-level spectra of $ZnFe_2O_4$-800 and $ZnFe_2O_4$–Al_2O_3. Upon de-convolution, the Fe 2p peaks of $ZnFe_2O_4$-800 and $ZnFe_2O_4$–Al_2O_3 are fitted into Fe $2p_{3/2}$, Fe $2p_{1/2}$, and two shake-up satellite peaks. Further de-convolution of the asymmetric Fe $2p_{3/2}$ peaks produces two peaks at BEs of 710.2 eV and 712 eV in $ZnFe_2O_4$ and 710.3 eV and 712.1 eV in $ZnFe_2O_4$–Al_2O_3, which correspond to octahedral or the B-site and tetrahedral or the A-site, respectively. The presence of Fe $2p_{3/2}$, Fe $2p_{1/2}$ and two shake-up satellite peaks ascertains the presence of Fe(III) in these compounds.[24] The Al 2p core level XPS spectra of $ZnFe_2O_4$–Al_2O_3 arise at the BE of 73.4 eV corresponding to Al(III) as shown in **Figure 3.3.3(d)**.[18]

Part of this chapter has been published in **Chem. Commun., 2018, 54, 10483.**

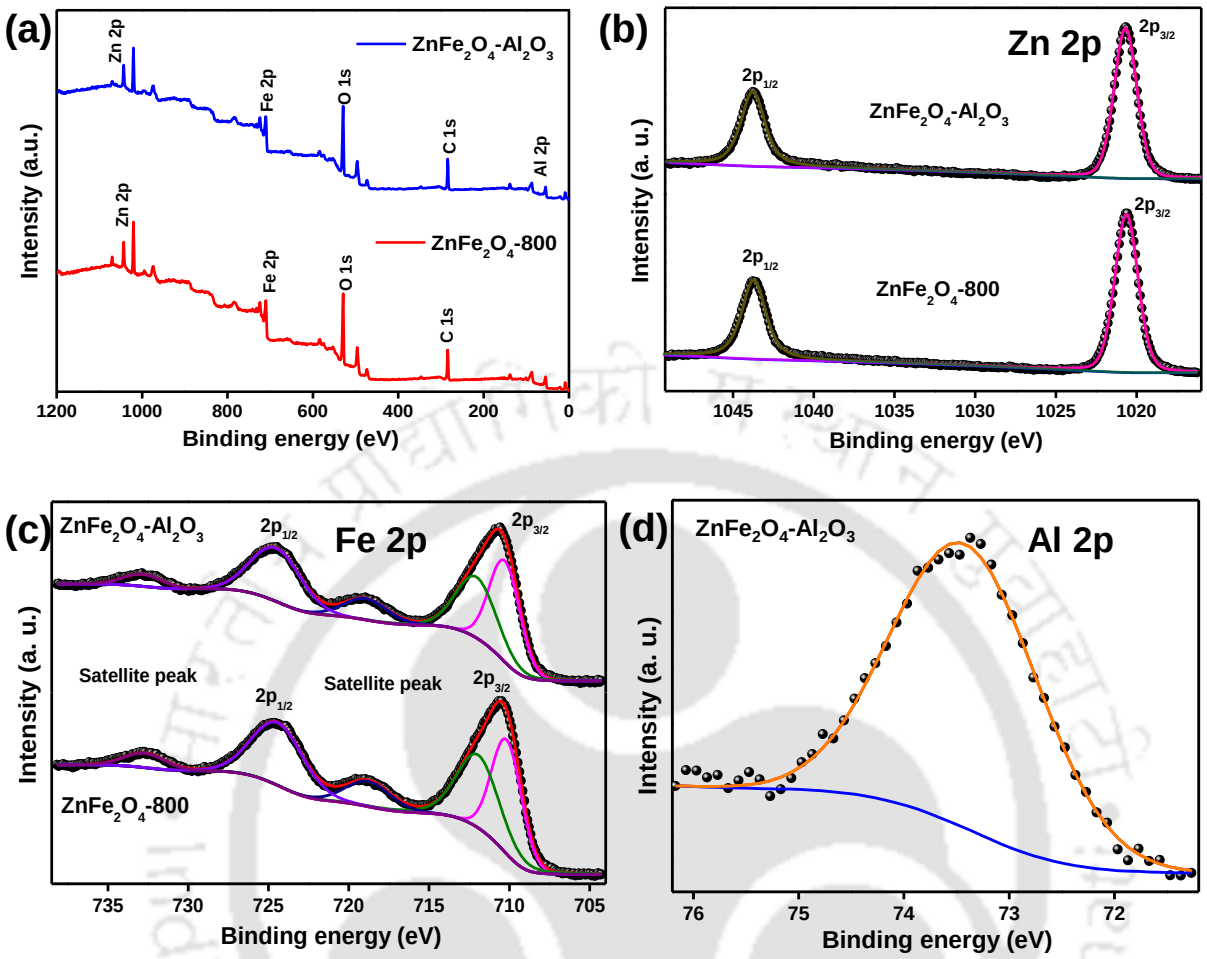

Figure 3.3.3 (a) XPS survey spectra, (b) Zn 2p core level (c) Fe 2p core level and (d) Al 2p core level of $ZnFe_2O_4$–Al_2O_3 (Al_2O_3 annealed at 550 °C).

As Shown in **Figure 3.3.4(a)**, de-convolution of the asymmetric O 1s XPS core level spectra of $ZnFe_2O_4$ and $ZnFe_2O_4$–Al_2O_3 gives three peaks at BEs of 528.6 eV, 530.2 eV, 531.7 eV, and 528.8 eV, 530.5, 531.8 eV, respectively. The peak at higher BE corresponds to the adsorbed surface hydroxyl groups[12] and the peak at lower BE corresponds to lattice oxygen (O_2^{2-}) in both the compounds.[25] The peaks in the middle region are due to oxygen vacancy for bare $ZnFe_2O_4$ and Al–O and oxygen vacancy for $ZnFe_2O_4$–Al_2O_3.[10] The shift in this region as well as the increase in the area for $ZnFe_2O_4$–Al_2O_3 confirms the presence of Al–O (**Figure 3.3.4(b)**). In comparison, the Zn 2p, Fe 2p and O 1s peaks in $ZnFe_2O_4$–Al_2O_3 slightly shifted towards the higher binding energies compared to $ZnFe_2O_4$, which may be due to the partial chemical interaction between $ZnFe_2O_4$ and the Al_2O_3 layer.

Part of this chapter has been published in **Chem. Commun., 2018, 54, 10483.**

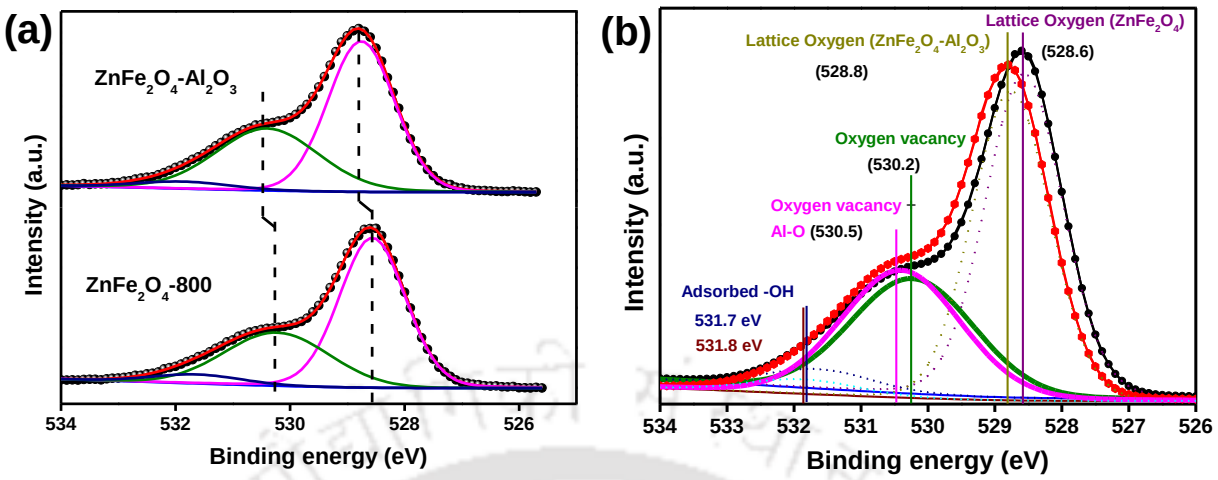

Figure 3.3.4 (a) O 1s core level spectra of $ZnFe_2O_4$ and $ZnFe_2O_4$–Al_2O_3 and (b) overlapped O 1s core level spectra of $ZnFe_2O_4$ and $ZnFe_2O_4$–Al_2O_3 to get more insights in to the changes caused by passivation layer.

3.3.4 Materials morphology

Figure 3.3.5 shows the morphology of pristine $ZnFe_2O_4$ annealed at different temperatures and Al_2O_3 coated $ZnFe_2O_4$ photoanodes. **Figure 3.3.5(a)** shows the FESEM of β-FeOOH nanorods directly grown over FTO substrate before annealing. The growth of β-FeOOH over FTO substrate was optimized to achieve nanorods morphology, as overgrowth of β-FeOOH may leads to formation of Fe_2O_3 impurities after calcination. **Figure 3.3.5(b)** shows the FESEM of pristine $ZnFe_2O_4$ nanorods annealed at 550 °C, where uniform growth of 1-D $ZnFe_2O_4$ nanorods over the FTO substrate can be clearly seen. It can be seen that the nanorods structure did not deform when calcined at 550°C. However, the compactness of the $ZnFe_2O_4$ nanorods increased with increasing the annealing temperature to 800 °C as shown in **Figure 3.3.5(c)**. Also, there was a negligible deformation in the nanorods structure due to high temperature annealing. This 1-D structure gives rise to efficient charge separation and provides a very short diffusion path for holes to reach the photoelectrode/electrolyte interface.[26] Due to the overlayer growth of Al_2O_3 using CBD, the morphology of the $ZnFe_2O_4$ photoanodes did not change, as shown in **Figure 3.3.5(d)**. This may be due to very thin and transparent layer deposition of alumina over $ZnFe_2O_4$.

Part of this chapter has been published in **Chem. Commun., 2018, 54, 10483.**

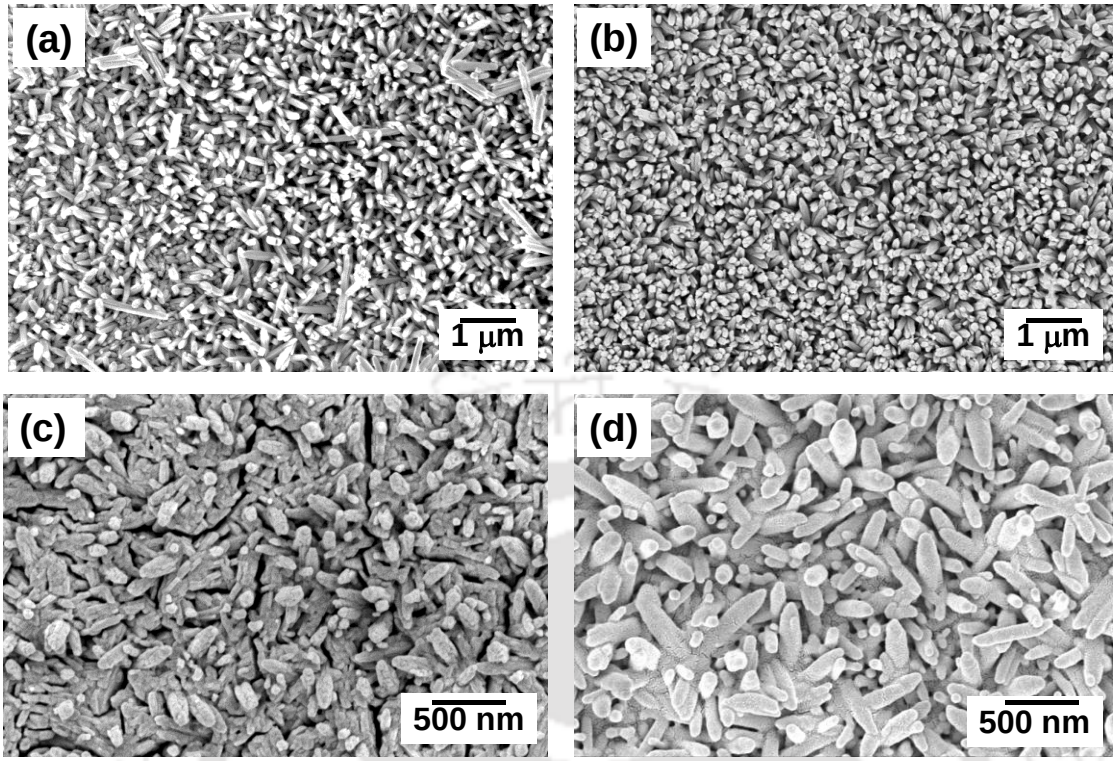

Figure 3.3.5 Top-view FESEM images of (a) as synthesized β-FeOOH before annealing, (b) pristine $ZnFe_2O_4$ annealed at 550°C, (c) pristine $ZnFe_2O_4$ annealed at 800°C and (d) $ZnFe_2O_4$-Al_2O_3 directly fabricated over FTO conductive substrate.

The cross-sectional FESEM image of β-FeOOH shows vertical growth of nanorods over FTO substrate as shown in **Figure 3.3.6(a)**. When the phase was changed to $ZnFe_2O_4$ with annealing, there was a slight deformation in the nanorods structure due to high temperature annealing as shown in **Figure 3.3.6(b)** and **(c)**.

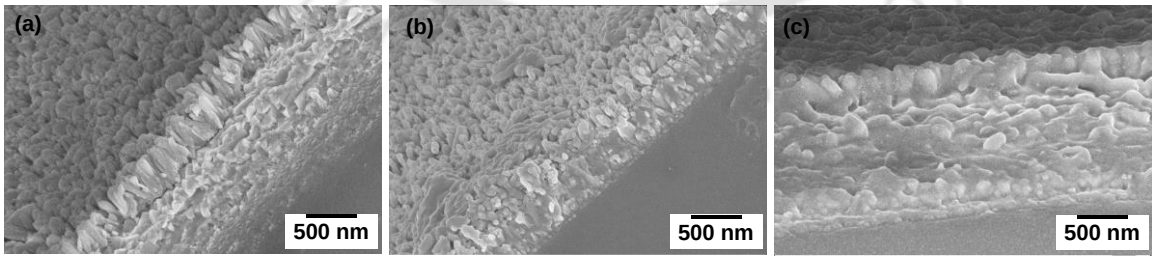

Figure 3.3.6 (a) Cross-sectional FESEM image of (a) β-FeOOH, (b) $ZnFe_2O_4$-800 and (c) $ZnFe_2O_4$-Al_2O_3 directly grown over FTO substrate.

Part of this chapter has been published in **Chem. Commun., 2018, 54, 10483.**

The FETEM image of pristine $ZnFe_2O_4$ shown in **Figure 3.3.7(a)**, confirmed the formation of nanorods over FTO substrate with width around 50 nm. The selected area electron diffraction (SAED) pattern shown in **Figure 3.3.7(b)** indicates the single crystalline structure of the pristine $ZnFe_2O_4$.

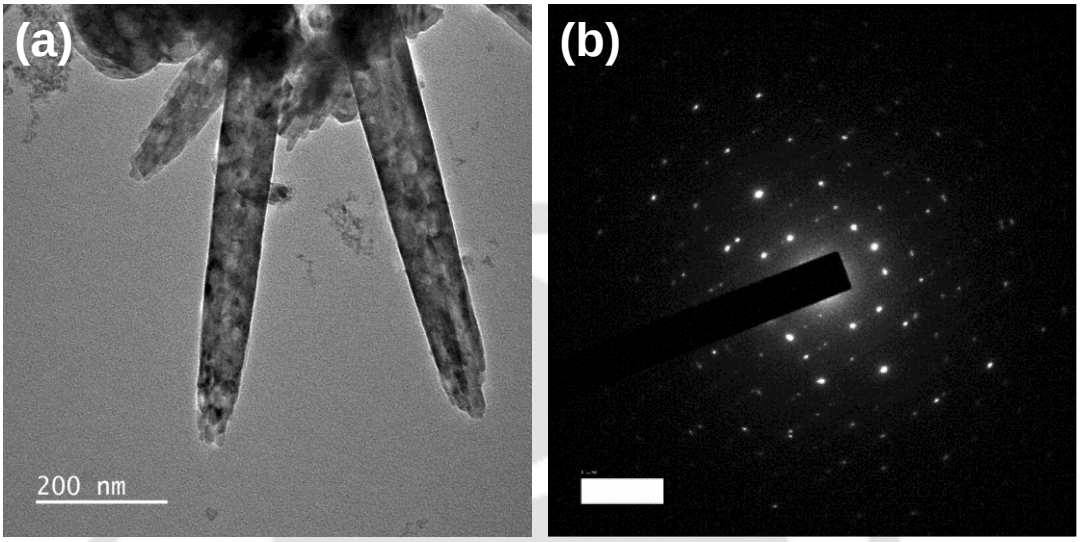

Figure 3.3.7 (a) FETEM image of pristine $ZnFe_2O_4$ annealed at 800°C and (b) the corresponding selected area electron diffraction (SAED) pattern.

Further, the high-resolution TEM image of $ZnFe_2O_4$-Al_2O_3 shows a uniform layer of amorphous Al_2O_3 with a thickness of around 5 nm on the surface of the $ZnFe_2O_4$ nanorods (**Figure 3.3.8(a)**). Possible formation of an Al_2O_3 layer can be explained by the adsorption of $Al(OH)_3$ during CBD method and dehydroxylation upon calcination of the $ZnFe_2O_4$ surface.[18] The *d*-spacing of ~0.292 nm, corresponding to the (220) crystal plane of $ZnFe_2O_4$, confirmed the formation of a pure $ZnFe_2O_4$ phase as shown in **Figure 3.3.8(b)**.[12] The polycrystalline nature of $ZnFe_2O_4$–Al_2O_3 was well supported by the SAED pattern shown in the inset of **Figure 3.3.8(b)** due to amorphous Al_2O_3 overlayer.

Part of this chapter has been published in **Chem. Commun., 2018, 54, 10483.**

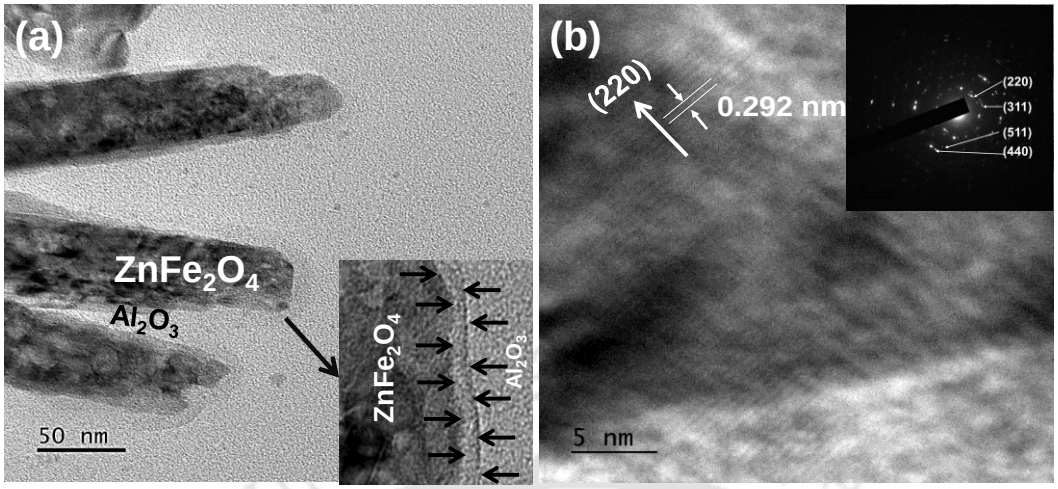

Figure 3.3.8 (a) FETEM of $ZnFe_2O_4$–Al_2O_3 (the inset showing the uniform coating of alumina with a thickness of around 5 nm). (b) HR-TEM of $ZnFe_2O_4$–Al_2O_3 (the inset showing the selected area electron diffraction (SAED) pattern of $ZnFe_2O_4$–Al_2O_3).

In order to confirm the uniform growth and distribution of Al_2O_3 over $ZnFe_2O_4$, the elemental mapping of the composite photoanode was recorded using energy dispersive X-ray analysis as shown in **Figure 3.3.9(a)**. The elemental mapping and composition proves the homogeneous distribution of Zn, Fe, O and Al in the composite photoanode thin film as shown in **Figure 3.3.9(b)-(f)**.

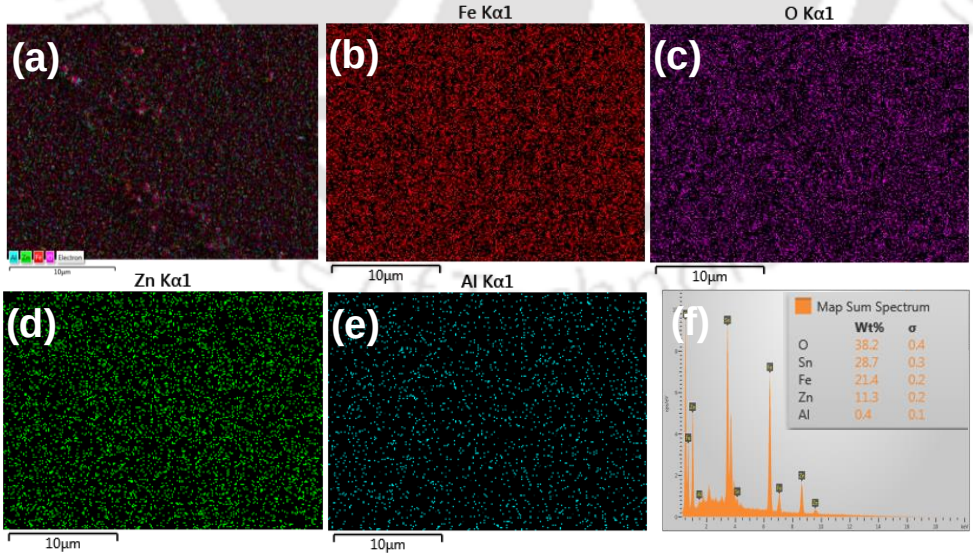

Figure 3.3.9 (a) Elemental mapping of $ZnFe_2O_4$–Al_2O_3 showing the uniform distribution of (b) Fe, (c) O, (d) Zn, and (e) Al. (f) FESEM-EDX showing elemental composition.

Part of this chapter has been published in **Chem. Commun., 2018, 54, 10483.**

3.3.5 Photoelectrochemical characterizations

Photocurrent measurements of all the photoanodes were carried out by sweeping potential from −0.4 V to 0.8 V *vs.* Ag/AgCl in a 1 M NaOH electrolyte solution under one-sun illumination and dark conditions. **Figure 3.3.10(a)** shows that the $ZnFe_2O_4$-800 photoanode sintered at 800 °C exhibited a photocurrent of 0.161 mA cm^{-2} at 1.23 V *vs.* RHE, a dramatic improvement compared to that of $ZnFe_2O_4$-550 sintered at 550 °C (0.067 mA cm^{-2}). This low current density of $ZnFe_2O_4$ annealed at 550 °C was in good agreement with a previous report.[23] Under the same experimental conditions with a thin Al_2O_3 overlayer, the photocurrent increased up to 0.484 mA cm^{-2}, which was around 7-fold and 3-fold higher than those of $ZnFe_2O_4$-550 and $ZnFe_2O_4$-800, respectively.

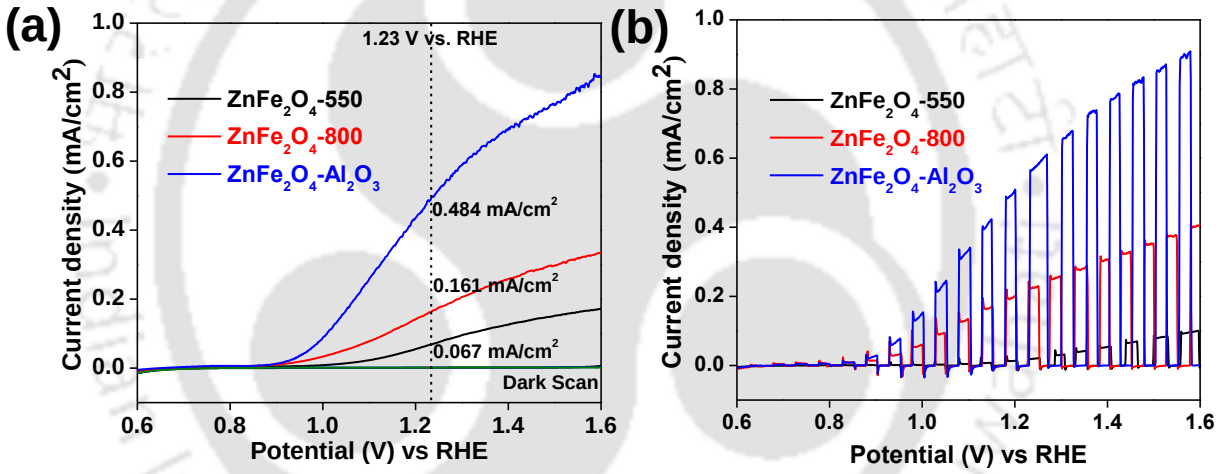

Figure 3.3.10 (a) *J–V* curves of $ZnFe_2O_4$-550, $ZnFe_2O_4$-800 and $ZnFe_2O_4$-Al_2O_3 photoanodes under light illumination at a scan rate of 10 mV s^{-1} in 1 M NaOH, (b) *J–V* curves of $ZnFe_2O_4$-550, $ZnFe_2O_4$-800 and $ZnFe_2O_4$-Al_2O_3 photoanodes with chopping with a regular interval of time.

It is noteworthy that the onset potential of $ZnFe_2O_4$ did not change after the addition of the Al_2O_3 overlayer. These results suggested that the conduction band edge (photocurrent onset potential) remains fixed upon alumina deposition.[27] This result was in good agreement with earlier reports of CBD deposited Al_2O_3/Fe_2O_3[18] and ALD deposited Al_2O_3/WO_3,[20] but opposite to ALD deposited Fe_2O_3[16,18] where a lowered onset potential was observed with alumina deposition. These results suggested that the Al_2O_3 passivation effect was highly dependent on the parent materials and also on the extent of surface coverage.[28] The increase in photocurrent from $ZnFe_2O_4$-550 to

Part of this chapter has been published in **Chem. Commun., 2018, 54, 10483.**

$ZnFe_2O_4$-800 was mainly due to the improved crystallinity and may be due to increasing compactness of the nanostructured $ZnFe_2O_4$, as seen from FESEM of the respective photoanodes. The increase in photocurrent with the deposition of the Al_2O_3 overlayer was mainly attributed to the surface passivation of $ZnFe_2O_4$ rather than the added contribution of the oxygen evolution reaction (OER) from the passivated layer. Also, it is noteworthy that the thin overlayer reportedly contributed to the change of the lattice strain of $ZnFe_2O_4$ layers which decreased the density of surface trap states.[15] As shown in **Figure 3.3.10(b)**, the anodic current spikes and cathodic transient peaks of $ZnFe_2O_4$-Al_2O_3 disappeared when the bias was more positive than 1.23 V *vs.* RHE, indicating that accumulation and recombination of holes were prevented by CBD-Al_2O_3. In contrast, the cathodic transient peaks of $ZnFe_2O_4$-550 and $ZnFe_2O_4$-800 were visible after 1.23 V *vs.* RHE. This experimental evidence confirmed that the PEC performance improved with introduction of CBD-Al_2O_3.

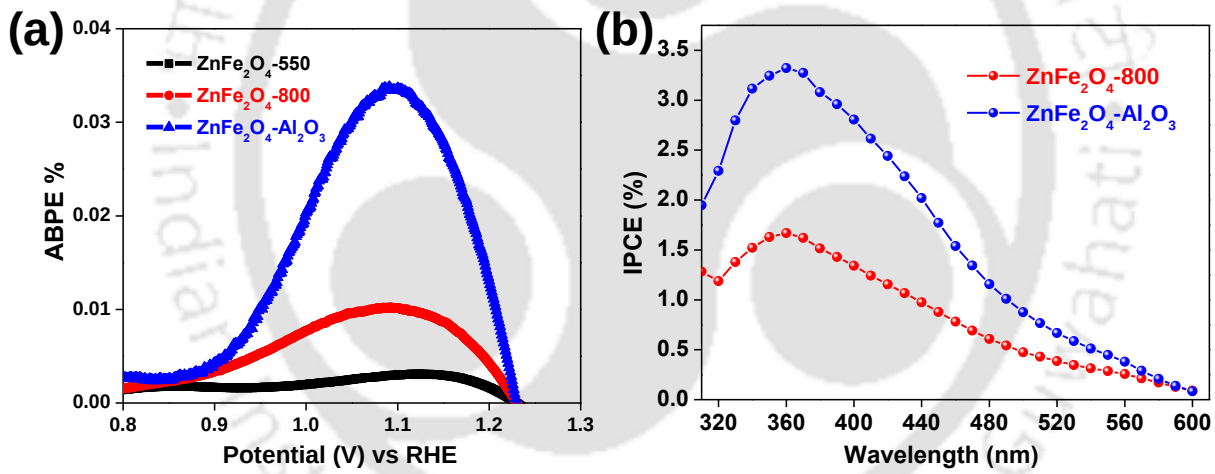

Figure 3.3.11 (a) ABPE of $ZnFe_2O_4$-550, $ZnFe_2O_4$-800 and $ZnFe_2O_4$-Al_2O_3 photoanodes to quantitatively evaluate the PEC water oxidation efficiency (b) the IPCE spectra of the as-prepared $ZnFe_2O_4$-800 and $ZnFe_2O_4$-Al_2O_3 photoanodes at 1.23 V vs. RHE.

The applied bias photon-to-current efficiencies (ABPE) of all the photoanodes were calculated to quantitatively evaluate the PEC water oxidation efficiency as shown in **Figure 3.3.11(a)**. Al_2O_3 modified $ZnFe_2O_4$ shows higher ABPE in the whole potential range. The incident photon-to-current efficiencies (IPCE) of the photoanodes were measured at 1.23 V *vs.* RHE as shown in **Figure 3.3.11(b)**, which were in agreement with the *J*–*V* curves as well as followed the trend of light absorption.

Part of this chapter has been published in **Chem. Commun., 2018, 54, 10483.**

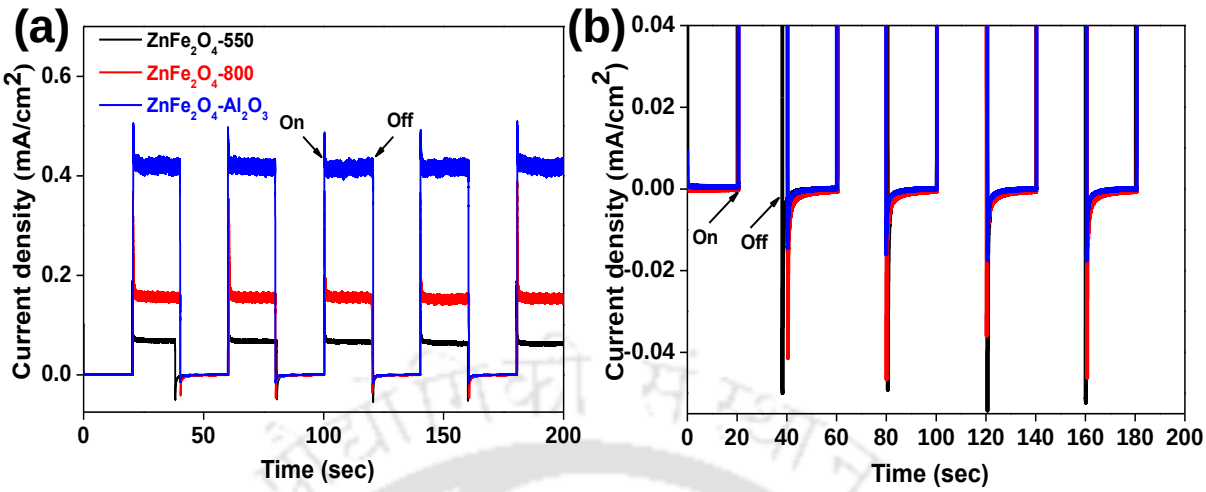

Figure 3.3.12 (a) Curves of current density *versus* time at 1.23 V *vs.* RHE for $ZnFe_2O_4$-550, $ZnFe_2O_4$-800 and $ZnFe_2O_4$-Al_2O_3 films. The light was turned on and off at an interval of 20 s. (b) Enlarged current–time curves of (a) to show the reverse transients when light is off.

Chronoamperometric measurements under repeated light-on and light-off conditions were conducted for all the $ZnFe_2O_4$ films with and without the Al_2O_3 overlayer. As shown in **Figure 3.3.12 (a)**, ON/OFF photocurrent measurements gave rise to smaller photocurrents for $ZnFe_2O_4$-550 and ZnF_2O_4-800 compared to $ZnFe_2O_4$-Al_2O_3, which was consistent with the *J–V* (current density *vs.* applied voltage) measurements. *J–t* (current density *vs.* time) curves recorded at a potential of 1.23 V *vs.* RHE under chopped illumination showed excellent stability and good optical response. For all the photoanodes, sharp anodic current spikes were observed at the moment when light was on. This type of behaviour was often observed in PEC studies with semiconductor photoanodes, wherein the charge recombination due to the accumulation of holes in the photoanode–liquid interface happens. Reversed transients were observed in all the curves at the moment when light was off, which could be attributed to the backflow of electrons. The reversed transients of all the curves are shown in an enlarged figure (**Figure 3.3.12(b)**). It was observed that after introducing the Al_2O_3 overlayer the reversed transient of $ZnFe_2O_4$–Al_2O_3 significantly reduced as compared to bare $ZnFe_2O_4$. This could be attributed to the reduced recombination of the majority of charge carriers in the case of $ZnFe_2O_4$–Al_2O_3.[29]

Part of this chapter has been published in **Chem. Commun., 2018, 54, 10483.**

3.3.5 Electrochemical impedance spectroscopy (EIS) analysis

In order to understand the enhanced PEC properties of $ZnFe_2O_4$–Al_2O_3, electrochemical impedance measurements under one-sun illumination were performed at 1.23 V *vs.* RHE. The Nyquist plots of all the photoanodes are shown in **Figure 3.3.13(a)**. The arch for the $ZnFe_2O_4$–Al_2O_3 photoanode was smaller than that of the bare $ZnFe_2O_4$ photoanodes, indicating that the Al_2O_3 coated on the surface of $ZnFe_2O_4$ nanorods enhanced the electron mobility by reducing the recombination of electrons and holes.

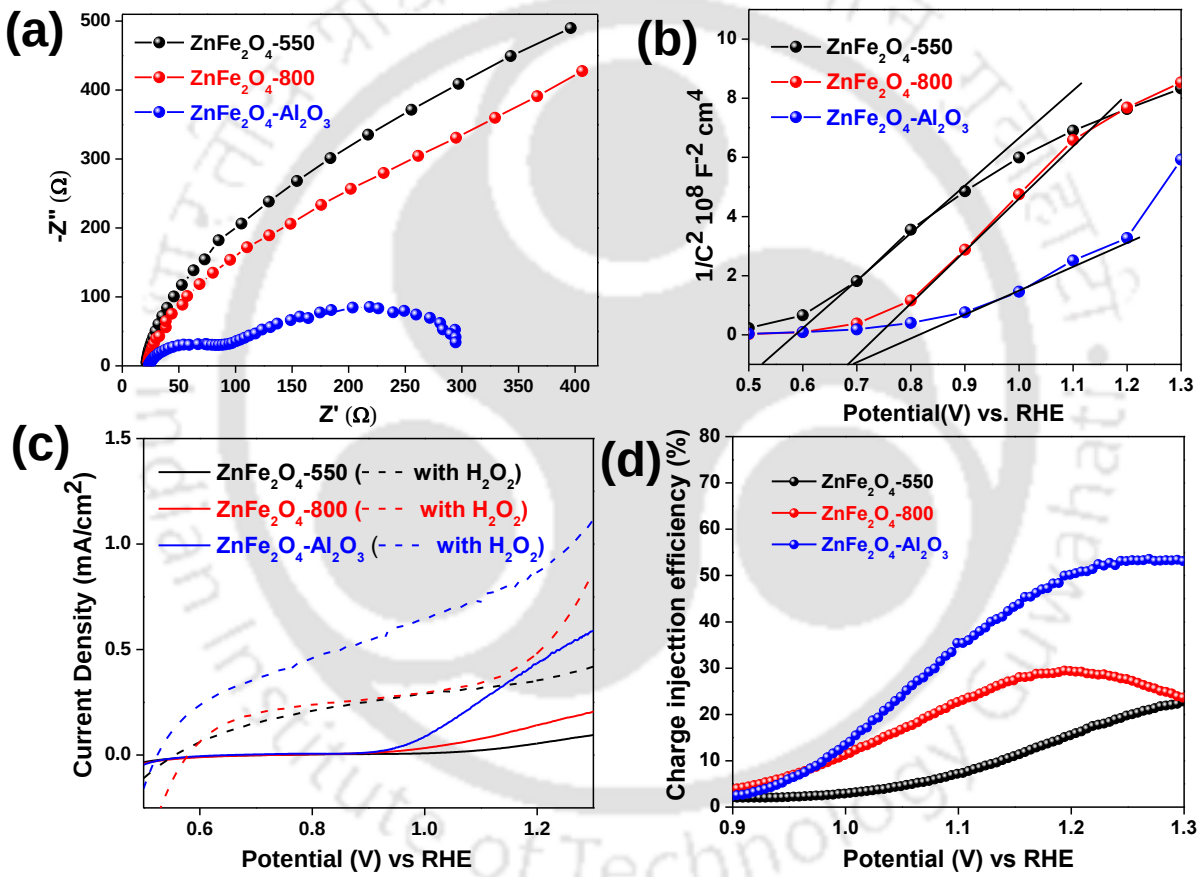

Figure 3.3.13 (a) The Nyquist plots of bare $ZnFe_2O_4$ treated at different temperatures and $ZnFe_2O_4$–Al_2O_3 under light illumination, (b) Mott–Schottky plots, (c) photocurrent density of photoanodes with and without hole scavenger and (d) charge injection efficiency.

Figure 3.3.13(b) shows the Mott–Schottky plots for the photoanodes. The positive slopes obtained from the linear portions of the curves in the Mott–Schottky plot demonstrated that all the samples

Part of this chapter has been published in **Chem. Commun., 2018, 54, 10483.**

were n-type semiconductors. The charge carrier density (N_D) was estimated from the slopes of the Mott–Schottky curve and the following **equation (3.1)**:

$$\frac{1}{C^2} = \frac{1}{A^2 N_D e\varepsilon\varepsilon_0}\left[E - E_{FB} - \frac{kT}{e}\right] \quad (3.1)$$

where C is the capacitance of the semiconductor, N_D is the electron carrier density of semiconductor, e is the fundamental charge constant, ε_0 is the permittivity of the vacuum, ε is the relative permittivity of the semiconductor, E is the applied potential, k is the Boltzmann constant, and T is the temperature. The charge carrier density (N_D) found to be 8.43×10^{20} cm^{-3} and 18.83×10^{20} cm^{-3} for $ZnFe_2O_4$-800 and $ZnFe_2O_4$–Al_2O_3, respectively. This increase in carrier density confirmed a lower density of surface states along with a reduced recombination due to the chemical passivation effect of the Al_2O_3 coating.[21] As there were no differences in the light absorption ability of the photoanodes measured from UV-visible absorption, in order to get more insights about the charge transfer at the surface of $ZnFe_2O_4$ photoanodes, the hole injection efficiency (η_{inj}) was calculated using **equation (3.2)** with H_2O_2 as a hole scavenger. The photocurrent density with and without hole scavenger is shown in **Figure 3.3.13(c)**. An increase of the photocurrent is observed in the whole potential range, indicating that the injection barrier for minority carriers has been removed. Slightly more cathodic onset of Al_2O_3 modified $ZnFe_2O_4$ as compared to pristine $ZnFe_2O_4$ suggest that surface defects has a significant contribution in decreasing the photocurrent. The water splitting photocurrent (J_{water}) is a product of the rate of photon absorption expressed as a current density (J_{abs}), the charge separation yield of the photogenerated carriers (η_{sep}), and charge injection yield to the electrolyte (η_{inj}): The water splitting photocurrent, (J_{water}), can be expressed as:

$$J_{water} = J_{abs} \times \eta_{sep} \times \eta_{inj} \quad (3.2)$$

η_{inj} is the yield of those holes that have reached the electrode/electrolyte interface and that are injected into the electrolyte to oxidize the water, or in other words, do not recombine with electrons at surface traps. It can be obtained from the following equation:

$$\eta_{inj} = \frac{J_{water}}{J_{H_2O_2}} \quad (3.3)$$

As shown in **Figure 3.3.13(d)**, the η_{inj} of $ZnFe_2O_4$-Al_2O_3 was much larger than $ZnFe_2O_4$-550 and $ZnFe_2O_4$-800 which indicates that the surface properties of $ZnFe_2O_4$ have been significantly improved by removal of surface trap sites and surface passivation by Al_2O_3.

Part of this chapter has been published in **Chem. Commun., 2018, 54, 10483.**

3.3.6 Probable mechanistic pathway and stability of the photoanode

The plausible mechanism for the improved photoelectrochemical activity is shown in **Figure 3.3.14(a)**. Pristine $ZnFe_2O_4$ formed surface states due to the requirement of high temperature for its formation. These surface states hindered its photoelectrochemical performance through rapid recombination of electron–hole pairs. With Al_2O_3 overlayer, the surface states at the surface of $ZnFe_2O_4$ can be effectively covered which results in less recombination of electron–hole pairs and effective charge separation and transfer at the surface for efficient photoelectrochemical water oxidation.

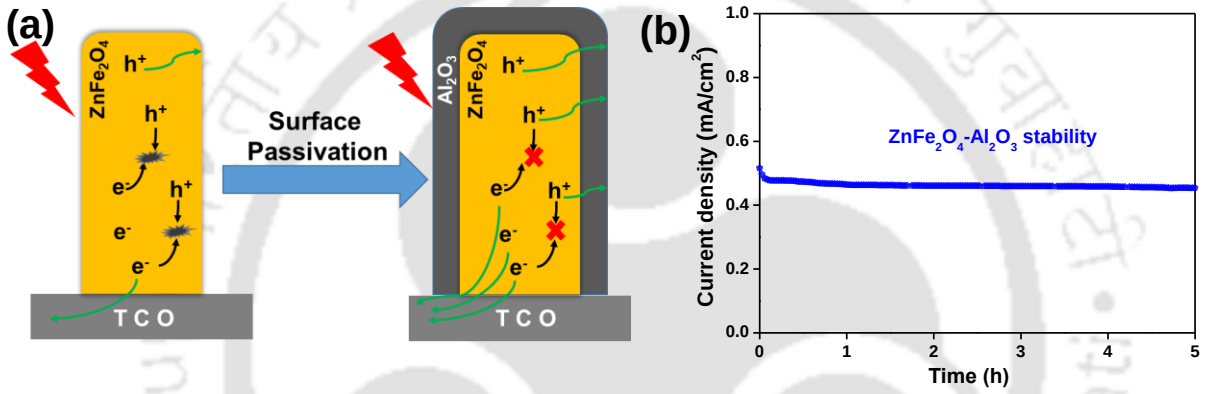

Figure 3.3.14 (a) Schematics of the charge transport in Al_2O_3 passivated $ZnFe_2O_4$ NRs photoanode under one sun illumination and (b) operational stability of $ZnFe_2O_4$-Al_2O_3 photoanode under constant light illumination at 1.23 V vs. RHE.

Additionally, the operational photo-stability of the Al_2O_3 coated photoanode was also tested under constant illumination for 5 h, as shown in **Figure 3.3.14(b)**. It can be seen that there was very negligible change in the photocurrent density even after the stability test, which shows the stability of as synthesized photoanode.

3.4 CONCLUSIONS

In summary, we have successfully fabricated 1-D zinc ferrite nanorods with different annealing temperatures as well as an Al_2O_3 overlayer. The PEC water oxidation performance of the 1-D zinc ferrite nanorods based photoanode was significantly improved by high-temperature annealing and coating of an Al_2O_3 overlayer. A photocurrent density of 0.48 mA cm^{-2} at 1.23 V *vs.* RHE was

Part of this chapter has been published in **Chem. Commun., 2018, 54, 10483.**

obtained for the Al_2O_3 coated zinc ferrite photoanode, which is 7-fold and 3-fold higher than those of bare zinc ferrite annealed at 550 °C and 800 °C, respectively. The Al_2O_3 coated photoanode exhibits excellent photostability under constant light illumination and retains almost 100% of its photocurrent after 5 h. Overall, the improvement in the PEC performance originated from surface passivation and suppression of charge recombination. The present method for the modification of a zinc ferrite photoanode with an Al_2O_3 overlayer is simple and effective, and might provide several ways of getting stable and high-performance photoelectrodes.

3.5 REFERENCES

(1) J. H. Kim, Y. J. Jang, J. H. Kim, J.-W. Jang, S. H. Choi and J. S. Lee, *Nanoscale*, 2015, **7**, 19144.

(2) S.Y. Cao, X. Q. Yan, Z. Kang, Q. J. Liang, X. Q. Liao and Y. Zhang, *Nano Energy*, 2016, **24**, 25-31.

(3) Z. Luo, C. Li, D. Zhang, T. Wang and J. Gong, *Chem. Commun.*, 2016, **52**, 9013.

(4) S. Hussain, S. Hussain, A. Waleed, M. M. Tavakoli, S. Yang, M. K. Rauf, Z. Fan and M. A. Nadeem, *J. Phys. Chem. C*, 2017, **121**, 18360.

(5) K. J. McDonald and K. S. Choi, *Chem. Mater.*, 2011, **23**, 4863.

(6) C. Miao, S. Ji, G. Xu, G. Liu, L. Zhang and C. Ye, *ACS Appl. Mater. Interfaces*, 2012, **4**, 4428.

(7) T. W. Kim and K.-S. Choi, *J. Phys. Chem. Lett.*, 2016, **7**, 447.

(8) A. A. Tahir and K. G. U. Wijayantha, *J. Photochem. Photobiol., A* 2010, **216**, 119.

(9) D. Peeters, D. H. Taffa, M. M. Kerrigan, A. Ney, N. Jöns, D. Rogalla, S.Cwik, H.-W. Becker, M. Grafen, A. Ostendorf, C. H. Winter, S. Chakraborty, M. Wark and A. Devi, *ACS Sustainable Chem. Eng.*, 2017, **5**, 2917.

(10) Y. Guo, N. Zhang, X. Wang, Q. Qian, S. Zhang, Z. Li and Z. Zou, *J. Mater. Chem. A*, 2017, **5**, 7571.

(11) M. Wang, Y. Sun, H. Chen, Y. Zhang, X. Wu, K. Huang and S. Feng, *CrystEngComm*, 2017, **19**, 772.

(12) J. H. Kim, Y. J. Jang, J. H. Kim, J.-W. Jang, S. H. Choi and J. S. Lee, *Nanoscale*, 2015, **7**, 19144.

(13) J. H. Kim, J. H. Kim, J.-W. Jang, J. Y. Kim, S. H. Choi, G. Magesh, J. Lee and J. S. Lee, *Adv. Energy Mater.*, 2015, **5**, 1401933.

(14) A. G. Hufnagel, K. Peters, A. Müller, C. Scheu, D. Fattakhova-Rohlfing and T. Bein, *Adv. Funct. Mater.*, 2016, **26**, 4435.

(15) T. Hisatomi, F. Le Formal, M. Cornuz, J. Brillet, N. Tétreault, K. Sivula and M. Grätzel, *Energy Environ. Sci.*, 2011, **4**, 2512.

(16) F. Le Formal, N. Tetreault, M. Cornuz, T. Moehl, M. Gratzel and K.Sivula, *Chem. Sci.*, 2011, **2**, 737.

(17) P. Zhang, T. Wang and J. Gong, *Chem. Commun.*, 2016, **52**, 8806.

(18) Z. Fan, Z. Xu, S. Yan and Z. Zou, *J. Mater. Chem. A*, 2017,**5**, 8402.

(19) C. Hu, K. Chu, Y. Zhao and W. Y. Teoh, *ACS Appl. Mater. Interfaces*, 2014, **6**, 18558.

(20) W. Kim, T. Tachikawa, D. Monllor-Satoca, H.-i. Kim, T. Majima and W. Choi, Energy Environ. Sci., 2013, **6**, 3732.

(21) M. Zeng, X. Peng, J. Liao, G. Wang, Y. Li, J. Li, Y. Qin, J. Wilson, A. Song and S. Lin, *Phys. Chem. Chem. Phys.*, 2016, **18**, 17404.

(22) J. Wang, L. Ge, Z. Li, L. Li, Q. Guo and J. Li, *Ceram. Int.*, 2016, **42**, 8545.

(23) N. Guijarro, P. Bornoz, M. Pr´evot, X. Yu, X. Zhu, M. Johnson, X. Jeanbourquin, F. Le Formal and K. Sivula, *Sustain. Energy Fuels*, 2018, **2**, 103.

(24) L. Zhang, T. Wei, J. Yue, L. Sheng, Z. Jiang, D. Yang, L. Yuan and Z. Fan, *J. Mater. Chem. A*, 2017, **5**, 11188.

(25) H. Song, L. P. Zhu, Y. G. Li, Z. R. Lou, M. Xiao and Z. Z. Ye, *J. Mater. Chem. A*, 2015, **3**, 8353.

(26) A. Annamalai, A. G. Kannan, S. Y. Lee, D.-W. Kim, S. H. Choi and J. S. Jang, *J. Phys. Chem. C*, 2015, **119**, 19996.

(27) D. Monllor-Satoca, T. Lana-Villarreal and R. Gómez, *Langmuir*, 2011, **27**, 15312.

(28) J. Li, X. Xiao, Y.-T. Cheng and M. W. Verbrugge, *J. Phys. Chem. Lett.*, 2013, **4**, 3387.

(29) D. Wang, X.-T. Zhang, P.-P. Sun, S. Lu, L.-L. Wang, Y.-A. Wei and Y.-C. Liu, *Int. J. Hydrogen Energy*, 2014, **39**, 16212.

(30) H. Dotan, K. Sivula, M. Grätzel, A. Rothschild and S. C. Warren, *Energy Environ. Sci.*, 2011, **4**, 958.

CHAPTER 4

Sequential Metal and Non-metal Incorporation in Hematite Photoanode: Fabrication, Bulk and Interfacial Charge Transfer Dynamics and Photoelectrochemical Water Oxidation Performance

In this chapter, we reported the design and synthesis of stable hematite photoanode with sequential metal and non-metal incorporation to resolve the limiting factors such as low carrier density and high charge recombination. A comprehensive morphological, optical and photoelectrochemical properties of the doped hematite photoanodes are presented to understand the mechanisms by which the dopant incorporation impacts the photoanode performance.

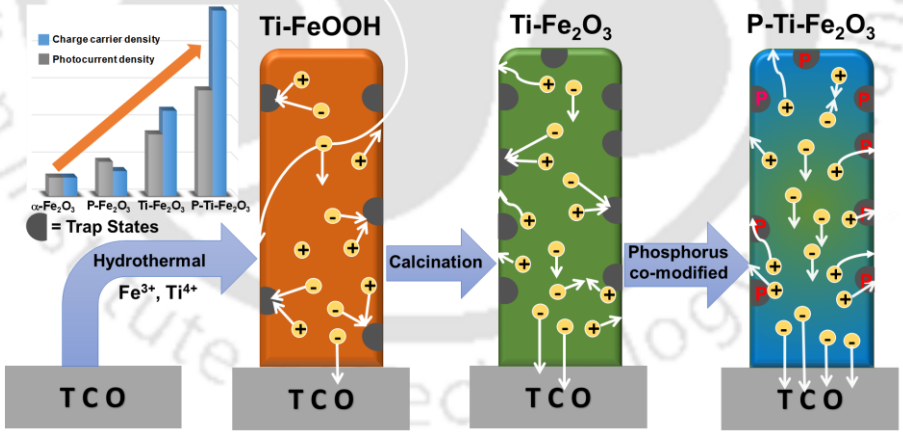

ACS APPLIED ENERGY MATERIALS

T. K. Sahu *et al.,* 2019, **2**, 4325

4.1 INTRODUCTION

Hematite (α-Fe_2O_3) is a most promising material as a photoanode due to its suitable band gap (1.9-2.2 eV), non-toxicity, low cost and high photochemical stability.[1] α-Fe_2O_3 have a theoretical maximum Solar-to-Hydrogen (STH) photo conversion efficiency of 16% due to its suitable band gap.[2] Despite having these properties, practical applications are limited due to its poor conductivity,[3] short hole diffusion length (L_h = 2-4 nm),[4-5] poor oxygen evolution reaction kinetics[6] and very short minority carrier lifetime (10^{-12} s).[7] Enormous effects have been made to overcome the above-mentioned limitations and improve solar conversion efficiency by tuning different nanostructures morphology,[8-9] coupling with suitable photoanode and photocathode materials forming heterojunctions,[10-12] by incorporation of impurities[13-17] and surface modifications.[18-20] Among different morphological growth, well aligned one-dimensional (1-D) nanorod or nanowire arrays are favourable for attaining higher photocurrent densities by virtue of its diameter control, in the range of its carrier (hole) diffusion length. Beside these morphological tuning, doping in hematite photoanode is also an effective strategy for enhanced performance in water oxidation.[21,22] Introduction of metal dopants into the hematite lattice has proven to be a successful approach as it increases the electrical conductivity as well as carrier density of hematite photoanode. Among various metal dopants Sn[9, 13], Ti[14, 15] and Si[16, 17] are widely studied due to their performance in enhancing the charge carrier density of hematite photoanode. Generally, in-situ doping procedures alter the crystallinity and morphology of hematite, which may affect the performance of the PEC device.[23] Among various metal dopants, Ti has been proved to be a suitable candidate as it retains the one-dimensional nanostructures of hematite with in-situ doping, improves carrier density and reduce charge recombination. For Ti doping in hematite, optimal doping content is found to be less than 1 % .[15] The advantage of low dopant concentration is that it enhances the performance without altering the morphology of hematite. In the recent past, besides metal doping in hematite, non-metal doping such as P,[24,25] F[26] and S[27] has been studied. Among these non-metallic dopants, phosphorus as an n-type dopant has more valence electrons than many metallic dopants and suitable for evading the surface electron trapping sites in hematite, thus, competently facilitate charge separation. Additionally, the covalent nature of P–O bonds in

Part of this chapter has been published in **ACS Appl. Energy Mater. 2019, 26, 4325**

hematite was comparatively higher than other Dopant-O bonds, which is suitable in evading the electron trapping sites in hematite.[24] However, studies involving dual doping/incorporation to improve the photocurrent density of hematite photoanode is limited to metal-metal co-modification.[23,28,29] A theoretical study suggests that (Ti/Zr, N) co-modified hematite is expected to improve PEC performance.[30] Although, the effect of various metal and non-metal dopants have been studied separately, the effect of co-modification with both metal and non-metal on hematite is not well studied. In this work, we have studied the effect of metal and non-metal incorporation on hematite photoanode. The metal dopant, Ti has been incorporated by an *in-situ* and non-metal dopant, phosphorus has been incorporated by *ex-situ* methods.

4.2 EXPERIMENTAL

4.2.1 Fabrication of Fe_2O_3 and Ti-Fe_2O_3

The α-Fe_2O_3 nanorods arrays were prepared by modification of earlier reports, with improved reaction times from 24 h to 6 h.[31] In a typical synthesis, 0.15M $FeCl_3$ was dissolved in 60 mL distilled water taken in a 100 mL Teflon lined stainless steel vessel and to this solution 1M $NaNO_3$ was added with stirring. Further, 15 μL concentrated HCl was added to maintain the pH at 1.5. The FTOs were masked with a polyimide tape before putting into the solution. Four cleaned FTOs (2.5 cm x 1.00 cm) were put in to the above solution with the conductive side facing up and heated in a hot-air oven for 6 h at 100^{o}C. After naturally cooling to room temperature the thin films were cleaned with distilled water and dried in hot-air oven at 100^{o}C overnight. As prepared β-FeOOH films were calcined at 800^{o}C for 15 min to obtained α-Fe_2O_3. Ti-doped films were fabricated by taking different atomic weight percentage of Ti precursor (Fe:Ti=0.05-0.15 at%) following the similar procedure.

4.2.2 Fabrication of P-Fe_2O_3 and P-Ti-Fe_2O_3

To fabricate P-Fe_2O_3 and P-Ti-Fe_2O_3; as-prepared Fe_2O_3 and Ti-Fe_2O_3 films were dipped in 0.5M Na_2HPO_4 solution for 10 min and then annealed at different temperature for 30 min to 1 h (350 °C- 1 h, 550 °C- 1 h and 750 °C- 30 min).[34] After naturally cooling it to room temperature,

Part of this chapter has been published in **ACS Appl. Energy Mater. 2019, 26, 4325**

the films were washed with distilled water to remove the residues present on the surface (**Scheme 4.2.1**).

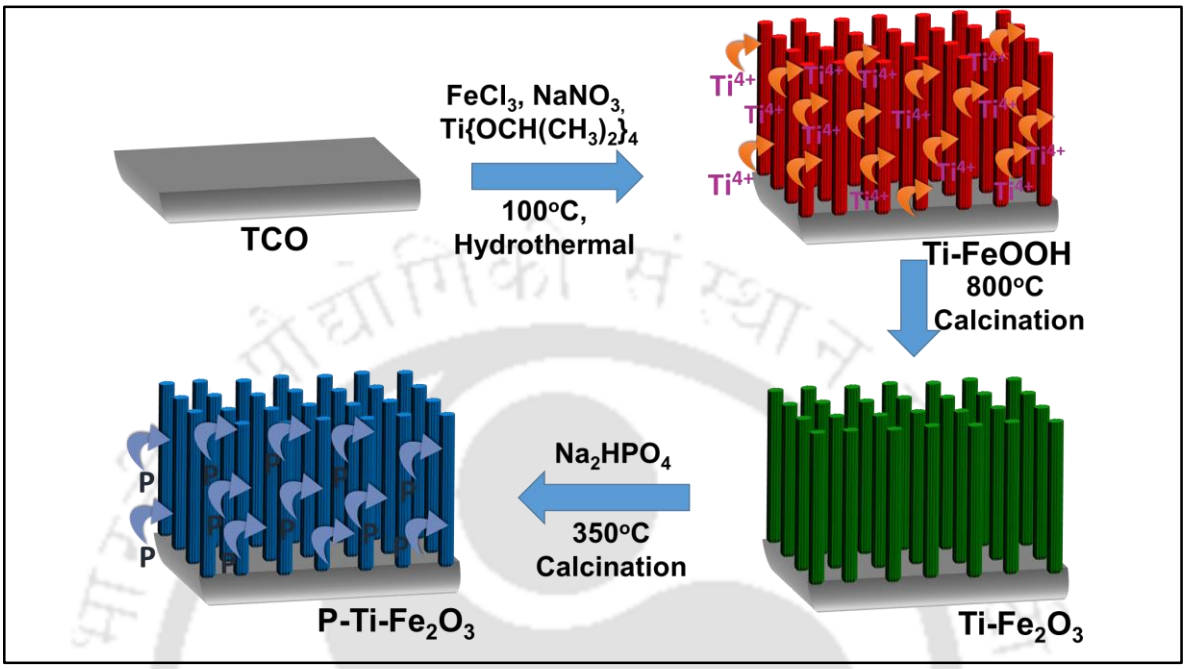

Scheme 4.2.1 Schematic illustration of the fabrication process of P-Ti-Fe_2O_3 photoanode with *in-situ* doping of Ti and *ex-situ* doping of P.

4.3 RESULTS AND DISCUSSION

4.3.1 Powder x-ray diffraction and Raman analysis

The powder XRD measurements of α-Fe_2O_3, P-Fe_2O_3, Ti-Fe_2O_3 and P-Ti-Fe_2O_3 samples were carried out to examine the crystallinity and phase purity (**Figure 4.3.1**). The peaks at 2θ values 35.6° and 64° correspond to (110) and (300) planes of α-Fe_2O_3 which can be indexed to JCPDS card number 33-0664, indicating that the crystalline structure is retained even after doping. The strong diffraction peak of (110) plane implies that the α-Fe_2O_3 nanorods are extremely oriented in the [110] direction on the FTO substrate as well highly crystalline.[1,13] There is no peak shift, as well as additional peaks, appeared in the XRD patterns of both doped and co-modified α-Fe_2O_3. The peaks for FTO substrate is clearly visible as all the photoanodes were directly fabricated over it.

Part of this chapter has been published in **ACS Appl. Energy Mater. 2019, 26, 4325**

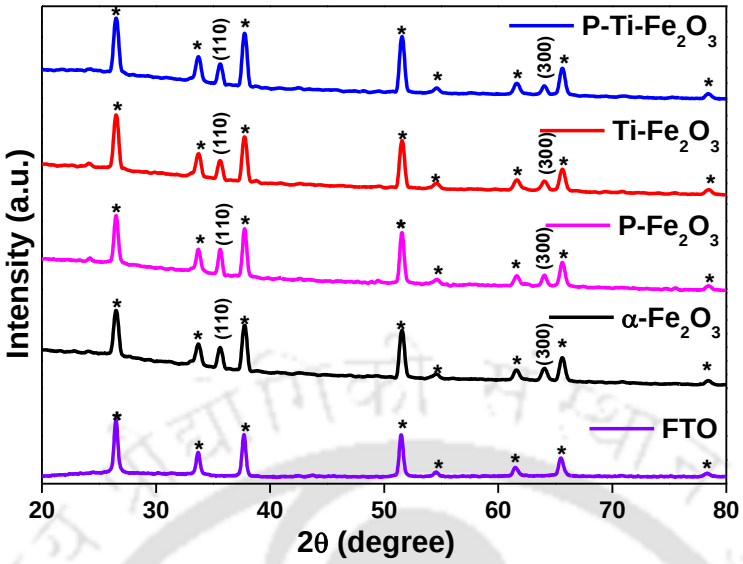

Figure 4.3.1 Powder XRD of FTO, α-Fe_2O_3, P-Fe_2O_3, Ti-Fe_2O_3 and P-Ti-Fe_2O_3 thin films.

In order to confirm the incorporation of dopants in α-Fe_2O_3, Raman analysis was performed for all the samples as shown in **Figure 4.3.2(a)**. A weak peak around 660 cm^{-1} for Ti-doped and co-modified hematite could be ascribed to the disorder induced by Ti-doping, which is absent in bare and P-incorporated Fe_2O_3.[25] The absence of this peak for P-incorporated Fe_2O_3 indicate that phosphorus is mostly present at the surface of Fe_2O_3 due to low-temperature calcination.

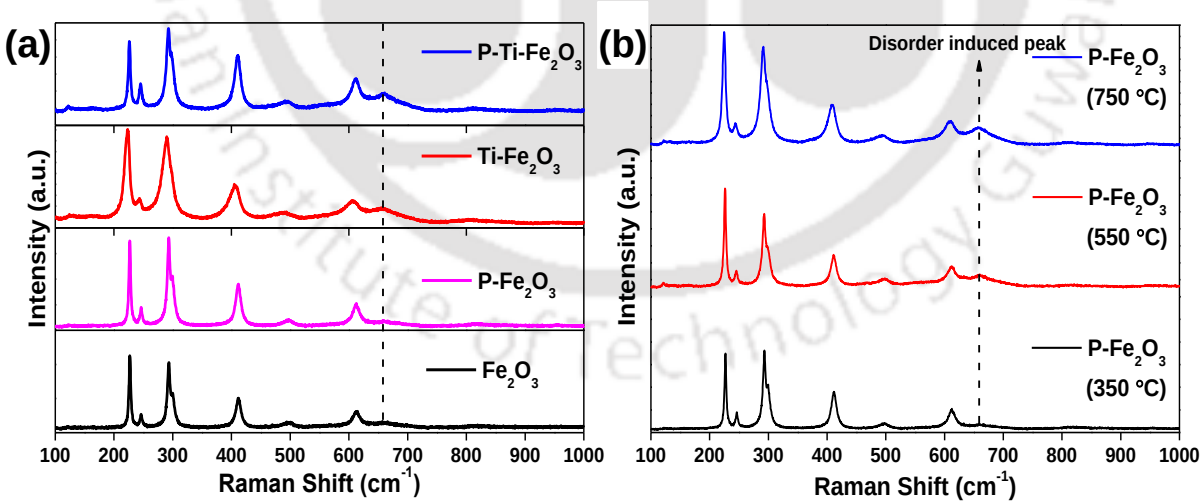

Figure 4.3.2 Raman spectra of (a) α-Fe_2O_3, P-Fe_2O_3, Ti-Fe_2O_3 and P-Ti-Fe_2O_3 thin films and (b) P-incorporated over α-Fe_2O_3 calcined at different temperatures. A weak peak around 660 cm^{-1} could be ascribed to the disorder induced by dopants.

Part of this chapter has been published in **ACS Appl. Energy Mater. 2019, 26, 4325**

When P-incorporated Fe_2O_3 was calcined at high temperature (550 °C and 750 °C), a weak peak around 660 cm^{-1} arises due to disorder induced by P-doping into the lattice as shown in **Figure 4.3.2(b)**. Similar Raman spectra of bare and doped Fe_2O_3 indicates that the crystal phase has not been changed with doping of titanium and phosphorus.[32]

4.3.2 UV-visible absorption spectra analysis

UV−visible spectra of bare hematite, doped hematite, and co-modified hematite photoanodes are shown in **Figure 4.3.3(a)**. The profile of the absorption curves and the band gaps calculated from the corresponding Tauc analysis are almost the same as shown in **Figure 4.3.3(b)**. All the modified photoanodes show similar optical band gap (~2.15 eV) values of α-Fe_2O_3. It is indicated that the Ti and P incorporation into the lattice of α-Fe_2O_3 are quite low and a slight change in the band gap energy after dopant incorporation is not a foremost reason for the shift in onset potential and increased photocurrent density.[28]

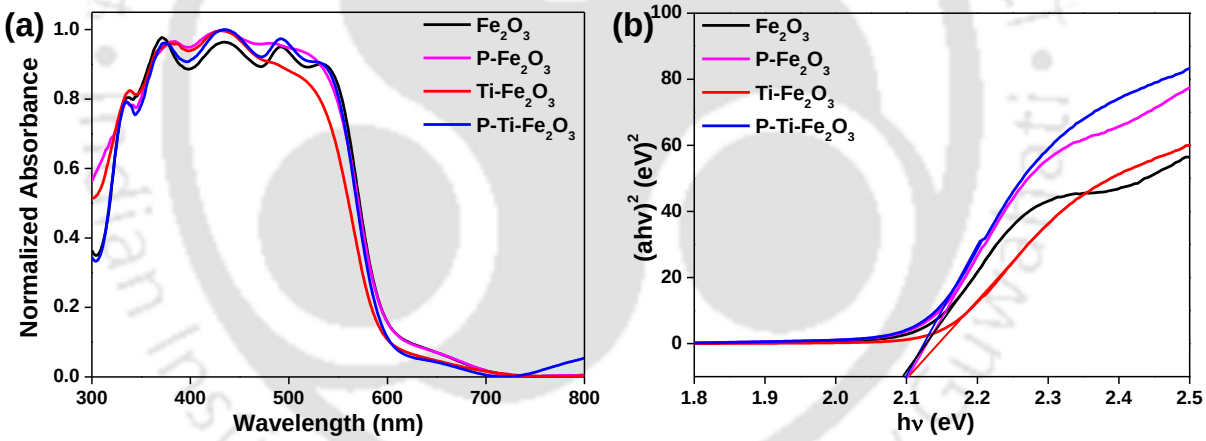

Figure 4.3.3 (a) UV-Visible diffuse reflection spectra and (b) Tauc's plots of α-Fe_2O_3, P-Fe_2O_3, Ti-Fe_2O_3 and P-Ti-Fe_2O_3.

4.3.3 Materials morphology

Figure 4.3.4 shows the FESEM images of bare, Ti-doped, P-incorporated and co-modified hematite photoanodes. It was found that modification with Ti and P dopants did not change the morphology of hematite. As shown in inset to **Figure 4.3.4(d)**, the cross-sectional FESEM image of co-modified hematite confirmed uniform growth of hematite nanorods over the FTO substrate.

Part of this chapter has been published in **ACS Appl. Energy Mater. 2019, 26, 4325**

The average length of the nanorods is found to be around 450 nm from the cross-sectional image of co-modified hematite. All the nanorod structures are vertically aligned to the FTO substrate. This 1-D structure results in an efficient separation of electron-hole pairs and provides shorter diffusion path for holes to reach the interface of electrode/electrolyte.[9]

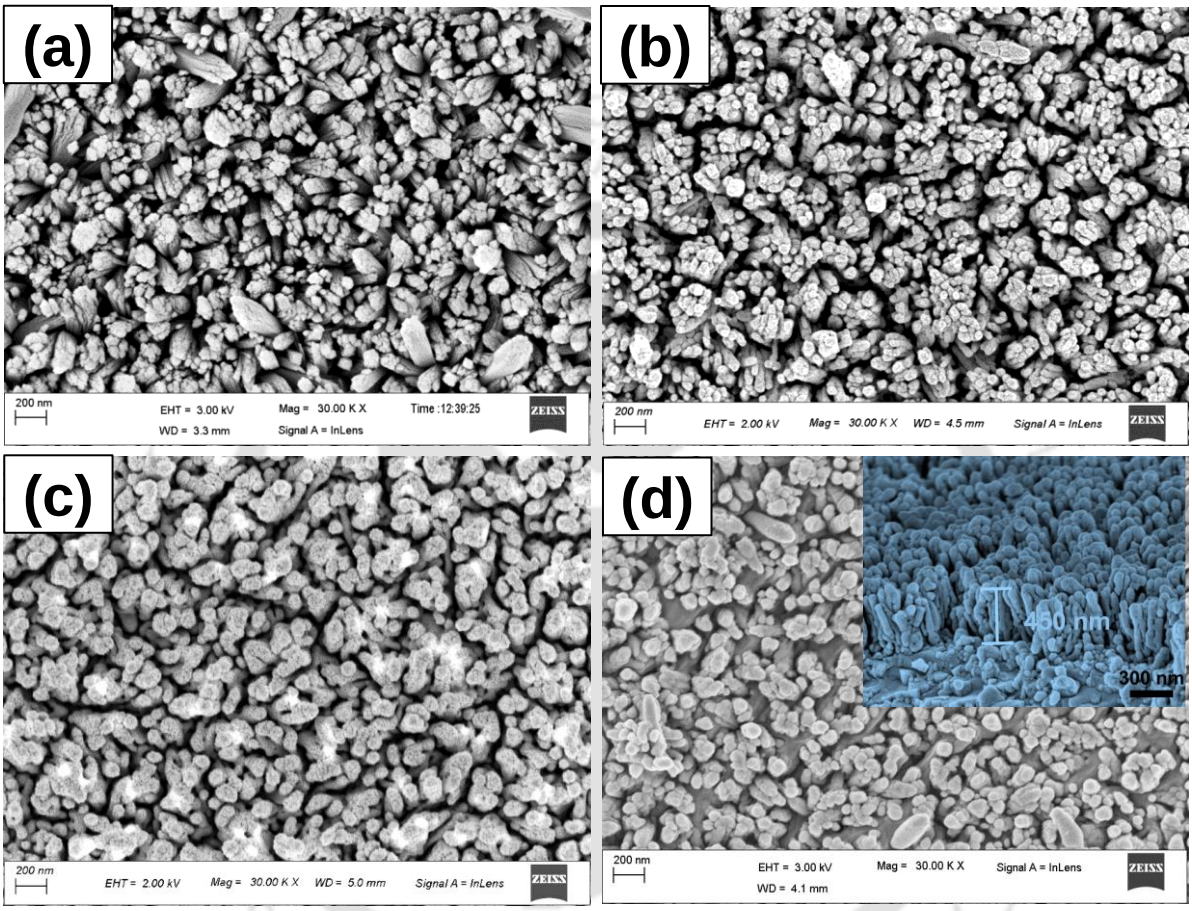

Figure 4.3.4 FESEM images of (a) α-Fe_2O_3, (b) P-Fe_2O_3, (c) Ti-Fe_2O_3 and (d) P-Ti-Fe_2O_3.

It is observed from the FETEM image in **Figure 4.3.5(a)** that the diameter of the nanorods are below 100 nm. The d-spacing of ~0.25 nm, corresponding to the (110) crystal plane of α-Fe_2O_3, confirmed that doping does not change the crystallinity of the hematite photoanode (**Figure 4.3.5(b)**).[15] The SAED pattern of Fe_2O_3 is shown in the inset of **Figure 4.3.5(b)** matched with the powder XRD pattern of hematite. The FETEM-EDX analysis of P-Ti-Fe_2O_3 was carried out in a series of spots across the nanorod as shown in **Figure 4.3.5(c)**. The concentration of P in different

spots are summarized in **Figure 4.3.5(d)** confirms that the P concentration from the surface to the core decreases along the radial direction.

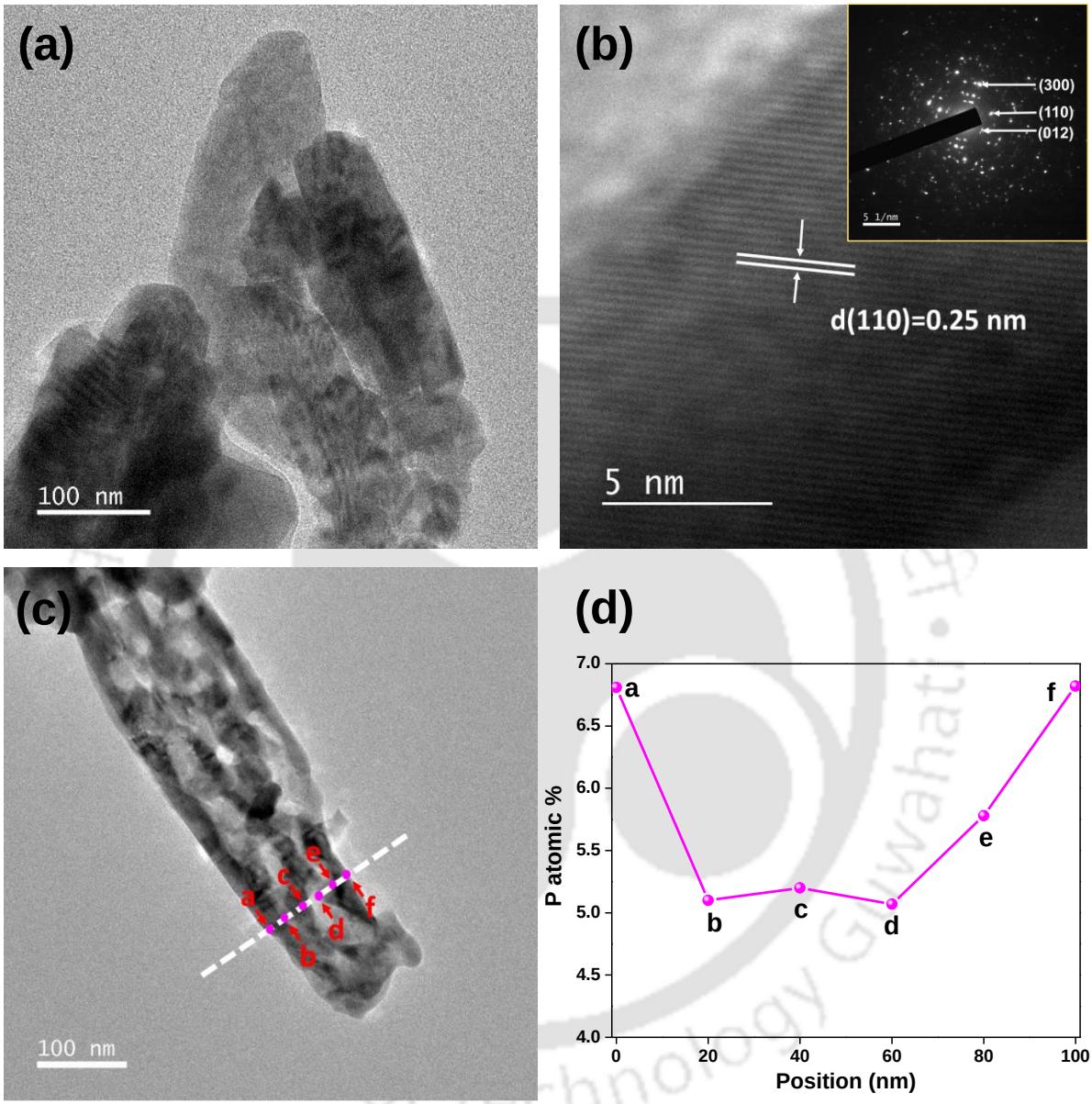

Figure 4.3.5 (a) FETEM image of P-Ti-Fe_2O_3, (b) HRTEM of P-Ti-Fe_2O_3 (inset showing the SAED pattern of P-Ti-Fe_2O_3), (c) FETEM-EDX analysis of P-Ti-Fe_2O_3 at different spots and (d) the corresponding P concentration data.

The STEM-EDX elemental mapping of P-Ti-Fe_2O_3 photoanode is shown in **Figure 4.3.6(a) to (e)** which confirms the presence of Fe, Ti, O and P elements. The low Ti doping content in the sample is evidenced by the weak Ti signals.

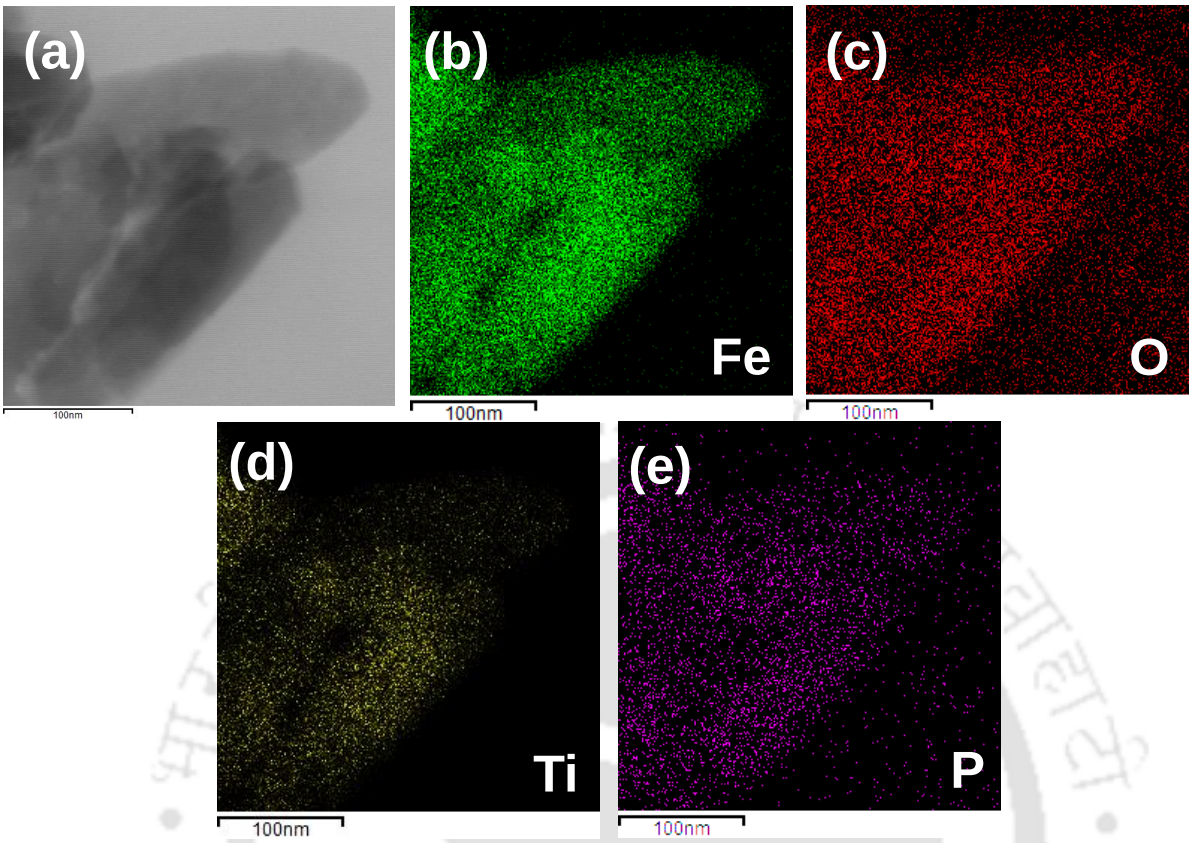

Figure 4.3.6 (a) STEM-EDX elemental mapping of P-Ti-Fe_2O_3 viewing the uniform distribution of (b) Fe, (c) O, (d) Ti and (e) P.

4.3.4 X-ray photoelectron spectroscopy (XPS) analysis

To further confirm the composition and surface bond states of the α-Fe_2O_3, Ti-Fe_2O_3 and P-Ti-Fe_2O_3 photoanodic films, X-ray photoelectron spectroscopy (XPS) measurement was conducted as shown in **Figure 4.3.7**. The existence of Fe, O, Ti and P elements in P-Ti-Fe_2O_3 thin film was confirmed through XPS and the corresponding survey scan spectrum is shown in **Figure 4.3.7(a)**. In **Figure 4.3.7(b)**, for P-Ti-Fe_2O_3 the two peaks centered at 710.0 eV and 723.27 eV have appeared upon de-convolution, which can be allotted to Fe $2p_{3/2}$ and Fe $2p_{1/2}$, respectively. This result, as well as two shake-up satellite peaks at 718.3 eV and 732 eV, ascertains the presence of Fe in +3 oxidation state.[33] For the Ti 2p spectrum shown in **Figure 4.3.7(c)**, existence of a normal state of Ti^{4+} in the P-Ti-Fe_2O_3 photoanode was confirmed from the two peaks with binding energies of around 458.2 eV and 463.8 eV , which were assigned to Ti $2p_{3/2}$ and Ti $2p_{1/2}$, respectively.[33] As

shown in **Figure 4.3.7(d)**, P 2p exhibits a binding energy of 132.75 eV in P-Ti-Fe_2O_3, while Fe 2p and P 2p signals of P-Ti-Fe_2O_3 are close to that of $FePO_4$, which point to a strong interaction between the P and Fe in P-Ti-Fe_2O_3 with an oxidation state of P as +5.[25]

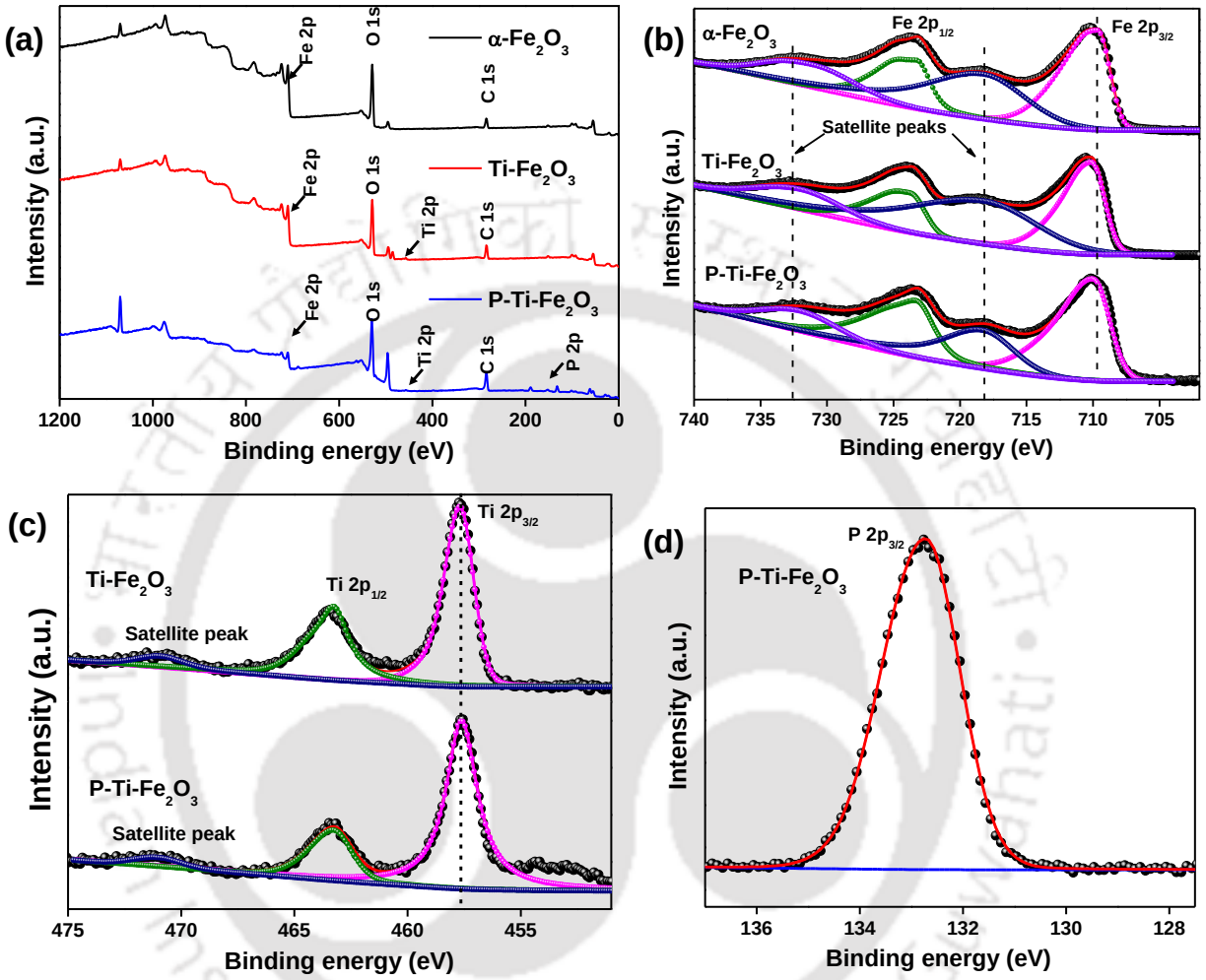

Figure 4.3.7 (a) XPS survey spectra, (b) Fe 2p, (c) Ti 2p and (d) P 2p core-level spectra of a-Fe_2O_3, Ti-Fe_2O_3 and P-Ti-Fe_2O_3 photoanodes.

O1s core level spectrum is shown in **Figure 4.3.8**, where the broad peak centered at 529.95 eV was attributed to lattice Metal-Oxygen (M-O) bonds for P-Ti-Fe_2O_3. Additionally, peak at the binding energy of 531.5 eV corresponds to surface absorbed oxygen species and PO_4^{3-} and peak at 534.5 eV was ascribed to adsorbed H_2O for P-Ti-Fe_2O_3. There was a shift in the peaks of Fe 2p and O 1s for both Ti-Fe_2O_3 and P-Ti-Fe_2O_3 towards higher binding energy due to introduction of

Part of this chapter has been published in **ACS Appl. Energy Mater. 2019, 26, 4325**

Ti in to Fe lattice. The concentration of Ti and P were found to be 0.1 atomic% and 7 atomic% from XPS analysis of P-Ti-Fe_2O_3, respectively.

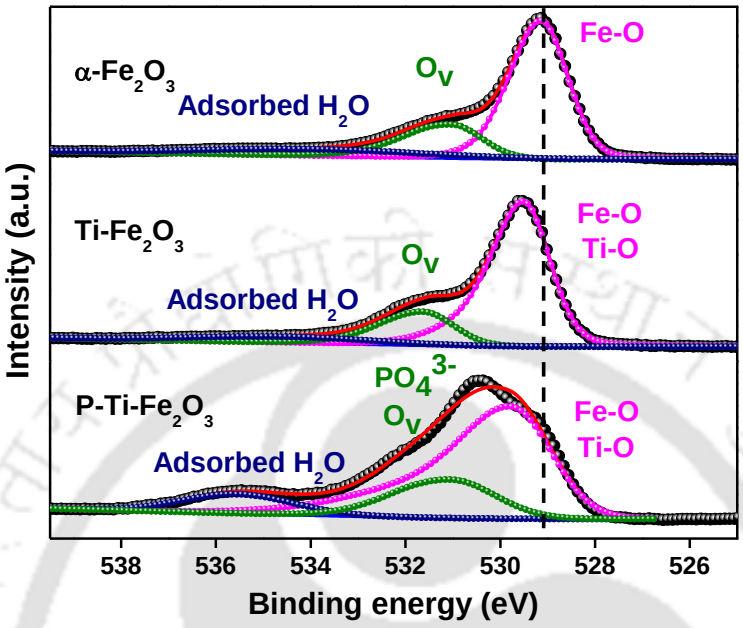

Figure 4.3.8 O 1s core-level XPS spectra of α-Fe_2O_3, Ti-Fe_2O_3 and P-Ti-Fe_2O_3.

4.3.5 Photoelectrochemical characterizations

The PEC performance of pristine, Ti-doped, P-incorporated and Ti/P co-modified hematite photoanodes are shown in **Figure 4.3.9(a)**. The photocurrent density of α-Fe_2O_3 was found to be 0.45 mA/cm^2 at 1.23V vs RHE. To further increase the photocurrent density, Ti was used as a metal dopant in hematite. Ti-doping in hematite was first optimized by varying the concentration of Ti in the precursor solution. The photocurrent densities of hematite photoanodes with different doping percentage of Ti are shown in **Figure 4.3.9(b)**. It was found that 0.1 atomic % of Ti in the hematite photoanode is the optimized doping level for higher photocurrent density. Doping concentration of Ti was found to be less than 1 atomic %, which is in a good agreement with previous report on Ti-doped hematite.[23] The photocurrent density of optimized Ti-doped hematite was found to be 1.50 mA/cm^2. To know the effect of one-time annealing on co-modification, as prepared optimized Ti-FeOOH (before calcination) was treated with phosphorus and calcined at higher temperature same as bare hematite. Although, the current density was found to be more as compared to bare hematite photoanode, but it was less as compared to Ti-doped hematite.

Part of this chapter has been published in **ACS Appl. Energy Mater. 2019, 26, 4325**

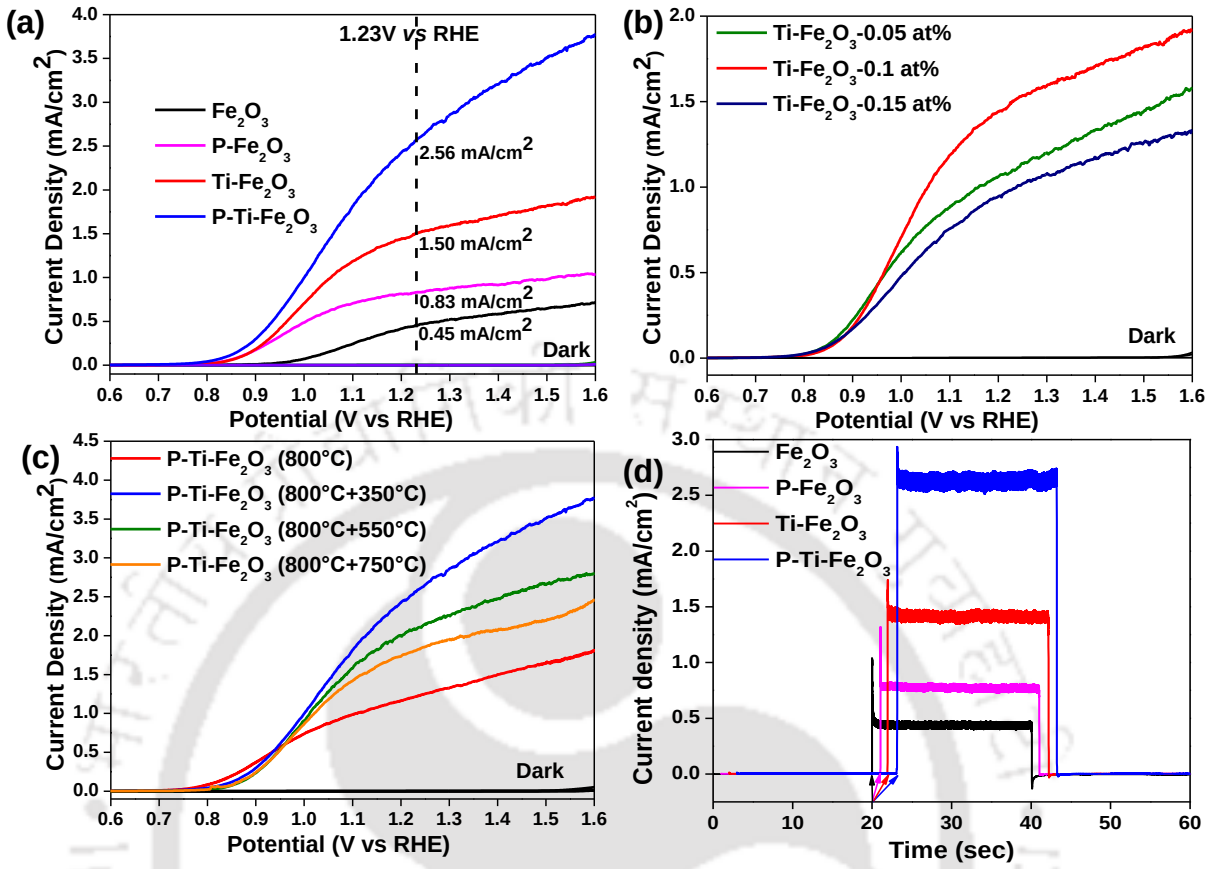

Figure 4.3.9 (a) Current density (J) vs. applied voltage (V) curves of bare as well as modified hematite photoanodes under light illumination at a scan rate of 10 mV/s in 1 M NaOH, (b) J-V characteristics of Ti-doped Fe_2O_3 photoanodes with different Ti contents. (Fe:Ti =0.05 to 0.15 at %) and (c) J-V characteristics of P-incorporation with Ti-doped Fe_2O_3 with different annealing temperatures (d) current density (J) vs. time (t) curves of all the photoanodes at 1.23 V vs. RHE.

To further know the effect of phosphorus incorporation, Ti-doped hematite (after calcination) was treated with phosphorus and calcined at different temperature to induce gradient phosphorus doping (**Figure 4.3.9(c)**). In this case, the concentrations of phosphorus from the surface to the core of hematite will gradually decrease.[23] With both Ti and phosphorus, the lower calcination temperature (350 °C) was found to be more suitable for achieving higher photocurrent density. A photocurrent density of 2.56 mA/cm^2 at 1.23V vs RHE was observed for Ti and P co-modified hematite. Moreover, an unprecedented cathodic shift of the onset potential with a large value of around 90 mV was observed in case of both Ti and P co-modification. The cathodic shift obtained using co-modification is comparable with results seen in the case of surface passivation and co-

Part of this chapter has been published in **ACS Appl. Energy Mater. 2019, 26, 4325**

catalyst loading.[18-20] With further increase in temperature (550 °C and 750 °C), the photocurrent densities of co-modified hematite photoanodes decrease as compared to lower temperature treatment (350 °C). The decrease in photocurrent density with higher temperature may be due to the creation of more trap sites on the surface as well as deformation of FTO due to repeated calcination at temperature above 550ºC. Although, incorporation of only phosphorous onto the hematite with lower temperature calcination (350 °C) does not enhance the current so efficiently, but with the incorporation of both Ti and P with lower temperature there is a synergistic enhancement of photocurrent density was observed. While *in-situ* Ti-doping increases the conductivity and carrier concentration of hematite, the presence of surface trap states cannot be suppressed due to high-temperature calcination.[13] Wherein, the combined effect of faster carrier mobility due to Ti-doping and reduced surface trap states due to P-modification results in better current density in case of co-modified hematite. So, the P-modification on Ti-doped hematite may reduce the surface electron–hole recombination and decreases the surface hole accumulation on hematite surface.[2,34,35] The chronoamperometric or transient photocurrent measurements were done with chopping light in a regular interval with a biased potential of 1.23V vs RHE as shown in **Figure 4.3.9(d)**. The photocurrent densities were found to be consistent with the photocurrent densities of the J-V (current density vs. applied voltage) at 1.23V vs RHE. The anodic and cathodic current spikes were diminished with both Ti and P incorporations, indicates that charge recombination is suppressed with dual modifications.[36]

The FT-IR analysis of co-modified photoanodes calcined at different temperatures are shown in **Figure 4.3.10**. When the phosphorus treated sample was calcined at 350°C, peaks arises due to phosphate group was negligible. However, after calcined at 550°C and 750°C the phosphate peaks became sharp due to oxidation of phosphorus. It shows that, besides FTO deformation, partial oxidation of P may affect the photocurrent density of co-modified photoanodes.

Part of this chapter has been published in **ACS Appl. Energy Mater. 2019, 26, 4325**

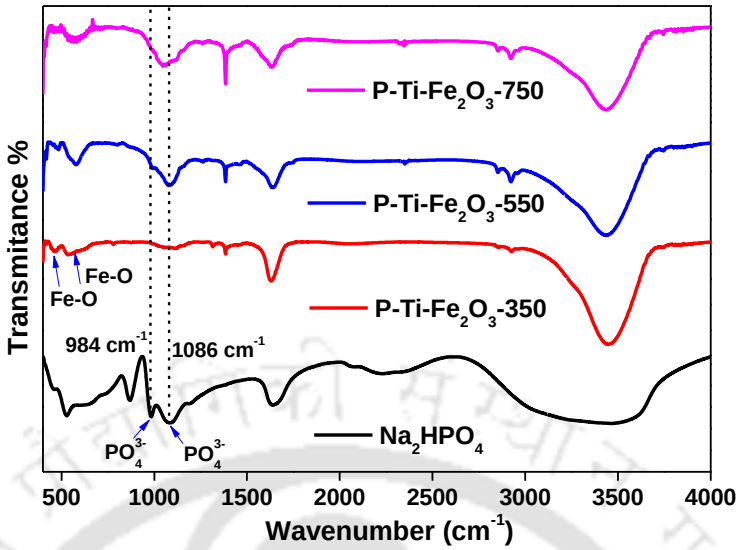

Figure 4.3.10 FTIR spectra of Na_2HPO_4 and P-Ti-Fe_2O_3 photoanodes calcined at different temperatures.

4.3.6 Electrochemical impedance spectroscopy (EIS) analysis

To understand the influence of doping on internal resistance and charge transport kinetics of hematite photoanodes, electrochemical impedance measurements were performed under illumination at 1.23V vs. RHE. **Figure 4.3.11(a)** shows the Nyquist plots for all the photoanodes with fittings. The Nyquist plots of all photoanodes are composed of two semicircles, where the semicircle at high-frequency region is correlated to charge transfer resistance at bulk and low-frequency region is associated to the charge transfer resistance at photoanode/electrolyte interface.[37] An equivalent circuit model was used to fit all the impedance data (**Figure 4.3.11(b)**), where R_s denotes the series resistance, R_{ct} denotes the charge transfer resistance across photoanode/electrolyte interface, C_{bulk} represent space charge depletion region capacitance, R_{trap} denotes the resistance accounting for surface-state trapping and C_{trap} represents the trap-state capacitance.[38] Herein, a smaller R_{ct} specifies a lower charge-transfer resistance in the hematite. The values obtained from the fittings of all the photoanodes are shown in **Table 4.3.1**. The values of R_{ct} were found to be 1104 Ω, 890.5 Ω, 341.2 Ω and 146.7 Ω for bare, P-incorporated, Ti-doped and co-modified hematite photoanodes, respectively. A lower R_s value for co-modified hematite photoanode signified that electrical conductivity was improved and a lower R_{ct} value indicates that interfacial charge transfer was more favorable in case of co-modified hematite as compared to bare, Ti-doped and P-incorporated hematite.[23,27] Also, a significant decrease in R_{trap} values for co-

Part of this chapter has been published in **ACS Appl. Energy Mater. 2019, 26, 4325**

modified hematite revealed improved hole transfer property with co-modification due to less surface trap sites. The C_{trap} values for bare and P-modified Fe_2O_3 are comparable, where as an increase in trap states (C_{trap}) with Titanium doping is observed. To know the effect of calcination temperature on PEC performance, the impedance of co-modified hematite calcined at different temperatures were measured **(Figure 4.3.11(c)**). It was found that with an increase in calcination temperature from 350°C to 750°C, the R_{trap} and R_{ct} values increases as shown in **Table 4.3.2**. The higher value of R_{trap} indicates the creation of more trap sites with higher calcination temperature which results in a decreased photocurrent density.

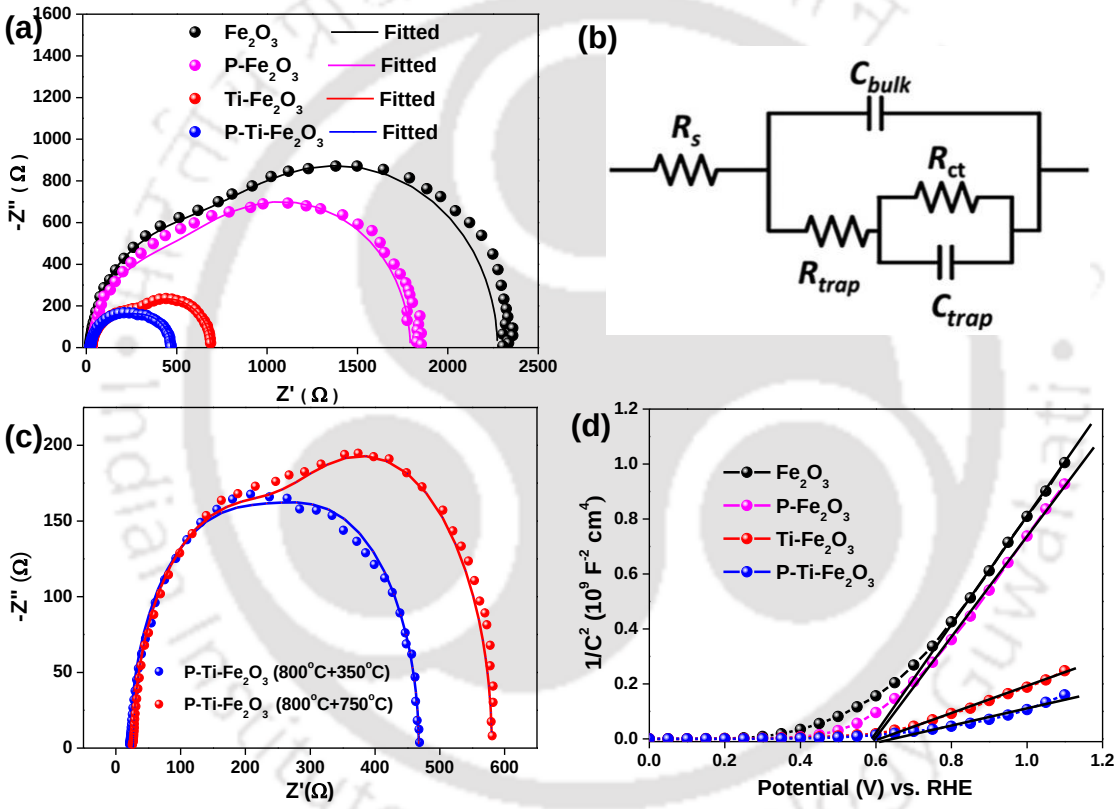

Figure 4.3.11 (a) The Nyquist plots of α-Fe_2O_3, P-Fe_2O_3, Ti-Fe_2O_3 and P-Ti-Fe_2O_3 photoanodes with fittings under light illumination. (b) The equivalent circuit used for fitting all the curves. (c) The Nyquist plots of Ti and P co-modified α-Fe_2O_3 with different calcination temperature with fittings under light illumination. (d) Mott–Schottky plots.

Increase in current density in Titanium doped sample can be explained based on the compensation of more carrier density compared to the trap states contribution. In P, Ti – Hematite, due to

Part of this chapter has been published in **ACS Appl. Energy Mater. 2019, 26, 4325**

synergistic effect between increment in carrier concentration and reduced trap states, overall PEC performance is enhanced. For clarity, the carrier density values are summarized in **Table 4.3.1**.[39,40]

Table 4.3.1 Fitting results of the EIS and carrier density from Mott-Schottky plots of bare Fe_2O_3, P-Fe_2O_3, Ti-Fe_2O_3 and P-Ti-Fe_2O_3 photoanodes.

Photoanode	**R_S/Ω**	**R_{trap}/Ω**	**10^{-6} x C_{bulk}/F**	**R_{ct}/Ω**	**10^{-5} x C_{trap}/F**	**N_D (cm^{-3})**
α-Fe_2O_3	20.28	1149	4.916	1104	2.409	5.1 x 10^{19}
P-Fe_2O_3	32.7	868.8	5.75	890.5	2.462	6.3 x 10^{19}
Ti-Fe_2O_3	28.23	318	22.29	341.2	17.03	2.5 x 10^{20}
P-Ti--Fe_2O_3	22.34	298.4	13.11	146.7	10.74	5.7 x 10^{20}

Table 4.3.2 Fitting results of the EIS of Ti and P co-modified α-Fe_2O_3 with different calcination temperature.

Photoanode	**R_S/Ω**	**R_{trap}/Ω**	**10^{-6} x C_{bulk}/F**	**R_{ct}/Ω**	**10^{-5} x C_{trap}/F**
P-Ti-Fe_2O_3 (800°C+750°C)	27.08	307.8	22.52	245.3	17.38
P-Ti-Fe_2O_3 (800°C+350°C)	22.34	298.4	13.11	146.7	10.74

Mott−Schottky analysis was performed to verify the enhanced charge transport property upon incorporation of Ti and P, as shown in Figure **Figure 4.3.11(d).** The flat-band (E_{FB}) and carrier density (N_D) of bare Fe_2O_3, doped Fe_2O_3, and co-modified Fe_2O_3 were calculated from the following formula:

$$\frac{1}{C^2} = \frac{1}{A^2 N_D e \varepsilon \varepsilon_0}\left[E - E_{FB} - \frac{kT}{e}\right] \quad (4.1)$$

where C stands for capacitance of the semiconductor, A is the surface area of the photoanode, N_D is the charge carrier density of semiconductor, e is the charge of electron, ε is the dielectric constant

 Part of this chapter has been published in **ACS Appl. Energy Mater. 2019, 26, 4325**

of the semiconductor, ε_0 is the permittivity of the vacuum, E is the applied bias, k is the Boltzmann constant, and T is the temperature.[27] Calculation of charge carrier density by Mott - Schottky should include actual surface area of the photoanode for the films, which has more surface roughness, similar to the system under study, where one dimensional growth of rod has been studied, and hence, including the real surface area term derived from AFM measurements (**Figure 4.3.12(a)-(d)**) in **equation (1)** minimizes the error.[15]

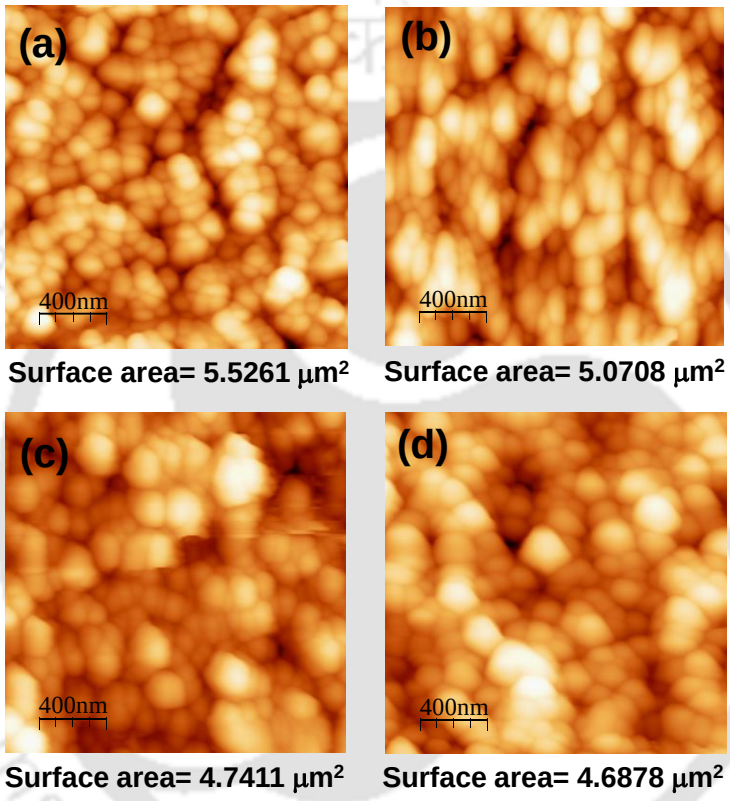

Figure 4.3.12 (a) AFM images and surface area of (a) Fe_2O_3, (b) P-Fe_2O_3, (c) Ti-Fe_2O_3 and (d) P-Ti-Fe_2O_3.

The slope of doped and co-modified photoanodes are subsequently smaller than bare hematite photoanode and positive slope for bare as well as doped hematite suggests that both Ti and P acts as n-type carrier dopant for hematite.[25] Charge carrier density calculated from the slopes of Mott-Schottky plot for bare, P-incorporated, Ti-doped and co-modified hematite are $5.1x10^{19}$ cm^{-3}, $6.3x10^{19}$ cm^{-3}, $2.5x10^{20}$ cm^{-3} and $5.7x10^{20}$ cm^{-3}, respectively. Significant increment in carrier density with Ti-doped hematite indicates an improvement in electrical conductivity as well as lengthen the lifetime of charge carriers.[41] Although only P-incorporated hematite photoanode did

not have any significant improvement in carrier density, P-incorporation onto Ti-doped hematite shows a significant two-fold increment in carrier density. In co-modified hematite, probability of mobile charge carriers getting trapped on the surface is reduced due to decrease in surface trap sites.[34] Thus, increase in charge carrier density as well as reduced electron-hole recombination are the main reasons for enhanced PEC performance of co-modified hematite.

4.3.7. Charge separation and injection efficiencies analysis

To quantify the charge separation efficiencies due to doped and co-modified hematite, photocurrents were measured in the presence of a hole-scavenger in the electrolyte. The photocurrent densities of all the photoanodes with and without hole-scavenger are shown in **Figure 4.3.13(a)**. For this process, 0.5 M H_2O_2 was used as a hole-scavenger in 1M NaOH electrolyte. H_2O_2 eliminates the barrier to interfacial hole transfer for water oxidation by quickly scavenging photogenerated holes transported to the surface of hematite photoanode.[27] The water splitting photocurrent, (J_{water}), can be expressed as:

$$J_{water} = J_{abs} \times \eta_{sep} \times \eta_{inj} \quad (4.2)$$

where J_{abs} is the photo-current density when absorbed photons are completely converted to current, η_{inj} is the hole injection efficiency to the electrolyte and η_{sep} is the charge separation efficiency of photogenerated carriers.[27] In presence of hole scavenger H_2O_2, hole injection efficiency can be treated as unity, which gives

$$\eta_{sep} = \frac{J_{H_2O_2}}{J_{abs}} \quad (4.3)$$

and

$$\eta_{inj} = \frac{J_{water}}{J_{H_2O_2}} \quad (4.4)$$

The separation efficiency and injection efficiency, calculated from the above equations are shown in **Figure 4.3.13(b) and (c)**. Separation efficiency, as shown **Figure 4.3.13(b)**, for co-modified hematite was found to be around 20%, which is more as compared to bare and doped hematite. A low separation efficiency value indicates that charge separation is a significant limitation in the

Part of this chapter has been published in **ACS Appl. Energy Mater. 2019, 26, 4325**

photocurrent value. The injection efficiency was plotted as a function of applied bias, as shown in **Figure 4.3.13(c)**. Co-modified hematite has higher hole injection efficiency near to almost 100% at 1.23V vs RHE. The charge separation and injection efficiencies are in agreement with the photocurrent enhancement in standard 1M NaOH electrolyte at 1.23V vs. RHE.

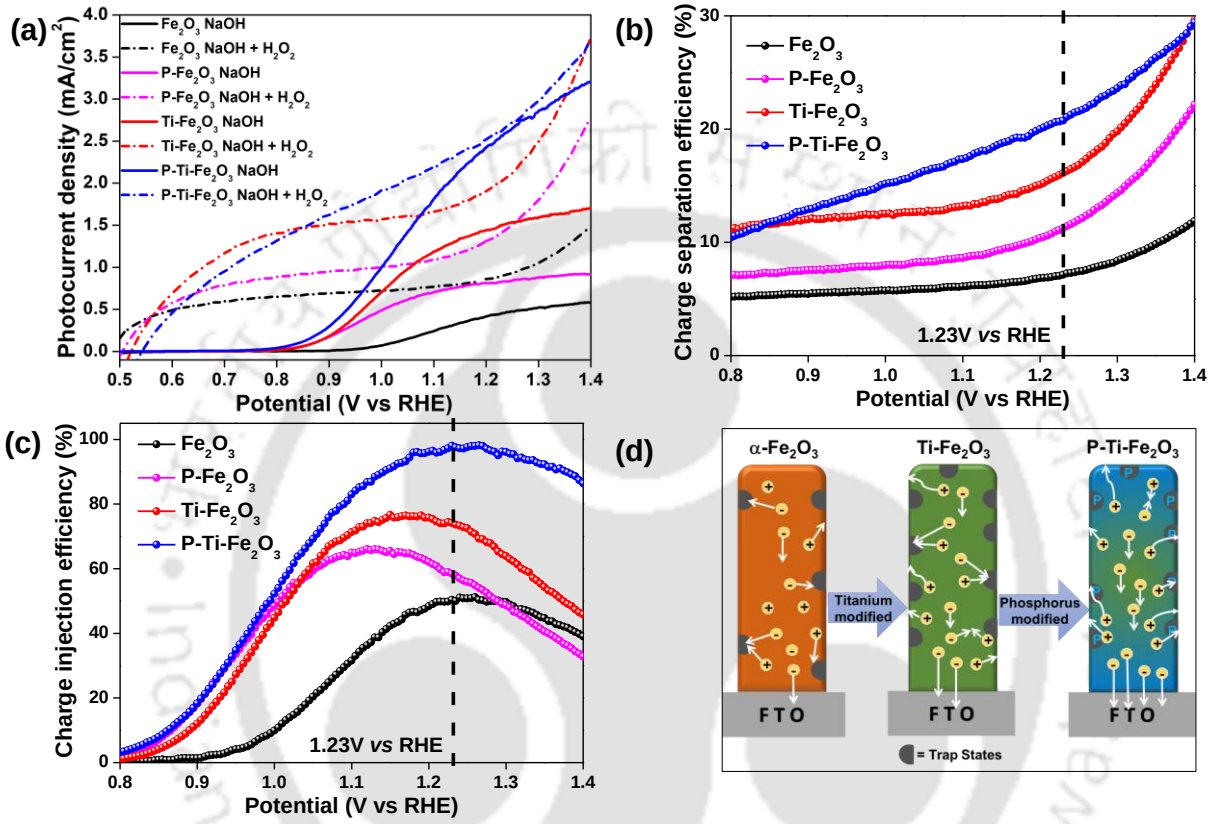

Figure 4.3.13 (a) J-V curves of all the photoanodes under light illumination at a scan rate of 10 mV/s with and without the presence of hole-scavenger H_2O_2, (b) Charge separation efficiency (η_{sep}) and (c) Charge injection efficiency (η_{inj}) of all the photoanodes as a function of applied potential and (d) the graphical of modified photoanodes depicting enhanced charge carrier density.

Figure 4.3.13(d) shows a graphical representation depicting the probable mechanism for significant enhancement in PEC performance of co-modified hematite. First, Ti-doping enhances the charge carrier density as well as provides an excellent electrical conductivity for better charge transport. Simultaneously, since surface trapping sites significantly decreased by P-incorporation, the probability of recombination at the surface decreases where holes can be easily utilized for water oxidation.

4.3.8 IPCE and operational stability

Incident photon-to-electron conversion efficiency (IPCE) measurement of bare and doped hematite photoanodes were performed to further confirm the enhancement of the PEC activity by co-modification. Compared with the bare photoanode, doped photoanodes exhibited a higher value of IPCE in the whole measurement regions due to increase in charge carrier density (**Figure 4.3.14(a)**). The co-modified hematite has the higher IPCE as compared to bare and doped hematite due to the better electrical conductivity and increase in charge carrier density due to Ti-doping as well as decrease in the formation of trap states due to incorporation of P. The dual effect of both Ti and P enhances the charge separation in P-Ti-Fe_2O_3 photoanode and hence, shows higher photocurrent density. The present result shows comparatively higher photocurrent density as compared to hematite based photoanode without any help of surface overlayer and co-catalyst.

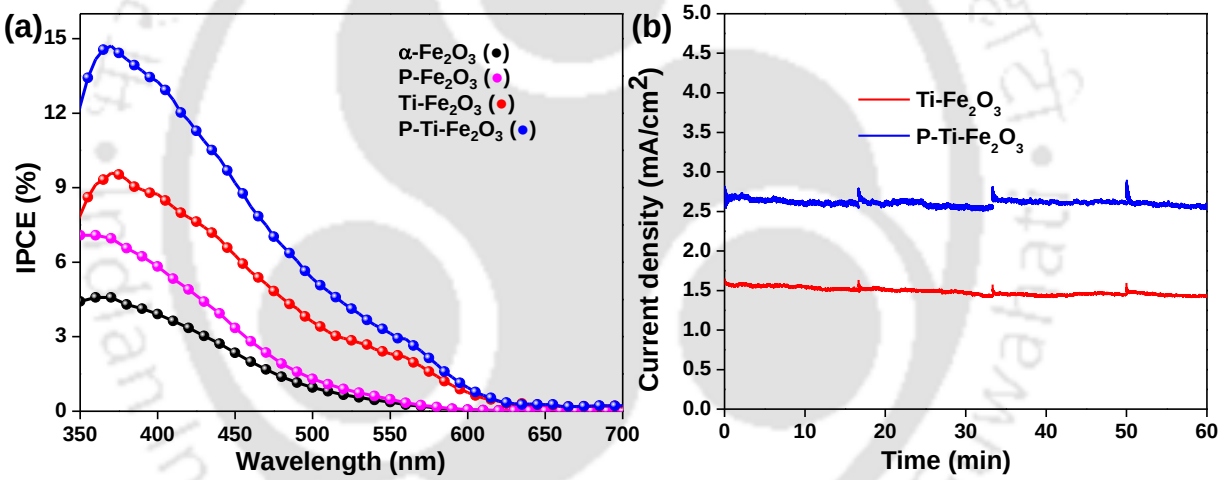

Figure 4.3.14 (a) Incident photon-to-electron conversion efficiency (IPCE) values collected for α-Fe_2O_3, P-Fe_2O_3, Ti-Fe_2O_3 and P-Ti-Fe_2O_3 photoanodes. (b) Stability test of Ti-Fe_2O_3 and P-Ti-Fe_2O_3 at 1.23V vs RHE under constant light illumination.

To investigate the stability of Ti-Fe_2O_3 and P-Ti-Fe_2O_3 photoanodes, a 1 h stability test at 1.23 V vs. RHE under constant light illumination was performed as shown in **Figure 4.3.14(b)**. Both the photoanodes showed good photostability after 1 h of light illumination. The surface P-doping has an advantage in term of stability as compared to different metal-phosphide co-catalyst as the latter undergo deactivation with long-term illumination.[24]

Part of this chapter has been published in **ACS Appl. Energy Mater. 2019, 26, 4325**

4.4 CONCLUSIONS

In conclusion, we have successfully incorporated metal and non-metal for enhanced performance in hematite photoanode. With Ti-doping the photocurrent density reached up to 1.5 mA/cm^2 due to enhanced carrier density and improved electrical conductivity. Further modification with P with suitable calcination temperature attained a photocurrent density of 2.56 mA/cm^2 due to the decreased surface trap states, thereby enhancing the charge carrier density. With co-modification utilizing Ti and P, the superior improvement in PEC performance of hematite was observed as a result of faster charge transfer kinetics. The present study demonstrates that with a suitable environment, the metal and non-metal co-modification of hematite can achieve higher PEC activities.

4.5 REFERENCES

1. K. Sivula, F. Le Formal, M. Grätzel, *ChemSusChem*, 2011, **4**, 432.
2. F. Le Formal, S. R. Pendlebury, M. Cornuz, S. D. Tilley, M. Grätzel and J. R. Durrant, *J. Am. Chem. Soc.*, 2014, **136**, 2564.
3. C.-Y. Lee, L. Wang, Y. Kado, M. S. Killian and P. Schmuki, *ChemSusChem*, 2014, **7**, 934.
4. K. Sivula, R. Zboril, F. L. Formal, R. Robert, A. Weidenkaff, J. Tucek, J. Frydrych and M. Grätzel, *J. Am. Chem. Soc.*, 2010, **132**, 7436.
5. B. Iandolo, B. Wickman, I. Zoric´, A. Hellman, *J. Mater. Chem. A*, 2015, **3**, 16896.
6. M. P. Dareedwards, J. B. Goodenough, A. Hamnett and P. R. Trevellick, *J. Chem. Soc., Faraday Trans. 1*, 1983, **79**, 2027.
7. N. J. Cherepy, D. B. Liston, J. A. Lovejoy, H. M. Deng and J. Z. Zhang, *J. Phys. Chem. B*, 1998, **102**, 770.
8. S. D. Tilley, M. Cornuz, K. Sivula and M. Grätzel, *Angew. Chem., Int. Ed.*, 2010, **49**, 6405.
9. M. Li, Y. Yang, Y. Ling, W. Qiu, F. Wang, T. Liu, Y. Song, X. Liu, P. Fang, Y. Tong and Y. Li, *Nano Lett.*, 2017, **17**, 2490.
10. H. Han, F. Riboni, F. Karlicky, S. Kment, A. Goswami, P. Sudhagar, J. Yoo, L. Wang, O. Tomanec, M. Petr, O. Haderka, C. Terashima, A. Fujishima, P. Schmuki and R. Zboril, *Nanoscale*, 2017, **9**, 134.

Part of this chapter has been published in **ACS Appl. Energy Mater. 2019, 26, 4325**

11. J. Li, F. Meng, S. Suri, W. Ding, F. Huang and N. Wu, *Chem. Commun.*, 2012, **48**, 8213.
12. H.-J. Ahn, K.-Y. Yoon, M.-J. Kwak, J.-S. Lee, P. Thiyagarajan and J.-H. Jang, *J. Mater. Chem. A*, 2015, **3**, 21444.
13. Y. Ling, G. Wang, D. A. Wheeler, J. Z. Zhang and Y. Li, *Nano Lett.*, 2011, **11**, 2119.
14. R. Franking, L. Li, M. A. Lukowski, F. Meng, Y. Tan, R. J. Hamers and S. Jin, *Energy Environ. Sci.*, 2013, **6**, 500.
15. K.D. Malviya, D. Klotz and H. Dotan, *J. Phys. Chem. C*, 2017, **121**, 4206.
16. W.D. Chemelewski, N.T. Hahn and C.B. Mullins *J. Phys. Chem. C*, 2012, **116**, 5255.
17. P. Dias, T. Lopes, L. Andrade and A. Mendes, *J. Power Sources*, 2014, **272**, 567.
18. Z. Fan, Z. Xu, S. Yan and Z. Zou, *J. Mater. Chem. A*, 2017, **5**, 8402.
19. T. Hisatomi, F. Le Formal, M. Cornuz, J. Brillet, N. Tétreault, K. Sivula and M. Grätzel, *Energy Environ. Sci.*, 2011, **4**, 2512.
20. F. Le Formal, N. Tetreault, M. Cornuz, T. Moehl, M. Grätzel and K. Sivula, *Chem. Sci.*, 2011, **2**,737.
21. Z. Li, W. Luo, M. Zhang, J. Feng and Z. Zou, *Energy Environ. Sci.*, 2013, **6**, 347.
22. Y. Zhang, H. Ji, W. Ma, C. Chen, W. Song and J. Zhao, *Molecules*, 2016, **21**, 868.
23. A. Annamalai, H. Lee, S. Choi, S. Lee, E. Gracia-Espino, A. Subramanian, J. Park and K. Kong, *Sci. Rep.*, 2016, **6**, 23183.
24. Y. Zhang, S. Jiang, W. Song, P. Zhou, H. Ji, W. Ma, W. Hao, C. Chen and J. Zhao, *Energy Environ. Sci.*, 2015, **8**, 1231.
25. Z. Luo, C. Li, S. Liu, T. Wang and J. L. Gong, *Chem. Sci.*, 2017, **8**, 91.
26. J. Xie, W. Liu, J. Xin, F. Lei, L. Gao, H. Qu, X. Zhang and Y. Xie, *ChemSusChem*, 2017, **10**, 4465.
27. R. Zhang, Y. Fang, T. Chen, F. Qu, Z. Liu, G. Du, A. M. Asiri, T. Gao and X. Sun, *ACS Sustainable Chem. Eng.*, 2017, **5**, 7502.
28. A. G. Tamirat, W.N. Su, A. A. Dubale, H. M. Chen and B. J. Hwang, *J. Mater. Chem. A*, 2015, **3**, 5949.
29. J. Wang, C. Du, Q. Peng, J. Yang, Y. Wen, B. Shan and R. Chen, *Int. J. Hydrogen Energy*, 2017,**42**, 29140.
30. H. Pan, X. Meng, D. Liu, S. Li and G. Qin, *Phys. Chem. Chem. Phys.*, 2015, **17**, 22179.

31. L. Vayssieres, N. Beermann, S.-E. Lindquist and A. Hagfeldt, *Chem. Mater.*, 2001, **13,** 233.
32. Z. Fu, T. Jiang, L. Zhang, B. Liu, D. Wang, L. Wang and T. Xie, *J. Mater. Chem. A*, 2014, **2**, 13705.
33. Z. Fu, T. Jiang, Z. Liu, D. Wang, L. Wang and T. Xie, *Electrochim. Acta*, 2014, **129**, 358.
34. A. Liu, YZhang, W. Ma, W. Song, C. Chen and J. Zhao, *J. Photochem. Photobiol., A* 2018, **355**, 290.
35. P. S. Shinde, A. Annamalai, J. H. Kim, S. H. Choi, J. S. Lee and J. S. Jang, *Sol. Energy Mater. Sol. Cells*, 2015, **141**, 71.
36. T. K. Sahu, A. K. Shah, G. Gogoi, A. S. Patra, M. S. Ansari and M. Qureshi, *Chem. Commun.*, 2018, **54**, 10483.
37. L. Zhao, J. Xiao, H. Huang, Q. Huang, Y. Zhao and Y. Li, *Int. J. Hydrogen Energy* 2018, **43**, 12646.
38. C. Miao, T. Shi, G. Xu, S. Ji and C. Ye, *ACS Appl. Mater. Interfaces*, 2013, **5**, 1310.
39. S. C. Riha, B. M. Klahr, E. C. Tyo, S. Seifert, S. Vajda, M. J. Pellin, T. W. Hamann and A. B. F. Martinson, *ACS Nano*, 2013, **7**, 2396.
40. Z. Hu, Z. Shen and J. C. Yu, *Chem. Mater.* 2016, **28**, 564.
41. C. Miao, S. Ji, G. Xu, G. Liu, L. Zhang and C. Ye, *ACS Appl. Mater. Interfaces*, 2012, **4**, 4428.

CHAPTER 5

Boron Nitride Quantum Dots as a Hole Extractor for Fluorine Doped Hematite Photoanode: Fabrication, Effect on Interfacial Charge Transfer Properties and Photoelectrochemical Water Oxidation Performance

In this chapter, we incorporated boron nitride quantum dots as a simple and effective strategy to overcome the main drawbacks of hematite based photoanodes. Hexagonal boron nitride quantum dots have been synthesized in a relatively low-temperature hydrothermal method which effectively acts as an efficient hole extractor for tuning the PEC performance with better charge separation and transfer at the photoanode/electrolyte interface.

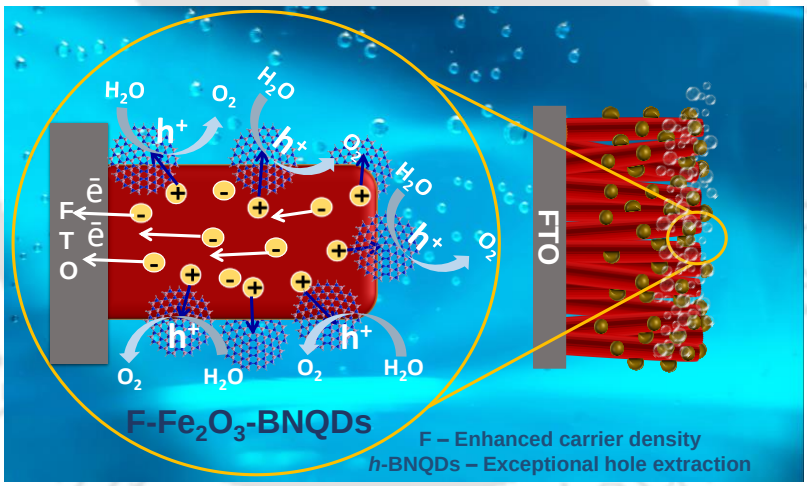

JOURNAL OF POWER SOURCES

T. K. Sahu *et al.*, 2020, **445**, 227341

5.1 INTRODUCTION

As discussed in previous chapter, non-metallic dopants such as P, S, and Si have been used to enhance the water-oxidation performance of hematite owing to their involvement in increasing carrier density and in addition greater carrier mobility.[1-3] Zhang et al. reported that non-metal P-dopant offers more number of valence electrons as compared to many metallic dopants which competently facilitate charge separation by eluding the surface electron trapping sites in hematite.[1] Recently, van de Krol et al. re-stated that water oxidation capability of a photoanode is strongly limited by its insufficient hole injection property.[4] Zhang et al. demonstrated that incorporation of black phosphorene layer onto $BiVO_4$ can accelerate the hole transport from the semiconductor to co-catalyst.[5] Therefore, promoting hole extraction from photoanode surface holds broader interest for significant improvement in PEC performance. In the recent past, boron nitride, also known as "white graphene" has received much attention due to its chemical and thermal stability and conductivity.[6] Intrinsically, boron nitride nanostructures were always negatively charged which makes them a good hole carrier acceptor, and could be used to improve the electron-hole carrier separation.[7] In this work, we incorporated boron nitride quantum dots to overcome the main drawbacks of hematite based photoanodes. The water oxidation of hematite photoanode was intended to be improved by fluorine doping and adsorption of BNQDs. For doping non-metal fluorine, a simple organic precursor Selectfluor has been utilized by an *ex-situ* method which helps to achieve higher charge carrier density with preservation of morphological features. Hexagonal boron nitride quantum dots have been synthesized in a relatively low-temperature hydrothermal method which effectively acts as an efficient hole extractor for tuning the PEC performance with better charge separation. The superior PEC activity of modified hematite is supported by various characterization techniques.

5.2 EXPERIMENTAL METHODS

5.2.1 Fabrication of α-Fe_2O_3 and F-doped Fe_2O_3

The α-Fe_2O_3 nanorod structures were directly grown over a conductive substrate by following earlier reports.[1] In a typical synthesis, $FeCl_3$ (0.15M) and $NaNO_3$ (1M) were added to 60 mL distilled water with stirring. To maintain the pH at 1.5, concentrated HCl was added to the

Part of this chapter has been published in **J. Power Sources, 2020, 445, 227341**

above solution. The solution was then transferred to a 100 mL Teflon lined stainless steel vessel. Four cleaned FTO (2.5 cm x 1.00 cm) with polyimide tape masking were put into the bottom of the solution such that the conductive side faced towards up. The autoclaved solution was put in a pre-heated hot-air oven for 6h at 100ºC. After the reaction, the autoclave was naturally cooled to room temperature and as synthesized β-FeOOH thin films were cleaned several times with distilled water and ethanol to remove any residue present over the films. The cleaned films were then dried overnight in a hot-air oven at 60ºC. As obtained β-FeOOH thin films were annealed at 800ºC for 15 min (20ºC/min) to obtained α-Fe_2O_3. F-doped Fe_2O_3 films were prepared by dipping as prepared β-FeOOH films in an aqueous solution of Selectfluor {1-Chloromethyl-4-fluoro-1, 4-diazoniabicyclo[2.2.2]octane bis(tetrafluoroborate)} for 15 min and annealed at 800ºC (20ºC/min) for 15 min.

5.2.2. Synthesis of boron nitride quantum dots (BNQDs)

Boron nitride quantum dots (BNQDs) were synthesized by hydrothermal method.[8] For synthesis, boric acid (100 mg) was dissolved in deionized water (10 mL). To the above solution, melamine (34 mg) was added under stirring. After stirring for 30 min, the white suspension was transferred to a 23 mL Teflon lined stainless steel vessel and heated in a hot-air oven at 200ºC for 15 h. A different set of quantum dots were synthesized by keeping reaction time for 20 h to get different sized quantum dots. After cooling, the product was filtered with a 0.22 μm syringe filter membrane to remove large particles. Finally, the solution was diluted to 40 mL with the addition of distilled water and used as a stock solution of BNQDs.

5.2.3 Fabrication of Fe_2O_3-BNQDs and F-Fe_2O_3-BNQDs

As-prepared Fe_2O_3 and F-Fe_2O_3 films were dipped in different concentrations of BNQDs solution for 6, 9, 12 and 15 h at 60°C to fabricate Fe_2O_3-BNQDs and F-Fe_2O_3-BNQDs. After the sensitization process, the films were cleaned with DI water to remove the excess BNQDs at the surface. Then the films were annealed at 400ºC for 1 h.

Scheme 5.2.1 shows the schematic representation of step-wise fabrication of F-Fe_2O_3-BNQDs photoanode. Selectfluor used as a source of fluorine which is known to be a good fluorinating agent and offers solubility in common organic solvents as well as water and shows less reactivity

towards glass. *Ex-situ* doping helps to achieve higher charge carrier density with preservation of morphological features. The BNQDs used for this purpose was synthesized by low-temperature hydrothermal method by using boric acid and melamine as a precursor.

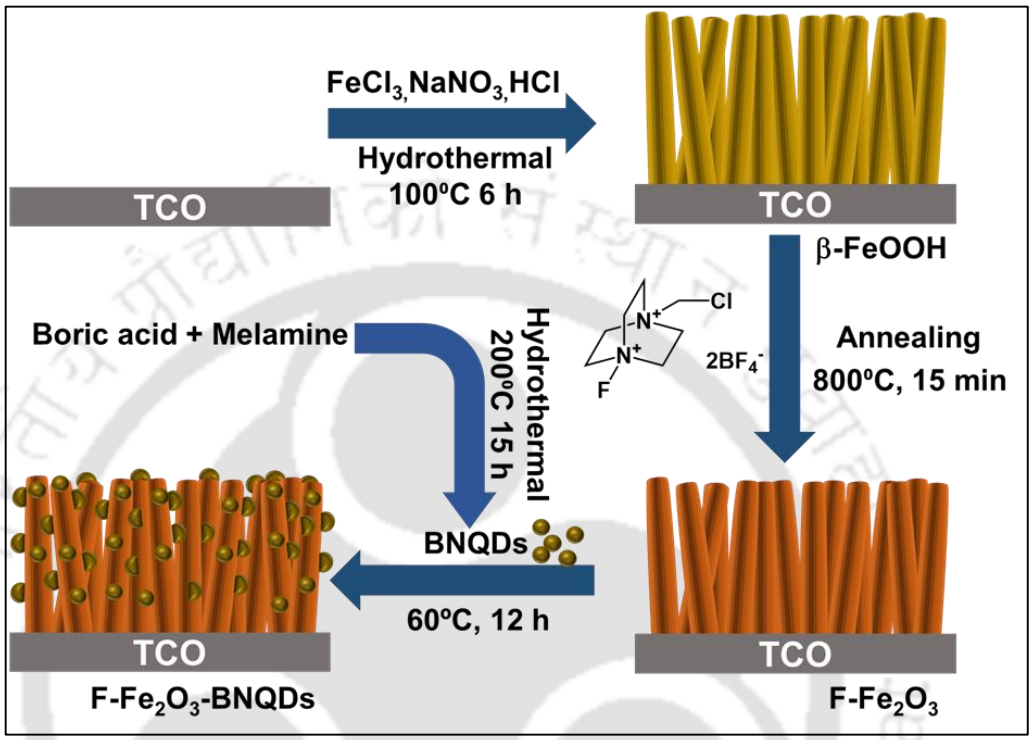

Scheme 5.2.1. Schematic representation for the synthesis of BNQDs and the fabrication process of F-Fe_2O_3-BNQDs.

5.3 RESULTS AND DISCUSSIONS

5.3.1 Powder x-ray diffraction (XRD) and Raman analysis

Powder XRD of α-Fe_2O_3, Fe_2O_3-BNQDs, F-Fe_2O_3, F-Fe_2O_3-BNQDs and BNQDs are shown in **Figure 5.3.1(a)**. All the peaks correspond to α-Fe_2O_3 (JCPDS-33-0664) and SnO_2 (from FTO substrate). The strong diffraction peak for (110) plane for the samples indicate that the nanostructures are oriented preferentially in the (110) direction over the FTO substrate.[9] For BNQDs, a weak peak at 2θ~27° corresponds to (002) plane of hexagonal boron nitride which agrees well with the literature.[10,11] No peaks for BNQDs were identified in the composite samples due to a very low concentration of BNQDs. To confirm the dopant incorporation in hematite, Raman analysis was performed as shown in **Figure 5.3.1(b)**. The Raman spectra of all

the samples show the characteristic vibrations of hematite comprising two A_{1g} modes (225 and 500 cm^{-1}) and four E_g modes (245, 293, 412 and 612 cm^{-1}). The Raman spectra of F-Fe_2O_3 and F-Fe_2O_3-BNQDs samples shows a new peak at 660 cm^{-1} which is absent in bare Fe_2O_3 and Fe_2O_3-BNQDs, could be attributed to the disorder induced by doping of fluorine.[12]

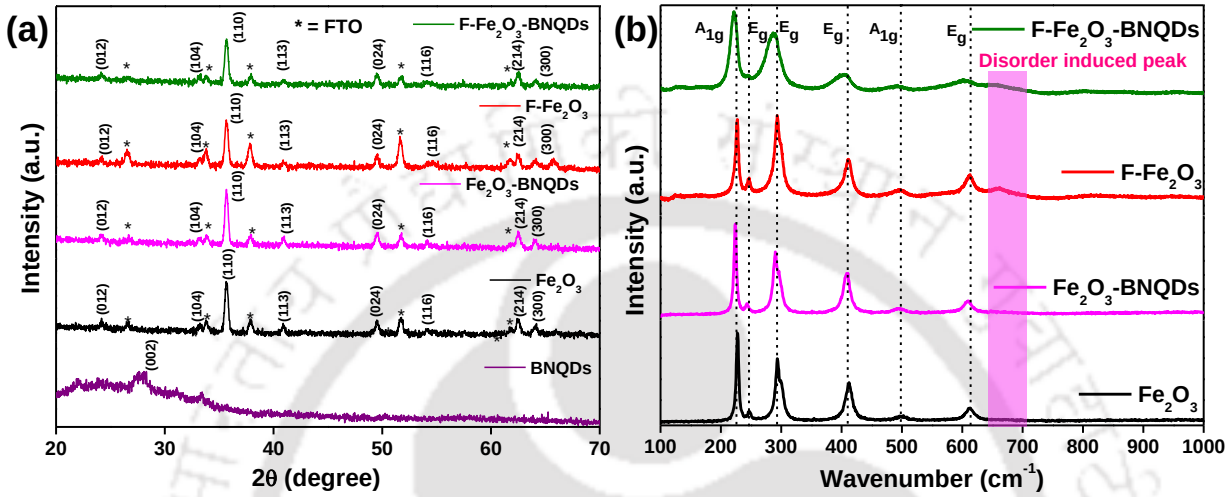

Figure 5.3.1 (a) Powder X-ray Diffraction analysis and (b) Raman spectra of Fe_2O_3, Fe_2O_3-BNQDs, F-Fe_2O_3, and F-Fe_2O_3-BNQDs photoanodes.

5.3.2 UV-visible absorption spectra and FTIR analysis

The optical absorption properties of all the photoanodes were analysed through UV−visible absorption spectra as shown in **Figure 5.3.2(a)**. BNQDs absorbs in the UV region (inset to **Figure 5.3.2(a)**). Similar optical curves and band gaps estimated from Tauc analysis (**Figure 5.3.2(b)**) shows that F-doping and BNQDs does not influence the absorption edge of Fe_2O_3 as well as band gaps.[13] The absorbance and photoluminescence spectra (**Figure 5.3.3(a)**) of BNQDs were consistent with reported literature of BNQDs.[14]

Part of this chapter has been published in **J. Power Sources, 2020, 445, 227341**

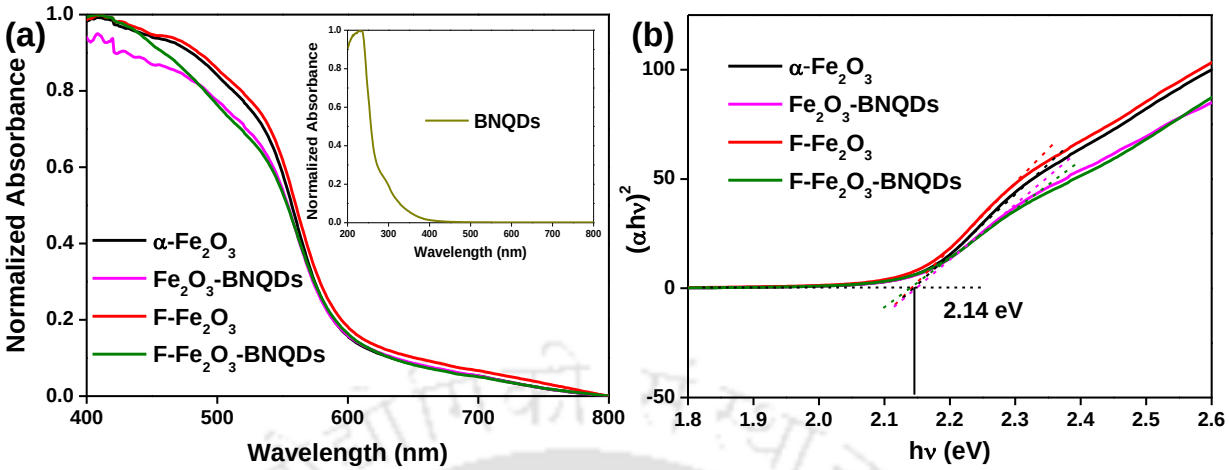

Figure 5.3.2 (a) UV-visible absorbance spectra of α-Fe_2O_3, Fe_2O_3-BNQDs, F-Fe_2O_3 and F-Fe_2O_3-BNQDs photoanodes (inset showing the absorption spectrum of BNQDs) and the corresponding (b) Tauc plots.

Figure 5.3.3(b) shows the FT-IR spectra of F-Fe_2O_3, BNQDS, and F-Fe_2O_3-BNQDs. The FT-IR spectrum of F-Fe_2O_3 shows two strong absorption peaks at 483 and 579 cm^{-1} which can be assigned to Fe-O band. The broad peak at 3436 cm^{-1} could be attributed to hydroxyl group stretching. The FT-IR spectrum of BNQDs shows peaks at 807 and 1448 cm^{-1} corresponds to B-N bending and stretching modes, respectively.[15] The peak at 1194 cm^{-1} corresponding to B-O band.[15] In addition, peaks at 3224 cm^{-1} corresponds to B-OH stretching.[15] The FT-IR spectrum of F-Fe_2O_3-BNQDs shows all the peaks corresponds to both F-Fe_2O_3 and BNQDs.

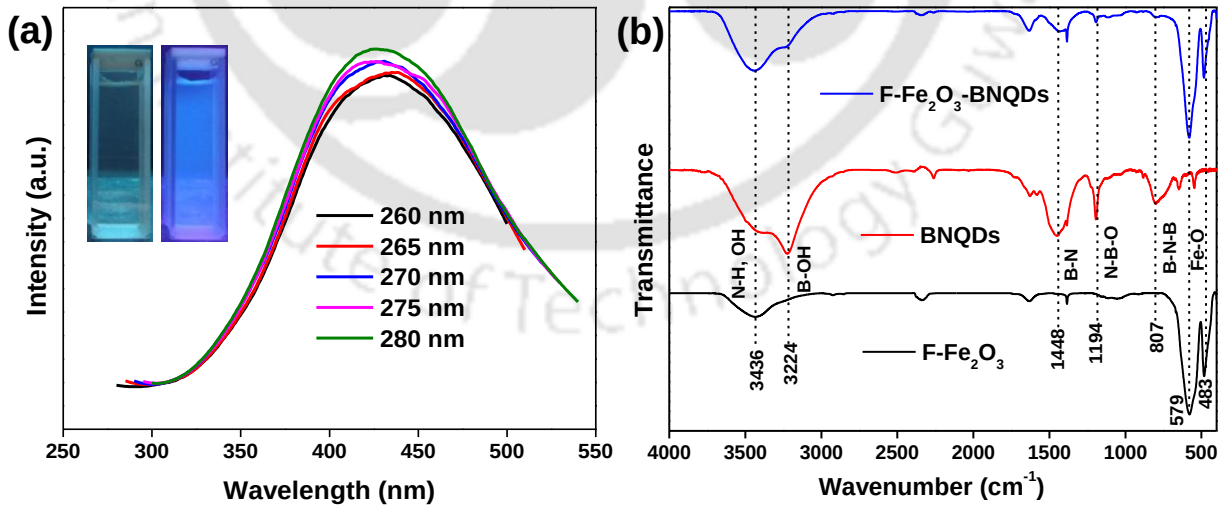

Figure 5.3.3 Photoluminescence spectra of BNQDs at different wavelength of emission. Inset showing the fluorescence property under UV light illumination. (b) FT-IR spectra of F-Fe_2O_3, BNQDs and F-Fe_2O_3-BNQDs.

5.3.3 Materials morphology

Figure 5.3.4 shows the FESEM images of all the photoanodes. It can be seen that the morphology of all the photoanodes are same after modification and the hematite nanorods structures are uniformly distributed over the conductive substrate. The morphological features of hematite were found to be intact after the doping of fluorine. The cross-sectional FESEM image of F-Fe_2O_3-BNQDs confirms the vertical growth of nanorods over the conductive substrate as shown in inset to **Figure 5.3.4(d)**. The lengths of hematite nanorods over the conductive substrate were found to be ~450 nm.

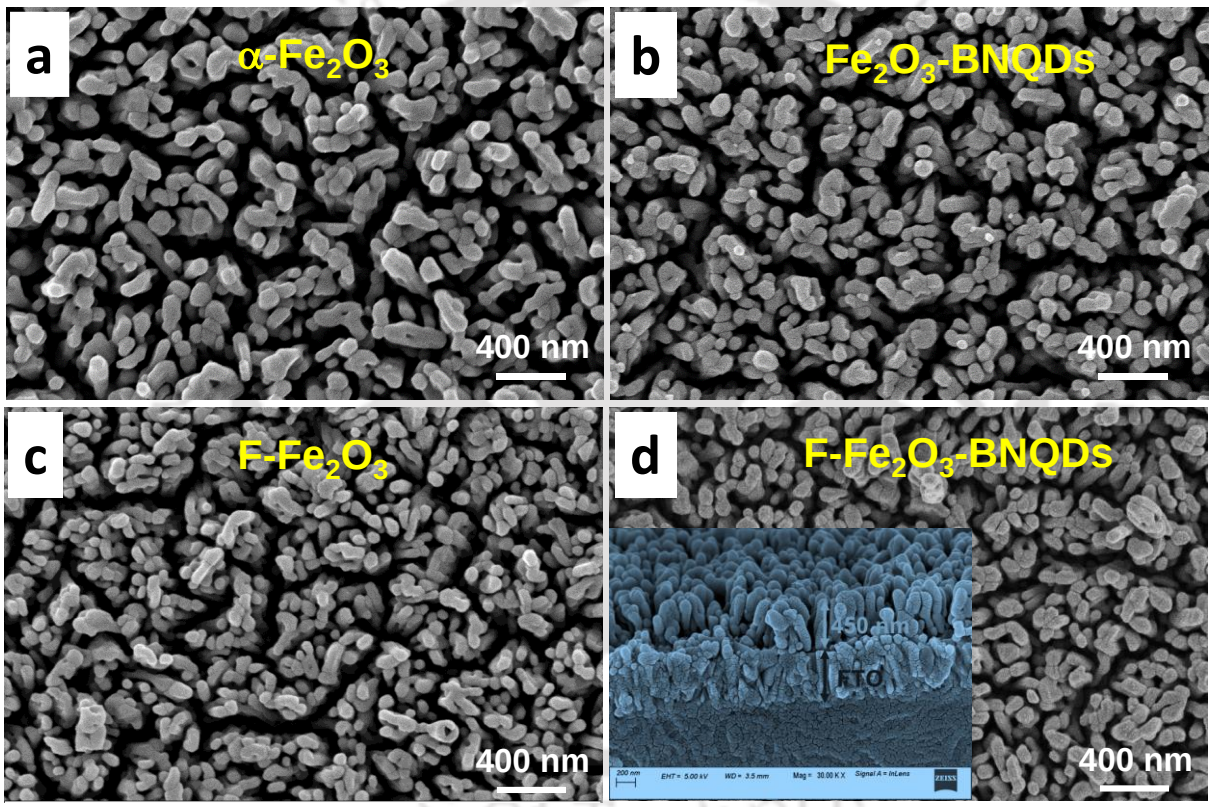

Figure 5.3.4 FESEM image of (a) α-Fe_2O_3, (b) Fe_2O_3-BNQDs, (c) F-Fe_2O_3 and (d) F-Fe_2O_3-BNQDs. Inset to (d) shows the cross-sectional FESEM image of F-Fe_2O_3-BNQDs.

The FETEM of boron nitride quantum dots synthesized hydrothermally for 15h is shown in **Figure 5.3.5(a)**, confirms the size of the quantum dots which were found to be around ~5 nm. Inset to **Figure 5.3.5(a)** shows the HR-TEM of BNQDs with a d-spacing of 0.21 nm corresponds to (100) plane of BNQDs.[8] **Figure 5.3.5(b)** shows the FETEM of BNQDs synthesized

Part of this chapter has been published in **J. Power Sources, 2020, 445, 227341**

hydrothermally for 20h which shows that size of the BNQDs increases with increase in synthesis time. The FETEM of F-Fe_2O_3-BNQDs shown in **Figure 5.3.5(c)** display the presence of BNQDs over hematite nanorods. As shown in **Figure 5.3.5(d)**, the HR-TEM of F-Fe_2O_3-BNQDs shows d-spacing of 0.21 nm and 0.25 nm corresponds to (100) plane of BNQDs and (110) plane of Fe_2O_3, respectively.[2,8]

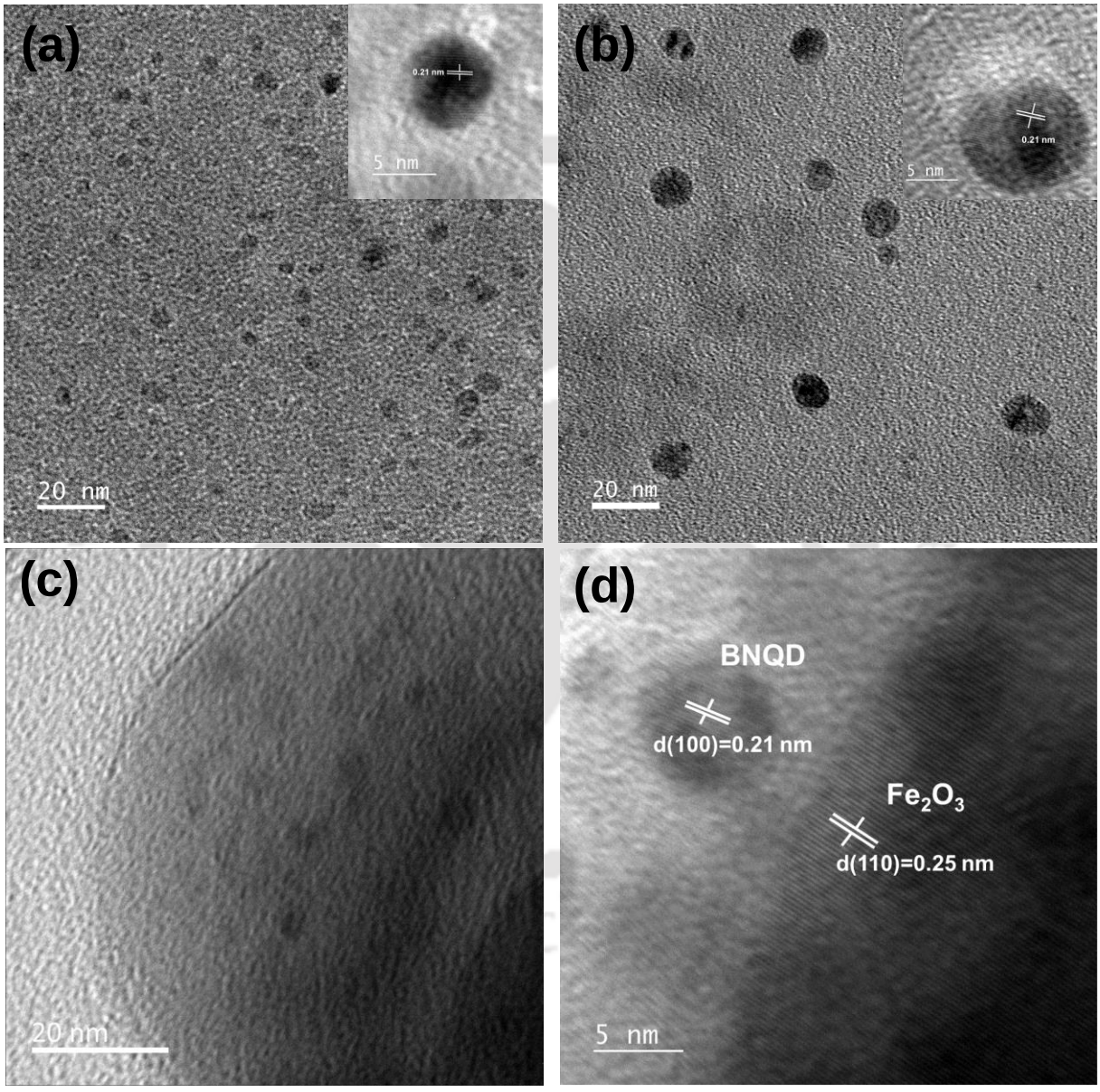

Figure 5.3.5 FETEM image and the corresponding HRTEM (inset) of boron nitride quantum dots (BNQDs) synthesized at different time (a) 15h and (b) 20h. (c) FETEM image of F-Fe_2O_3-BNQDs and (d) HRTEM of F-Fe_2O_3-BNQDs.

The STEM-EDX elemental mapping shown in **Figure 5.3.6** confirms the presence of Fe (b), O (c), F (d), B (e), N (f) over nanorod structures.

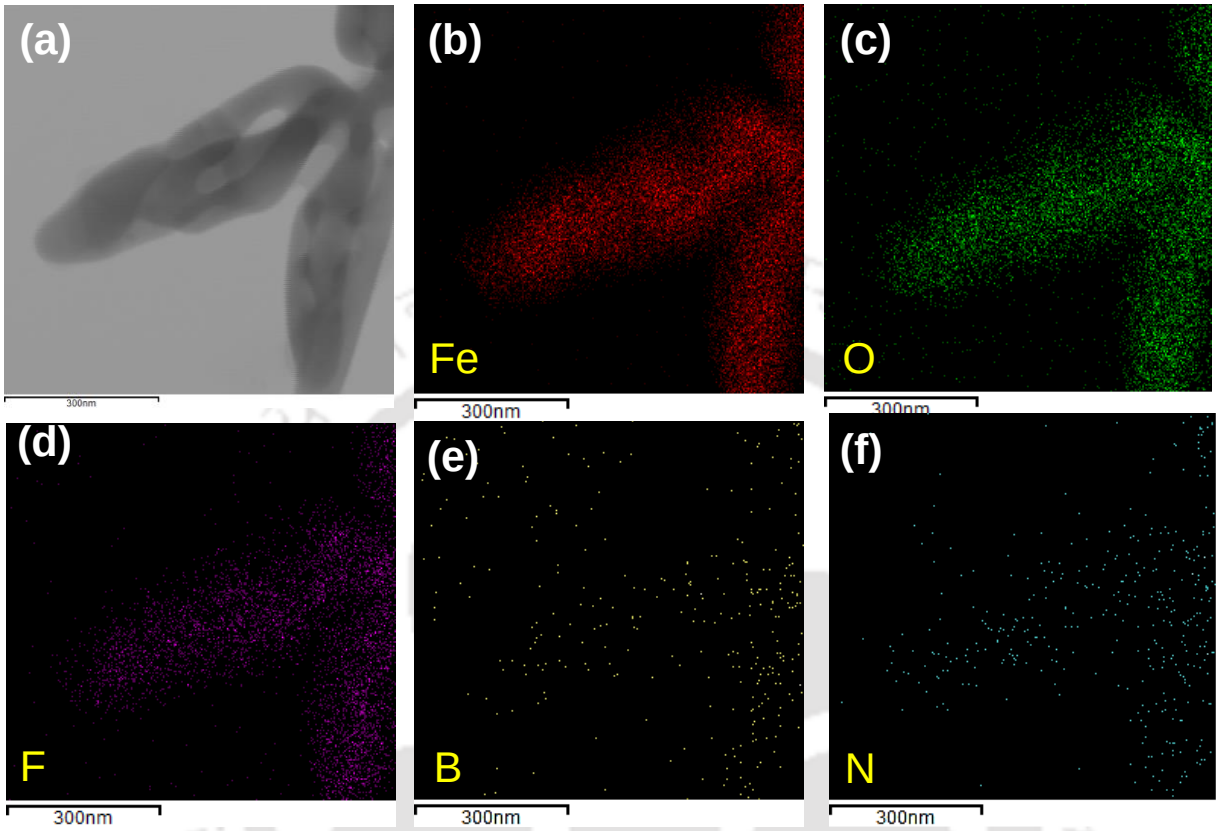

Figure 5.3.6 STEM-EDX elemental mapping of F-Fe_2O_3-BNQDs showing the uniform distribution of Fe(e), O(f), F(g), B(h) and N(i) over nanorod structures.

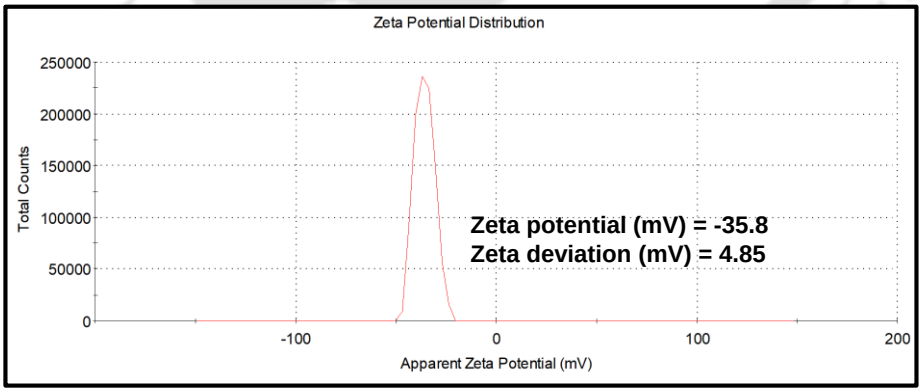

Figure 5.3.7 Zeta potential of boron nitride quantum dots (BNQDs)

Zeta potential measurement was carried out to know the surface charge over BNQDs, to prove its hole extraction ability. A highly negative zeta potential value of -35.8 mV was found for BNQDs as shown in **Figure 5.3.7**, which shows its ability to extract positive ions (holes).

5.3.4 Photoelectrochemical characterizations

To evaluate the effects of F-doping and BNQDs decoration on the water oxidation activity of Fe_2O_3 photoanodes, photocurrent was measured in 1M NaOH electrolyte under light illumination. For comparison, the bare Fe_2O_3, F-Fe_2O_3, and Fe_2O_3-BNQDs photoanodes have also been measured under the same conditions. As shown in **Figure 5.3.8(a)**, bare Fe_2O_3 photoanodes exhibits a low photocurrent density of 0.35 mA cm^{-2} at 1.23V vs. RHE. Fluorine was doped to Fe_2O_3 with different concentration of Selectfluor solution and the corresponding photocurrent densities are shown in **Figure 5.3.8(b)**. With *ex-situ* fluorine doping, the optimized photocurrent density of F-Fe_2O_3 could reach up to 1.45 mA cm^{-2}, which is four times higher than the bare Fe_2O_3. This enhancement in the photocurrent density could be attributed to the increase in charge carrier density and mobility with F-doping.[2] Decoration of BNQDs with Fe_2O_3 exhibit a photocurrent density of 1.1 mA cm^{-2}, which is three times higher than that of Fe_2O_3. The enhancement in photocurrent density due to BNQDs incorporation could be accredited to better charge separation induced by BNQDs. It is known in the literature that hexagonal boron nitride has high negative charge density, particularly on the edge geometry,[16] due to which it shows exceptional hole extraction properties, extracting holes from the surface of hematite, resulting in efficient charge separation.[7] The hole extracting ability of BNQDs by virtue of its charges located on the edge geometry is further proved by its highly negative zeta potential value of -35.8 mV (**Figure 5.3.7**), as results it can readily extract the holes from the surface of hematite. BNQDs incorporation to F-Fe_2O_3 was optimized with different chemical bath deposition times and the corresponding photocurrent densities are shown in **Figure 5.3.8(c)**. With both F-doping and BNQDs incorporation, the photocurrent density reaches up to a remarkable value of 2.24 mA cm^{-2}. These results clearly reveal a significant improvement of the PEC performance which mainly be attributed to the synergistic effects of F-doping and the BNQDs incorporation. This enhancement in photocurrent density is due to increase in charge carrier density and mobility as a results of non-metal F-doping as well as efficient hole extraction by negatively charged BNQDs at the interface which supress the recombination by rapid

oxidation of holes. **Figure 5.3.8(d)** shows the transient photocurrent measurement of all the photoanodes at 1.23V vs. RHE under chopped light illumination. The sharp photocurrent spikes demonstrate the rapid recombination of charge carriers during their transportation to the semiconductor surface. With both F-doping and BNQDs modification, the photocurrent spikes diminished due to increase in electrical conductivity induced by F-doping and efficient hole extraction by BNQDs for faster water oxidation, indicating that charge recombination is suppressed with dual modification. To know the effect of the size of BNQDs on the photoelectrochemical performance of F-Fe_2O_3, BNQDs synthesized with different time periods are also studied as shown in **Figure 5.3.9**. The BNQDs synthesized hydrothermally with 15h are found to be more effective. The decrease in the photoelectrochemical performances with increase in sizes may be attributed to the decrease of negative charges over the surface/edge geometry.

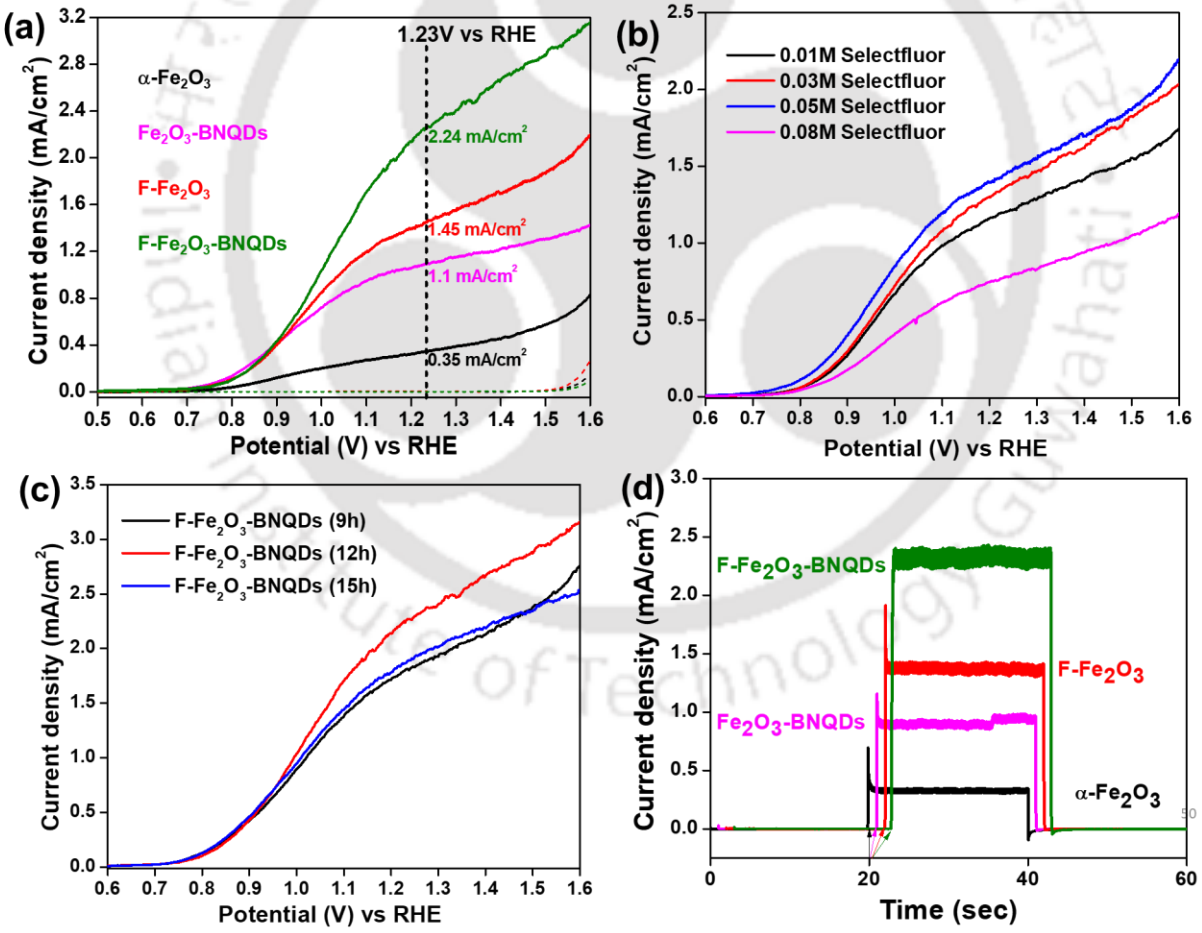

Figure 5.3.8 (a) J-V curves of Fe_2O_3, Fe_2O_3-BNQDs, F-Fe_2O_3 and F-Fe_2O_3-BNQDs photoanodes under light illumination (b) J-V curves of fluorine doped Fe_2O_3 with different concentration of Selectfluor, (c) J-V curves of F-

Fe_2O_3-BNQDs with optimized BNQDs with different time of chemical bath deposition and (d) chronoamperometry of all the optimized photoanodes at 1.23V vs. RHE.

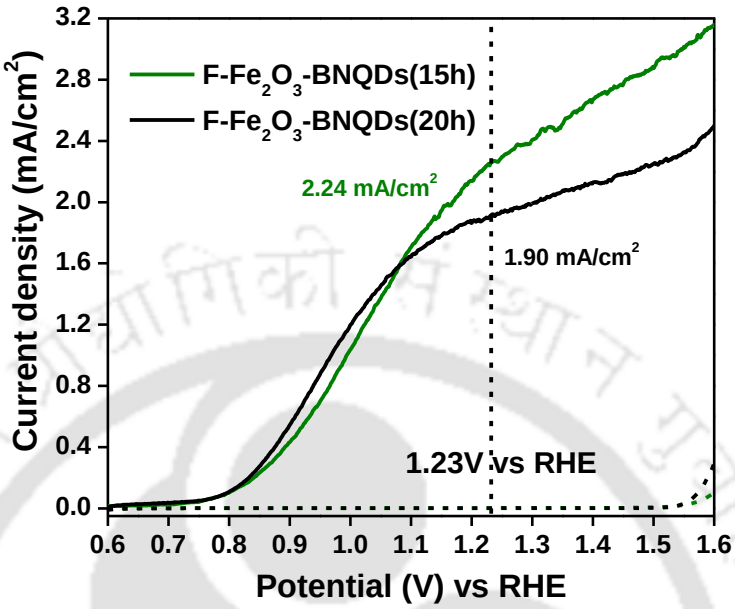

Figure 5.3.9 J-V curves of F-Fe_2O_3-BNQDs with BNQDs synthesized at different time.

5.3.5 Electrochemical impedance spectroscopy (EIS) analysis

To explore the interfacial charge separation and charge transfer process, electrochemical impedance spectroscopy (EIS) measurements were carried out for all these samples. **Figure 5.3.10(a)** shows the Nyquist plots derived from EIS for bare and modified photoanodes. An equivalent circuit model was used (inset to **Figure 5.3.10(a)**) to fit all the Nyquist plot and the results listed in **Table 5.3.1**. R_s expresses the series resistance at the interface between semiconductor/FTO substrate. The Nyquist plot consists of two semicircles, where in the arch in the low-frequency region corresponds to charge transfer resistance (R_{ct}) at the photoelectrode/electrolyte interface and the arch in the high-frequency region related to charge transfer resistance (R_{trap}) at the bulk of photoelectrode.[17,18] With F-doping, the R_{ct} value (441.9 Ω) decreases due to increase in electrical conductivity of hematite as compare to its bare counterpart (5061 Ω).[1] In case of Fe_2O_3-BNQDs, due to hole extraction ability of BNQDs the R_{ct} (500 Ω) decreases as compared to bare hematite (5061 Ω).[5] With incorporation of BNQDs over F-Fe_2O_3 the R_{ct} value (130.8 Ω) significantly decreases as compared to bare Fe_2O_3, F-Fe_2O_3 and Fe_2O_3-BNQDs at the bulk as well as in the interface of F-Fe_2O_3-BNQDs due to increase in

electrical conductivity and carrier density induced by F-doping and enhanced hole extraction by BNQDs at the photoelectrode/electrolyte interface. Furthermore, the increase in the capacitance (C_{trap}) value at photoelectrode/electrolyte interface of Fe_2O_3-BNQDs and F-Fe_2O_3-BNQDs signifies better hole extraction properties of BNQDs as compared to bare Fe_2O_3 and F-Fe_2O_3. The better hole extraction property of BNQDs leads to accumulation of charges on the photoanode/electrolyte interfaces which results in increasing value of capacitance value at photoanode/electrolyte interface.[5]

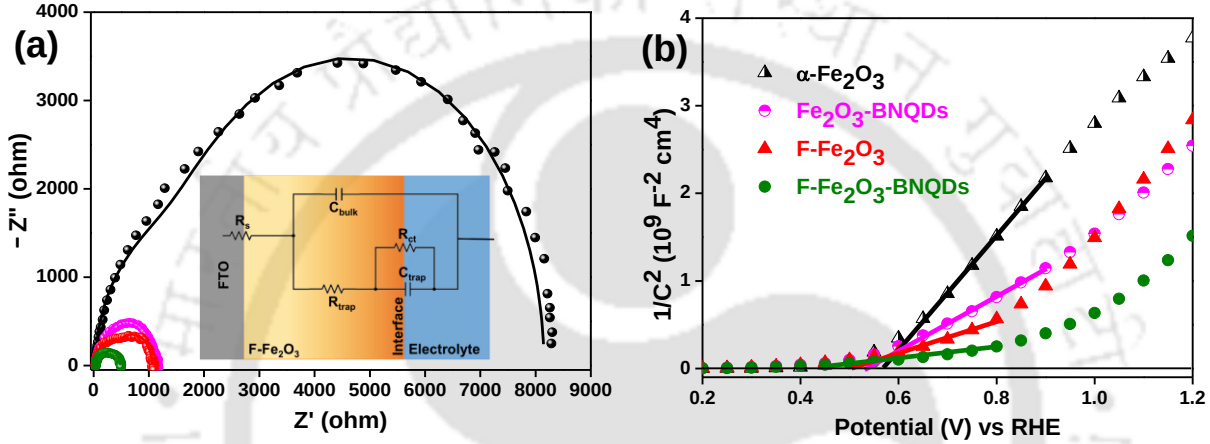

Figure 5.3.10 (a) The Nyquist plots for Fe_2O_3 (black), Fe_2O_3-BNQDs (magenta), F-Fe_2O_3 (red), and F-Fe_2O_3-BNQDs (olive) photoanodes under light illumination and their equivalent circuit used for fitting, (b) corresponding Mott–Schottky plots.

The Mott–Schottky (M-S) measurements were carried out to calculate the charge carrier densities of different photoanodes as shown in **Figure 5.3.10(b)**. From the M-S plot, charge carrier density (N_D) can be calculated from the following equation:

$$\frac{1}{C^2} = \frac{1}{A^2 N_D e \varepsilon \varepsilon_0}\left[E - E_{FB} - \frac{kT}{e}\right] \quad (5.1)$$

where C represents the capacitance of the semiconductor/electrolyte interface, A is the surface area of the photoanode, e is the charge of an electron, ε is the dielectric constant of the semiconductor, ε_0 is the vacuum permittivity, E is the applied potential, k is the Boltzmann constant, and T is the temperature.[19] To minimize the error in the calculation of charge carrier density, the actual surface area of the photoanodes are obtained from AFM analysis as shown in **Figure 5.3.11(a-d)**. Positive slopes for all the samples including F-doping indicates that fluorine

is an n-type dopant and the significant increase in carrier density is primarily accredited to doping of fluorine.[2] BNQDs incorporation also responsible for enhanced carrier density due to an efficient charge separation and transport as a result of effective hole extraction by BNQDs as compared to bare Fe_2O_3.[20] With dual modification, the carrier density further increases due to combined effect of both F-doping and BNQDs. More specifically, the carrier densities calculated from the slopes of the Mott–Schottky plots of all the photoanodes are shown in **Table 5.3.1**.

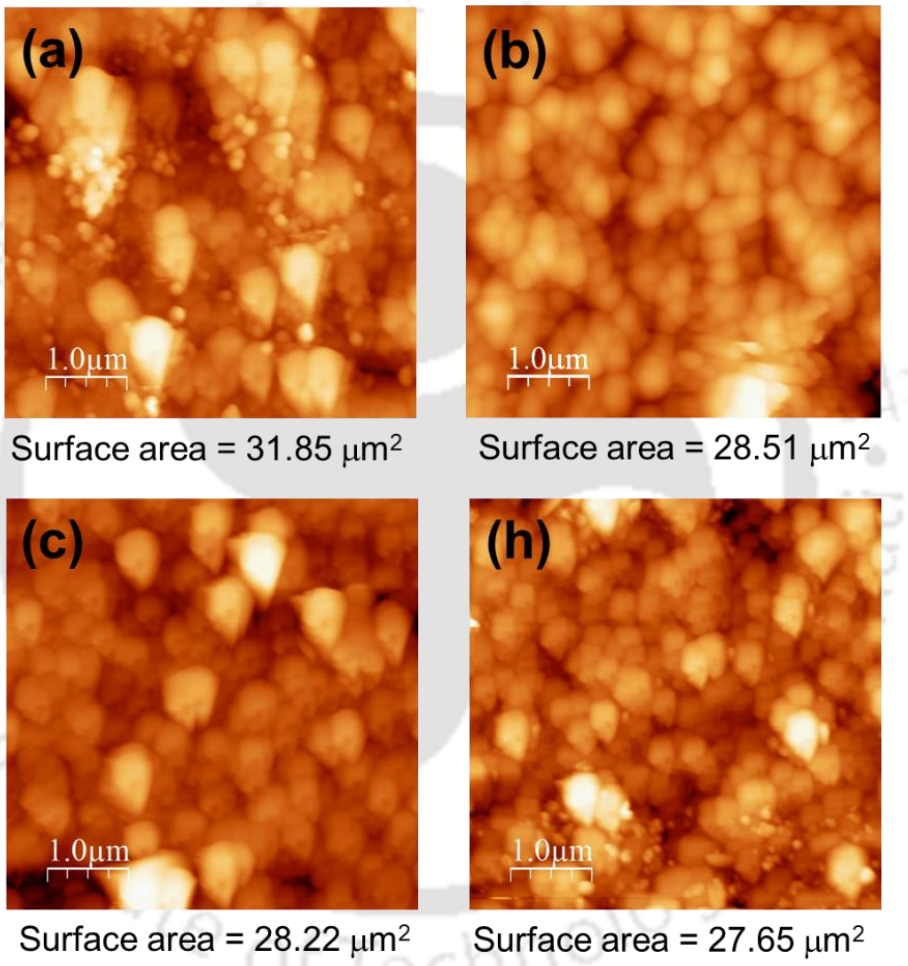

Figure 5.3.11 AFM analysis of (a) a-Fe_2O_3, (b) F-Fe_2O_3, (c) Fe_2O_3-BNQDs and (d) F-Fe_2O_3-BNQDs for calculation of Mott-Schottky plot.

Table 5.3.1. Fitting results of the Nyquist plots and M-S plots of bare Fe_2O_3, F-Fe_2O_3, Fe_2O_3-BNQDs and F-Fe_2O_3-BNQDs photoanodes.

Photoanode	**α- Fe_2O_3**	**Fe_2O_3-BNQDs**	**F- Fe_2O_3**	**F- Fe_2O_3-BNQDs**
R_S/Ω	37.69	34.88	36.13	**40.09**
R_{trap}/Ω	3051	529.5	443.7	**441.3**
C_{bulk}/μF	2.75	3.74	3.59	**4.73**
R_{ct}/Ω	5061	500	441.9	**130.8**
C_{trap}/μF	7.9	19.1	12.1	**23.4**
N_D(cm^{-3})	4.57×10^{18}	9.27×10^{18}	2.02×10^{19}	**2.08×10^{20}**

5.3.6 Charge separation and charge injection efficiencies

To quantify the effect of F-doping and BNQDs incorporation, charge separation efficiency (η_{sep}) and charge injection efficiency (η_{inj}) were employed with the help of a hole scavenger (0.5M H_2O_2) in the electrolyte (1.0M NaOH).[21] **Figure 5.3.12(a)** shows the photocurrent densities of bare and modified photoanodes with and without H_2O_2 in the 1M NaOH electrolyte under light illumination. The η_{sep} and η_{inj} are calculated based on the following equations:

$$\eta_{sep} = \frac{J_{H_2O_2}}{J_{abs}} \quad (5.2)$$

and

$$\eta_{inj} = \frac{J_{water}}{J_{H_2O_2}} \quad (5.3)$$

where J_{water} is the measured photocurrent density, $J_{H_2O_2}$ is the photocurrent density in the presence of hole scavenger H_2O_2, J_{abs} is the maximum theoretical water oxidation photocurrent

Part of this chapter has been published in **J. Power Sources, 2020, 445, 227341**

density.[2] As shown in **Figure 5.3.12(b)**, a significant improvement in the η_{sep} at 1.23 V_{RHE} has been achieved for F-Fe_2O_3-BNQDs (37%) as compared to F-Fe_2O_3 (31%), Fe_2O_3-BNQDs (24%) and bare Fe_2O_3 (14%). The η_{inj}, as shown in **Figure 5.3.12(c)**, is higher for F-Fe_2O_3-BNQDs (64%) as compared to F-Fe_2O_3 (48%), Fe_2O_3-BNQDs (45%) and bare Fe_2O_3 (27%). The enhancement in η_{sep} and η_{inj} suggests that both F-doping and BNQDS incorporation has positive impacts in the enhancement in the photocurrent density.

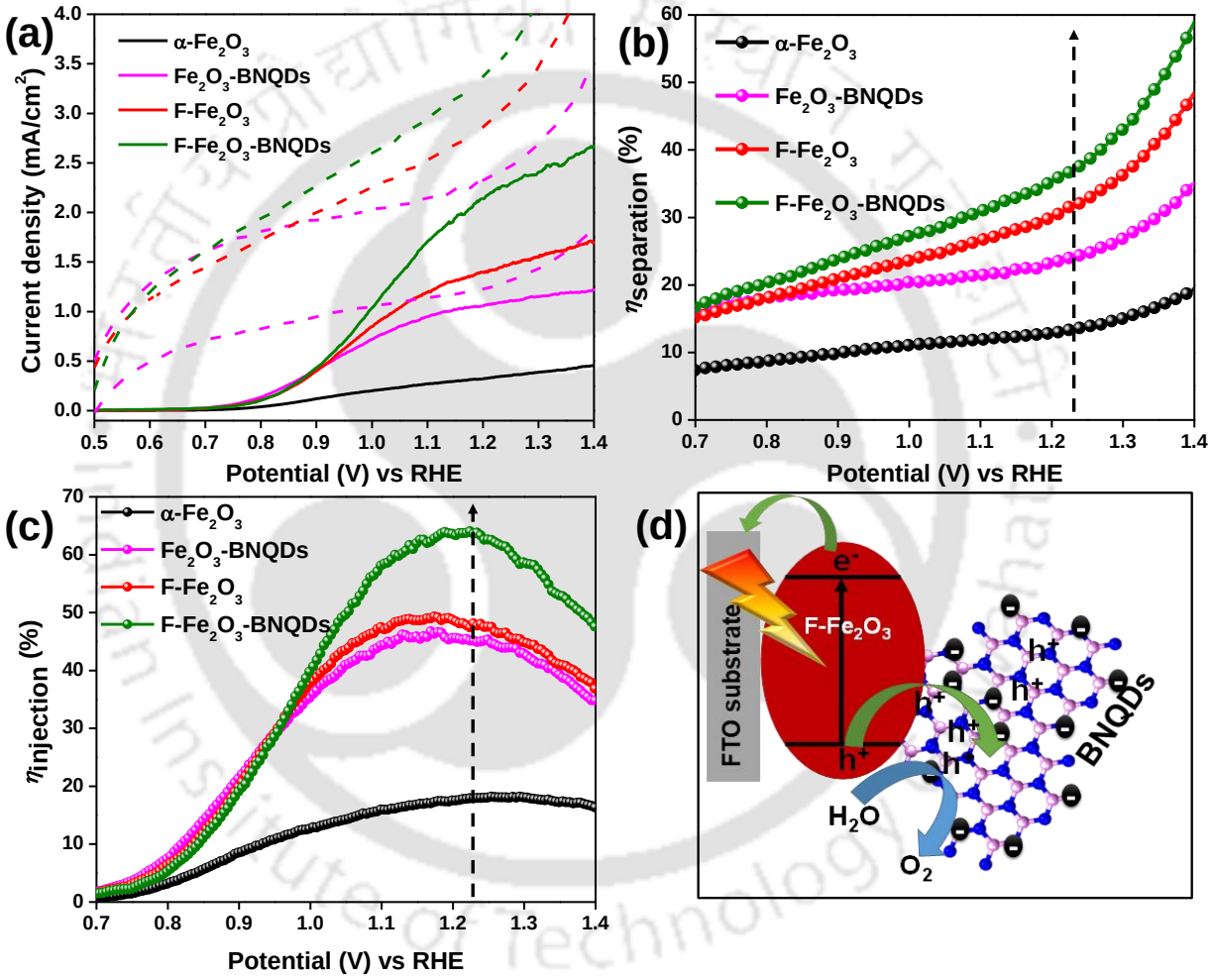

Figure 5.3.12 (a) J-V curves of α-Fe_2O_3, Fe_2O_3-BNQDs, F-Fe_2O_3 and F-Fe_2O_3-BNQDs photoanodes under light illumination with and without the presence of hole-scavenger H_2O_2. The dotted lines represents the presence of hole-scavenger, (b) charge separation and (c) charge injection efficiencies of all the photoanodes with respect to applied potential.(d) Graphical representation of hole extraction process in F-Fe_2O_3-BNQDs.

The schematic of probable mechanism involved in F-Fe_2O_3-BNQDs is shown in **Figure 5.3.12(d)**. F-doing controls the electron mobility of hematite through enhancing the carrier density by forming covalent bond with oxygen. With increase in carrier mobility, the electrons and holes are separated efficiently, where the holes reaches to the surface of hematite. The holes at the surface are efficiently collected by BNQDs due to their negatively charged edge geometry, followed by water oxidation.

3.3.7 Faradaic efficiency and operational stability of the photoanodes

Oxygen gas evolved was measured in order to confirm that the photocurrent observed was really due to PEC water oxidation. The faradaic efficiency, which is the ratio between measured and calculated gas evolution, was found to be ~90% after 1 h of irradiation as shown in **Figure 5.3.13(a)**. Thus, most of the photogenerated charges were utilized for water oxidation. **Figure 5.3.13(b)** shows the operational stability of bare hematite and co-modified hematite with 1h continuous illumination. F-Fe_2O_3-BNQDs shows only 2% decrease in photocurrent density after 1h of illumination, which confirms the stability of as synthesized material with modification.

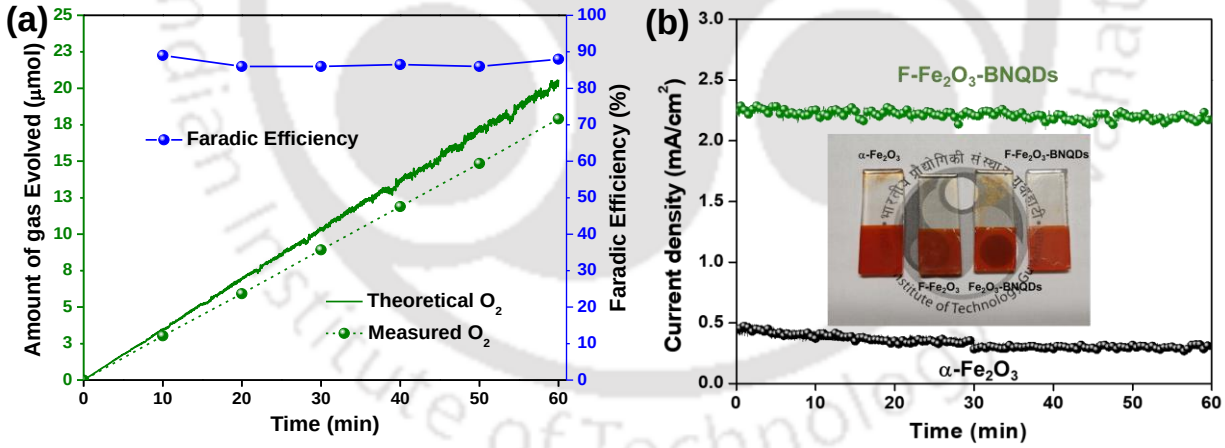

Figure 5.3.13 (a) Faradic efficiency test of F-Fe_2O_3-BNQDs for oxygen evolution and (b) operational stability of Fe_2O_3 and F-Fe_2O_3-BNQDs at 1.23V vs RHE under continuous light illumination.

5.4 CONCLUSIONS

In summary, we have successfully doped fluorine onto hematite using Selectfluor as dopant source and incorporated low temperature synthesized BNQDs for enhanced

photoelectrochemical water oxidation. It is apparent that F-doping on Fe_2O_3 nanorods facilitate charge carrier transport by providing excellent electrical conductivity and charge carrier density. As a result, the one-dimensional Fe_2O_3 nanorod arrays can quickly transfer the separated electrons to the FTO substrate. At the same time, the BNQDs acts as an efficient hole extractor and can endorse surface charge separation, so that the holes on the surface can be utilized for water oxidation. An excellent photocurrent density of 2.24 mA cm^{-2} was achieved with the synergistic effects of both F-doping and BNQDs modification, which is six-fold higher than bare hematite. Present strategy can be extrapolated as a model system in designing novel photoanodes for efficient extraction of holes.

5.5 REFERENCES

1. Y. Zhang, S. Jiang, W. Song, P. Zhou, H. Ji, W. Ma, W. Hao, C. Chen and J. Zhao, *Energy Environ. Sci.*, 2015, **8**, 1231.
2. R. Zhang, Y. Fang, T. Chen, F. Qu, Z. Liu, G. Du, A. M. Asiri, T. Gao and X. Sun, ACS *Sustainable Chem. Eng.*, 2017, **5**, 7502.
3. P. Dias , T. Lopes , L. Andrade and A. Mendes , *J. Power Sources*, 2014, **272** , 567.
4. C. Zachäus, F. F. Abdi, L. M. Peter and R. van de Krol, *Chem. Sci.*, 2017, **8**, 3712.
5. K. Zhang, B. Jin, C. Park, Y. Cho, X. Song, X. Shi, S. Zhang, W. Kim, H. Zeng and J. H. Park, *Nat. Commun.* 2019, **10**, 2001.
6. H. Zeng, C. Zhi, Z. Zhang, X. Wei, X. Wang, W. Guo, Y. Bando and D. Golberg, *Nano Lett.*, 2010, **10**, 5049.
7. N. Wang, G. Yang, H. Wang, R. Sun and C.-P. Wong, *Front Chem.*, 2018, **6**, 440.
8. B. Huo, B. Liu, T. Chen, L. Cui, G. Xu, M. Liu, J. Liu, *Langmui*r, 2017, **33**, 10673.
9. P. S. Shinde, S. H. Choi, Y. Kim, J. Ryu and J. S. Jang, *Phys. Chem. Chem. Phys.*, 2016, **18**, 2495.
10. J.-H. Jung, M. Kotal, M.-H. Jang, J. Lee, Y.-H. Cho, W.-J. Kimc and I.-K. Oh, *RSC Adv.*, 2016, **6**, 73939.

11. Z. Lei, S. Xu, J. Wan and P. Wu, *Nanoscale*, 2015, **7**, 18902–18907
12. Z. Fu, T. Jiang, L. Zhang, B. Liu, D. Wang, L. Wang and T. Xie, *J. Mater. Chem. A*, 2014, **2**, 13705.
13. A. G. Tamirat, W.N. Su, A. A. Dubale, H. M. Chen and B. J. Hwang, *J. Mater. Chem. A*, 2015, **3**, 5949.
14. B. Liu, S. Yan, Z. Song, M. Liu, X. Ji, W. Yang and J. Liu, *Chem. – Eur. J.*, 2016, **22**, 18899.
15. P. Nautiyal, A. Loganathan, R. Agrawal, B. Boesl, C. Wang and A. Agarwal, *Sci. Rep.*, 2016, **6**, 29498.
16. S. Meng, X. Ye, X. Ning, M. Xie, X. Fu and S. Chen, *Appl. Catal., B*, 2016, **182**, 356.
17. L. Zhao, J. Xiao, H. Huang, Q. Huang, Y. Zhao and Y. Li, *Int. J. Hydrogen Energy*, 2018, **43**, 12646.
18. C. Miao, T. Shi, G. Xu, S. Ji and C. Ye, *ACS Appl. Mater. Interfaces*, 2013, **5**, 1310.
19. Z. Luo, C. Li, S. Liu, T. Wang and J. Gong, *Chem. Sci.* 2017, **8**, 91.
20. S.-S. Yi, J.-M. Yan and Q. Jiang, *J. Mater. Chem. A*, 2018, **6**, 9839.
21. H. Dotan, K. Sivula, M. Grätzel, A. Rothschild and S. C. Warren, *Energy Environ. Sci.*, 2011, **4**, 958.

CHAPTER 6

Cobalt - Cerium Mixed Double Hydroxide as Co-catalyst over $BiVO_4$ Photoanode: Role of Cerium, its Effect on Water Oxidation Kinetics, Stability and Photoelectrochemical Performance

In this chapter, we designed the $BiVO_4$ photoanode, coupled with a mixed metal hydroxide containing cobalt and rare-earth element cerium, where the addition of catalytically silent cerium to $Co(OH)_x$ not only enhanced the stability, but also improved the water oxidation kinetics. The water oxidation performance of $BiVO_4$ - $CoCe(OH)_x$ could be attributed to the synergistic effect of both cobalt and cerium, where cerium incorporation enhanced the surface passivation aiding the stability of the photoanode and formation of Co(II)/(III) active sites increase the rate of the surface kinetics of $BiVO_4$.

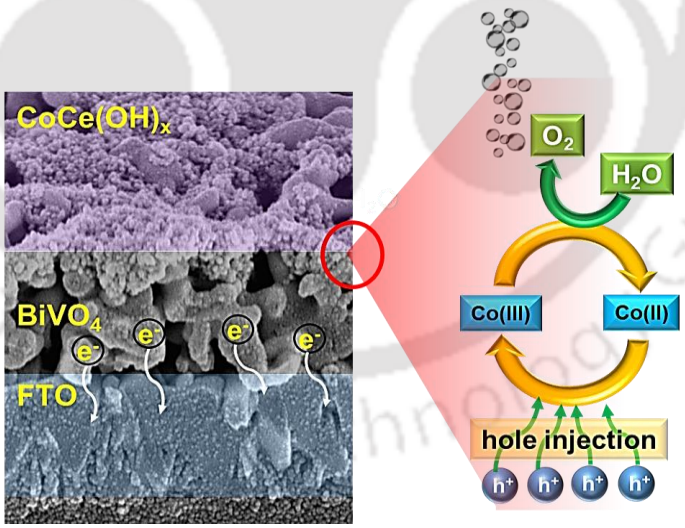

ACS APPLIED ENERGY MATERIALS

T. K. Sahu *et al.*, 2020, **3**, 5610

6.1 INTRODUCTION

Among different n-type metal oxides, bismuth vanadate ($BiVO_4$) with a band gap of 2.4~2.5 eV with a theoretical solar-to-hydrogen efficiency of 9.1%, has drawn attention as one of the promising photoanode material for its capability of promoting water oxidation.[1-9] However, faster recombination of photogenerated electron-hole pairs due to low carrier mobility, surface trap sites and sluggish water oxidation kinetics of $BiVO_4$, hinders efficacy in reaching close to the theoretical solar-to-hydrogen efficiency.[1] Several strategies have been proposed to optimize the charge recombination and/or accelerate reaction kinetics, including designing hetero-junctions or core-shell composites, surface modification or coupling with a suitable co-catalyst.[10-14] The efficient charge transfer process at the photoelectrode/electrolyte interface forms another key factor that should be addressed for photoanodes besides the light-harvesting for carrier generation.[15] Coupling the photoelectrode materials with a co-catalyst is an effective approach for enhancing the surface oxygen evolution reaction (OER) kinetics and to inhibit the surface recombination due to the surface trap sites.[10,11] Most of the monometallic and mixed metal oxide and hydroxide including layered double hydroxides used in OER are amorphous.[16] Although, amorphous mixed metal hydroxides are active, it exhibits lower catalytic activity than the crystalline mixed metal hydroxide due to the low conductivity.[17-18] Markovic et al. stated that the amorphous phase is expected to have lower stability as a result of faster dissolution rate of cations in the electrolyte during the OER although it has higher catalytic activity.[19] In this regard, mixed metal hydroxides with good crystallinity are beneficial for the fabrication of highly stable PEC systems. Most of the double metal hydroxides used as co-catalysts have dual metal active sites, where the mechanism for enhanced PEC activity is very clear. Double metal hydroxides with metal active as well as metal inactive sites have not been studied much and limited to only transition metals whereas rare earth metals have not been explored adequately for OER as well as PEC water oxidation.[20-23] In this work, we have designed a mixed metal hydroxide with catalytically active cobalt anchored with catalytically silent cerium and studied its effect on the PEC performance of $BiVO_4$ photoanode.

Part of this chapter has been published in **ACS Appl. Energy Mater. 2020, 3, 5610**

6.2 EXPERIMENTAL

6.2.1 Fabrication of $BiVO_4$ photoanode

For the fabrication of $BiVO_4$ photoanodes, firstly, BiOI precursor solution was electrodeposited over the FTO substrate.[24] A 50 mL aqueous solution of precursor was prepared by mixing 0.04 M $Bi(NO_3)_3.5H_2O$ and 0.4 M KI with pH adjusted to 1.7 by adding concentrated HNO_3 (65–68%) in distilled water. To the above solution, 20 mL 0.23 M p-benzoquinone in absolute ethanol was added slowly. The solution was stirred vigorously for 30 min before use. For the deposition of BiOI, a potential of -0.1V vs. Ag/AgCl was applied for 200s. 50 μL dimethyl sulfoxide (DMSO) solution containing 0.2M vanadyl acetylacetonate ($VO(acac)_2$) was drop-casted onto the as prepared BiOI electrodes, and then annealed in a muffle furnace at 450°C for 2h (ramp rate of 2°C/min) to form $BiVO_4$. Finally, to remove excess V_2O_5 from the $BiVO_4$ electrodes, electrodes were treated in a 1M NaOH solution for 30 min. The resulting $BiVO_4$ electrodes were thoroughly rinsed with distilled water and dried in air.

6.2.2 Deposition of $Co(OH)_x$, $Ce(OH)_x$ and $CoCe(OH)_x$ over $BiVO_4$

Typically, a solution was prepared by dissolving 0.75 mmol $Co(NO_3)_2.6H_2O$, 0.25 mmol $Ce(NO_3)_3.6H_2O$, 2.5 mmol NH_2CONH_2 and 1 mmol NH_4F in 50 mL distilled water. The solution was transferred to a 100 mL Teflon lined stainless steel vessel where $BiVO_4$ films were placed at the bottom with the conductive side facing upward and it was kept in a hot air oven at 100°C for 4h. After cooling, as prepared $BiVO_4$-$CoCe(OH)_x$ was rinsed thoroughly with distilled water and dried in a hot air oven at 60°C overnight. Different compositions were synthesized by changing the Co to Ce ratio in the precursor solutions. $Co(OH)_x$ was prepared by replacing $Ce(NO_3)_3.6H_2O$ with $Co(NO_3)_2.6H_2O$ and $Ce(OH)_x$ was prepared by replacing $Co(NO_3)_2.6H_2O$ with $Ce(NO_3)_3.6H_2O$. **Scheme 6.2.1** depicts the step-wise fabrication process for the fabrication of $BiVO_4$-$CoCe(OH)_x$. Bare $Co(OH)_x$, $Ce(OH)_x$ and $CoCe(OH)_x$ were deposited over carbon paper following the above procedure without $BiVO_4$ photoanode with an extended reaction time of 12 h.

Part of this chapter has been published in **ACS Appl. Energy Mater. 2020, 3, 5610**

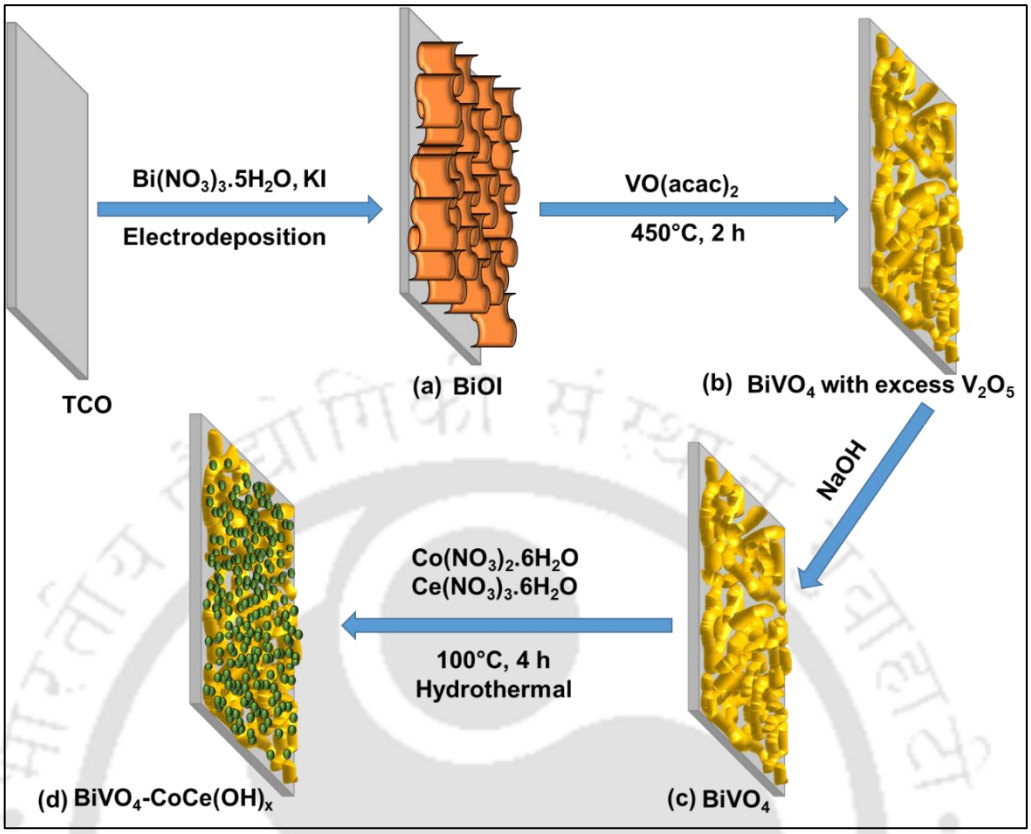

Scheme 6.2.1. Schematic representation for step-wise fabrication of $BiVO_4$-$CoCe(OH)_x$, (a) electrodeposition of BiOI over FTO, (b) drop-casting of vanadium precursor over BiOI film and subsequent annealing, (c) removal of excess V_2O_5 formed over $BiVO_4$ and (d) surface deposition of $CoCe(OH)_x$ by hydrothermal method.

6.3 RESULTS AND DISCUSSION

6.3.1 Powder x-ray diffraction (XRD) analysis

The crystalline phase of all the materials were confirmed by XRD analysis. Thin-film XRD of $BiVO_4$, $BiVO_4$-$CoCe(OH)_x$ and $CoCe(OH)_x$ are shown in **Figure 6.3.1**. All the peaks of $BiVO_4$ correspond to the monoclinic phase (JCPDS No- 14-0688).[25] The XRD of $CoCe(OH)_x$ can be indexed to cobalt hydroxide carbonate (#=JCPDS No. 48-0083) and cerium hydroxide carbonate (*=JCPDS No. 41-0013), which confirms that it is in mixed phase. The diffraction peaks of bare $BiVO_4$ and modified $BiVO_4$ are identical as the amount of $CoCe(OH)_x$ in the composite is low and has low crystallinity compared to $BiVO_4$ to be detected by XRD.

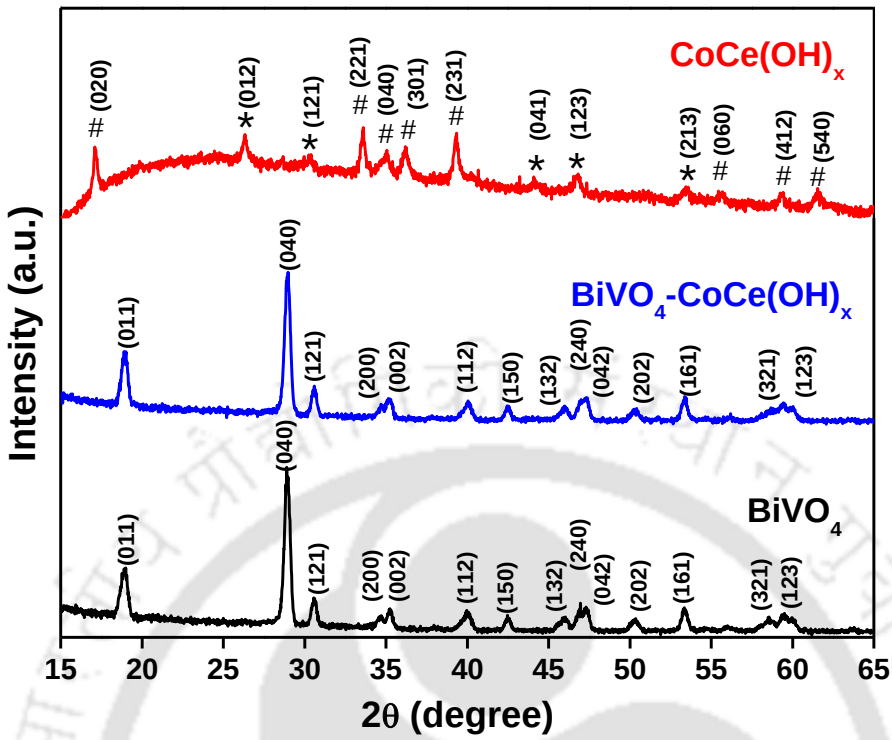

Figure 6.3.1. Thin film XRD of $BiVO_4$, $CoCe(OH)_x$ modified $BiVO_4$ and $CoCe(OH)_x$. XRD of both photoanodes are identical as the amount of $CoCe(OH)_x$ in the composite was less to be detected by XRD.

6.3.2 UV−visible absorption spectra analysis

The optical properties of the photoanodes were analyzed through UV−Visible absorption spectra. Similar optical absorption behaviour was observed for $BiVO_4$ and $BiVO_4$-$CoCe(OH)_x$ films as shown in **Figure 6.3.2(a)**. An absorption edge of around 510 nm was observed for both films, which corresponds with the typical band gap of $BiVO_4$. Optical curves and band gaps estimated from Tauc analysis (**Figure 6.3.2(b)**) for bare, and modified $BiVO_4$ photoanodes, shows that co-catalyst modification does not influence the absorption edge of $BiVO_4$ as well as band gaps.

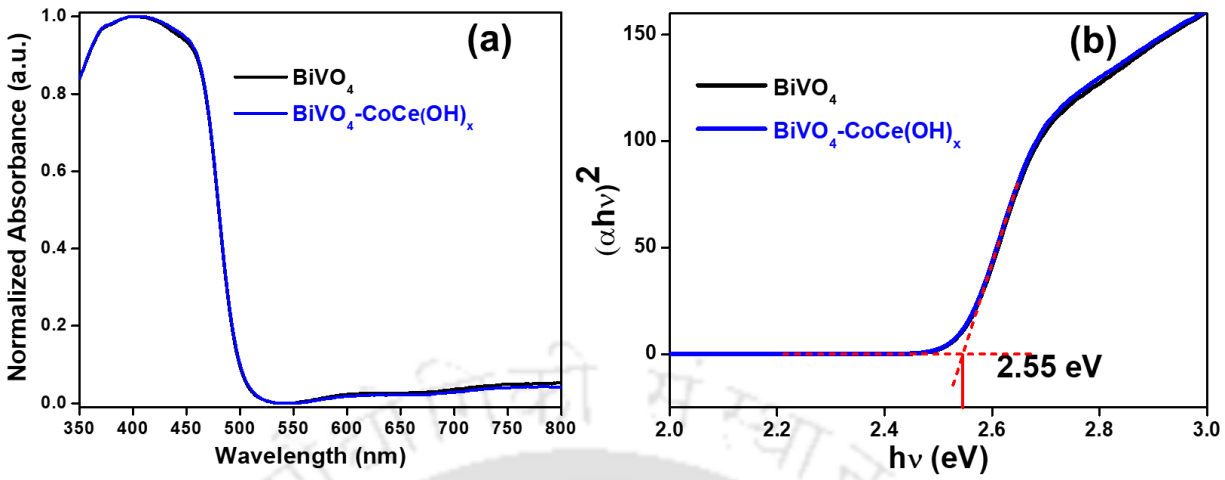

Figure 6.3.2. (a) UV-visible absorption spectra and the corresponding (b) Tauc's plots of $BiVO_4$ and $BiVO_4$-$CoCe(OH)_x$.

6.3.3 Materials morphology

The morphology of $BiVO_4$ and $CoCe(OH)_x$ modified $BiVO_4$ fabricated over the FTO substrate with top and cross-sectional views were investigated by FESEM analysis. **Figure 6.3.3(a)** shows the top view FESEM image with worm-like shaped three-dimensional $BiVO_4$ fabricated by electrodeposition and subsequent annealing. Subsequently, the $CoCe(OH)_x$ nanoparticles were deposited over a $BiVO_4$ photoanode through solvothermal synthesis as shown in **Figure 6.3.3(b)**. The cross-sectional FESEM of $BiVO_4$ shown in **Figure 6.3.3(c)** possesses voids between the particles, which is beneficial for easy access of electrolyte throughout the $BiVO_4$ films. The cross-sectional view FESEM image of $BiVO_4$- $CoCe(OH)_x$ as shown in **Figure 6.3.3(d)** also confirms the growth of $CoCe(OH)_x$ over $BiVO_4$. The cross-sectional FESEM images of both photoanodes confirms that they have a similar thickness of ~600 nm.

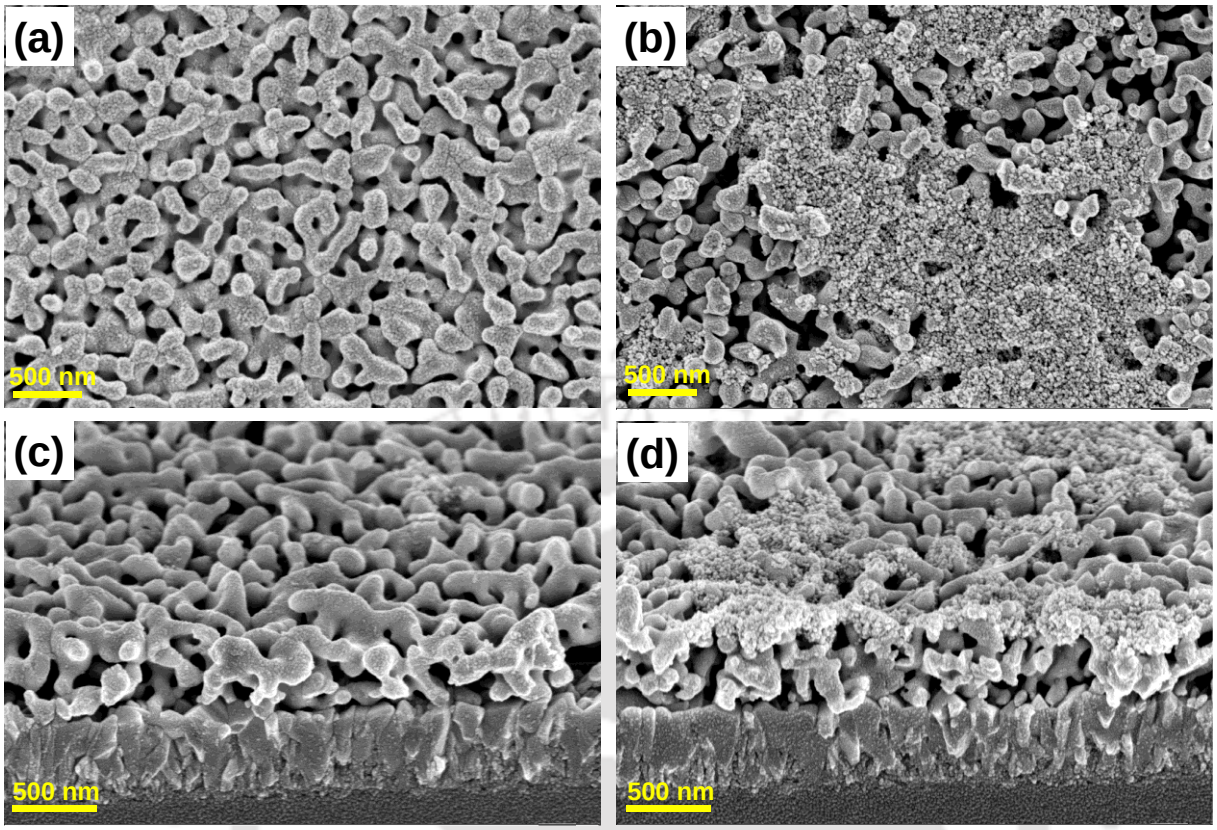

Figure 6.3.3. FESEM images with top and cross-sectional view of (a, c) $BiVO_4$ and (b, d) $BiVO_4$- $CoCe(OH)_x$ with worm-like shaped three-dimensional structure.

The structure and crystalline quality of the photoanodes were characterized by FETEM analysis. The FETEM image of bare $BiVO_4$ (**Figure 6.3.4(a)**) shows that it consists of irregular nanoparticles of 100~200 nm and stacked up with each other. From the HRTEM image (**Figure 6.3.4(b)**), the defined lattice spacing of 0.48 nm corresponds to the (011) planes of monoclinic $BiVO_4$. The FETEM image of $BiVO_4$- $CoCe(OH)_x$ (**Figure 6.3.4(c)**) shows that smaller sized $CoCe(OH)_x$ nanoparticles are attached on the surface of larger size $BiVO_4$ particles. The HRTEM image (**Figure 6.3.4(d)**) of the composite shows a lattice spacing of 0.48 nm corresponds to (011) plane of $BiVO_4$, a d-spacing of 0.34 nm corresponds to (220) plane of $Co(OH)_x$ and a d-spacing of 0.33 nm corresponds to (012) plane of $Ce(OH)_x$. Two distinct d-spacing for $CoCe(OH)_x$ further support the result obtained from XRD analysis.

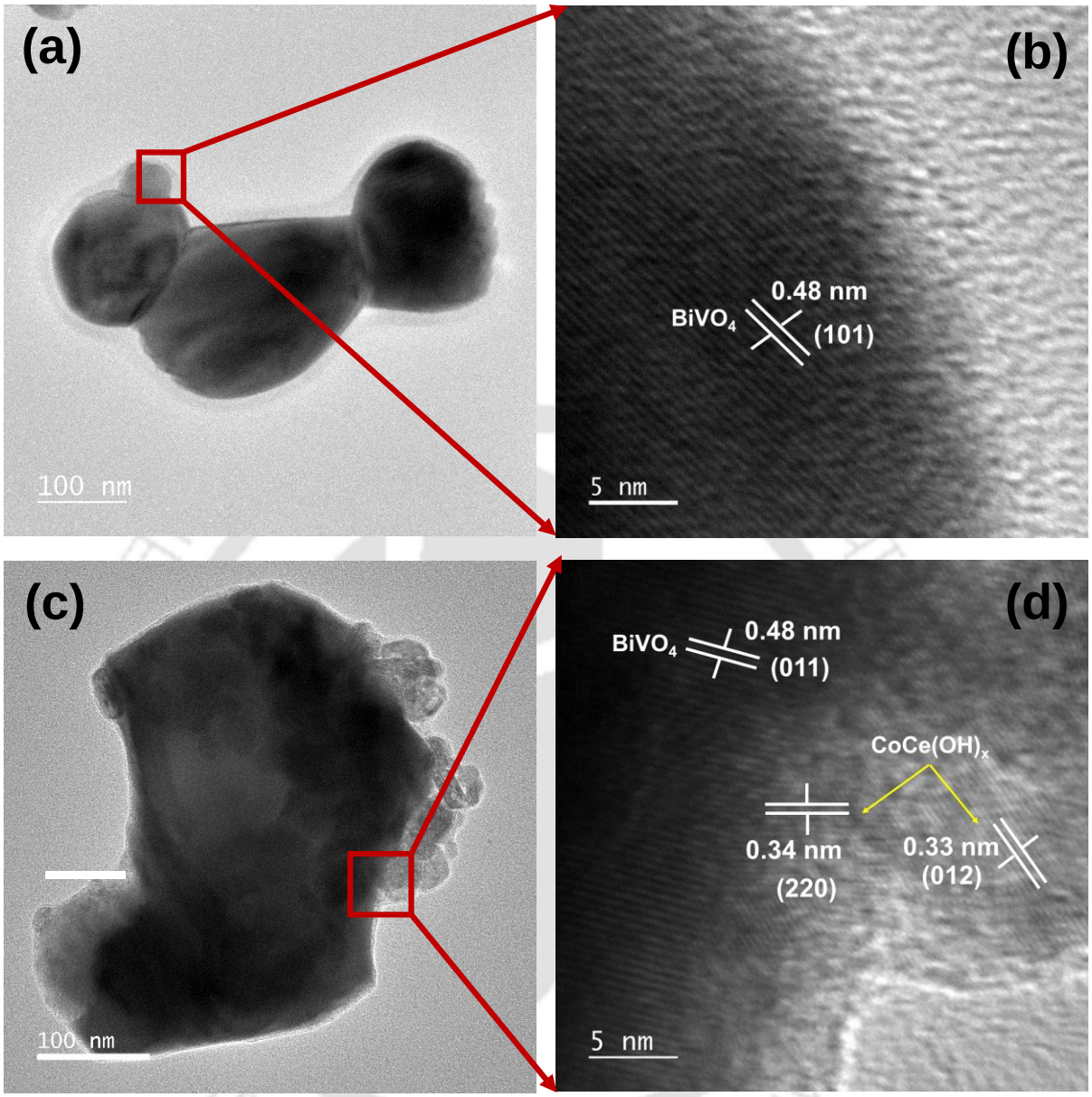

Figure 6.3.4. (a) FETEM image and (b) HRTEM image of bare $BiVO_4$, (c) FETEM image and (d) HRTEM image of $BiVO_4$- $CoCe(OH)_x$.

The STEM-EDS elemental mapping of $BiVO_4$- $CoCe(OH)_x$ shown in **Figure 6.3.5(a)-(f)** reveals that $CoCe(OH)_x$ nanoparticles were deposited over the surface of $BiVO_4$.

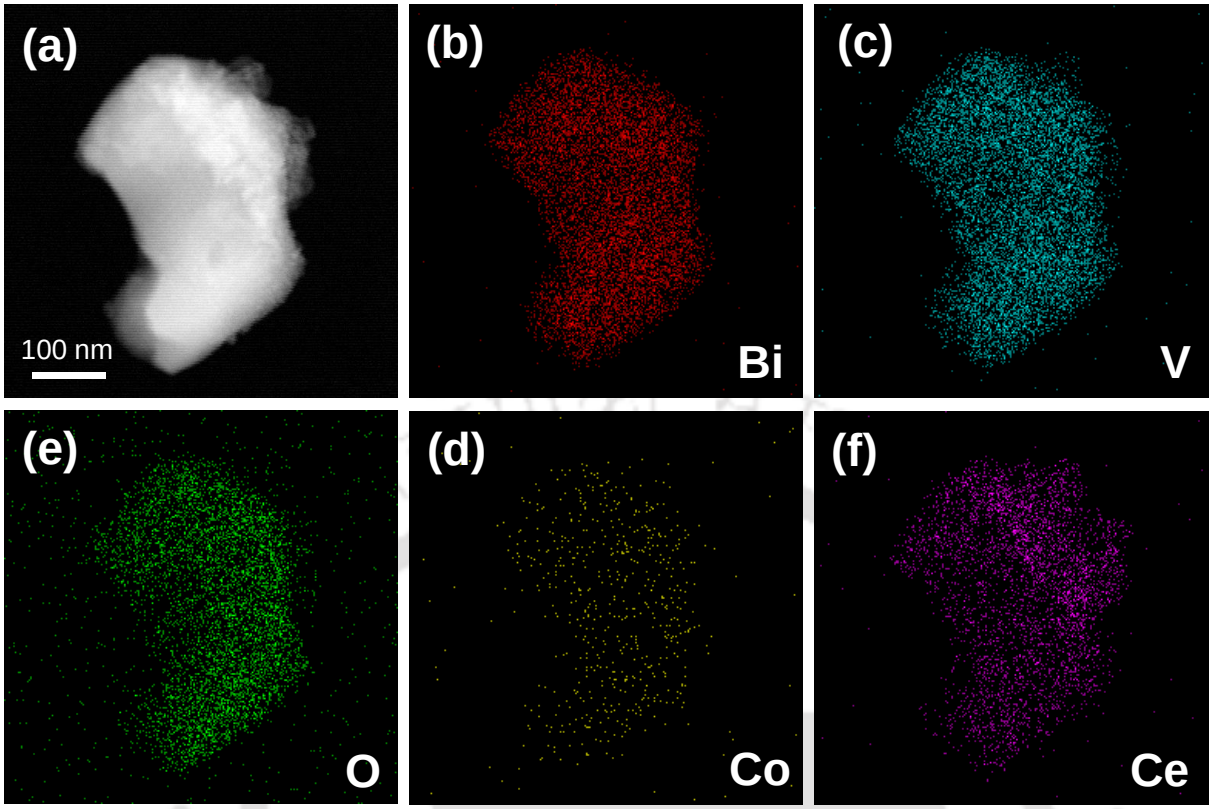

Figure 6.3.5 (a) STEM image and corresponding EDS mapping images of $BiVO_4$- $CoCe(OH)_x$ containing (b) Bi, (c) V, (d) O, (e) Co and (f) Ce.

6.3.4 X-ray photoelectron spectroscopy (XPS) analysis

To determine the surface chemical states of $BiVO_4$ and $BiVO_4$- $CoCe(OH)_x$, X-ray photoelectron spectroscopy (XPS) of the samples were analysed and the results are represented in **Figure 6.3.6**. From the survey spectra (**Figure 6.3.6(a)**), the characteristic peaks of Bi, V, and O was confirmed for bare $BiVO_4$ and composite photoanode exhibiting Bi, V, O, Co and Ce peaks. With reference to a C 1s value of 284.7 eV, the binding energies of obtained analyses in XPS were rectified. The high-resolution XPS spectra of Bi (**Figure 6.3.6(b)**) shows two symmetric peaks at 158.7 eV and 164.1 eV which can be attributed to the Bi $4f_{7/2}$ and Bi $4f_{5/2}$, respectively, indicating the presence of Bi^{3+} in $BiVO_4$.[26] The two peaks in the V 2p spectra (**Figure 6.3.6(c)**) shows binding energy at 516.3 eV and 523.7 eV which could be assigned to the V $2p_{3/2}$ and V $2p_{1/2}$, respectively, proving vanadium is present as V^{5+}.[26] The O 1s XPS spectra (**Figure 6.3.6(d)**) could be fitted into two signals at 529.5 eV and 531.8 eV assign to lattice oxygen (O_L) and the hydroxide hydrated and oxygen vacancy (O_V) species, respectively.[27] Due to presence of hydroxide hydrated (OH) and

oxygen vacancy (O_V) peaks in same position, it is difficult to comment on the exact amount of vacancy in the composite photoanode. The XPS spectra of Bi, V, and O in $BiVO_4$- $CoCe(OH)_x$ shows significant changes from those of $BiVO_4$, with a shift toward higher binding energies in Bi 4f, V 2p, and O 1s peaks in the composite sample. The shift in XPS for the composite as compared to bare $BiVO_4$ suggests that there is a change in electronic environment around $BiVO_4$ with incorporation of $CoCe(OH)_x$ confirming a strong interaction between $BiVO_4$ and $CoCe(OH)_x$.[27]

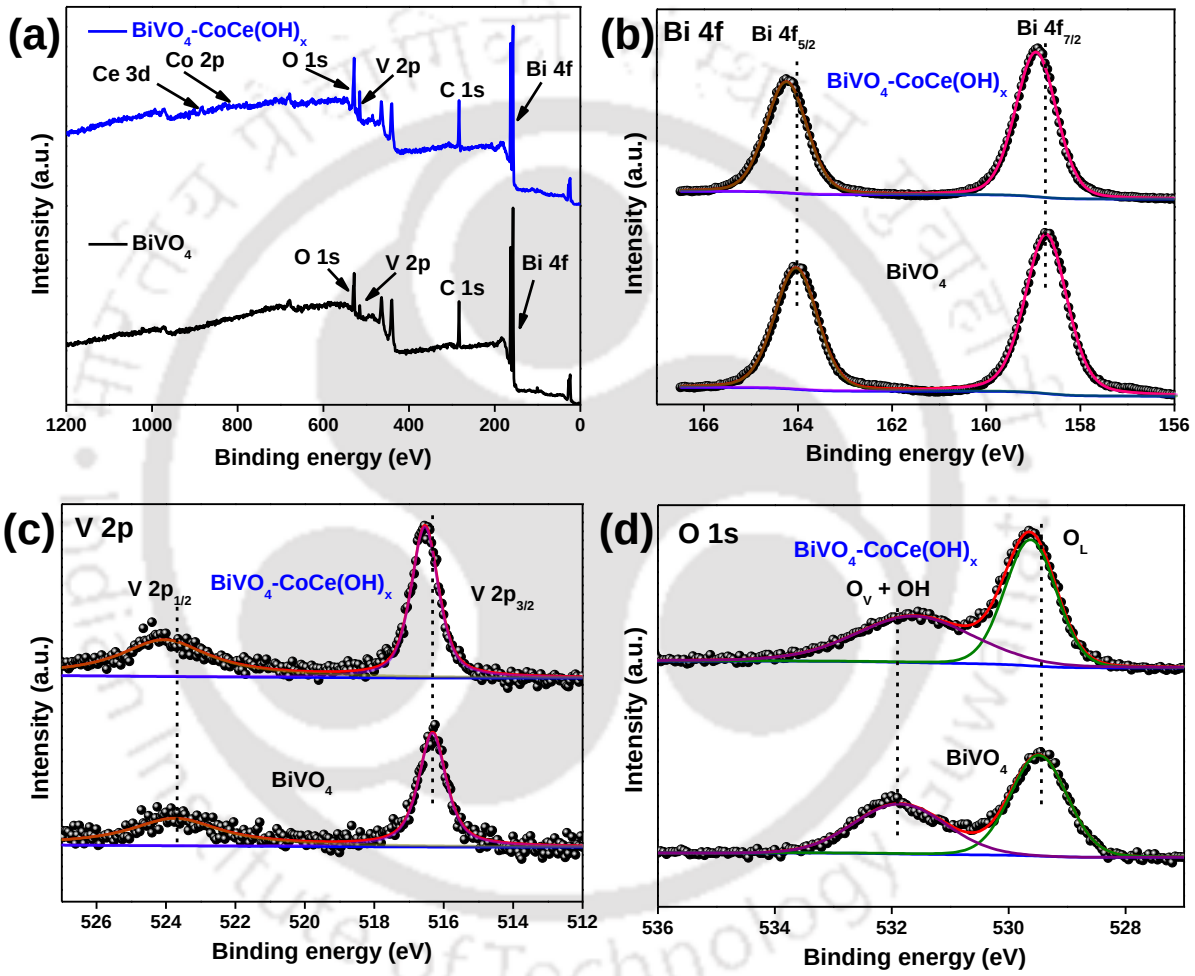

Figure 6.3.6. XPS spectra of $BiVO_4$ and $BiVO_4$- $CoCe(OH)_x$ samples for (a) survey spectrum, (b) Bi 4f, (c) V 2p and (d) O 1s.

Compared to the bare $BiVO_4$, two extra peaks observed for $BiVO_4$-$CoCe(OH)_x$, which are attributed to cobalt and cerium. The valencies of Co species in the composite are investigated by de-convoluting Co 2p core-level spectra. Two peaks at 780.8 and 796.8 eV are assigned to Co^{2+}

Part of this chapter has been published in **ACS Appl. Energy Mater. 2020, 3, 5610**

which indicates the existence of Co^{2+} species in the composite (**Figure 6.3.7(a)**).[28] The Ce 3d core-level XPS shows that the two sets of peaks correspond to +3 state of cerium (**Figure 6.3.7(b)**).[29]

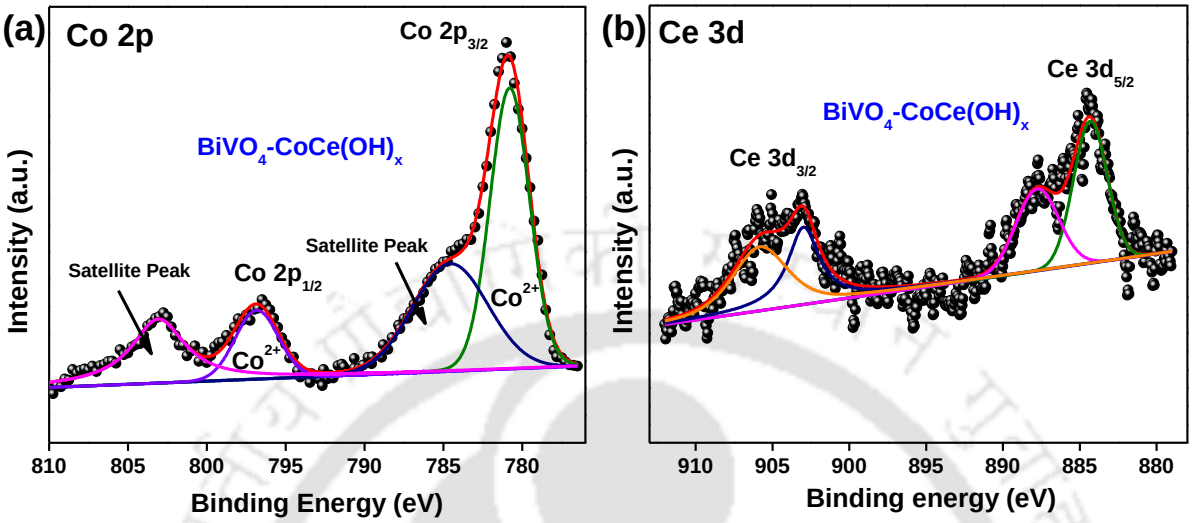

Figure 6.3.7 XPS core-level spectra of (a) Co 2p and (b) Ce 3d for $BiVO_4$-$CoCe(OH)_x$.

6.3.5 Photoelectrochemical measurements of the photoanodes

The effect of $CoCe(OH)_x$ co-catalyst decoration on the PEC water oxidation activity of $BiVO_4$ photoanode was studied by linear sweep voltammetry (LSV) in 0.5 M potassium borate electrolyte under light illumination. As shown in **Figure 6.3.8(a)**, bare $BiVO_4$ photoanode shows a photocurrent onset at 0.57 V vs. RHE which reaches up to 1.38 mA/cm^2 at 1.23 V vs. RHE. Further modification with $CoCe(OH)_x$ co-catalyst containing different ratios of cobalt to cerium (**Figure 6.3.8(b)**), $Co_{0.75}Ce_{0.25}(OH)_x$ was found to be more effective with a significant negative shift of photocurrent onset of ~370 mV where the photocurrent density reaches up to 3.74 mA/cm^2 at 1.23 V vs. RHE. As cerium is catalytically silent, excess amount of cerium in mixed metal hydroxide may leads to blockage of active sites. Notably, with $CoCe(OH)_x$ decoration over $BiVO_4$, a three-fold enhancement in photocurrent density has been achieved. The reproducibility of the co-catalyst modification was checked with 5 different samples and found to be similar in all cases as shown in **Figure 6.3.8(c)**. The photocurrent density of $BiVO_4$- $CoCe(OH)_x$ was found to be superior compared to bare $BiVO_4$ in the whole bias range, indicating the potential of $CoCe(OH)_x$ for better charge injection and faster water oxidation kinetics. For comparison, $Co(OH)_x$ and $Ce(OH)_x$ decorated samples have also been studied under the same conditions. $BiVO_4$-$Co(OH)_x$ shows a better photocurrent onset as compared to $BiVO_4$ with improvement in photocurrent

density up to 2.4 mA/cm^2 at 1.23 V vs. RHE. In the case of $Ce(OH)_x$ modified $BiVO_4$ photoanodes, the photocurrent was similar to bare $BiVO_4$ with a ~150 mV cathodic shift in onset potential. All the optimized photocurrent density of bare and modified $BiVO_4$ photoanodes are shown in **Figure 6.3.8(a)**. A substantial onset potential shift of ~370 mV with $Co(OH)_x$ and $CoCe(OH)_x$ modified $BiVO_4$ suggests that cobalt is the only active component for water oxidation at the photoanode surface, whereas cerium is catalytically silent. The result suggests that $Ce(OH)_x$ doesn't have any active catalytic sites for PEC water oxidation and a slight shift in the onset potential is only due to weak passivation of the surface states.[30,31] The reproducibility is confirmed by taking 4 different samples with $Ce(OH)_x$ modification which shows similar trends for all as shown in **Figure 6.3.8(d)**. These results suggest that cobalt is the main active catalytic site for water oxidation in $CoCe(OH)_x$.

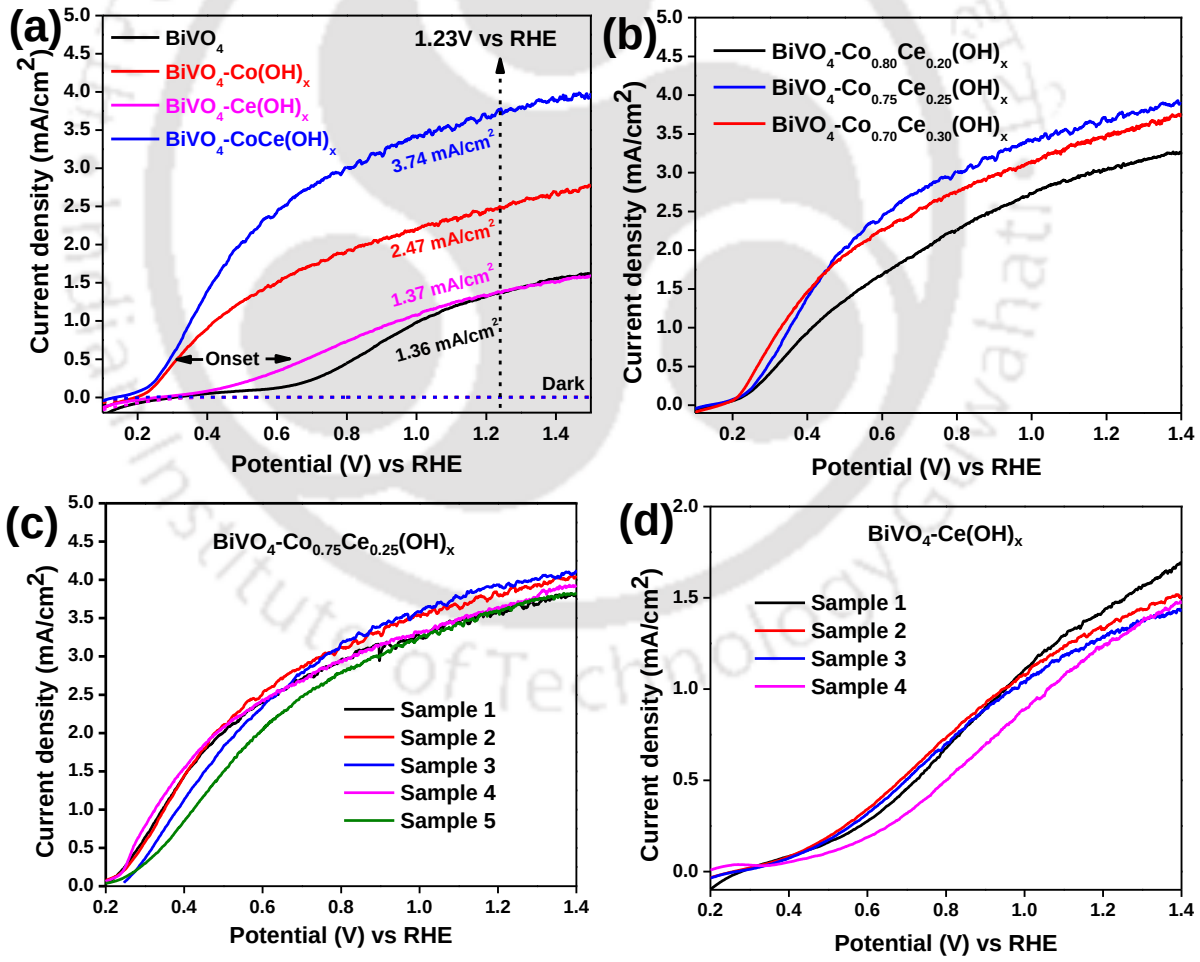

Figure 6.3.8. (a) J-V curves of $BiVO_4$ and optimized $BiVO_4$-$Co(OH)_x$, $BiVO_4$-$Ce(OH)_x$ and $BiVO_4$-$CoCe(OH)_x$ photoanodes; (b) J-V curves of $BiVO_4$-$Co_xCe_y(OH)_x$ with different ratios of cobalt to cerium; photoanode with 5

different films, (c) J-V curves of optimized $BiVO_4$-$CoCe(OH)_x$ photoanode with 5 different films and (d) J-V curves of $BiVO_4$-$Ce(OH)_x$ photoanode with 4 different films.

The LSV of $Co(OH)_x$, $CoCe(OH)_x$ and $Ce(OH)_x$ in dark condition (**Figure 6.3.8**) confirmed that cerium has role in improving the electrocatalytic activity of $Co(OH)_x$ and hence, $CoCe(OH)_x$ coupling has a function of modifying the OER kinetics of $BiVO_4$ photoanode.

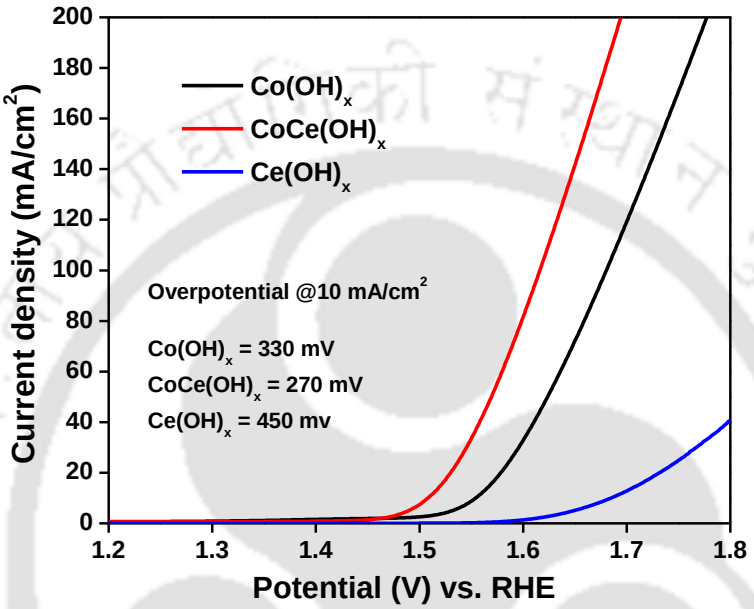

Figure 6.3.9 J-V curves of Co(OH)x, CoCe(OH)x and Ce(OH)x electrocatalysts in dark condition.

Figure 6.3.10(a) shows the chronoamperometry of bare $BiVO_4$, $BiVO_4$-$Ce(OH)_x$, $BiVO_4$-$Co(OH)_x$ and $BiVO_4$-$CoCe(OH)_x$ photoanodes at 1.23 V vs. RHE. There was a significant decrease in anodic spikes with co-catalyst modification, indicates that charge recombination is suppressed with $CoCe(OH)_x$ incorporation.[7] Although the photocurrent density of $BiVO_4$ and $BiVO_4$-$Ce(OH)_x$ is comparable, the ON-OFF response shows that $BiVO_4$-$Ce(OH)_x$ is more stable than bare $BiVO_4$. Comparable photocurrent in different pH concludes the versatility of co-catalyst which can be applicable to different photoanodes as shown in **Figure 6.3.10(b)**. Furthermore, the photoelectric conversion capabilities were evaluated by applied bias photon-to-current efficiency (ABPE) and incident photon-to-current conversion efficiency (IPCE) analyses. As calculated from the LSV curves in **Figure 6.3.7(a)**, the maximum ABPE of 1.55% at 0.57 V vs. RHE was obtained using the $BiVO_4$-$CoCe(OH)_x$ photoanode, which is much higher than that of $BiVO_4$ (0.2% at 0.97 V vs. RHE) under the same conditions as shown in **Figure 6.3.10(c)**. Although there is not much

difference in performance of $BiVO_4$ and $BiVO_4$-$Ce(OH)_x$, latter has comparatively higher ABPE as compared to bare $BiVO_4$ in the whole range. The IPCE value for $BiVO_4$- $CoCe(OH)_x$ photoanode (**Figure 6.3.10(d)**) is found to be around 64%, while only 28% have been obtained for pristine $BiVO_4$. These results demonstrated that incorporation of $CoCe(OH)_x$ on to $BiVO_4$ photoanode could effectively improve its PEC performance.

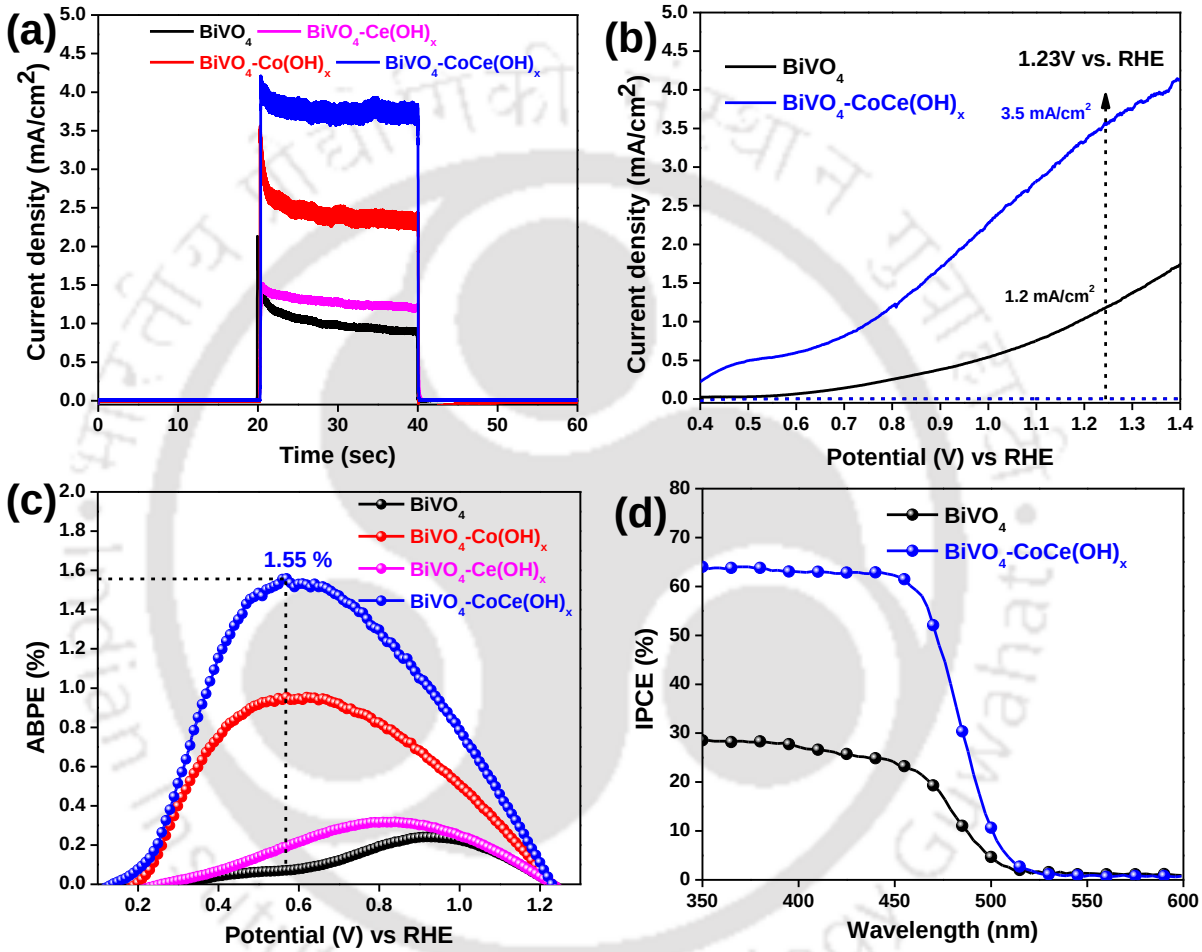

Figure 6.3.10. (a) J-t curves of bare and modified $BiVO_4$ photoanodes with KBi electrolyte (pH 11) under dark and light illumination, (b) J-V curves of bare $BiVO_4$ and $BiVO_4$- $CoCe(OH)_x$ photoanodes with Na_2SO_4 electrolyte (pH~7) at 1.23 V vs. RHE, (c) Applied bias photon-to-current efficiency (ABPE) and (d) incident photon-to-current conversion efficiency (IPCE) collected at 1.23 V vs. RHE.

6.3.6 Electrochemical impedance spectroscopy (EIS) analysis

The influence of $CoCe(OH)_x$ modification on the charge transfer process and water oxidation kinetics at the interface of photoanode/electrolyte were analyzed through electrochemical impedance spectroscopy (EIS) plots measured at 1.23 V vs. RHE. The Nyquist

Part of this chapter has been published in **ACS Appl. Energy Mater. 2020, 3, 5610**

plots of all the photoanodes are shown in **Figure 6.3.11(a)**, where the measured data are shown in dots and the fitted results provided by the equivalent circuit are shown as solid lines. In the Nyquist plots for all photoanodes, only one semicircle arc was observed related to charge transfer kinetics at the photoanode/electrolyte interface. The semicircle related to $BiVO_4$-$CoCe(OH)_x$ is much smaller than bare $BiVO_4$, $BiVO_4$-$Ce(OH)_x$ and $BiVO_4$-$Co(OH)_x$ implicating a faster charger transfer in case of $CoCe(OH)_x$ modification. The Nyquist plots were fitted through the equivalent circuit as shown in inset to **Figure 6.3.11(a)**, where R_s represents the sheet resistance, R_{ct} is the resistance related to charge transfer kinetics at the photoanode/electrolyte interface and CPE is the constant phase elements for photoanode/electrolyte interface.[13] All the fitting parameters obtained from the equivalent circuit are present in **Table 6.3.1**. The R_{ct} value obtained for $BiVO_4$-$CoCe(OH)_x$ is 560 Ω, which is much smaller than bare $BiVO_4$ (1788 Ω), $BiVO_4$-$Ce(OH)_x$ (1722 Ω) and $BiVO_4$-$Co(OH)_x$ (928 Ω) due to faster charge transfer process in case of $BiVO_4$-$CoCe(OH)_x$.[32] Slightly lower R_{ct} value for $BiVO_4$-$Ce(OH)_x$ as compared to $BiVO_4$ suggests that charge transfer at the interface is improved with $Ce(OH)_x$ modification due to proposed passivation of surface states.[30] Increase in CPE value with deposition of $CoCe(OH)_x$ can be attributed to the efficient transfer of holes from $BiVO_4$ to $CoCe(OH)_x$.[33] To know the effect of co-catalyst modification on charge carrier density (N_D), Mott-Schottky (M-S) analysis was performed in dark as shown in **Figure 6.3.11(b)**. The carrier densities of the photoanodes did not change appreciably with co-catalyst modification as it doesn't affect the electronic structure of the photoanode.

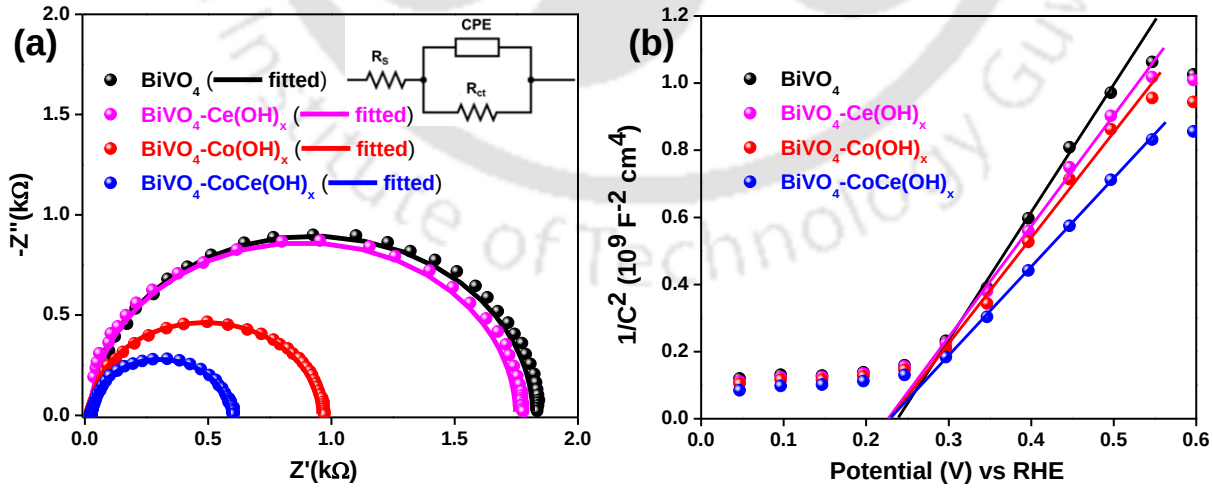

Figure 6.3.11. (a) Nyquist plots under light illumination, (b) Mott–Schottky plots under dark for bare $BiVO_4$, $BiVO_4$-$Ce(OH)_x$, $BiVO_4$-$Co(OH)_x$ and $BiVO_4$-$CoCe(OH)_x$ photoanodes.

Table 6.3.1. Fitted results of Nyquist plot from the equivalent circuit.

Photoanode	R_s (Ω)	R_{ct} (Ω)	CPE (μF)	N_D (cm^{-3})
$BiVO_4$	27.6	1788	6.5	6.9×10^{19}
$BiVO_4$-Ce$(OH)_x$	24.6	1722	6.6	7.5×10^{19}
$BiVO_4$-Co$(OH)_x$	23.3	928	11.5	7.8×10^{19}
$BiVO_4$-CoCe$(OH)_x$	20.8	560	14.4	9.8×10^{19}

6.3.7 Charge separation and injection efficiency analysis

To estimate the contribution of CoCe$(OH)_x$, charge separation efficiency (η_{sep}) and charge injection efficiency (η_{inj}) of the photoanodes were measured by adding a kinetically competitive hole scavenger, Na_2SO_3 to the electrolyte. It is known that Na_2SO_3 water oxidation kinetics are much faster and can be approximated to 100% compared to the general semiconductor water oxidation kinetics. The charge separation efficiency (η_{sep}) was calculated using the following equation:

$$\eta_{\text{sep}} = \frac{J_{sulphite}}{J_{\text{abs}}} \quad (1)$$

where J_{abs} was the theoretical current density assuming the complete conversion of the absorbed irradiation.[27] The surface charge injection efficiency (η_{inj}) was calculated using the equation:

$$\eta_{\text{inj}} = \frac{J_{H_2O}}{J_{\text{sulphite}}} \quad (2)$$

where (J_{H_2O}) was the current density acquired in the 0.5 M KBi without Na_2SO_3, $(J_{sulphite})$ was the current density acquired in the presence of 0.2 M Na_2SO_3 in 0.5 M KBi. The LSV curves with and without hole scavenger are shown in **Figure 6.3.12(a)**, where $BiVO_4$-CoCe$(OH)_x$ shows higher photocurrent as compared to bare $BiVO_4$, $BiVO_4$-Ce$(OH)_x$ and $BiVO_4$-Co$(OH)_x$. As an efficient hole scavenger, sulphite can be oxidized on photoanode with favourable kinetics, and thus, the interfacial hole-transfer kinetics on photoanode is normally negligible. The η_{sep} increases from 53% ($BiVO_4$) to 60% ($BiVO_4$-Co$(OH)_x$) and 67% ($BiVO_4$-CoCe$(OH)_x$) with co-catalyst

modification as shown in **Figure 6.3.12(b)**. The η_{sep} remains same with $Ce(OH)_x$ modification pointing out that cerium is effective in promoting charge transfer on the surface only. There is an increment in η_{inj} of $BiVO_4$ with $Co(OH)_x$ and $CoCe(OH)_x$ modification where as an insignificant increment can be observed with $Ce(OH)_x$ modification attributed to partial passivation of surface states promoting charge transfer at the photoanode/electrolyte interface **(Figure 6.3.12(c))**. This increment in η_{inj} suggest that charge transport at the photoanode/electrolyte interface was improved and the recombination process was suppressed by co-catalyst modification. A consistently good η_{sep} value for $BiVO_4$ as compared to its η_{inj} value suggests that PEC performance of $BiVO_4$ is hindered due to its poor hole diffusion on the surface.[27] Thus significant improvements in charge injection efficiency with co-catalyst is the main factor for efficient PEC efficacy of the photoanode.

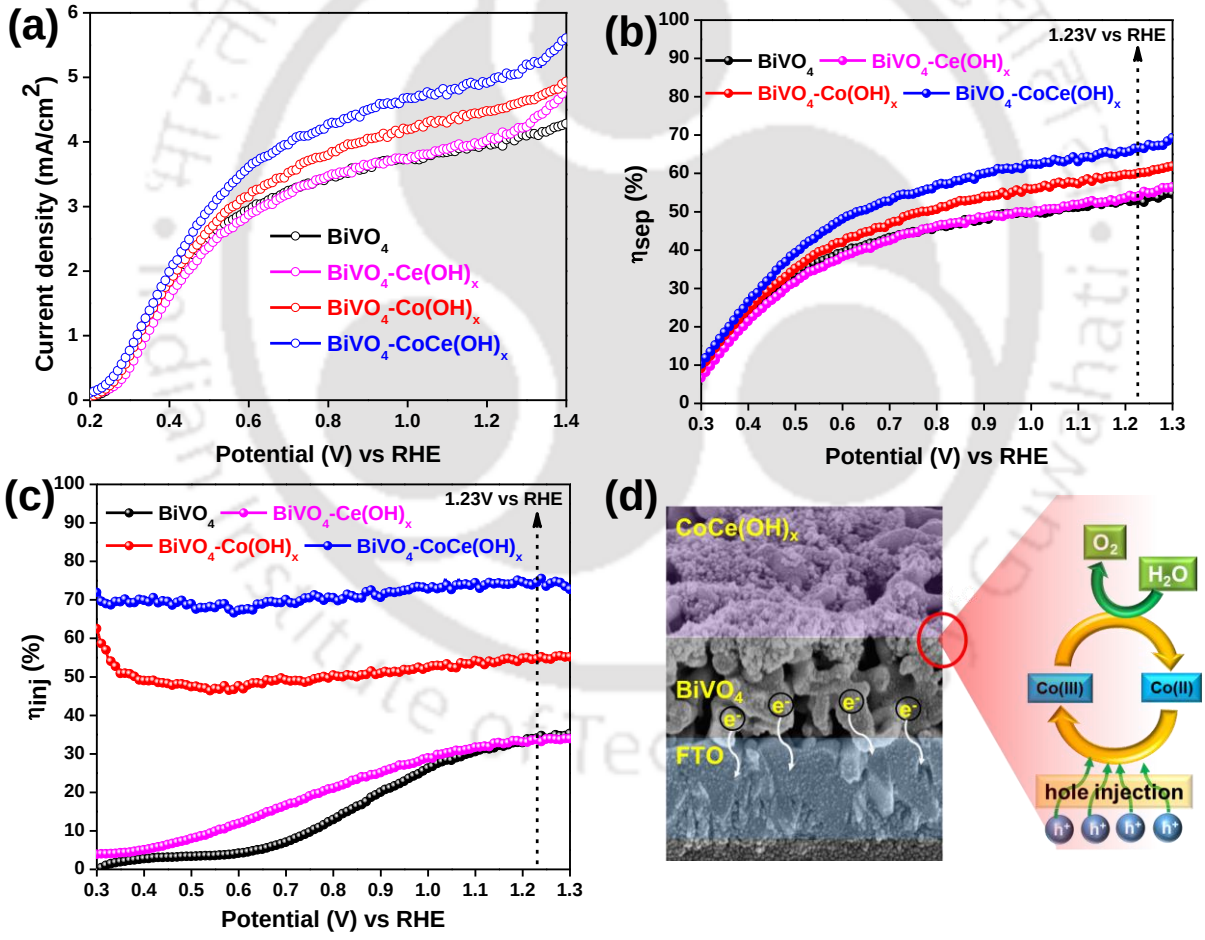

Figure 6.3.12. (a) J-V curves of the photoanodes with addition of hole scavenger Na_2SO_3 in potassium borate electrolyte; (b) Charge separation efficiencies and (c) charge injection efficiencies of bare $BiVO_4$ and $BiVO_4$-$CoCe(OH)_x$ photoanodes; (d) Schematic representation of probable mechanism for faster water oxidation kinetics.

Figure 6.3.12(d) shows the schematic of probable mechanism involves in $BiVO_4$-$CoCe(OH)_x$. The accelerated water oxidation kinetics of $BiVO_4$-$CoCe(OH)_x$ photoanode can be ascribed to the formation of Co^{3+}-active sites on $CoCe(OH)_x$ through holes-oxidizing, which could synergistically oxidize H_2O to molecular O_2 with stable activity and restrain the $BiVO_4$ anodic photocorrosion accordingly. To further confirm the active redox species involved in $CoCe(OH)_x$ in water oxidation, cyclic voltammetry (CV) measurements of co-catalyst and the photoanodes, were analyzed. The CV of Co $(OH)_x$ and $CoCe(OH)_x$ shows oxidation-reduction peaks corresponds to Co(II)/Co(III) as shown in **Figure 6.3.13(a)**. As shown in **Figure 6.3.13(b)**, the CV of $BiVO_4$ and $BiVO_4$-$Ce(OH)_x$ are similar without any oxidation-reduction peaks corresponding cerium shows that the standard redox potential could be beyond the decomposition of water and does not contribute in the present case.[34] The CV of $BiVO_4$-$Co(OH)_x$ and $BiVO_4$-$CoCe(OH)_x$ are similar which shows only oxidation-reduction peaks correspond to Co(II)/Co(III). The results from CV confirms that cobalt is the only active site in the mixed hydroxide.[28]

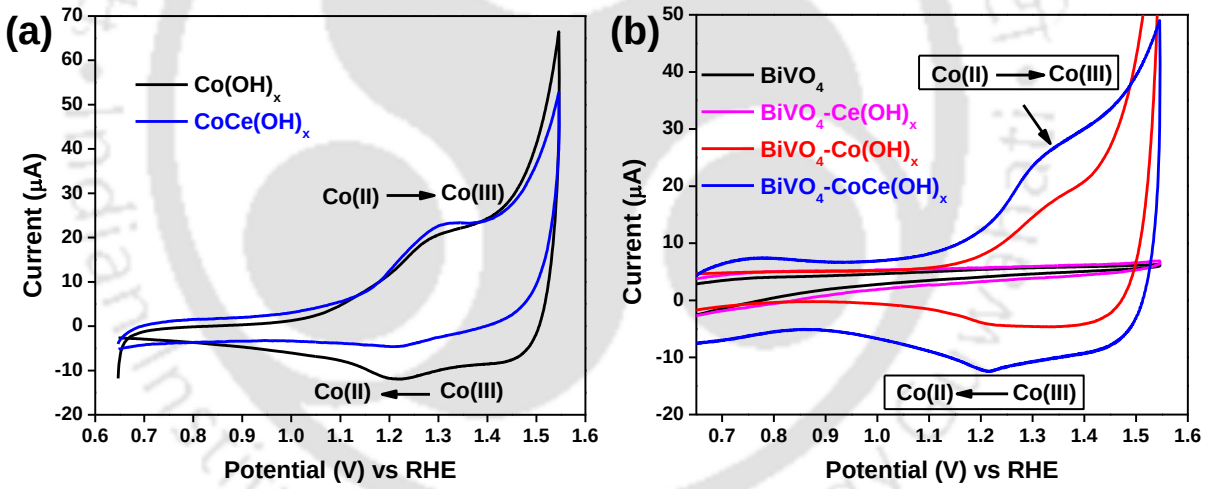

Figure 6.3.13. (a) Cyclic voltammetry measurement of $Co(OH)_x$ and $CoCe(OH)_x$ and (b) Cyclic voltammetry measurement of all the photoanodes before illumination.

6.3.8 Stability and faradaic yield measurements

The operational stability of the photoanodes were examined from the amperometric J-t plots. As shown in **Figure 6.3.14(a)**, after 90 min of continuous illumination $BiVO_4$-$CoCe(OH)_x$ photoanode retain ~98% of initial photocurrent while $BiVO_4$-$Co(OH)_x$ retains 90% of the initial photocurrent and bare $BiVO_4$ retains 82% of the initial photocurrent. Surprisingly $BiVO_4$-$Ce(OH)_x$ retains 99% of the initial photocurrent, which confirms that the stability of $BiVO_4$-$CoCe(OH)_x$

increases mainly due to the presence of cerium hydroxide.[35] These results show that cerium is acting as an excellent overlayer material for enhancing the photostability of $BiVO_4$. The amount of hydrogen and oxygen generated by the $BiVO_4$-$CoCe(OH)_x$ photoanode during PEC water oxidation was measured by gas chromatography. As shown in **Figure 6.3.14(b)**, an average Faradaic yield of 94% was obtained for both hydrogen and oxygen, confirms that the majority of the photogenerated charges are used for the oxidation of water to produce oxygen.

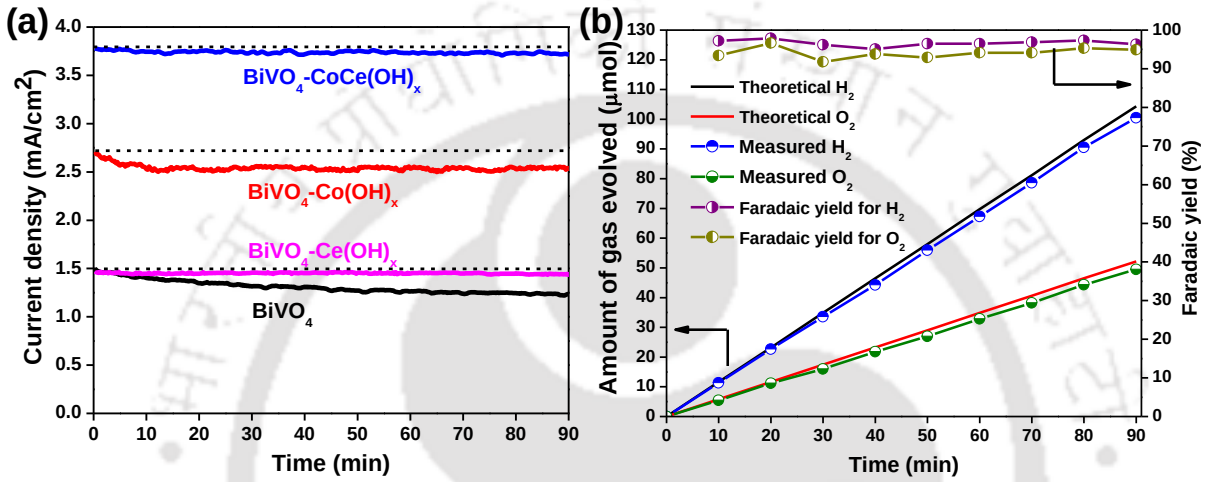

Figure 6.3.14. (a) Operational stability of all the photoanodes at 1.23V vs. RHE under continuous light illumination and (b) Faradic yield test of $BiVO_4$-$CoCe(OH)_x$ for hydrogen and oxygen evolution.

6.4 CONCLUSIONS

In summary, we have demonstrated a facile method for the incorporation of cerium based hydroxide to cobalt-based co-catalyst which enhances the PEC performance and stability of $BiVO_4$ photoanode towards solar water oxidation. The enhanced water oxidation performance of $BiVO_4$-$CoCe(OH)_x$ attributed to the synergistic effect of both cobalt and cerium, where cerium incorporation enhanced the stability and electrocatalytic activity of $Co(OH)_x$ and formation of Co(II)/(III) active sites fasten the surface kinetics of $BiVO_4$. A photocurrent density of 3.74 mA/cm^2 at 1.23 V vs. RHE was obtained, which is three-fold higher as compared to bare $BiVO_4$. A cathodic shift in onset potential of ~370 mV for the composite having cobalt signifies efficient charge transfer and faster oxidation kinetics at the interface is only due to the presence of cobalt whose activity is enhanced by catalytically silent cerium in promoting the efficient PEC. The present method of modification with rare earth elements may be helpful for increasing the stability and performance of other co-catalyst materials.

6.5 REFERENCES

1. Y. Park, K. J. McDonald and K.-S. Choi, *Chem. Soc. Rev.*, 2013, **42**, 2321.
2. Y. He, T. Hamann and D. Wang, *Chem. Soc. Rev.*, 2019, **48**, 2182.
3. A. G. Tamirat, J. Rick, A. A. Dubale, W. N. Su and B. J. Hwang, *Nanoscale Horiz*, 2016, **1**, 243.
4. S. Kment, F. Riboni, S. Pausova, L. Wang, L. Wang, H. Han, Z. Hubicka, J. Krysa, P. Schmuki and R. Zboril, *Chem. Soc. Rev.*, 2017, **46**, 3716.
5. D. K. Lee, D. Lee, M. A. Lumley and K.-S. Choi, *Chem. Soc. Rev.*, 2019, **48**, 2126.
6. G. Wang, H. Wang, Y. Ling, Y. Tang, X. Yang, R. C. Fitzmorris, C. Wang, J. Z. Zhang and Y. Li, *Nano Lett.*, 2011, **11**, 3026.
7. T. K. Sahu, A. K. Shah, G. Gogoi, A. S. Patra, M. S. Ansari and M. Qureshi, *Chem. Commun.*, 2018, **54**, 10483.
8. J. H. Kim, Y. J. Jang, S. H. Choi, B. J. Lee, M. H. Lee and J. S. Lee, *ACS Sustainable Chem. Eng.*, 2019, **7**, 944.
9. I. D. Sharp, J. K. Cooper, F. M. Toma and R. Buonsanti, *ACS Energy Lett.*, 2017, **2**, 139.
10. S. K. Pilli, T. E. Furtak, L. D. Brown, T. G. Deutsch, J. A. Turner and A. M. Herring, *Energy Environ. Sci.*, 2011, **4**, 5028.
11. D. K. Zhong, S. Choi and D. R. Gamelin, *J. Am. Chem. Soc.*, 2011, **133**, 18370.
12. Y. Shi, Y. Yu, Y. Yu, Y. Huang, B. Zhao and B. Zhang, *ACS Energy Lett.*, 2018, **3**, 1648.
13. X. Chang, T. Wang, P. Zhang, J. Zhang, A. Li and J. Gong, *J. Am. Chem. Soc.*, 2015, **137**, 8356.
14. M. García-Tecedor, D. Cardenas-Morcoso, R. Fernández-Climent and S. Giménez, *Adv. Mater. Interfaces*, 2019, **6**, 1900299.
15. C. Zachäus, F. F. Abdi, L. M. Peter and R. van de Krol, *Chem. Sci.*, 2017, **8**, 3712.
16. M. Chhetri, S. Dey and C. N. R. Rao, *ACS Energy Lett.*, 2017, **2**, 1062.
17. H. Han, H. Choi, S. Mhin, Y.-R. Hong, K. M. Kim, J. Kwon, G. Ali, K. Y. Chung, M. Je, H. N. Umh, D.-H. Lim, K. Davey, S.-Z. Qiao, U. Paik and T. Song, *Energy Environ. Sci.*, 2019, **12**, 2443.
18. M. Gong, Y. Li, H. Wang, Y. Liang, J. Z. Wu, J. Zhou, J. Wang, T. Regier, F. Wei and H. Dai, *J. Am. Chem. Soc.*, 2013, **135**, 8452.

Part of this chapter has been published in **ACS Appl. Energy Mater. 2020, 3, 5610**

19. N. Danilovic, R. Subbaraman, K. Chang, S. H. Chang, Y. J. Kang, J. Snyder, A. P. Paulikas, D. Strmcnik, Y. Kim, D. Myers, V. R. Stamenkovic and N. M. Markovic, *J. Phys. Chem. Lett.*, 2014, **5**, 2474.
20. Y. Tang, R. Wang, Y. Yang, D. Yan and X. Xiang, *ACS Appl. Mater. Interfaces*, 2016, **8**, 19446.
21. R. R. Wang , L. Luo , X. L. Zhu , Y. Yan , B. Zhang , X. Xiang and J. He , *ACS Appl. Energy Mater.*, 2018, **8** , 3577.
22. Y. Zhu, J. Ren, X. Yang, G. Chang, Y. Bu, G. Wei, W. Han and D. Yang, *J. Mater. Chem. A*, 2017, **5**, 9952.
23. W. He, R. Wang, L. Zhang, J. Zhu, X. Xiang and F. Li, *J. Mater. Chem. A*, 2015, **3**, 17977.
24. J. W. Gu, Q. T. Huang, Y. F. Yuan, K. H. Ye, Z. L. Wang and W. J. Mai, *J. Mater. Chem. A*, 2017, **5**, 20195.
25. W. Zhang, R. Li, X. Zhao, Z. Chen, A. W.-K. Law and K. Zhou, *ChemSusChem*, 2018, **11**, 2710.
26. S. L. Bai, J. C. Liu, M. Cui and R. X. Luo, *Dalton Trans.* 2018, **47**, 6763–6771
27. T. Palaniselvam, L. Shi, G. Mettela, D. H. Anjum, R. Li, K. P. Katuri, P. E. Saikaly and P. Wang, *Adv. Mater. Interfaces*, 2017, **4**, 1700540.
28. J. D. Du, X. H. Zhong, H. C. He, J. Huang, M. J. Yang, G. L. Ke, J. Wang, Y. Zhou, F. Q. Dong, Q. Ren and L. Bian, *ACS Appl. Mater. Interfaces*, 2018, **10**, 42207.
29. Z. Jiang, Y. Liu, T. Jing, B. Huang, X. Zhang, X. Qin, Y. Dai and M.-H. Whangbo, *J. Phys. Chem. C*, 2016, **120**, 2058.
30. H. Lim, J. Y. Kim, E. J. Evans, A. Rai, J. H. Kim, B. R. Wygant and C. B. Mullins, *ACS Appl. Mater. Interfaces*, 2017, **9**, 30654.
31. D. Xu, Y. Rui, Y. Li, Q. Zhang and H. Wang, *Appl. Surf. Sci.*, 2015, **358**, 436–442
32. B. Klahr, S. Gimenez, F. Fabregat-Santiago, T. Hamann and J. Bisquert, *J. Am. Chem. Soc.*, 2012, **134**, 4294.
33. T. G. Vo, H. M. Liu and C. Y. Chiang, *Catal. Sci. Technol.* 2019, **9**, 4588.
34. L. F. Arenas, C. Ponce de León and F. C. Walsh, *Electrochim. Acta*, 2016, **205**, 226.
35. K. Obata and K. Takanabe, *Angew. Chem., Int. Ed.*, 2018, **57**, 1616.

THESIS OVERVIEW
AND
FUTURE PRESPECTIVE

THESIS OVERVIEW

This thesis focused on the multiple aspects on the design of metal oxide based photoanode devices and their effect on photoelectrochemical water splitting performance, mainly using $ZnFe_2O_4$, α-Fe_2O_3 and $BiVO_4$ as examples. The thesis is arranged as follows: Firstly, an introduction is given to the global energy consumption and challenges emerging to achieve a sustainable and zero emission production of energy (**Chapter 1**). A potential route to derive sustainable fuel from the conversion of solar energy via photoelectrochemical water splitting is also outlined in this chapter. Comprehensive literature survey with numerous ways to achieve efficient solar water splitting have been discussed. Finally, this chapter is concluded by a generalised framework to further improve the photoelectrochemical performance, as thesis objective. In **Chapter 2**, different instrumental techniques, performance parameters and experimental setup have been outlined to evaluate and understand the effectiveness of photoanodes. **Chapter 3** to **Chapter 6** provides some valuable outcomes which are obtained from the research done during my PhD tenure and it is summarised as follows:

- In **Chapter 3**, we have fabricated a solution processed $ZnFe_2O_4$ photoanode directly over FTO substrate. We discovered that with proper annealing temperature the photoelectrochemical water oxidation performance of $ZnFe_2O_4$ photoanode can be further improved. Also, the 1-D structure of $ZnFe_2O_4$ gives rise to efficient charge separation and provides a very short diffusion path for holes to reach the photoanode/electrolyte interface. With a thin Al_2O_3 overlayer with $ZnFe_2O_4$, the photocurrent increased up to 3-fold higher than those of optimized $ZnFe_2O_4$. Increased PEC performance is mainly due to (i) increase in compactness and improved crystallinity with higher annealing temperature, (ii) thin alumina overlayer reportedly contributed to the change of the lattice strain of $ZnFe_2O_4$ layers which decreased the density of surface trap states, (iii) surface passivation of $ZnFe_2O_4$ rather than the contribution of the oxygen evolution reaction (OER) from the passivation layer and (iv) efficient interfacial charge transfer by reducing the recombination processes i.e., the back transferring of photoexcited electron at photoanode/electrolyte interface.
- In **Chapter 4**, we demonstrated the design and synthesis of a stable hematite photoanode with sequential metal and non-metal incorporation to resolve the limiting factors such as

low carrier density and high charge recombination which hinder its practical applications. The effect of annealing temperature with P-modification have been studied and found that, when it was combined with Ti-doped Fe_2O_3, low temperature annealing is suitable for improved photoelectrochemical water oxidation performance. More than 5-fold enhancement in photocurrent density was observed for Ti and P co-modified hematite with an unprecedented cathodic shift of the onset potential. The enhanced PEC performance can be attributed to the combined effect of faster carrier mobility due to Ti-doping and reduced surface trap states due to P-modification results in better current density in the case of co-modified hematite. The present study concluded that, with a suitable environment the metal and non-metal co-modification of hematite can achieve higher PEC activities.

- In **Chapter 5**, we demonstrated a facile one step low temperature hydrothermal route for the controlled synthesis of boron nitride quantum dots (BNQDs). BNQDs has high negative charge density, particularly on the edge geometry, therefore it can act as an efficient hole extractor, which enhances the carrier separation on hematite surface and decreases the hole trapping probability. This work emphasized on two important parameters, i.e. (i) enhancement in carrier density via fluorine doping directly onto the substrate using soluble precursor, organic Selectflour (ii) modification with BNQDs to provide a simple, novel and effective strategy for the design and development of more efficient PEC water splitting systems. A 6-fold increment in photocurrent density was achieved for the co-modified hematite photoanode.
- In **Chapter 6**, we presented the surface co-catalytic modification of $BiVO_4$ for promoting water oxidation kinetics to enhance the interfacial charge transfer, lowering of onset potential for efficient photoelectrochemical (PEC) water oxidation. We have designed the $BiVO_4$ photoanode, coupled with a mixed metal hydroxide containing cobalt and rare-earth element cerium, where the addition of catalytically silent cerium to $Co(OH)_x$ not only enhanced the stability, but also improved the water oxidation kinetics. With $CoCe(OH)_x$ catalytic overlayer, a ~370 mV onset cathodic shift was observed, indicative of an efficient charge injection and enhanced surface oxidation kinetics with 3-fold enhancement in photocurrent density The water oxidation performance of $BiVO_4$ - $CoCe(OH)_x$ could be attributed to the synergistic effect of both cobalt and cerium, where cerium incorporation enhanced the surface passivation aiding the stability of the photoanode and formation of

Co(II)/(III) active sites fasten the surface kinetics of $BiVO_4$. We believe that the present design of $BiVO_4$ photoanode with mixed metal hydroxide provides a promising and efficient strategy for modification of photoanode with stable and highly active oxygen evolution co-catalysts.

FUTURE PRESPECTIVE

At present, the power conversion efficiencies of these metal oxides appear to be rather low. Although, $ZnFe_2O_4$ has a suitable band gap with high theoretical conversion efficiency, its fabrication is quite difficult due to need of high temperature for better crystallinity. Therefore, the fabrication methodologies for this material should be further improvised for a better photoelectrochemical performance. On the other hand, the major setback for hematite photoanode is its short hole diffusion length and slow surface water oxidation kinetics. The higher onset potential for both $ZnFe_2O_4$ and α-Fe_2O_3 is also another drawback which hinders their performance. Although, various surface modification methodologies significantly improved the abovementioned drawbacks up to some extent, still here is an urgent need to understand some other aspects such as electron mobility in the bulk, improving the lifetime of charge carriers and minimizing the surface defects. Compared to $ZnFe_2O_4$ and α-Fe_2O_3, $BiVO_4$ is on the positive side due its performance as a photoanode material and will remain to be of interest in the future. However, the performance of $BiVO_4$ is limited by its weak hole extraction properties at the surface, which needs to be resolved for improvising its performance. In my opinion, there are still many scopes available to further extend the presented work which is as follows:

- The poor crystallinity of $ZnFe_2O_4$ and α-Fe_2O_3 hindered its PEC performance. Increasing the crystallinity of these nanostructured photoanode would be beneficial to its PEC performance. Post-annealing for these nanostructured photoanode is the most direct way to improve its crystallinity, but the control of ramp rate, annealing temperature, duration, and atmosphere needs to be investigated carefully so as not to damage the nanostructure or undermine carrier mobility.
- Introduction of porosity to the nanostructured photoanode is a feasible way to increase the surface area for better water oxidation reaction. Combination of nanoporosity with a suitable morphology may possibly improve the performance of these photoanodes.

- Exploring new materials such as inorganic perovskite oxides with tunable crystallinity and morphology is another possible way to achieve improved PEC performance.
- Prediction of future structural properties by designing the photoelectrode materials with theoretical calculations, and combination of both theoretical investigation and experimental analysis will solve the limitations of new materials.
- Use of innovative and cost effective fabrication and synthetic methods for wide range of applications.

LIST OF PUBLICATIONS
AND
CONFERENCES ATTENDED

JOURNAL ARTICLES:

Included in the thesis:

1. **Tushar Kanta Sahu,** Suhaib Alam, Devipriya Gogoi, Nageswara Rao Peela and Mohammad Qureshi*, Effect of Catalytically Silent Cerium Hydroxide in Cobalt–Cerium Mixed Double Hydroxide for Enhanced Water Oxidation Kinetics in a $BiVO_4$ Photoanode. ***ACS Appl. Energy Mater.***, 2020, **3**, 5610-5619, DOI:10.1021/acsaem.0c00551

2. **Tushar Kanta Sahu,** Manoj Kumar Mohanta and Mohammad Qureshi*, Modulating Water Oxidation Kinetics Utilizing h-BN Quantum Dots as an Efficient Hole Extractor on Fluorine Doped Hematite Photoanode. ***J. Power Sources***, 2020, **445**, 227341, DOI: 10.1016/j.jpowsour.2019.227341

3. **Tushar Kanta Sahu,** Adit Kumar Shah, Avishek Banik, Mohammad Qureshi*, Enhanced Surface and Bulk Recombination Kinetics by Virtue of Sequential Metal and Non-Metal Incorporation in Hematite Based Photoanode for Superior Photoelectrochemical Water Oxidation. ***ACS Appl. Energy Mater.***, 2019, **2**, 4325-4334, DOI: 10.1021/acsaem.9b00548

4. **Tushar Kanta Sahu,** Adit Kumar Shah, Gaurangi Gogoi, Anindya Sundar Patra, Mohammad Shaad Ansari and Mohammad Qureshi*, Effect of Surface Overlayer in Enhancing the Photoelectrochemical Water Oxidation of in-situ Grown One Dimensional Spinel Zinc Ferrite Nanorods Directly onto the Substrate. ***Chem. Commun.***, 2018, **54**, 10483-10486, DOI: 10.1039/C8CC04882G

Work contributed /performed off the thesis:

5. Suhaib Alam, **Tushar Kanta Sahu** and Mohammad Qureshi*,One-Dimensional Co(OH)F as a Noble Metal-Free Redox Mediator and Hole Extractor for Boosted Photoelectrochemical Water Oxidation in Worm-like Bismuth Vanadate. ***ACS Sustainable Chem. Eng.***, 2021, **9**, 5155-5165, DOI: 10.1021/acssuschemeng.1c00288
6. Ching Thian Moi, Sourav Bhowmick, **Tushar Kanta Sahu** and Mohammad Qureshi*, Electrocatalytic Oxygen Evolution Surpassing Benchmark RuO_2 Using Stable, Noble Metal Free Vanadium Doped Hematite Co-modified by NiFe Layered Double Hydroxide. ***Electrochim. Acta***, 2021, **370**, 137726, DOI: 10.1016/j.electacta.2021.137726

7. Manoj Kumar Mohanta, **Tushar Kanta Sahu**, Suhaib Alam and Mohammad Qureshi*, Tuning the Electronic Structure of Monoclinic Tungsten Oxide Nanoblocks by Indium Doping for Boosted Photoelectrochemical Performance. ***Chem.: Asian J.***, 2020, **15**, 3886-3896, DOI: 10.1002/asia.202000787

8. Adit Kumar Shah, **Tushar Kanta Sahu**, Devipriya Gogoi, Peela Nageswara Rao, Mohammad Qureshi*, Surface-engineering of Decahedron Shaped Bismuth Vanadate for Improved Photoelectrochemical Water Oxidation by Indium Doping Coupled with Graphitic Carbon Nitride Quantum Dots. ***J. Power Sources***, 2020, **477**, 229024, DOI: 10.1016/j.jpowsour.2020.229024

9. Suhaib Alam, **Tushar Kanta Sahu**, Devipriya Gogoi, Nageswara Rao Peela and Mohammad Qureshi*, Bio-template Assisted Hierarchical ZnO Superstructures Coupled with Graphene Quantum Dots for Enhanced Water Oxidation Kinetics. ***Solar Energy***, 2020, **199**, 39-46, DOI: 10.1016/j.solener.2020.02.015

10. Sourav Bhowmick, Ankit Dhankar, **Tushar Kanta Sahu**, Rohan Jena, Devipriya Gogoi, Shane Ardo, Nageswara Rao Peela and Mohammad Qureshi*, Low Overpotential and Stable Electrocatalytic Oxygen Evolution Reaction Utilizing Doped Perovskite Oxide, $La_{0.7}Sr_{0.3}MnO_3$, Modified by Cobalt Phosphate. ***ACS Appl. Energy Mater.***, 2020, **3**, 1279-1285, DOI: 10.1021/acsaem.9b02167

11. Ching Thian Moi, Gaurangi Gogoi, **Tushar Kanta Sahu**, Devipriya Gogoi, Nageswara Rao Peela and Mohammad Qureshi*, Design of noble metal free hierarchical VS_2 onto WO_3 nanoflakes as an effective heterojunction strategy for enhanced photoelectrochemical water oxidation. ***Sustainable Energy Fuels***, 2019, **3**, 3481-3488, DOI: 10.1039/C9SE00719A

12. Manoj Kumar Mohanta, **Tushar Kanta Sahu**, Devipriya Gogoi, Nageswara Rao Peela, Mohammad Qureshi*, Hexagonal Boron Nitride Quantum Dots as a Superior Hole Extractor for Efficient Charge Separation in WO_3-Based Photoelectrochemical Water Oxidation. ***ACS Appl. Energy Mater.***, 2019, **2**, 7457-7466, DOI: 10.1021/acsaem.9b01450

13. Adit Kumar Shah, **Tushar Kanta Sahu**, Avishek Banik, Devipriya Gogoi, Peela Nageswara Rao, Mohammad Qureshi*, Reduced Graphene Oxide Modified $CuBi_2O_4$ as an Efficient and Noble Metal Free Photocathode for Superior Photoelectrochemical Hydrogen Production. ***Sustainable Energy Fuels***, 2019, 2019, **3**, 1554-1561, DOI: 10.1039/C9SE00129H

14. Gaurangi Gogoi, Sam Keene, Anindya Sundar Patra, **Tushar Kanta Sahu**, Shane Ardo and Mohammad Qureshi*, Hybrid of g-C_3N_4 and MoS_2 Integrated onto $Cd_{0.5}Zn_{0.5}S$: Rational Design with Efficient Charge Transfer for Enhanced Photocatalytic Activity. ***ACS Sustainable Chem. Eng.***, 2018, **6**, 6718-6729, DOI: 10.1021/acssuschemeng.8b00512

15. **Tushar Kanta Sahu**, Sonia Arora, Avishek Banik, Parameswar Krishnan Iyer and Mohammad Qureshi*, Efficient and Rapid Removal of Environmental Malignant Arsenic(III) and Industrial Dyes Using Reusable, Recoverable Ternary Iron Oxide - ORMOSIL - Reduced Graphene Oxide Composite. ***ACS Sustainable Chem. Eng.***, 2017, **5**, 5912-5921, DOI: 10.1021/acssuschemeng.7b00632

16. Avishek Banik, Mohammad Shaad Ansari, **Tushar Kanta Sahu** and Mohammad Qureshi*, Understanding the Role of Silica Nanospheres with their Light Scattering and Energy Barrier Properties in Enhancing the Photovoltaic Performance of ZnO Based Solar Cells. ***Phys. Chem. Chem. Phys.***, 2016, **18**, 27818-27828, DOI: 10.1039/C6CP05544C

CONFERENCES ATTENDED

1. Poster presentation at **International Conference on Advanced Nanomaterials and Nanotechnology** (ICANN-2017), IIT Guwahati, Guwahati, India, December 2017

2. Poster Presentation at **4th National Workshop on NEMS/MEMS and Theranostics Devices (NWNTD – 2018)**, IIT Guwahati, Guwahati, India, February 2018

3. Oral presentation at **International Conference on Frontiers in Chemical Sciences (FICS - 2018)**, IIT Guwahati, Guwahati, India, December 2018

3. Oral presentation at **International Conference on Advanced Nanomaterials and Nanotechnology (ICANN-2019)**, IIT Guwahati, Guwahati, India, December 2019

4. Poster presentation at **International Conference on Electrochemistry in Industry Health & Environment**, EIHE-2020, BARC, Mumbai, India, January 2020